RETROFITTING OF BEAM COLUMN JOINTS USING CONFINED HIGH PERFORMANCE HYBRID FIBER REINFORCED CONCRETE

A

Thesis

Submitted in fulfilment of the requirement

for the award of the degree of

DOCTOR OF PHILOSOPHY

by

Raju

Under the supervision of

Dr. Prem Pal Bansal

Associate Professor & Head

Department of Civil Engineering

Thapar Institute of Engineering and Technology

PATIALA

DEPARTMENT OF CIVIL ENGINEERING

THAPAR INSTITUTE OF ENGINEERING AND TECHNOLOGY

PATIALA-147004 (PUNJAB)

Dedicated

to

My Family

CERTIFICATE

Certified that the work presented in the thesis entitled "**RETROFITTING OF BEAM COLUMN JOINTS USING CONFINED HIGH PERFORMANCE HYBRID FIBER REINFORCED CONCRETE**" which is being submitted by Mr. Raju (Regn. No. 951502002) in fulfilment of the requirement for the award of the degree of 'Doctor of Philosophy' in the Department of Civil Engineering, Thapar Institute of Engineering and Technology, Patiala, is an authentic record of the candidate's own work carried out during the period from June 2015 to December 2019 at this Institute under my supervision. The matter presented in this thesis has not been submitted for the award of any other degree in any University.

17/2/2020

Dr. Prem Pal Bansal
Associate Professor and Head
Department of Civil Engineering
Thapar Institute of Engineering and Technology
Patiala 147004

DECLARATION

I hereby certify that the work which is being presented in this thesis, entitled **"RETROFITTING OF BEAM COLUMN JOINTS USING CONFINED HIGH PERFORMANCE HYBRID FIBER REINFORCED CONCRETE",** in the fulfilment of the requirement for the award of degree of 'Doctor of Philosophy' in Civil Engineering Submitted to Civil Engineering Department of Thapar Institute of Engineering and Technology (Deemed to be University), Patiala is an authentic record of my own work carried out under the supervision of Dr. Prem Pal Bansal, and wherever other research work is referred, it is indexed in the list of references.

The matter presented in this thesis has not been submitted in part or full to any other university or institute for the award of any degree in India or abroad.

Raju

ACKNOWLEDGEMENT

First of all, I would like to express my gratitude to my supervisor Dr. Prem Pal Bansal, Associate Professor and Head, Department of Civil Engineering, Thapar University, Patiala for his invaluable guidance, moral support and encouragement during the entire period of this research which cannot adequately be expressed in words in this acknowledgement.

I would like to extend my acknowledgment to my Doctoral committee member Dr. Rafat Siddique, Dr. Shruti Sharma and Dr. Rajiv Mehta for their valuable observations, suggestions, and feedback. Also, the inputs provided by Professor Dr. Naveen Kwatra and Associate Professor Dr. A. B. Danie Roy during the early stages of this research are invaluable.

During the execution of experiments, the help and support provided by technical staff Er. Varinder Kumar Sharma and Shri Ram Sumiran, Mr. Manreet Singh, Mr. Hitesh, and Mr. Suneet are greatly appreciated. I am very much grateful to my friends Sandeep Sharma, Rattandeep Singh Poonia, Upender Bishnoi, Kamal Anand for their help and support.

I would like to thanks my parents, Sh. Ganga Bishan, Smt. Leela Sharma, whose consistent love and support motivate me throughout the period of research. I would also like to thank my brother, Mr. Naveen Sharma, Sister-in-law Mrs. Ritu Sharma for their understanding, patience and valuable support.

Special thanks to my wife Nidhi Sharma for her understanding and support during the whole research program.

Above all, I thank almighty whose blessings have enabled me to accomplish this research work.

LIST OF PUBLICATION

Sharma R, Bansal PP Behavior of RC exterior beam column joint retrofitted using UHP-HFRC, Construction and Building Material (2019); 195: 376-389. (DOI: 10.1007/s40996-018-0202-4), (SCI, I.F – 4.046)

Sharma R, Bansal PP, Efficacy of Supplementary Cementitious Material and Hybrid Fiber to develop the Ultra High Performance Hybrid Fiber Reinforced Concrete, Advances in Concrete Construction 2019; 8 (1): 21-31. (DOI: https://doi.org/10.12989/acc.2019.8.1.000) (SCI, I.F – 2.618)

ABSTRACT

Presently, various multi storey buildings are serving to the societies which were constructed before the implementation of seismic codal guidelines. The change in occupancies of building, amendment in codal provisions and to meet the present seismic demand, there is an urgent need for up-gradation of these structures. In the past, various methods, such as steel plate adhesion, jacketing, and fiber reinforced polymer (FRPs), have been successfully deployed to retrofit the pre-seismically detailed structures. Nonetheless, the demerits associated with these techniques depict the limitation in the performance of the retrofitted BCJ. The initial damage level also significantly governs the retrofitting strategies and affects the performance of the retrofitted BCJ.

The newly developed high performance hybrid fiber reinforced concrete (HP-HFRC) revealed excellent properties (post-elastic ductility, strain hardening, higher tensile strain, higher bond strength and durability) which are expected from the retrofitting materials. Hence, it can be used as a new retrofitting material. Moreover, in past studies, much attention was not paid to the fact that what is the initial damage level of the beam-column joint before the time of retrofitting. Therefore, the present study explores the possibility of using HP-HFRC in the retrofitting of beam column joint which is initially damaged to different damage levels. In the study firstly, the HP-HFRC is developed using trial and error method and fresh, mechanical and durability properties were evaluated. Thereafter, the design mix is refined using Andreasen and Andersen (A&A) packing model. The fresh, mechanical, durability and microstructural properties are evaluated after 28 days of curing and are further used for retrofitting the initially damaged beam column joint.

In the second phase of the study, sixteen beam column joint specimens are cast and set of two specimens are tested as control specimens for each retrofitting strategy. The complete load displacement hysteresis behaviour of control specimens subjected to quasi-static reversed cyclic loading is recoded. Based on the obtained load displacement hysteresis of control specimen, the different damage levels viz., slight, moderate, severe and complete have been calculated using Park and Ang model. Further beam column joints have been initially damaged to achieve the above mentioned damage levels. Thereafter, the initially damaged specimens have been retrofitted using HP-HFRC and wire mesh confined HP-HFRC and tested under cyclic loading. The performance of retrofitted beam column joints has been measured in terms of load displacement behaviour, ultimate lateral drift capacity

displacement ductility, energy dissipation, stiffness, strength degradation, and principal tensile stress.

The proposed retrofitting strategies significantly affect the performance of the initially damaged beam column joint. An improvement of 14.28% and 28.57%, in ultimate drift ratio (UDR), as compared to control specimens has been observed after retrofitting with HP-HFRC and wire mesh confined HP-HFRC beam column joint, respectively. The ductility of HP-HFRC retrofitted beam column joint and wire mesh confined HP-HFRC depicts the maximum improvement of 45.29% and 63.23% respectively than control specimen. The energy dissipation capacity of HP-HFRC confined and wire mesh confined HP-HFRC retrofitted specimen is 8894 kN-mm and 11827.67 kN-mm, respectively. The maximum improvement in energy dissipation in wire mesh confined retrofitted specimen exhibited the 1.32 times improvement over the HP-HFRC confined retrofitted specimen. The maximum improvement in stiffness and strength retention has been observed in wire mesh confined retrofitted specimen than HP-HFRC retrofitted specimen. The excellent improvement in principal tensile resistance capacity along with lower rate of post elastic principal tensile resistance degradation is observed in wire mesh confined HP-HFRC.

The effect of initial damage level on the performance of HP-HFRC and wire mesh confined HP-HFRC retrofitted specimen is also evaluated. It has been found that the ultimate drift capacity (UDC) of confined HP-HFRC retrofitted initially complete damaged specimen decreased up to 28.57% and at the same initial damage level, wire mesh confined HP-HFRC retrofitted specimen regains the original drift capacity. Also, the increment in initial damage level decreases the ductility or vice versa. The slope of stiffness and strength degradation is decreased as the initial damage level shifting from complete to slight damage level which reflects the improvement in post elastic behaviour. The maximum improvement in energy dissipation has been found in initially slight damage specimen in both types of retrofitting strategy. Therefore, it is concluded that retrofitting of beam column joint using HP-HFRC and wire mesh confined HP-HFRC improves the overall performance of the beam column joint. However, the behaviour of BCJ retrofitted with wire mesh confined HP-HFRC is superior to HP-HRFC retrofitted joints, due to confinement provided by wire mesh. Further, the initial damage level significantly affects the performance of the retrofitted beam column joint. The performance of the retrofitted specimen improves as the damage level shifts from complete to slight.

TABLE OF CONTENTS

LIST OF TABLE

LIST OF FIGURES

CHAPTER 1
INTRODUCTION

1.1 GENERAL

The beginning of multi-storey framed structures revolutionized the urban development and participates significantly in nation development. The flexibility in the selection of architectural shape, less area coverage of the ground, better performance than brick masonry structures, freedom in the planning of inside space of a building and standard procedure for the construction are the significant characteristics which brought the attention of the user towards the use of framed structures. Initially, the concept of multi storey framed structures has not gained much popularity, but later it grew rapidly in the society due to the advantages as mentioned above offered by the framed structures and, in a very short period, the number of multi storeys framed structures had been constructed. At that point of time, the engineering skills were applied at the stage of designing of the framed structures only and mostly execution was done without any professional supervision and not much attention had been given to the quality control. These structures had performed well under gravity loads, and contractors were confident enough on their non-engineered construction skills. However, this illusion has been shattered soon when these structures were subjected to strong ground motion/earthquake. The serviceability of multi-story framed structure very much depends upon the performance of these structures during lateral forces. The forces imposed by the wind force exhibited the non-zero mean oscillation. Consequently, the building experienced one direction of motion and corresponding stresses; the building may experience a cyclic motion and stresses due to the wind, but, it never happened in a short interval of time. Apart from this, the earthquake forces exhibited the zero mean oscillation within a fraction of seconds and imposed an enormous amount of stresses on the multi-story framed structure.

In the last three decades, across the globe, numerous higher magnitude earthquakes *(India 2001; Indonesia 2004; China 2008; Japan 2011; Nepal 2015)* are noted consequently, tremendous devastations have been observed. It has recognized that the failure of framed structures due to an earthquake is one of the major contributors for the devastation, humanity loss, and economic loss e.g. 20,000 person death and over 1,67,000 injured in Bhuj earthquake *(Jain and Jaiswal, 2002).* The estimated economic loss because of this earthquake is placed at around Rs.22,000 crores reported by the national information centre of

earthquake engineering, Kanpur, India. The post-earthquake survey of Bhuj revealed that the absence of seismic resistance design and poor execution of construction practices are one of the reasons for the many kinds of failure in framed structures, as shown in Fig 1.1 *(Jaiswal et al., 2002)*. Also, various reasons such as poor material quality and execution skills; inefficient lap of rebar or more than 50% of rebar were lapped at one location; insufficient lateral ties in a column resulted in a buckling of the columns; strong beam weak column; floating columns; absence of ductility under strong ground motion and, brittle failure in beam column joint was responsible for the failure of framed structures. Among these, the *"weak column strong beam"* and *"brittle failure in beam column joint"* are the significant reasons for the complete collapse of framed structures. This key issue pushed the researchers/scientists to execute the research on BCJ, and results revealed that the joint under lateral loading led to the premature failure and ineffective post-elastic rotational ductility *(Beckingsale, 1980)*. The continuous research on joint subjected to lateral loading highlighted the key reasons for brittle failure and ineffectiveness in post-elastic stage *(Ali, 2014)*. These findings open up the new era of building studies, and subsequently, new guidelines were published in many countries regarding the ductility, strong column weak beam design philosophy and design of beam column joint (BCJ). These guidelines especially considering the effect of lateral loading viz., wind load, and seismic forces.

The BIS 13920 (2009) published the guidelines regarding the confinement of the joint using transverse reinforcement to achieve the efficient in-elastic rotation and ductility. The code emphasis on detailing of reinforcement in the joint through development length, stirrups in joint and special confinement detailing of reinforcement in the adjacent members (beam and column) up to the defined length. These standards are capable enough to construct the earthquake resistance building along with ductile behaviour. Recently, the new amendments in BIS 13920 (2016) regarding performance up-gradation of beam column joints are introduced viz., shear design of BCJ and principal to achieve the strong column weak beam joint. The implementation in BIS 13920 is the result of failure observed in frame structure during Jabalpur, 1997; Bhuj 2001; Sumatra 2004; Sikkim 2006, 2011 earthquakes. These earthquakes mentioned above resulted in a greater extent of damage to the infrastructures which are constructed using pre-seismic codal provisions; even some of the buildings constructed before the implementation of codal provision are still functioning and serving on a large scale to the society. The performance of framed structures significantly depends upon the basic seismic capacity parameters (strength, stiffness, in-elastic deformation capacity, and

energy dissipation capacity) of BCJ. All parameters are expected to deteriorate as the number of damaging cycles and the amplitude of cycles increases *(Karayannis et al., 2008; Chalioris et al., 2008).* Therefore, to meet the present seismic demand, it is mandatory to increase the capacity of pre-seismically designed beam column joint by offering the ductility and post-yield rotation parameters. The strengthening/rehabilitation/retrofitting is one of the most feasible solutions to increase the seismic capacity of BCJ or early age built structure.

The strengthening/rehabilitation/retrofitting is the scientific method for the up-gradation of the damaged structures. The previous literature revealed that the retrofitting of the early age built beam column joint improves the seismic performance. The increased stiffness, improved energy dissipation and a lower rate of strength and stiffness degradation are the improvements observed by retrofitted beam column joint *(Chidambaram and Agarwal, 2015; Kheni et al., 2015).* The retrofitting of damaged BCJ using steel plate, concrete jacketing, FRP wrapping, are the popular technique at the local and global scale *(Lakshmanan 2006; Niroomandi et al., 2010)*. However, the demerits associated with each technique and different extent of damage to the BCJ of the building at each story level urgently required a new level of versatile material and suitable methodology of retrofitting based on the level of the initial damage.

The extent of damage is the matter of concern to decide the methodology and material for the strengthening/ retrofitting of damaged buildings. The guidelines published for the damage assessment, analysis, and retrofitting strategy published by ACI 31, ASCE 356, and ACI 41 inline the retrofitting practitioner of a different country.

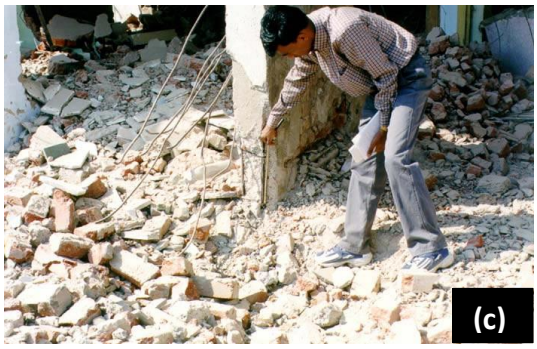

Fig. 1.1 - a) Lower Amount of Lateral Reinforcement and Poor Construction Material Led to Brittle Failure of Column Just Below the Beam-Column Junction (2001 Bhuj Earthquake); (b) Inappropriate Confinement and Maximum Lapping of Bars at One Location Led to Severe Damage and Plastic Hinge Occurred at Ground-Floor Column (2001 Bhuj Earthquake); (c) Measuring Damage Length in Ground Floor Columns *(Jaiswal et al., 2002)*

Recently, the development in the field of material i.e., High-performance concrete (HPC); Ultra high-performance fiber reinforced concrete (UHP-FRC), and Ultra high-performance hybrid fiber reinforced concrete (UHP-HFRC) are also one of the novel solutions for the retrofitting of structures. These materials remove the congestion of steel and also successfully applied for the retrofitting of damaged BCJ *(Khana et al., 2018*). The confinement effect offered by FRP; HPC; UHP-FRC; UHP-HFRC enhanced the hysteresis performance of initially damage beam column joint. The confinement effect of FRP on ultra high performance concrete exhibits 98% and 195% improvement in ultimate strength and ultimate strain, respectively, as compared with unconfined UHPC *(Zohrevand and Mirmiran, 2012).*

1.2 BUILDING FRAMES

A building is an enclosed structure that has walls, floors, a roof, and usually a window. The early built Monadnock Building, 1889 in Chicago, is the example of the beginning of an era of building construction using brickwork (Fig 1.2). This structure is the best example of ever built tallest load-bearing brickwork building. The building provides floor wise livelihood to many human beings and occupies the very less inbuilt area. The flexibility of less inbuilt area with the maximum livelihood facility raises the interest of the use of building frames in the society. The research and development in building construction resulted as a building frame, which is a skeleton of concrete containing horizontal (beam and slab), and vertical members (columns) are connected in a fixed/partially fixed manner. The consistent research on building offered the paradigm shift in terms of the load transfer mechanism using frame construction. The load transfer using different reinforced concrete building elements i.e., slab,

beam, column, and the foundation, has been observed in an efficient way to achieve better performance (Fig 1.3).

Fig. 1.2 - Tallest Load-Bearing Brick Structure in the World “Monadnock Building, 1889” Stored in Chicago Historical Society (HB-19320-C). (Photographer: Hedrich Blessing.)

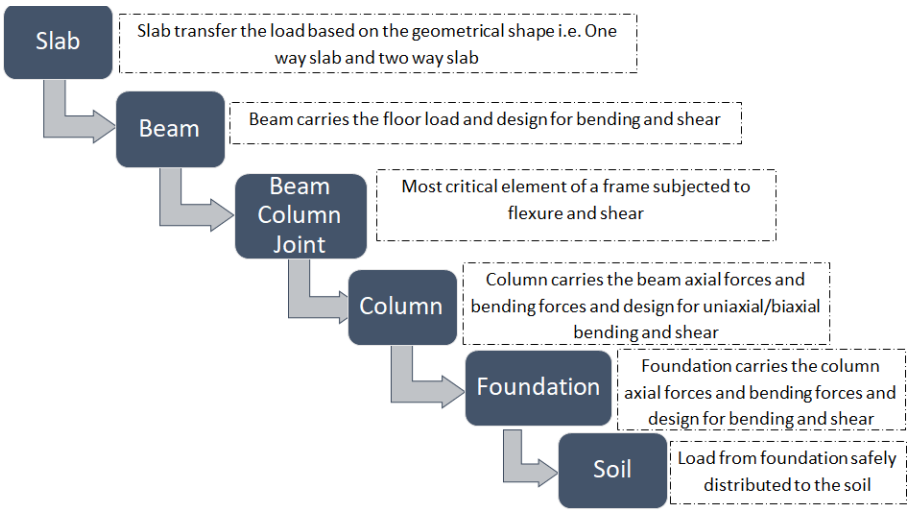

Fig. 1.3 - Load Transfer Mechanism in Building Frame (Slab – Beam – Column – Foundation – Soil)

This mechanism is efficient under the gravity loading action, however, many types of failure such as ponding, soft story, and failure of the individual structural element during earthquake across the globe developed a better understanding of structural engineers in designing the

building frame to resist the lateral loading. Knowledge of additional parameters such as seismic configuration, lateral stiffness, strength, and ductility/post elastic rotation, etc. of the building frames is required to improve its performance during an earthquake. The importance of the parameters is briefly described below;

- **Seismic Configuration** - The simple geometry of the building eliminates the plan irregularities i.e., torsional irregularities, re-entrant corner, diaphragm discontinuity and vertical irregularities (stiffness irregularity and mass irregularities). The building with very less plan and vertical irregularities resist higher earthquake force with minimal losses. Often the limitation of land availability and architectural challenges led to the construction of plan/vertical irregularities. The plan/vertical irregularities also nowhere mentioned in IS 1893:1962, 1966, 1970, 1975, and 1984. The amendments in IS 1893:2002 published the types of irregularities and their effect on lateral behaviour of the building frame.
- **Lateral Stiffness** – The lateral stiffness is the ratio of the applied lateral load to the corresponding lateral deflection. The minimal lateral stiffness is required to safeguard the occupants.
- **Lateral Strength** – The maximum load carrying capacity of the building under earthquake forces is considered the lateral strength of the building. The minimum lateral strength is significantly required in each direction of the building frame to bear the moderate earthquake.
- **Ductility** – The ratio of ultimate lateral displacement to the yield displacement defines the ductility. A higher unit less number (ductility) eliminate the brittle collapse of the frame and provide the higher serviceability (see Fig. 1.4).

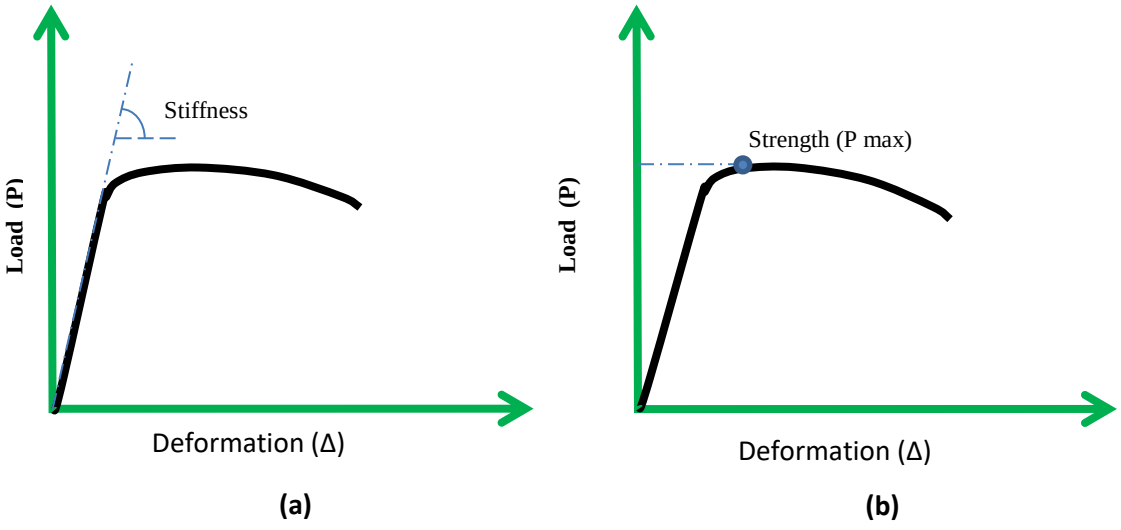

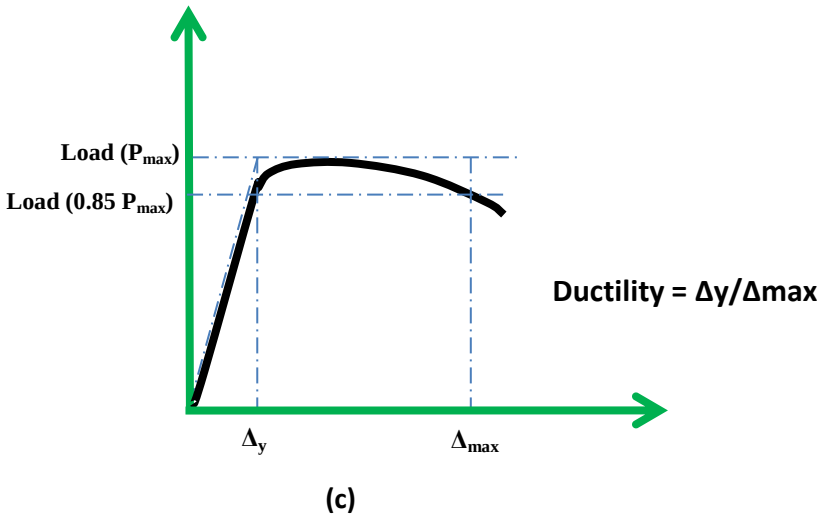

Fig. 1.4 – Lateral Load Displacement Curves of a RC Building, Showing (a) Stiffness, (b) Strength, and (c) Displacement Ductility *(Murthy et al., 2012)*

The requirement of the above-described parameter laid the foundation of different types of reinforced concrete frame, which are moment resisting frame (MRF), ordinary moment resisting frame (OMRF) and special moment resisting frame (SMRF). IS 1893 defined that the member and joint resist the forces mainly by flexure in MRF. Further, the MRF categorize in an ordinary and special category. The frame is called ordinary if the reinforcement detailing is not enabled to offer the ductile performance, whereas the frame which reinforcement detailing is done under the guidelines of IS 4326/13920/SP 34 is called special moment resisting frame. These guidelines are the resultant of a better understanding of parameter associated with the load transfer mechanism of building frame during post yielding state. Consequently, the structural engineers minimize the extent of damage of the building frame under severe dynamic loading.

1.2.1 Behaviour of Building Frames during Earthquake

The behaviour of building frames during an earthquake depends on the dynamic characteristics of the building. Oscillation and damping are significant dynamic characteristics that need to be studied to understand the behaviour of the building during an earthquake. The natural period and deformed shape in which the building is oscillated is used to define the mode of oscillation. The natural period depends upon the mass and stiffness of the building frame. Also, the natural period of the building depends on the distribution of mass and stiffness along with the building. Usually, the natural period of 1 to 20 stories normal RC buildings are in the range of 0.05 - 2.00 seconds. The light and stiff buildings

have a lower natural period than heavy and flexible building. For the same height and plan of the building frame, the increment in stiffness reduces the natural period. The increases in the mass of a building for the constant height and plan result in the larger natural period. Apart from these parameters, if the height of the building is increased for the constant plan dimensions, the natural period increases. Also, the study of mode shape revealed the significance of deformed shape subjected to lateral forces. The mode shape can be affected with the alteration in structural elements of the building e.g., the increment in flexural stiffness of bending member relative to the column changes the mode shape from flexural type to shear type. In the context of failure behaviour of frame building, the maximum energy released in the non-linear stage. Fig. 1.5 shows the concentration of plastic hinge at the ground story because of facilitating the parking and in-filled wall constructed above the ground floor. This type of failure is termed as soft story failure as described in the sixth revision of IS 1893 clause 20.4.1 i.e., "*It is one in which the lateral stiffness is less than in the story above. The story lateral stiffness is the total stiffness of all seismic force resisting elements resisting lateral earthquake shaking effect in the considered direction*". The concentration of stresses has occurred in the column at both ends and maximum energy is dissipated through these ends. Such a building does not show ductile behaviour under lateral forces. Likewise, the pre-seismic practices are unable to incorporate the required dynamic characteristics in the post-elastic region of framed structures to resist the strong ground motion. Consequently, the brittle failure in a joint is the cause of the brittle collapse of the structure. Further, the research revealed that the column reinforcement ratio less than 2%, column lap splices just above floor level, large spaced column transverse reinforcement, construction joint adjacent to the joint, strong-beam weak-column condition and absence of confinement in the joint has resulted in a brittle collapse of the frame structures (see Fig. 1.6).

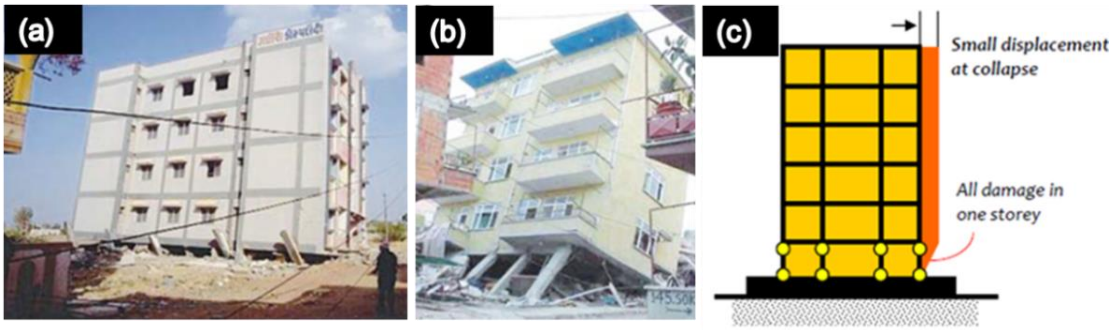

Fig. 1.5 – (a) Building Collapse Due to Soft Story During the Gujarat Earthquake M 7.7 *(Patnala et al., 2016),* (b) Soft Story Failure Observed During Earthquake in Turkey M7.4 *(Patnala et al., 2016)* (c) Schematic Representation of Damage Location in Soft Story Failure *(Murthy et al., 2012)*

Therefore, the huge amount of research has taken place in last three decades dedicated to studying the effect of lateral stiffness, unconfined beam column joint, confined beam column joint and weak-column strong-beam or strong-column weak-beam to differentiate the effectiveness of all these key elements on the behaviour of frame structure during the post-elastic stage.

Fig. 1.7 shows the uniform distribution of plastic hinges throughout the height of the building, which exhibited ductile performance. The energy is dissipated uniformly rather than dissipated from a specific area of the building frame, which avoids global failure. To achieve the ductility in a building frame, it is imperative to adopt the strong column weak beam theory. The ratio of moment of the column to beam should be near to 1.4, as shown in eq. 1-3. The hinge formation in the beam does not exhibit the brittle failure further, the confinement in the joint regain enable the member to sustain the stress for a longer duration by reducing the stiffness degradation in each cycle. This concept is recently introduced in the first revision held in 2016 of IS 13920 clause 7.2 (see Fig. 1.8) to achieve the ductility through rotation in a beam in the post elastic state.

Fig. 1.6 - Shear Failure of Beam Column Joint under Strong Ground Motion in Kocaeli, *1999 (Ghobarah and Said, 2002)*

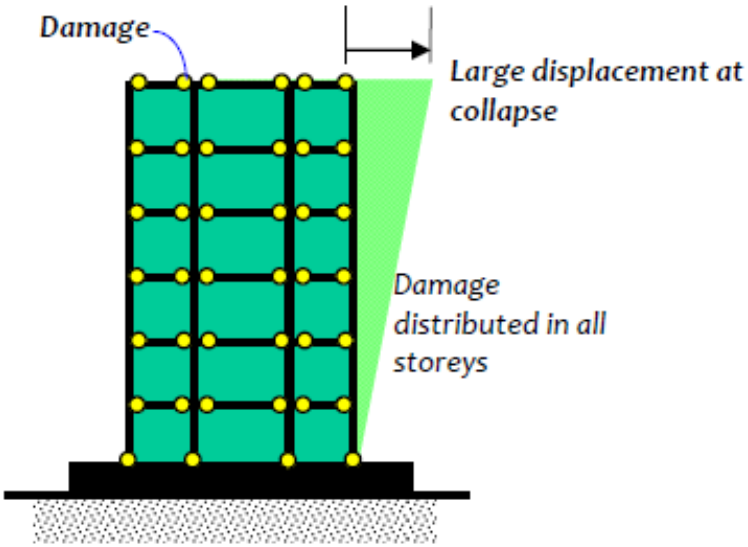

Fig. 1.7 - Uniform Distribution of Plastic Hinges in a Framed Structure *(Murthy et al., 2012)*

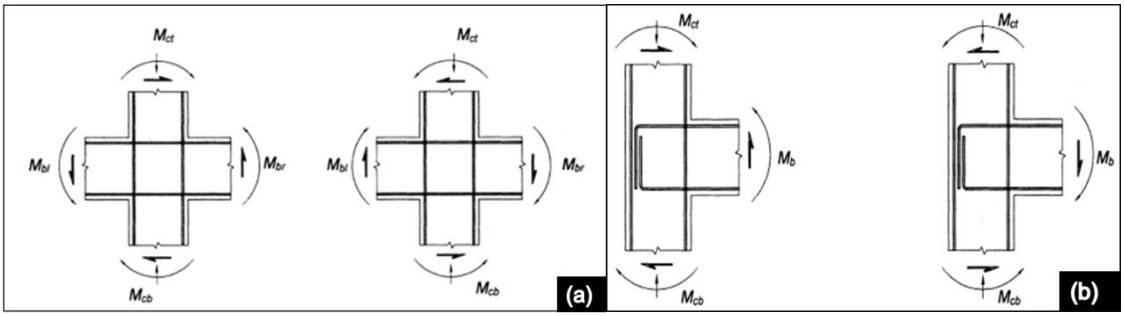

Fig. 1.8 - Schematic Representation of Strong Column Weak Beam Concept Introduced in, a) Interior Beam Column Joint, b) Exterior Beam Column Joint

$$\Sigma M_c = 1.4\Sigma M_b \quad (1.1)$$

Where, $\Sigma M_b = M_{bl}+M_{br}$ (1.2)

$\Sigma M_c = M_{ct}+M_{cb}$ (1.3)

Mc is the moment in the column is a summation of the moment of a column above the floor (M_{ct}), and below the floor, M_{cb}, and M_b is the moment in a beam is a summation of the moment of beam right of the joint (M_{br}) and beam left of the joint (M_{bl}). The amalgamations of the above-mentioned parameters in a codebook reflect the significance of beam column joint for the ductile performance of the R.C. frame building in the post-elastic region. These parameters achieve the lower strength degradation, higher stiffness retention, control in energy dissipation per cycle, higher ductility of the whole frame subjected to cyclic loading.

1.2.2 Type of Beam Column Joint in Frame

The type of beam column joint can be categorized based on;

1. Geometrical Configurations
2. Performance Expectancies

Based on geometrical configurations, the BCJ can be interior, exterior, and corner type. The interior joint can be defined as the location on the column face where the beams from all sides are meeting. The meeting point is considered as the interior joint. In the case of the exterior joint, one beam meets a column face and at the same location, the other two beams from perpendicular directions are meeting. The corner joints are those in which the two adjacent faces of the columns are supporting the beams which are coming from their respective directions. Based on performance type, the ACI352R-02 defined the BCJ as Type I and Type II BCJ. The BCJ is defined as Type I, if the concrete frame members are designed to carry gravity loads and are not capable of offering inelastic deformations. However, if the concrete frame is designed to take care of gravity loads and dissipates energy through a reversal of deformation into the post elastic plateau, then the beam column joints are defined as Type II joints. The Type I joints have no reinforcement to resist the shear force through the joints whereas, type 2 joints are constructed in reliance with modern codes offering the following characteristics;

1. Adequate transverse reinforcement ties within the joint as shear reinforcement.
2. Adequate ductility in the joint regions
3. Strong column-weak beam joints.

Eventually, these entire features enable the joint to sustain higher lateral drifts and offer the opportunity for the plastic hinge to form in the flexural member. Also, the adjoining members utilized the ultimate capacity and exhibited a lower rate of strength degradation.

1.2.3 Forces Acting on a Beam Column Joint

It is imperative to comprehend the nature of forces acting in the beam column joint before the expected improvement in the performance of frame structures subjected to lateral loading. Fig.1.9a shows the 3D model of the RC framed structure. The locations of the corner, interior and exterior BCJ are marked in the plan of the structure as shown in Fig. 1.9b. Due to the external forces acting at the face of the joint, the bending moment and shear forces are generated in the beam, column, and joint area. The exterior BCJ is taken as an example to

explain the force mechanism, as shown in Fig 1.10. In the exterior beam column joint, the bending moment above and below the joint are opposite in nature. It has been seen that the nature of the bending moment changes in the joint region, which reflects the location of a large magnitude of shear force/shear stress. The higher magnitude of shear stress led to generate the higher principal diagonal tensile stresses. Sooner, the cracks in the joint appear once the magnitude of principal tensile stresses surpasses the tensile strength of the concrete, as shown in Fig. 1.11. Further, the joint subjected to cyclic loading exhibited excessive shear deformations. So, it is important to calculate the joint shear force capacity of the BCJ.

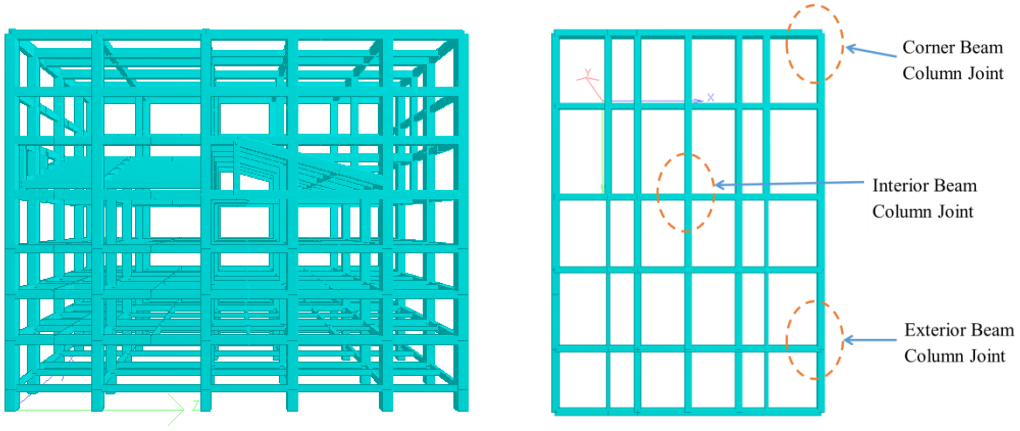

(a) (b)

Fig. 1.9 (a) STADD Modal of Multi-Story Framed Structure; (b) Plan of Multi-Story Framed Structure

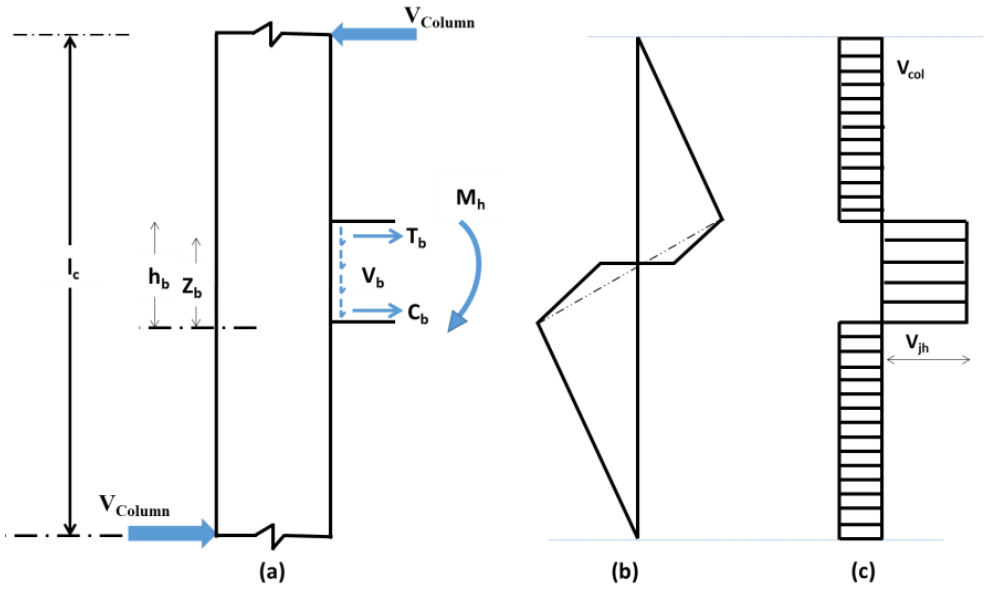

Fig. 1.10 - Exterior Joint Subjected to Horizontal Shear Force (a) Forces Acting on the Beam Column Joint Assembly; (b) Bending Moment in BCJ; (c) Shear Force in BCJ

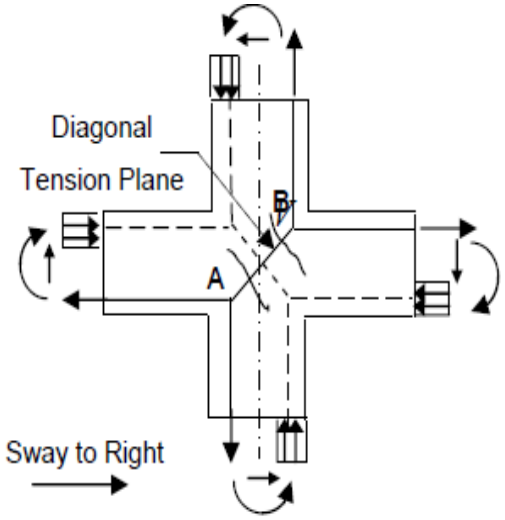

Fig. 1.11 - Interior Joint Panel Exposed to Lateral Forces *(Macgregor, 1988)*

The column and joint horizontal shear force can be found out using equilibrium principals. The shear force in the column is calculated equation 1.1

$$V_{col} = \frac{T_b Z_b + V_b \frac{h_c}{2}}{l_c} \tag{1.4}$$

The horizontal joint shear force across the joint can be calculated using eq. 1.2

$$V_{jh} = V_{col}\left(\frac{l_c}{Z_b} - 1\right) - V_b\left(\frac{h_c}{2z_b}\right) \tag{1.5}$$

$$V_{col} = Column\ shear$$
$$T_b = Tensile\ force\ of\ beam\ reinfrocement$$
$$Z_b = lever\ arm$$
$$h_c = column\ depth$$
$$l_c = Story\ height$$

Moreover, the engineering design approach is much easy than the above-explained method to estimate the horizontal shear in a joint. Fig. 1.12 represents the schematic illustrations of joint shear equilibrium in the exterior joint.

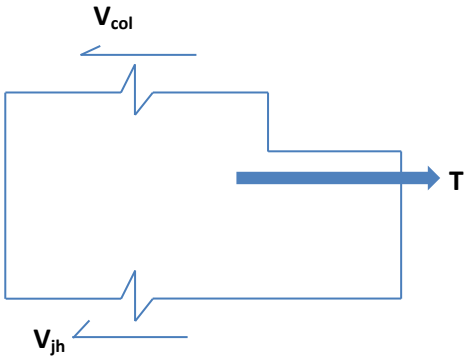

Fig. 1.12 - Joint Shear Equilibrium

The column shear, $V_{col}$is calculated using eq. 1.3

$$V_{col} = \frac{M_h}{l_c} \tag{1.6}$$

Where M_h is the hogging moment in a beam.

The corresponding joint shear $V_{jh}$is;

$$V_{jh} = T - V_{col} \tag{1.7}$$

Generally, the magnitude of joint shear calculates using an engineering design approach always higher than the joint shear calculated using equation 1.4 -1.5.

1.2.4 Behaviour of Beam Column Joint during Earthquake

The ACI 352R-02 defined the BCJ as "*The joint is defined as the portion of the column within the depth of the deepest beam that frames into the column*". The abrupt seismic forces stimulate the stresses in a BCJ. Therefore, if the BCJ is confined as per the latest guidelines published in BIS 13920 (2009; 2016)/ACI 352R-02, then the premature failure of the structure can be avoided. But, the non-seismically built beam column joint has an urgent need of strengthening/rehabilitation and retrofitting. These reasons are sufficient for researchers to deploy their keen interest in up-gradation/strengthening the behaviour of non-ductile or early built BCJ framed structures. Over the last decades, the researchers *(Kheni et al., 2015; Mukherjee and Joshi, 2005; Chidambaram and Agarwal, 2015; Singh et al., 2015)* are putting their sincere efforts to comprehend the behaviour of retrofitted BCJ. Figure 1.13 (a–d) illustrate the retrofitting of beam column joints by using novel material; geogrid and steel fiber reinforced concrete confinement, high performance concrete, up-gradation of early age built beam column joints using GFRP and CFRP, and retrofitting of early age beam column joints by CFRP rapping overlay by procured carbon plate (25mm wide and 1.2mm thick) respectively. The previous literature revealed that the retrofitting of early age BCJ improves seismic performance. The strengthening/up-gradation/rehabilitation/retrofitting is the prime way to improve the performance of BCJ, which eventually contributes to the ductile performance of R.C. framed structures subjected to higher magnitude earthquakes.

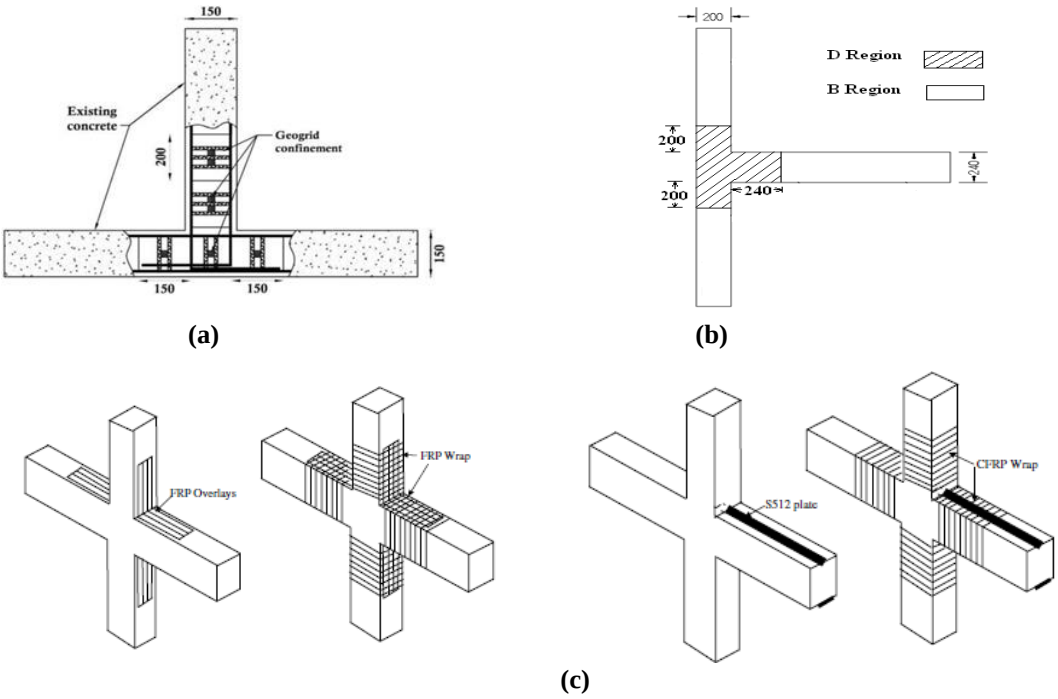

Fig. 1.13 - Retrofitting of Beam Column Joint by Various Techniques; *(a) Chidambaram and Agarwal, 2015; (b) Kheni et al., 2015; (c) Mukherjee and Joshi, 2005*

1.3 RETROFITTING

Specifically, the technique 'retrofitting' is evolved for the early age built structures to enhance the performance during the earthquake and fulfill the structural strength requirements. The consequences of retrofitting are strength improvement, improved energy absorption, improved ductility, and serviceability enhancements. As per ASCE/SEI 41-06 "*Seismic rehabilitation is defined as improving the seismic performance of structural and/or non-structural components of a building by correcting deficiencies identified in a seismic evaluation. Seismic evaluation is defined as an approved process or methodology of evaluating deficiencies in a building, which prevent the building from achieving a selected rehabilitation objective*". The application of retrofitting on any structure initially gone through the various stages; firstly the evaluation methodology for the building which is subjected to be retrofitted; secondly, based on available data from seismic evaluation, the retrofitting strategies need to be finalized. The detailed procedure of retrofitting is provided in ASCE/SEI 41-06. The various benefits of retrofitting of old structures as compared to building a new structure are cost optimization, less time required to make the structure fit for reuse, flexibility to opt the global retrofitting, and local retrofitting for immediate use. Generally, in the following cases, existing RCC structures are required retrofitting;

- The early degradation of structures due to various reasons e.g., irregular maintenance, aging of material and structure, code amendments (zone I merge in Zone II - IS 1893:2002).
- The structure partially degraded due to strong ground motion, strong wind, and fire, etc.
- Various historical monuments still serving in the society needs rehabilitation and
- Purpose of occupancy change led to an increase in load on the slab, beam, and column.

1.3.1 Requirement of Retrofitting

The beam column joint designed for gravity loading is not able to perform efficiently under lateral loading/seismic loading. Up to some extent, these joints sustained the lateral forces but, sooner, cross the elastic limit and perform very poor in the post elastic region. During the post elastic region, the strength and stiffness degradation of the joint is rapid and minimal ductility is achieved. Therefore, a mismatch between the seismic demand and seismic capacity of beam column joint urgently required an up-gradation/strengthening and retrofitting. Following are the conditions under which beam column joint required a strengthening/retrofitting;

1. Absence of confinement in the joint region
2. Weak column strong beam joint
3. Column main bar lapped just above and below the floor
4. Poor construction Practices

All these issues laid a foundation for the brittle failure of the BCJ during seismic forces and are the prime reason for destruction during an earthquake. Therefore, the non-ductile detailed structure required a retrofitting for the performance up-gradation.

1.3.2 Development in Retrofitting

The structural deficiencies and continuous material degradation in pre-seismically design structures or even in newly built structures established a platform for the development in the field of retrofitting.

Also, the retrofitting materials and techniques revealed the limitations in terms of durability. The various limitations are bonding of new with old material, a de-bonding failure between FRP and old concrete interface due to epoxy failure, the moderate ductile performance of

retrofitted structure, and rupture of FRP due to stress concentrations at the rectangular corner of the structural element. Nowadays, development in retrofitting is being happened in two categories;

1) Retrofitting through advanced material
2) Retrofitting through various techniques

1.3.2.1 Retrofitting through advanced material

The recent developments in materials enhanced the performance of retrofitting structures. The materials such as high performance concrete, FRP, and epoxy are the major concerned which fulfill the strengthening requirement of structural elements. Fig. 1.14 illustrates the material development and their merits, which enlarges the area of retrofitting.

1.3.2.2 Retrofitting through various techniques

The performance of retrofitting structure depends on techniques which are applied for strengthening the structures. The types of anchorage devices, pre-stressing of FRPs, laminates, and various standards cover the retrofitting development through techniques. Moreover, the orientation of overlay FRP has also revealed a substantial effect on the performance of the retrofitted structure. Fig. 1.15 shows the various techniques and their merits, which remarkably differentiate retrofitting development.

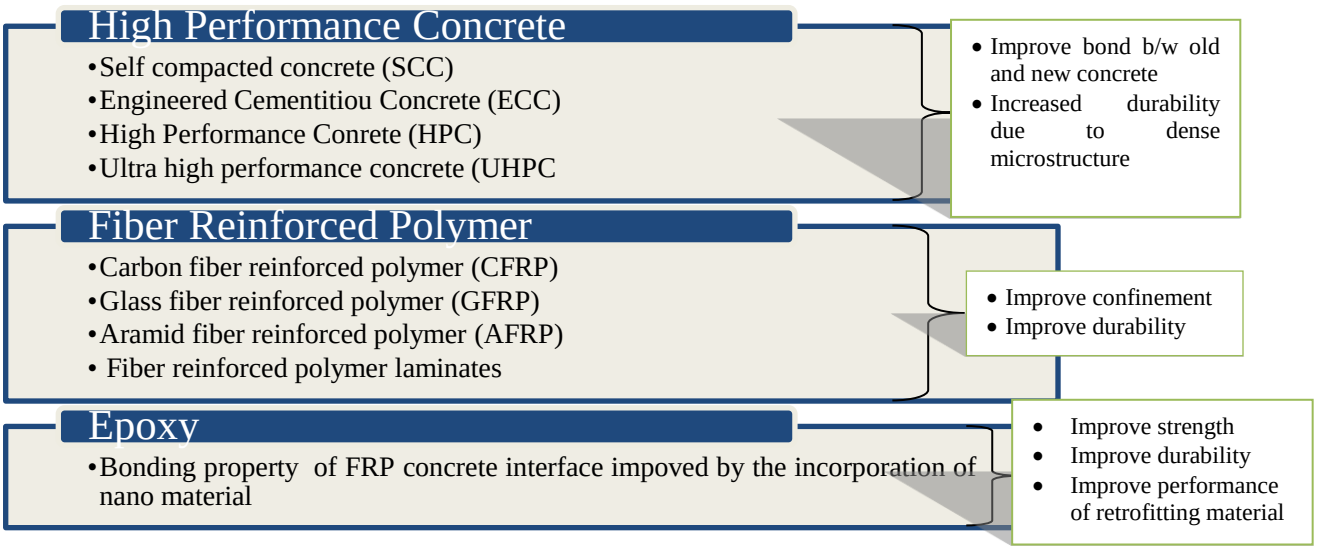

Fig.1.14 - Development in Retrofitting through Advanced Materials

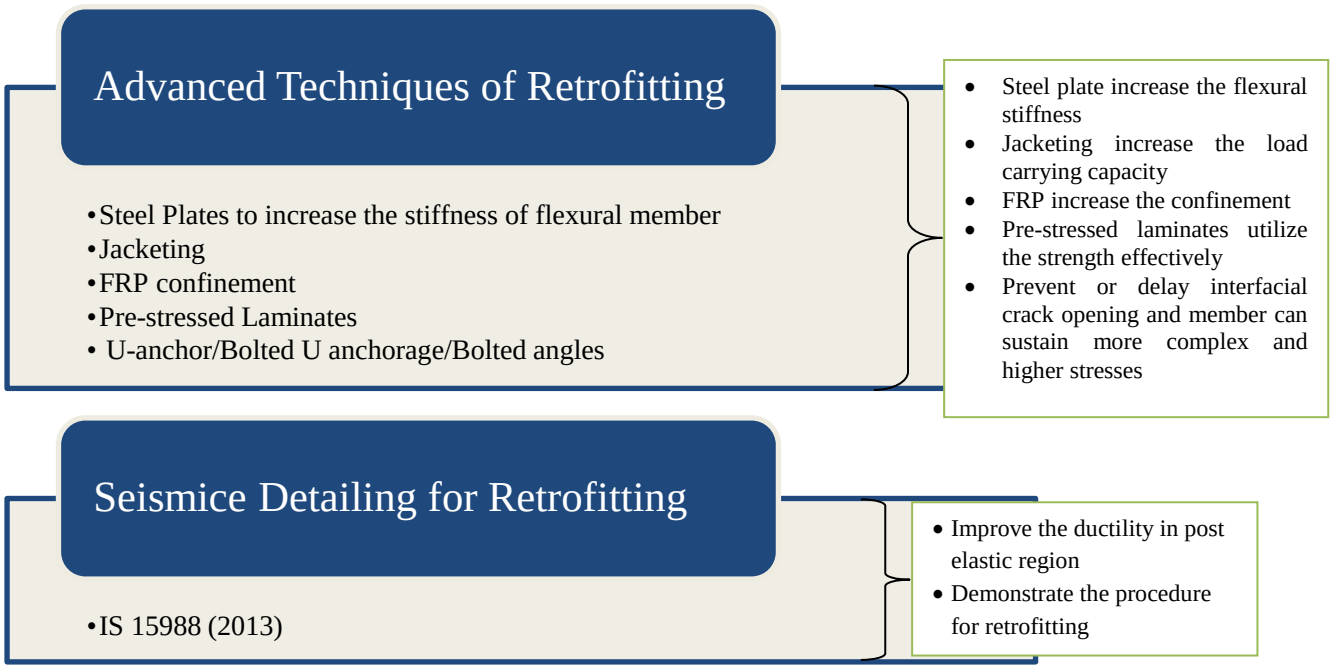

Fig.1.15 - Development in Retrofitting through Advanced Retrofitting Techniques

1.4 AIM OF THE STUDY

The pre-seismically designed beam column joint of the framed structures revealed the shear failure and rapid degradation of strength in post elastic rotation. The distress beam column joints have been retrofitted using various retrofitting techniques, e.g., steel plate adhesion on flexure members, jacketing, FRP sheets and laminates, anchor bolts, etc. However, the demerits associated with each retrofitting techniques such as steel plate starts corroded after environmental exposure, jacketing reduces the free inside space of building, de-bonding between the FRP concrete interface eliminates the ductility, stress concentration on the nearby area of anchor bolt restrict the utilization of efficiency of retrofitted material and resulted in brittle failure depicts the limitation in performance of retrofitted BCJ. It has also been observed that the initial damage level significantly determinates the type of material and technique used for retrofitting. Also, the extent of the initial damage level affects the performance of the retrofitted BCJ.

Therefore the present study aims is to develop novel material for retrofitting the BCJ. The material which will be developed in this study for retrofitting would offer benefits like eliminating the reduction in inside space of frame structure, corrosion due to environmental exposure, de-bonding between the interface and most significant property i.e., ductility.

Also, the effect of the extent of the initial damage on the performance of the retrofitted beam column using developed novel material will be evaluated.

1.5 ORGANIZATION OF THESIS

- ***Chapter 1 - Introduction***

  The chapter one discusses the behaviour of reinforced concrete framed structure, cause of premature failure in pre-seismically designed building, different country codal provisions for attaining the effective inelastic performance, the significance of beam column joint for the ductile performance of the building and the need of retrofitting of the damaged buildings.

- ***Chapter 2 - Literature Review***

  The literature review covers the various retrofitting techniques and their effects on the retrofitted non-ductile/ductile beam column joints. The effect of various parameters of retrofitting e.g., orientation of FRP, different anchorage techniques, different types of FRP sheets, and numbers of a layer of FRP, etc. on the performance of retrofitted specimen has been discussed. The performance of retrofitted beam column joint using advanced material such as high performance concrete (HPC), high performance hybrid fiber reinforced concrete (HP-HFRC) and ultra high performance hybrid fiber reinforced concrete (HP-HFRC) has also been discussed in detail.

- ***Chapter 3 - Development of HP-HFRC***

  The high performance hybrid fiber reinforced concrete has been prepared using two different methods; trail method and modified Andreasen and Andersen model. The fresh mechanical and microstructural properties of developed HP-HFRC have been reported.

Chapter 4 - Retrofitting of initially damaged Beam column joint using HP-HFRC

The performance of initially damage exterior beam column joint retrofitted using HP-HFRC has been reported in this chapter. The control beam is tested till failure under quasi-static reverse cyclic loading, and load displacement hysteresis has been prepared. Park and Ang's model has been used to calculate the different damage state of the beam column joint from the load displacement hysteresis of the control specimen. Further, the fresh beam column joints have been initially damaged to their corresponding damage level. Then all the initially damaged beam column joints are retrofitted and then tested

under reversed cyclic loading. The performance of retrofitted specimen is compared with the control specimen and the effect of initial damage level on the retrofitted beam column joint using HP-HFRC has been assessed.

- ***Chapter 5 - Retrofitting of initially damaged Beam column joint using wire mesh confined HP-HFRC***

  The procedure of testing, obtaining initial damage level, and retrofitting strategies is the same as described in chapter 3. Once the initial damage state of beam column joint has been achieved, the damaged specimens are retrofitted using wire mesh confined HP-HFRC and then tested under reverse cyclic loading. The performance of wire mesh confined HP-HFRC retrofitted specimen is compared with the control specimen, and effect of initial damage level on the retrofitted beam column joint has been reported.

CHAPTER 2

LITERATURE REVIEW

2.1 GENERAL

The beam column joints have a significant contribution to the long-term serviceability of concrete structures. During strong ground motion, beam column joints are susceptible to complex stresses, which make it more prone to failure. Specifically, the exterior beam-column connections suffer more in comparison to interior ones (*Kheni et al., 2015*). However, the level of damage in a beam column joint is one of the major factors for deciding the retrofitting methodology to enable the whole building again functional. The sequence of the most favourable technique of retrofitting using different material is; steel plate's adhesion on distress section of the structural element, jacketing using reinforced concrete (self-compacted concrete/high performance concrete (HPC)/high performance hybrid fiber reinforced concrete (HP-HFRC)) and fiber reinforced polymers (FRP). However, the steel plates adhesion on the distress section of the structural element very much depends upon the type of epoxy used to adhere to the plate with the surface and treatment offered on a steel plate to make the plate highly durable *(Kumar et al., 2017)*. Among these, the most adaptable material in the field of retrofitting is fiber reinforced polymer. Various researchers (*Alcocer and Jisra, 1993; Antonopoulos and Triantafillou, 2003; Karayannis et al., 2008; Akguzel and Pampanin, 2010; Hamid et al., 2013; Ganesan et al., 2014; Shah et al., 2016*) studied the seismic behaviour of retrofitted BCJ using FRP. These authors reported that the various parameters such as FRP orientation, FRP effectiveness in the non-seismically detailed specimen, type of FRP, and magnitude of axial load affect the performance of the retrofitted beam column joint. However, many researchers have adopted an analytical approach to establish the selection criteria for adopting the retrofitting material also, co-relate the experimental results of retrofitted structure elements with the analytical solutions using novel elements in the analysis *(Lee et al., 2009; Do and Kim, 2012)*. The time-dependent element is proposed in linear and non-linear analysis to assess the performance of repaired/retrofitted structure elements. There is a good correlation has been obtained between the analytical results containing the new time-dependent element and experimental results in terms of strength and stiffness *(Lee et al., 2009)*. Apart from the analytical solution, the fresh, hardened, and durability properties of recently developed high performance concrete are the

centre of attraction for the researchers who are seekers to apply the newly developed material in the field of retrofitting. Also, the usage of fibers improves the crack arresting phenomenon, ductility, and fatigue life of HPC *(Zang et al., 1999; Jang et al., 2014)*. Many researchers have conducted an experimental study to evaluate the feasibility of HPC to retrofit the beam column joint. They used the high performance concrete (HPC), high performance fiber reinforced concrete (HP-FRC) and HP-HFRC to retrofit the BCJ. The results show that the use of HPC/HP-FRC and HP-HFRC improves the seismic performance of RC beam column joint.

In this chapter, the literature review on the most commonly used retrofitting techniques and special materials used for retrofitting is presented.

The first part of the chapter discusses the effect of various parameters on the performance of FRP retrofitted beam column joint. The second part discusses the development history of ordinary concrete to HPC and recently developed ultra high performance concrete (UHPC). Afterward, the third part of the chapter covers the application of HPC/HP-FRC and HP-HFRC in the field of retrofitting of the beam column joint.

2.2 PARAMETRIC EFFECT ON THE PERFORMANCE OF FRP FOR RETROFITTING OF BEAM COLUMN JOINT

2.2.1 Orientation of FRP Wrapping

The orientation of FRP on BCJ altered the mode of failure and improved the performance of beam column joint *(Parvin and Wu, 2008; Le-Trung et al., 2010; Gergely et al., 1998; Endindeniz et al., 2005)*. The specimen (retrofitted non-seismic detailed) RNS-3 and RNS-4 were designed for cross-shaped configuration of wrapping, as shown in Fig. 2.1. The CFRP layout at 45° at the joint revealed the maximum strength and ductility improvement i.e., 17.5% and 5.3 times than the control specimen, respectively. It was observed that the CFRP exhibited the maximum improvement as a retrofitted material when the fiber direction inclined at 45° from the beam axis (in the cross-shaped configuration of wrapping). The detail of the specimen and positive lateral load improvement is shown in Table 2.1 and 2.2, respectively. The RNS-3 specimen is configured with single layer cross-shaped CFRP wrapping, which gives 80% positive lateral load improvement as compare to the non-seismic detailed specimen. The L shape sheet of CFRP was also used to retrofit the beam column joint. It was observed that the L shape CFRP was unable to enhance the strength and ductility of the BCJ. However, the

L shape sheet adjacent area of the beam revealed the higher strains, but the lateral strength capacity of the retrofitted specimen was reduced. It was concluded that the strip on the column could be a good choice for increasing the ductility of the beam column joints *(Le-Trung et al., 2010).*

The numerical method is also used to evaluate the performance improvement in terms of shear capacity and ductility of retrofitted beam column joint using CFRP wrapping. Three-dimensional nonlinear finite element models for the beam–column connections were developed and simulated using finite element analysis. The behaviour of three-dimensional beam–column connections strengthened with the CFRP wrapping with different combinations of angles such as 0^o, $45^{o,}$ and 90^o were studied. The interpretation of analysis output shows that the four layers of CFRP work effectively when placed 45^o to the horizontal axis to improve the shear capacity and ductility of BCJ under combined axial and cyclic loads

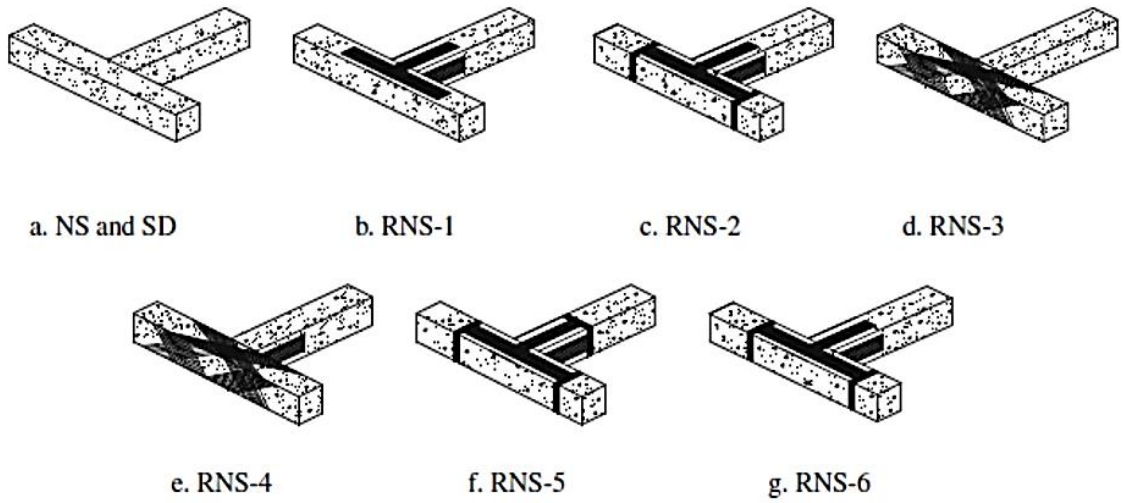

Fig. 2.1- Description of Various Retrofitted Specimens *(Le-Trung et al., 2010)*

Gergely et al., 1998 conducted an experimental study on the exterior BCJ to evaluate the effect of various wrapping layout of advanced composite retrofitted materials. The improvement in the retrofitted specimen was evaluated by comparing the performance of various configured CFRP retrofitted BCJ in terms of maximum lateral load carrying capacity, displacement ductility, and energy-dissipation capacity. It was reported that when the direction of the fiber inclined at ± 45°, the retrofitted specimen exhibited the maximum improvement. The orientation of the CFRP layer is similar to the direction of principal planes. By applying the composite at an angle of ± 45° on both faces, the symmetric and balanced layout was achieved. Moreover, there was no significant compression stresses

recorded in the inclined composite layers because the concrete in the joint could resist the diagonal compression forces.

Table 2.1 - Description of All Retrofitted Specimens *(Le-Trung et al., 2010)*

No	Specimen	T- Shape	L- Shape	X- Shape	Strip
1	NS	None	None	None	None
2	SD	None	None	None	None
3	RNS-1	Both sides	On top and bottom of beam	None	None
4	RNS-2	Both sides	On top and bottom of beam	None	Strip on Column
5	RNS-3	None	None	On three surfaces	None
6	RNS-4	None	On top and bottom of beam	On three surfaces	None
7	RNS-5	Both sides	On top and bottom of beam	None	Strip on column and beam
8	RNS-6	Both sides (two layers)	On top and bottom of beam	None	Strip on column

Table 2.2 – Comparison of Maximum Lateral Load Carrying Capacity between the Retrofitted and Control Specimen *(Le-Trung et al., 2010)*

Specimens	NS	SD	RNS-1	RNS-2	RNS-3	RNS-4	RNS-5	RNS-6
Max. of positive lateral load (kN)	8.56	10.42	10.10	9.87	10.06	9.90	9.52	11.27
Increasing (%) comparing with 'NS'	0.00	21.73	17.99	15.30	17.52	15.65	11.21	31.66
Positive lateral load (kN) at displacement of 40mm	5.50	9.60	5.82	8.70	9.90	9.30	7.70	10.60
Increasing (%) comparing with 'NS'	0.00	74.55	5.82	58.18	80.00	69.09	40.00	92.73

2.2.2 Retrofitting of Non-Seismic (NS) Detailed Specimen

Various authors confirmed that the non-seismic detailed beam column joint specimen revealed brittle failure *(Hadi et al., 2014; Sasmal et al., 2011; Le-Trung et al., 2010; Kalogeropoulos et al., 2016; Al-Salloum et al., 2008)*. The early age beam column joint is not detailed as per the seismic requirements. Therefore, the performance of NS (non-seismic) detailed specimen is brittle during lateral load. Fig. 2.2 shows the control specimen/non-seismic (NS) reinforcement detailing of beam column joint. From Fig. 2.3, it was reported

that the control specimen exhibited rapid degradation in post elastic strength. The maximum lateral load carrying capacity and ultimate displacement is denoted by P_{max} and P_{40}. The maximum lateral peak load carrying capacity i.e., 8.56 kN at the lateral displacement of 29mm is reported. The specimen collapse at 40 mm displacement (P_{40}), and the corresponding lateral load was 5.5 kN. The ultimate failure of BCJ exhibited the joint shear failure; it was observed due to the inadequate amount of ties in the joint panel. The retrofitted specimen (RNS-1) exhibited P_{max} 10.10 kN, and P_{40} was 5.82 kN. The increment of 18% and 5.82 % has been observed as compared with the original specimen (NS). The behaviour showed a non-ductile performance of retrofitted specimens due to the de-bonding of CFRP sheets. However, the lateral strength of the specimen still improves. Fig. 2.3 shows the relationship of lateral load versus column tip displacement of (NS) non-seismic and (RNS-1) retrofitted non-seismic specimen *(Le-Trung et al., 2010).*

An innovative technique of retrofitting of BCJ was proposed by *Hadi et al., 2014*. Two pre-seismically designed control specimens (BCJ) were cast and tested under cyclic loading. The concrete cover around the joint panel is adhered to using glue, and specimen rectangular geometry is transformed into square geometry. After that, the specimen is retrofitted using CFRP and tested to evaluate its performance. While, the second T connection (Repaired specimen, TR) was first loaded till serious failure and then repaired using repair scheme similar to the first specimen. Both the retrofitted specimen shows the improvement in the seismic performance. The concrete cover and CFRP overlay improve the seismic performance of retrofitted specimen in the following way; firstly, the glue concrete enables to resist the shear load and, secondly, the CFRP wrap on the circular geometry exhibited the effective confinement on the concrete. The probability of CFRP debonding was also reduced because of the circular geometry of the retrofitted specimen.

Sasmal et al., 2011 investigate the effectiveness of FRP wrapping and steel plate jacketing on a non- ductile BCJ. The Indian standard guidelines were used to design the BCJ without considering the ductile detailing. The non-ductile specimen (SP-3) revealed the rapid degradation in the post elastic strength consequently, the spalling of concrete in the foam of chunk from the joint was obtained. The insufficient column ties in the joint area were the prime reason for the compression failure. The damaged non-ductile specimen is retrofitted using steel plate jacketing and FRP wrapping.

It was observed that the control specimen revealed 18% and 55% strength deterioration at the ultimate positive and negative lateral displacement, respectively. But, only 8% and 15% strength degradation at the ultimate positive and negative lateral displacement level was observed in the retrofitted specimen. The higher rate of strength degradation in non-ductile specimens is observed, whereas the rate of the strength deformation was very lower in the retrofitted specimen. The load displacement hysteresis of the control specimen and the retrofitted specimen is shown in Fig. 2.4. The onset of diagonal crack on a non-ductile detailed beam column joint is reported by *Antonopoulos et al., 2003*. It has been reported that the diagonal cracking appeared in a controlled specimen (one stirrup at the joint) at a displacement between 10 - 15 mm.

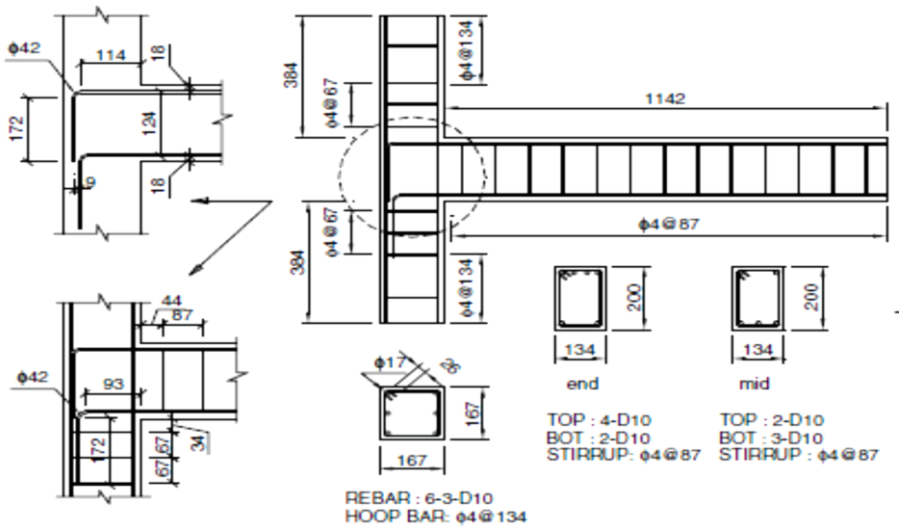

Fig. 2.2 - Reinforcement Detailing of Pre-Seismically Designed Test Specimens. (Lee-Trung et al., 2010)

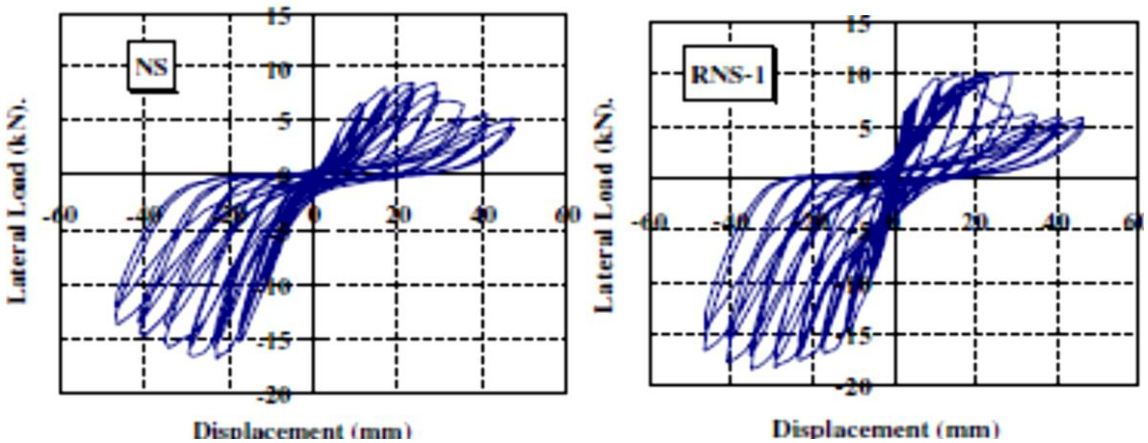

Fig. 2.3 – Load versus Column Tip Displacement of (NS) Non-Seismic and (RNS-1) Retrofitted Non-Seismic Specimen *(Lee-Trung et al., 2010)*

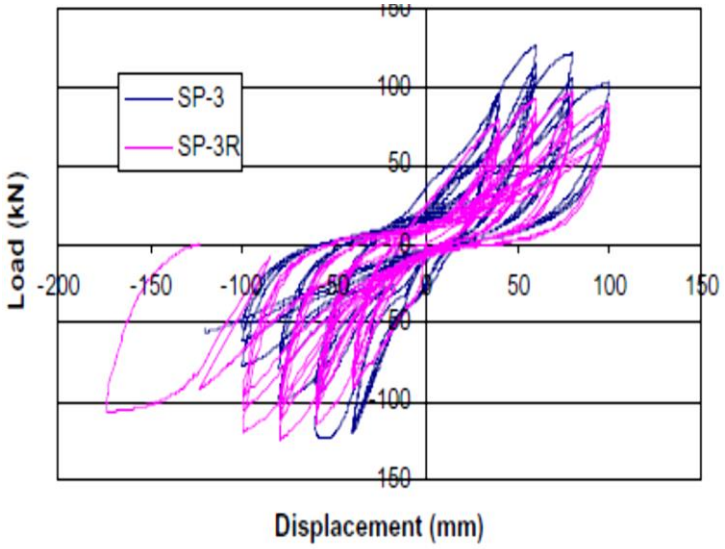

Fig. 2.4 – Hysteresis Response of Non-Ductile Control (SP-3) and Retrofitted Specimen (SP-3R) *(Sasmal et al., 2011)*

2.2.3 Use of Mechanical Anchorage

Even though most literature revealed that strengthening using externally bonded FRP sheets can enhance the joint shear strength and shift the failure towards ductile failure i.e., formation of hinging at the face of the joint, but the effectiveness of the strengthening schemes is affected by de-bonding of the concrete-FRP interface. Many studies stressed on the use of reliable mechanical anchorage methods in utilizing the full FRP strength in a joint panel. *Ghobarah and Said, 2002* strengthened four RC T-joints using a glass fiber reinforced polymer (GFRP) sheet. The two specimens were provided with cover plates and anchors driven through the joint. The specimens T4 and T9 were strengthened without mechanical anchors. The results from the testing of the specimen T4 showed no improvement in the shear capacity of the joint due to premature delamination of FRP as shear cracking occurred underneath. The performance of specimen T9 fell short of that of the anchored specimens also. The FRP wrap failed to confine the joint region and led to the bulging of concrete. The specimen eventually failed in a combined joint-shear and beam-hinging mechanism. The above observations demonstrated that anchoring of FRP is important in developing the strength of the fiber in the small joint area and providing confinement to the joint.

Gergely et al., 2000 tested fourteen, 1/3-scale specimens strengthened with CFRP composites. The composite layouts were varied by adjusting the length of L1 and L3 as shown in Fig. 2.5. The anchoring of FRP composites was provided by the transverse layers (L3) at the beam faces near the joint panel. The results show that the performance of the

specimens was largely depended upon the bond between the concrete and FRP composite. The only addition in the number of FRP layers without providing the proper anchorage to the sheet did not increase the joint strength. The anchoring of the FRP layers over the joint region was improved by the provision of transverse layers at the beam.

The role of mechanical anchorages in limiting premature debonding of FRP-concrete interface was demonstrated in the experimental testing conducted by *Antonopoulos and Triantafillou, 2003*. In the test, L-shaped mechanical anchors were provided to unit S33L at the ends of the beam, as shown in Fig. 2.6**.** The pair of 5-mm thick and 300-mm long unequal leg steel angles were used as an anchor. The two edges of the column were bonded by two angles using epoxy adhesive, and a welded steel plate was used in a transverse direction to connect both the angles. Another specimen unit F22W was provided with anchorage by wrapping two sheets at the ends of the joint where three members were meeting. The mechanical anchorages reported in the study excel the confinement of FRP sheets of unit F22W in terms of lateral strength and energy by 30% and 40%, respectively. For unit S33L, the strength increased from about 15% to around 40%, which was equivalent to an increase of 150%. The improvement mentioned above is appreciable for the field application for rehabilitation of structure elements using composite sheet along with the mechanical anchorage.

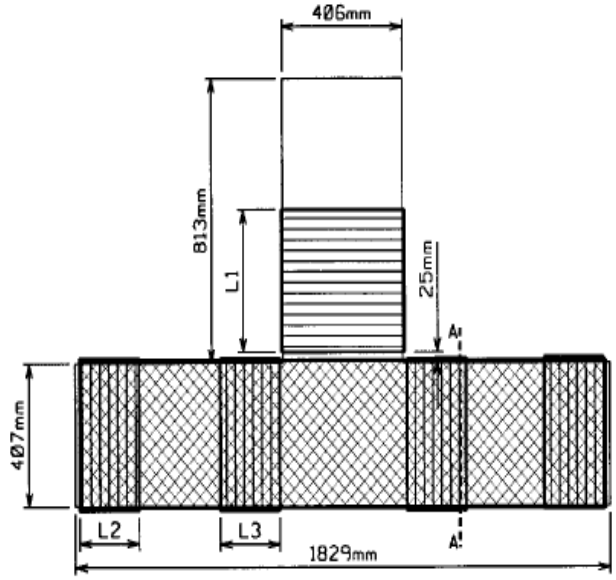

Fig. 2.5 – Composite Layout Proposed by *Gergely et al., 2000*

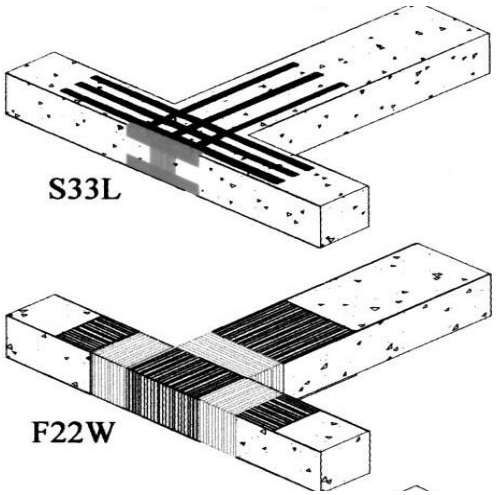

Fig. 2.6 - Layout of Mechanical Anchorages in Exterior Beam Column Joint *(Antonopoulos and Triantafillou, 2003)*

2.2.4 Choice of FRP Materials

Several types of FRP materials, such as carbon fiber, glass fiber, and aramid fibers, etc. are available in industries across the globe. Many researchers were in favor of the carbon fiber because of its high tensile strength and modulus of elasticity compared with other types of fibers *(Gergely et al., 2000; Geng et al., 1998; Balsamo et al., 2005; Pantelides et al., 1999; Pantelides et al., 2002&2004).* The other researchers were interested in strengthening the beam-column connections using glass fiber, as they are more ductile (i.e., having higher fracture strain), and the cost is cheaper. *Ghobarah and Said, 2002,* and *El-Amoury and Ghobarah, 2002* had made use of GFRP in their rehabilitation schemes. The experimental study conducted by *Granata and Parvin, 2001* evaluate the performance of Kevlar, which is a type of aramid fiber. The reason for the selection of Kevlar in their study was the higher tensile and shear strength of Kevlar fabric compared with the glass fabric, ease of installation with Kevlar fiber, and cheaper cost compared with carbon fiber. The scaled down exterior BCJ was strengthened with Kevlar fiber composite and tested to evaluate the moment capacity of the joint and the effect of various thicknesses and configuration of FRP fabrics. An improvement of 60% of the flexural capacity of the joint was observed, demonstrating that the external Kevlar fabric was effective in strengthening beam-column connections. The comparisons between the use of carbon fiber and glass fiber were also studied *(Antonopoulos and Triantafillou, 2003; Mukherjee and Joshi, 2005). Antonopoulos and Triantafillou, 2003* conducted an experimental study on shear-critical joints strengthened using FRP sheets.

Various parameters were investigated, including the performance of strengthened joints using carbon fiber versus that of glass fiber. To allow a fair comparison between the fabrics, the number of layers used for the GFRP-strengthened specimen was determined such that it would have the same axial rigidity as the specimens strengthened with CFRP. The ratio for carbon and glass sheets was calculated approximately equal to 2.5, meaning that the equivalent of one layer of carbon sheet would be "two and a half" layers of the glass sheet. The experimental results showed that glass fibers were only slightly more effective than carbon fibers in terms of strength, but they were more effective in terms of energy dissipation. In the study carried out by *Mukherjee and Joshi, 2005*, both carbon fiber and glass fiber laminates were provided to strengthen the joints with an adequate and deficient bond of reinforcement. While no apparent differences were observed for the joints with proper reinforcement detailing, GFRP-strengthened specimens showed a higher load capacity, higher initial stiffness, and reduction in the slope of strength degradation in the case of deficient joints. The higher energy dissipation for GFRP specimens was recorded as well since they exhibited higher deformation in the test.

2.2.5 Effect of Axial Load on Strengthened Joint

Previous research revealed the positive effect on the shear capacity of the FRP retrofitted joints *(Akguzel and pampanin, 2010*). The specimen F22 was subjected to an axial load of 46 kN and F22A specimen subjected to 115 kN; The different axial loads were applied to study the influence of axial load on the lateral load carrying capacity of the specimen. It has been observed that by changing the axial load from 46 kN to 115 kN, the strength capacity increase from 65% to 85% and the energy increase from 50% to 70% *(Antonopoulos and Triantafillou, 2003*). *Prota et al., 2004* conducted an experimental investigation to find the effect of axial load on the strengthened joint. The joint was subjected to a different amount of axial loads. It was reported that the higher axial load excel the column wrapping effect and boosted ductility by 24%. Moreover, in the type 2 scheme, the failure shifts from the compression to the tension side of the column for low column axial load. The specimen subjected to high axial load, a combined column-joint failure occurred.

2.2.6 Effect of Layers of Wrapping

Le Tarung et al., 2010 conducted an experiment to evaluate the effect of a number of layers of wrapping on the BCJ. Two layers of CFRP sheets were used to strengthen the specimen

RNS-6; detail of the specimen is shown in Table 2.1. The strengthened specimen shows the 31.7% improvement in lateral load carrying capacity than the control specimen. Also, the ultimate load carrying capacity was improved by 92.7% as compared to the control specimen. The lateral strength capacity and ductility of the retrofitted specimen significantly depend upon the number of CFRP layers.

2.3 DEVELOPMENT OF HPC/HP-FRC/HP-HFRC

2.3.1 Development of High Performance Concrete

The characteristics of concrete have been upgraded owing to the unanticipated requirements raised by the society, such as high rise buildings, long-span bridges, high earthquake-resistant concrete structures, etc. To achieve these desires, concrete should have outstanding performance in terms of its fresh, mechanical and durability properties. Currently, the advancement in the field of concrete has successfully used high performance concrete to construct the aforementioned innovative structures. Still, the advancement in concrete is going on to develop the ultra high performance concrete (UHPC), ultra high performance fiber reinforced concrete (UHP-FRC) and ultra high performance hybrid fiber reinforced concrete (UHP-HFRC) which are even more flexible than HPC to construct the innovative and aesthetically appealing structure because of tremendous hardened and durability properties.

Here, the inverted triangle for the illustration of the development of concrete from its beginning, until now, is shown in Fig. 2.7. The lower tip of an inverted triangle implies the introduction of concrete in a society which led the infrastructural development at a faster rate. The early age developed concrete had poor microstructure and durability properties. These limitations were overcome, up to some extent, by the use of fly ash, silica fume, metakaolin, bone china, and chemical admixture (plasticizer) in concrete. It was observed that the use of smaller particle sizes of mineral admixture enhances the chemical reaction due to increased surface area, and lower water-cement ratio maximizes the formation of calcium silicate hydrate gel (C-S-H) leading to the development of high strength concrete. The recent study shows that the use of bone china improve the denseness of the interfacial transition zone and increase the CSH gel formation *(Siddique et al., 2018).*

However, with the increase in strength, the concrete becomes more brittle. The increase in strength significantly changes the microstructure properties of concrete. The propagation of crack extends through the aggregate in high strength concrete, whereas most cracks extend around aggregates in normal strength concrete (Dong and Keru., 2001). The fracture tests and

microscopic studies at the aggregate-matrix interface show the profusion of calcium hydroxide and much less dense calcium silicate hydrate. Therefore, the cracks usually developed at this weak interface i.e., around coarse aggregate. The concrete develop for high strength concrete contained supplementary cementitious material (SCM) e.g., silica fume, the interfacial zone became stronger, more homogeneous, and dense. The cracks usually traversed the aggregates; a transgranular type of fracture was observed. Also, the fracture energy decreased dramatically, especially for the large size of the aggregate case, and as a result, the brittleness index increased significantly (Tasdemir et al., 1996). The results reported by Ozbakkaloglu and Saatcioglu, 2004 reported the strain at peak stress increases with strength, varying approximately between 0.0015 for 20 MPa concrete and 0.0025 for 100 MPa concrete. The stress strain behaviour of high strength concrete revealed more sudden failure and brittle as compared to normal strength concrete. The unloading beyond the peak stress becomes more rapid in high strength concrete. The brittle failure is the limitation of this category of concrete to construct the structures on a large scale. In the era of 1980s, the development of concrete properties was evolved through the development of steel fiber concrete, slurry infiltrated concrete (SIFCON), dense silica particle (DSP) concrete, and Macro defect-free (MDF) concrete/paste. Hoff and Lankard introduced the steel fiber concrete and SIFCON, respectively *(Hoff 1985; Lankard 1984).* Till date the effect of the aspect ratio, surface undulations, mono state/hybrid state and different types of fibers on the fresh, mechanical and crack pattern of concrete is assessed by the various researchers (*Mohammadi et al., 2008; Singh 2011; Badagha et al., 2018*). Numerous studies were carried out to improve the strength property and failure behaviour of concrete and transforming the concrete from high strength concrete (HSC) to high performance concrete (HPC).

Conventionally, the concrete that serves for a longer period is called high performance concrete. To achieve the long-term durability, the concrete ingredient must be designed using the scientific steps; the use of superplasticizer, water/cement not more than 0.4, exhibited a very low permeability, which is the utmost requirement of the structure which are subjected to the corrosive environment. Specifically, ASTM C1202 guidelines show the upper and lower limit of the permeability based on which the mineral admixture contained concrete also can be categorized. The Mehta and Aitcin 1990 introduced the term high performance concrete. According to the authors, the HPC must offer high workability, strength, and durability.

Later, in 1991, the American concrete institute (ACI) started an effort to develop the definition of HPC. In 1998, ACI approved the definition of HPC and documented in 'ACI CT-13' are as follows;

"HPC has defined as a concrete meeting special combination of performance and uniformity requirements that cannot always be achieved routinely using conventional constituents and normal mixing, placing, and curing practices".

The definition of HPC reported by ACI in a broad sense communicates that the concrete which develops to obtain the pre-decided property or for specific application and environment lies under the category of HPC. For example, concrete can be defined as an HPC if it is designed to achieve for characteristics such as high workability, uniformity in ingredients during flow, rapid strength attainment, long term strength, durability, exhibit no shrinkage, volume stability and least affected by long chemical exposure. This definition is different than the definition suggested by the Mehta and Aitcin. The result of the ACI definition was that many of the concrete mixtures came under the definition of HPC, but they were not durable enough against the severe environmental conditions. Also, as per the ACI definition, the HPC doesn't need to exhibit durability under severe environmental conditions. However, this definition contradicts the earlier assumption that the HPC exhibits a longer service life.

Later on, field experience with cast-in-place HPC mixtures revealed early age cracking due to the autogenous shrinkage and high thermal shrinkage. It is noteworthy to mention here that the excellent findings revealed by the U.S. Federal Highway Administration (FHWA) about the field testing of HPC bridge decks. The assumption that "stronger concrete mixtures would be more durable" did not turn out to be true in the case of many cast-in-place and exposed concrete structures. Therefore FHWA has revised the definition of HPC for highway structures. A recent publication contains the following statement:

"HPC is concrete that has been designed to be more durable and if necessary, stronger than conventional concrete. HPC mixtures are essentially composed of the same materials as conventional concrete mixtures. But the proportions are designed or engineered to provide the strength and durability needed for the structural and environmental requirements of the project."

The abovementioned definition covers the essential requirement of HPC i.e., durability. The durability is placed in the priority to categorize the concrete as an HPC. The strength is

considered optional and can be more than the normal concrete if required. This requirement of HPC fulfils the longer service life requirement and express that the strength is not synonymous with durability. It is also mentioned that the HPC mixture must be prepared using the material which is used to prepare the normal concrete. This guideline enables to maintain the cost, force the researchers to use the locally available material, and save the energy required to produce HPC. The elements of various special structures like offshore oil drilling platforms, long-span bridges, and highway bridge decks are being constructed using HPC. As the HPC did not exhibit early age cracking and revealed the higher long term durability, therefore this concrete is specifically used to those structures which are exposed to an aggressive environment.

Along with the HPC development, various other types of concrete also come up e.g., Dense Silica Particle (DSP) Concrete and Macro Defect Free (MDF) concrete/paste was introduced by *Bache 1981 and Birchall et al., 1981*. The DSP and MDF paste/concrete exhibit compressive strengths ranging from 120 to 270 MPa and greater than 200MPa, respectively. An outstanding achievement has been reported in the '90s with the development of the said Reactive Powder Concrete (RPC), offering compressive strength exceeding 200 MPa to 800 MPa and fracture energy up to 40 kJ/m^2 *(Cheyrezy et al., 1995; Richard and Cheyrezy, 1994).* The composition of RPC is OPC cement, silica fume, aggregates with very fine granulometry, sand with an average grain diameter of 250μm, crushed quartz (average grain diameter of 10 μm), and metallic fiber *(Richard and Cheyrezy, 1995)*. Also, the production of RPC is very low and consumes high energy because of the special requirement of curing regimes. *(Feylessoufi et al., 1997; Yazici 2007).*

The further improvement on RPC leads to ultra high performance concrete (UHPC) which is having a highly dense microstructure of the matrix *(Reda et al., 1999; Graybeal 2006; Sorelli et al., 2008; Justus 2013)*, high mechanical strength *(Yu et al., 2014; Xiao et al., 2014)*, and good workability *(Tuan et al., 2011).* However, the development of UHPC is still in progress, and optimization in controlling the ingredients without compromising the property is a major challenge. Due to the outstanding properties, in the last two decades, the HPC/UHPC/UHP-FRC and UHP-HFRC is also recognized as a feasible material for repair, rehabilitation and retrofitting *(Tayeh et al., 2013).*

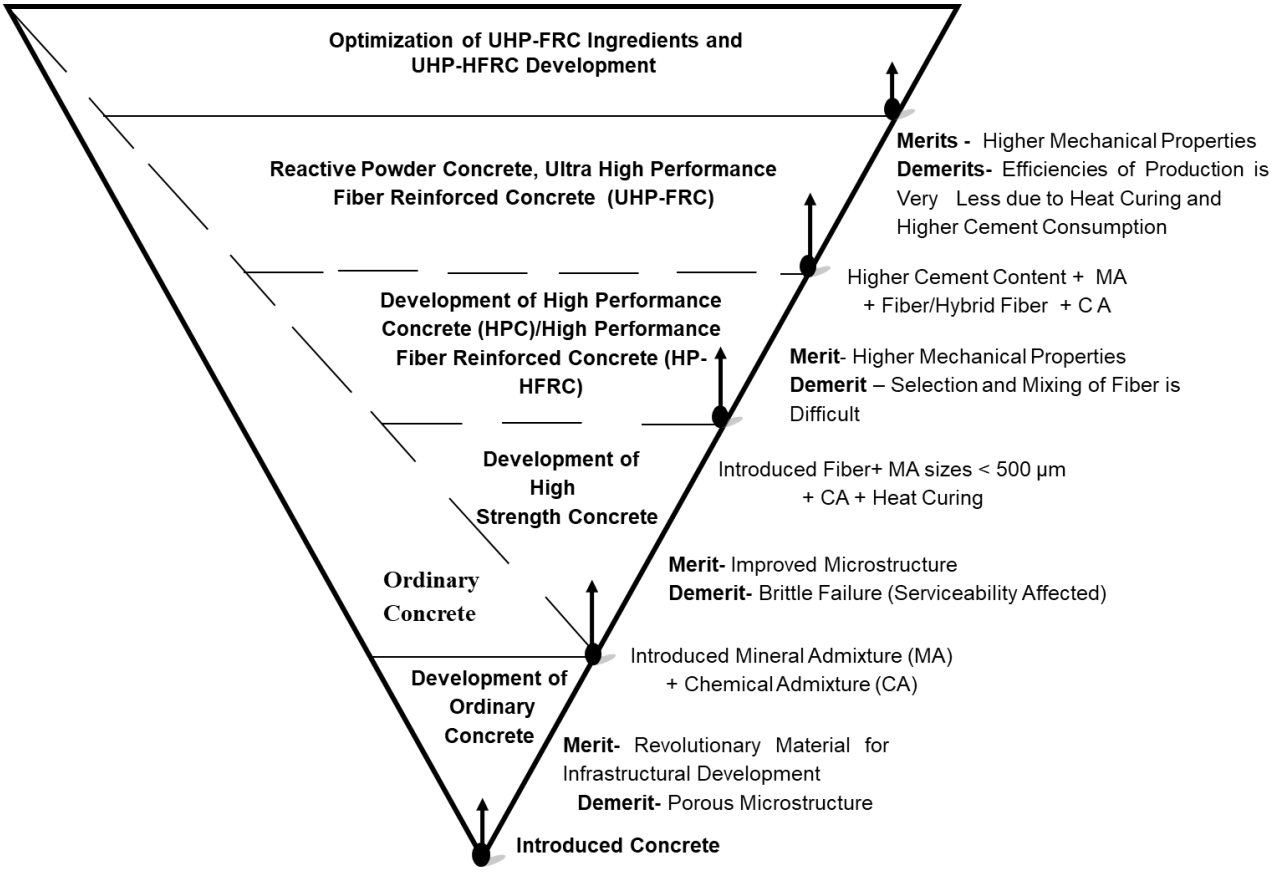

Fig. 2.7- History of Development of Concrete from Conventional Concrete to HPC and UHPC

2.4 APPLICATION OF HPC/HP-FRC/HP-HFRC IN RETROFITTING OF BEAM COLUMN JOINT

2.4.1 Retrofitting of Structures using HPC/HP-FRC/HP-HFRC

The highly workable, superior mechanical properties, bonding properties, and excellent durability make HPC feasible material for retrofitting and rehabilitation purpose. These properties led to tolerate the damage at a high drift level. Generally, the damage in a beam column joint can be controlled with the limitation of joint shear distortion up to 0.5% to achieve the damage between minor to moderate damage state and 1.0% to prevent the severe damage. With the use of HPC, the joint enable to sustain the higher joint displacement with minor damage and thus relieving other structural members from large inelastic deformation demands during earthquakes *(Pantazopoulou and Bonacci, 1992; Bonacci and Wight, 1996; Parra-Montesinos and Wight, 2002; Parra-Montesinos 2005).* The tremendous damage tolerance in HPC in post-elastic region is due to the addition of mono state or hybrid state fiber in a matrix. The addition of fiber delay the rate of growth of crack propagation, and a higher amount of energy is required to spread the crack compared with normal concrete. This

property transforms the brittle post-elastic behaviour of beam column joint into ductile failure when retrofitted using HP-FRC/HP-HFRC.

Shannag and Alhassan, 2005 studied the behaviour of retrofitted BCJ using HPC under cyclic loading. Total 10 BCJ designed to resist gravity load and cast. Four BCJ is tested to obtain the cyclic behaviour of control specimen and other six specimens retrofitted using a 25 mm thick jacket of high performance hybrid fiber reinforced concrete all around the joint (HP-FRC). The jacket of 25 mm thick was extended 100 mm from the original face along the beam from both sides. The comparison between the as-built and retrofitted beam column joint has been made. It has been observed that the specimen retrofitted using high performance concrete exhibited the ductile failure. The complete in-elastic strength utilization through effective nonlinear rotation away from the face of the joint has been observed. This pattern of failure revealed that the plastic hinge has occurred in the beam area, which exhibited ductile failure. The plastic hinge was formed at a distance of 100 mm from the joint interface. The retrofitted using brass coated fiber exhibited somewhat lower performance than steel fiber coated retrofitted specimen. The occurrence of extensive cracking at the column in brass coated fiber reinforced concrete retrofitted specimen is the cause of the inability to transfer the plastic hinge in the beam area. The HP-FRC shows the 114% improvement in ductility over the control specimen. The almost 6 times improvement in energy absorption of HP-HFRC retrofitted specimen compared with the conventional specimen has been observed. The lower degradation in stiffness of retrofitted specimens shows the effective confinement of HP-FRC. The specimen retrofitted using steel fiber high performance concrete exhibited stable secant stiffness degradation and larger initial secant stiffness than the specimen jacketed using brass coated steel high performance concrete due to the larger embedment length of the hooked fibers resulted in higher bond strength. The BCJ was retrofitted using self-compacting HP-FRC jackets. The retrofitted specimen shows the smooth cast surfaces, and no further plaster is required which reduce the geometry variations in the structure. It was observed that the HP-FRC jackets increase the load carrying capacity of the beam column joint also the retrofitted specimen achieves the required level of ductility (*Beschi et al., 2011*). The effect of hybrid fibers on the strength and behaviour of high performance reinforced concrete BCJ subjected to reverse cyclic loads were also studied. Crimped steel fibers and polypropylene fibers were used in hybrid form to prepare the high performance concrete of M-60 grade. The presence of fibers in a hybrid state enhances the first crack load, ultimate load, and displacement ductility of the matrix. The retrofitted beam column joint using a combination of steel fibers and polypropylene fibers of 1% + 0.15% volume fraction

respectively exhibited better performance in terms of energy dissipation capacity and stiffness degradation compared with the controlled specimen. The improvement in energy absorption and ductility in (hybrid fiber reinforced high performance concrete) HFRHPC5 (1% steel and 0.15% polypropylene fiber) specimen is 3.6 and 3.1 times, respectively than control specimen. The maximum lateral displacement i.e., 25 mm, has been observed in a mix HFRHPC5, as shown in Fig. 2.8. The HP-HFRC also capable of reducing the congestion of steel reinforcement in the BCJ, consequently reduces the construction difficulties (*Ganesan et al., 2014*).

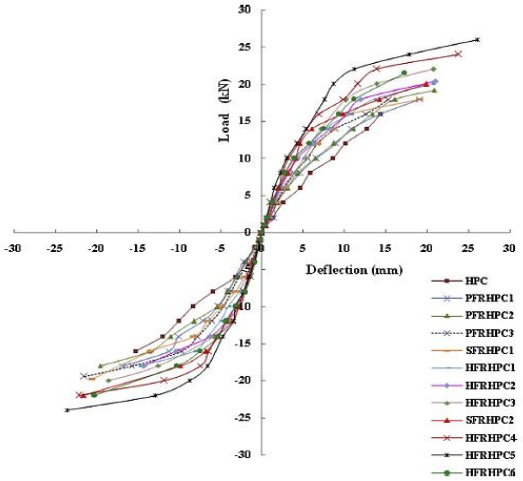

Fig. 2.8 - Load Deflection Envelope of Beam Column Joint Specimens *(Ganesan et al., 2014)*

Beschi et al., 2015 conducted an experiment on the exterior RC beam column joint. The RC beam column joint was designed as per the 1970s Italian construction practice i.e., use of plain bars, stirrups provided at large spacing, and hooked end anchorage. The designed specimens were subjected to cyclic loading. The two specimens were retrofitted using HP-FRC jacket around the joint and two specimens were tested as a control specimen. The results show that the HP-FRC jacket improves the seismic performance of pre-seismically detailed RC beam column joint. The HP-FRC retrofitted specimen exhibited the 40% higher shear strength of the joint with respect to controlled specimen. Also, the drift capacity of the retrofitted specimen increased to 6%.

Kheni et al., 2015 experimentally evaluated the performance of hybrid fiber reinforced retrofitted beam column joint and satisfying the condition of strong column-weak beam flexural design. The beam column joint was designed using the ductile detailing guidelines in IS 13920. A total three types of HP-FRC were prepared. There were two types of HP-HFRC prepared using steel + polypropylene fiber and steel + polyester fiber. Also, the third high performance concrete was prepared using only steel fiber. The control beam column joint was

tested under reversed cyclic loading and load deformation hysteresis was prepared. The HP-HFRC was used to retrofit the damaged beam column joint. The D region of control concrete was replaced by HP-HFRC. The B and D region is decided as specified in ACI 318 (Fig. 2.9).

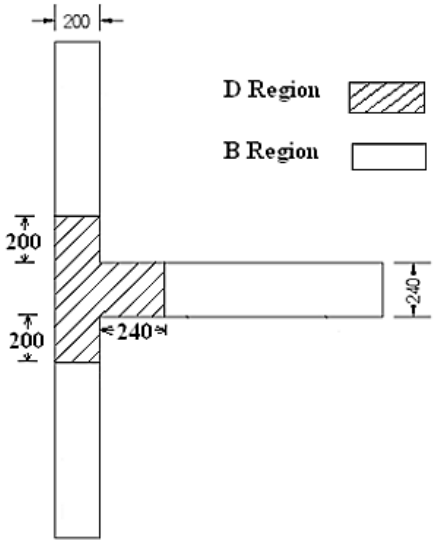

Fig. 2.9 - D and B Region of Beam Column Joint (*Kheni et al., 2015*)

It has been observed that the lateral displacement capacity of all the retrofitted specimens is significantly higher than the control specimen. The performance of all the tested specimens can be scaled in terms of peak load, and lateral displacement capacity is; beam column joint retrofitted using steel fiber and polypropylene fiber > steel fiber and polyester fiber > beam column joint retrofitted using steel fiber > control concrete.

The addition of hybrid fiber in high performance concrete extends the lateral capacity and lowers the strength degradation. Therefore superior ductility is obtained in HP-HFRC retrofitted specimen. In the same fashion, the specimen retrofitted using steel + polypropylene fiber able to dissipate the highest energy among retrofitted specimens. Therefore, it can be concluded that the hybrid (Steel + Polypropylene) HFRC retrofitted specimen revealed the excellent seismic behaviour as compared to other specimens.

The study conducted by *Chidambaram and Agarwal, 2015* revealed the seismic performance of the hybrid fiber reinforced cementitious composite (HFRCC) beam column joint. A total 5 types of HFRCC have been prepared using different fibers. Table 2.3 shows the mix proportions and fiber amount for preparing each mix.

Table 2.3 – Type of Fiber Reinforced Concrete Used for Beam Column Joint Retrofitting *(Chidambaram and Agarwal, 2015)*

Specimen detail	Cement	Sand	C. A*	Silica fume	Steel wool	W/b** ratio	S*	Fibers	Type of fiber
Conventional concrete	1	1.45	2.25	-	-	0.45	0.5	-	-
SFRC (steel fiber reinforced concrete	1	1.35	2.15	-		0.45	0.5	2%	Hooked end steel fiber
ECC (engineered cementitious composites)	1	1.35	2.15	0.1	0.1	0.45	0.5	3%	polypropylene ;
HECC Hooked end steel fiber engineered cementitious composites	1	1.35	2.15	0.1	0.1	0.45	0.5	1.5%+2 %	Polypropylene + Hooked end steel fiber
BECC brass coated steel fiber engineered cementitious composites	1	1.35	2.15	0.1	0.1	0.45	0.5	1.5%+2 %	Polypropylene + brass coated steel fiber

C.A* - Coarse Aggregate; W/b ratio - Water/ binder ratio; S^{+} - Super plasticizer

The specimen without confined reinforcement (SJ1) shows the brittle failure and rapid strength degradation after peak load has been observed. Whereas, the specimen prepared with confined reinforcement (SJ2) shows better ductile behaviour then SJ1. The specimen without confined reinforcement but SFRC placed at the joint (SJ3) shows the higher loop area then SJ1 and SJ2. The steel fiber placed in the joint shows the potential barrier for the growth of the crack in the joint region. The specimen without confined r/f but with ECC (SJ4) in the joint area shows the lower load carrying capacity but significantly improved post-peak behaviour with higher lateral drift capacity. The higher tensile strain capacity of ECC exhibited the crack resisting behaviour and prevent the failure due to early bond degradation of beam main reinforcement consequently, the post elastic load carrying capacity of the retrofitted specimen is compared with SJ1. The HECC (SJ5) composite achieved the peak load at 20 mm lateral deflection, and degradation of the load is only 48% of the peak load at the ultimate failure of the specimen, which shows the lower rate of strength degradation as compared to other specimens. The seismic performance of beam column joint with BECC (SJ6) is comparable with HECC contained specimen. However, the BECC unable to develop the anchorage strength compared to hooked end fiber. Consequently, the BECC could not resist the onset of diagonal crack as in the case of specimen SJ5 (retrofitted using HECC).

The maximum improvement in the ductility is shown by SJ5 i.e., 2.26 times than conventional specimen. The conventional specimen shows the ductility 4.2.

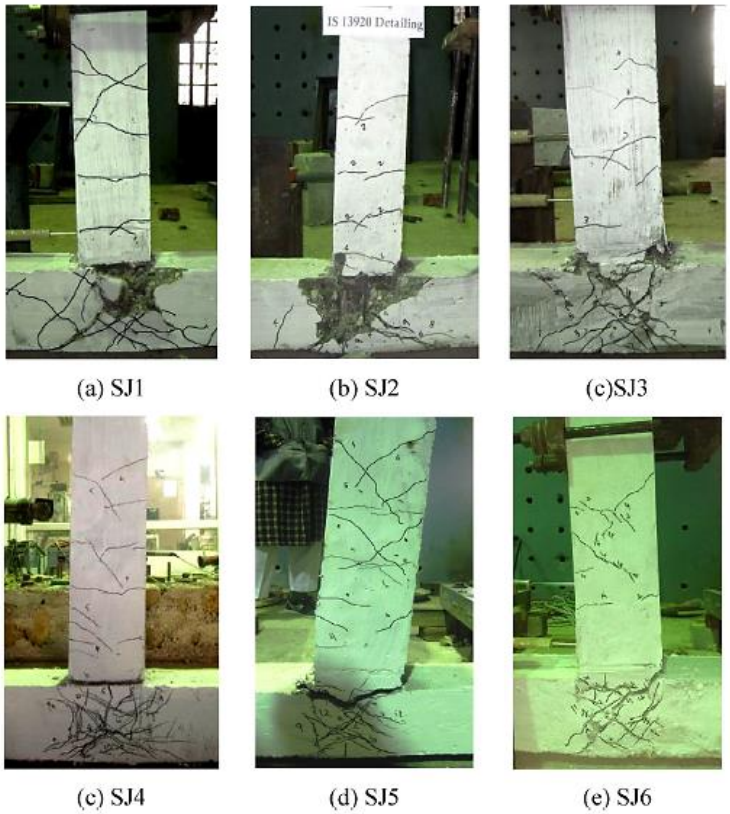

Fig. 2.10 - Cracking Pattern and Failure Mode of BCJ (*Chidambaram and Agarwal, 2015*)

Bedirhanoglu et al., 2013 conducted the experimental study on precast fiber reinforced cementitious composites retrofitted RC exterior BCJ. The exterior beam–column–slab–transverse beam sub-assemblies were constructed using low-strength concrete and plain round bars. Before testing the retrofitted specimen, the prefabricated HPFRCC panels have adhered to both sides of the control concrete panel and tested under diagonal tension as shown in Fig. 2.11. The retrofitted panel exhibited the higher strength and high deformability when the HPFRCC panel was properly anchored, however, the panel attached with the control specimen without proper bolting system, the premature de-bonding has been observed between the control and HPFRCC panel. Further, the beam column joint is retrofitted using the HPFRCC prefabricated 40 mm thick panel and tested under reverse cyclic loading to obtain the load hysteresis envelope (Fig. 2.12). The epoxy and bolt connection is used to make a bond of HPFRCC prefabricated panel with the joint area. It has been observed that the retrofitting of joint using this technique revealed the lower shear deformations in the joint core and delay the formation of shear damage consequently, the beam framing into the joint

reached its flexural capacity first. The improvement in drift capacity makes this retrofitting strategy more feasible for up-grading the seismic performance of the whole structure.

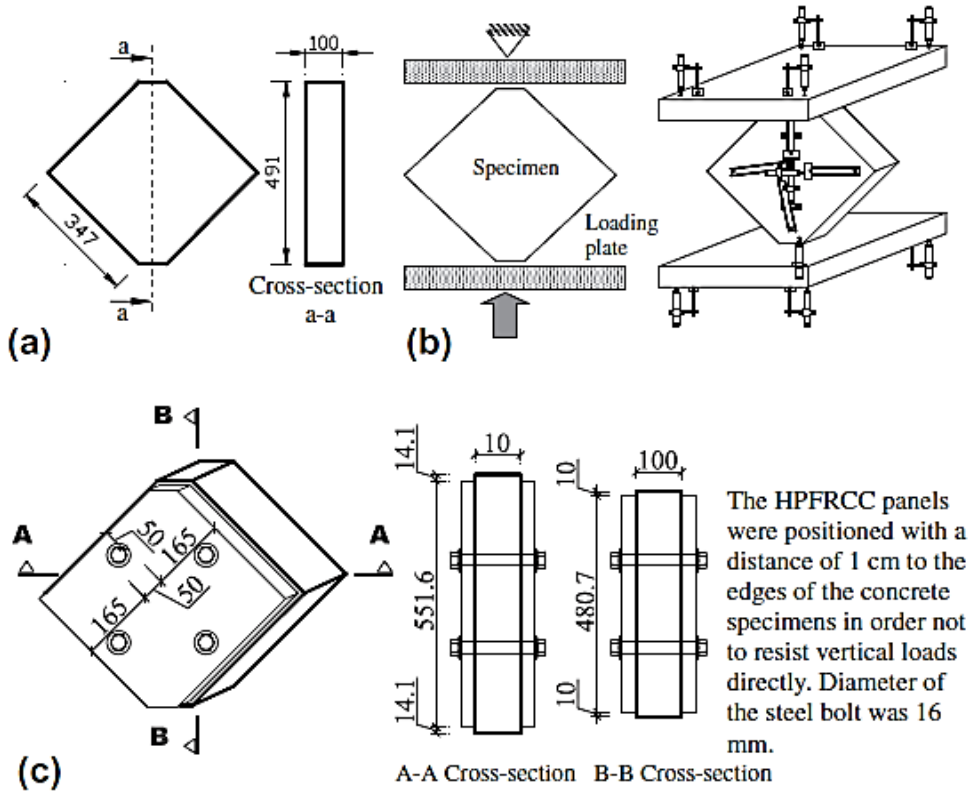

Fig. 2.11 - (a) Panel Dimensions of the Specimen; (b) Schematic Illustration of the Test Set Up; (c) Retrofitting Strategy Applied for the Panel Testing (*Bedirhanoglu et al., 2013)*

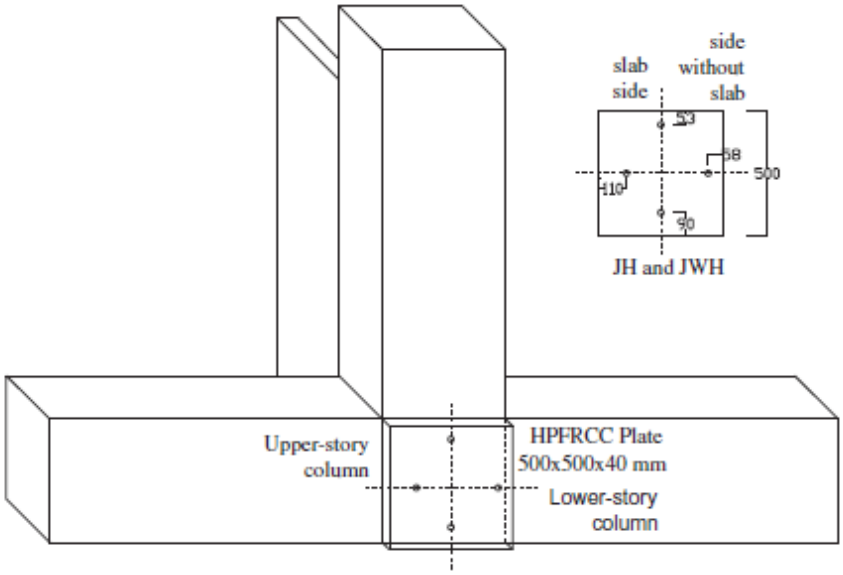

Fig. 2.12 - Retrofitted Exterior Beam-Column–Slab–Transverse Beam Sub-Assembly (*Bedirhanoglu et al., 2013)*

Both types of tests showed that retrofitting with prefabricated HPFRCC panel enhance the strength and lateral displacement capacity of the retrofitted specimen.

2.5 CONCLUSION

The detailed literature review revealed that the behaviour of BCJ subjected to seismic loading does not only depend on the peak load carrying capacity but also significantly reliant on post-elastic performance such as non-linear rotation, energy dissipation, post-elastic rate of strength degradation and stiffness retention and last but not the least *"ductility"*. The pre-seismically designed beam column joint are based on limit state design/working stress design methodology in which the study on nonlinear behaviour of a member having a constraint. In the real scenario, the impact of strong ground motion develops the higher stresses in a BCJ and shear demand of the joint is somewhat higher than the designed shear capacity, Therefore, in-between the onset of post-elastic zone to the ultimate failure, the rate of strength and stiffness degradation is rapid and consequently, slight/moderate or maybe severe damage occurs. At this stage, building a new structure by dismantling the damaged structure need much time to make it functional again, economic burden and environmental pollution are the challenging issues to resolve. Therefore, retrofitting is a feasible solution to make the distressed structure functional again. The type of retrofitting and extent of damage (slight/moderate or severe) is the prime factor in deciding retrofitting strategy.

The literature study shows that various techniques such as steel plate adhesion, jacketing, FRP wrapping, and anchor bolts have been used to retrofit the initial distress beam column joint. However, FRP retrofitting is widely used over the other techniques because of high strength to weight ratio and durability; FRPs significantly improves the performance of initially distress beam column joint. Also, the effects of type of FRP such as CFRP, GFRP, and AFRP on the performance of retrofitted structural elements have been reported. The performance of CFRP can be concluded in a manner that the one layer of carbon sheet performance would be equal to "two and a half" layers of the glass sheet. Apart from FRPs, the usage of mechanical anchorage while retrofitting excels the performance of retrofitted BCJ. The strength degradation is very sharp in the non-seismically detailed specimen, whereas, the retrofitting of non-seismically detailed specimen provides a low rate of strength degradation. But, many demerits are also associated with the aforementioned retrofitting technique as discussed in detail in section 1.3 of chapter 1. In a nutshell, the debonding of FRP concrete interface and inappropriate orientation of FRPs around the distress beam

column joint significantly affect the ductility, jacketing reduces the inside space because of increment in structural elements after retrofitting and corrosion of steel plate decreases the expected performance of retrofitted structural member.

The literature survey of recently developed concrete materials revealed that the HP-FRC/HP-HFRC offered those properties (post-elastic ductility, strain hardening, higher tensile strain, higher bond strength and durability) which are expected from the retrofitted material so that retrofitting of damaged beam column depicts the lower rate of strength and stiffness degradation and also enough capable to shift the hinge formation on the beam region (away from the joint). The HP-FRC/HP-HFRC is also a cost-effective solution for retrofitting and rehabilitation as compare to FRPs. Therefore, based on these arguments, it can be concluded that the retrofitting of pre-seismically designed BCJ using HP-FRC/HP-HFRC offers improved post-elastic behaviour. However, the retrofitting methodology always based on the extent of damage (slight/moderate/severe) in structure elements, which is covered by very few researchers till date on beam column joint using confined HP-HFRC.

2.6 GAPS IN LITERATURE

Hitherto, many research papers reported about the usage of various materials and retrofitting techniques to retrofit the initial distress beam column joint. The FRPs are the widely used material to excel in the performance of the retrofitted beam column joint. The performance of FRPs retrofitted beam column joint improves the seismic performance in terms of lower strength and stiffness degradation and higher energy dissipation. The confinements offered by FRPs excel the lateral load carrying capacity and up to some extent ductility. However, improvement in ductility depends upon the many factors, e.g., type of FRP, debonding/peeling, etc. which restrict the performance of the retrofitted beam column joint. Indeed, these are the serious matter of concern regarding expected performance from the retrofitted structural elements.

Recently, the superior mechanical, durability, and microstructural properties of newly developed HP-HFRC are reported in various literatures. Till date, the high performance confined HF-HFRC using novel retrofitting technique has not been reported so far, to retrofit the beam column joint. Also, the literature survey depicts that the extent of the initial distress level of beam column joint significantly effects of the performance of retrofitted beam column joint. However, the effect of confinement using confined HP-HFRC and wire mesh confined HP-HFRC is also not studied so far.

Therefore in the present dissertation, the seismic performance of retrofitted initially damage beam column joint using confined HP-HFRC can be studied. Also, the effect of different initial damage level of beam column joint on the effectiveness of confined HP-HFRC and wire mesh confined HP-HFRC as a retrofitting material can be evaluated.

2.7 OBJECTIVE AND SCOPE OF THE WORK

Based on the literature survey, it can be concluded that the HP-HFRC is a novel material and offers the higher mechanical, post elastic tensile strain, ductility, and durability property. These properties are very much expected from the retrofitting materials to obtain the efficient performance level from the retrofitted beam column joint. Therefore following objectives have been defined to carry out further research;

1. To develop the high performance hybrid fiber reinforced concrete (HP-HFRC).
2. To study the behaviour of exterior beam column joint retrofitted with HP-HFRC.
3. To study the behaviour of exterior beam-column joint retrofitted with HP-HFRC confined with wire mesh.
4. To study the effect of initial damage level on the behaviour of exterior beam column joint retrofitted with HP-HFRC and HP-HFRC confined with wire mesh.

CHAPTER 3

DEVELOPMENT OF HIGH PERFORMANCE HYBRID FIBER REINFORCED CONCRETE (HP-HFRC)

3.1 GENERAL

The paradigm shift in the field of concrete has been noted with the evolution of high performance concrete (HPC). The HPC exhibited higher durability, higher workability, stronger than conventional concrete, and prepared using the same material, which is used for producing the normal concrete. Nonetheless, the improvement in the tensile resistance capacity of HPC is still in progress. In the last two decades, the use of mono state fibers or hybrid fibers is the prime choice of researchers to enhance the tensile resistance capacity of HPC. Also, the presence of hybrid fibers renders the higher ductility and HPC become known as "*high performance hybrid fiber reinforced concrete (HP-HFRC).*" The existence of higher ductility brought the attention of the researcher to use HP-HFRC as a retrofitting material. Till date, very few studies have been reported the use of HP-HFRC to retrofit the beam column joint. Therefore, the present study applies the HP-HFRC as a retrofitting material along with the novel retrofitting technique.

In the present study, the HP-HFRC is developed using binder (Cement, Silica Fume, Metakaolin), filler material (Ennore sand), steel fibers (Short length crimped and long length hooked geometry), and superplasticizer to retrofit the initially damaged exterior beam column joint. To retrofit the distress structural element, often, the additional reinforcement cage is provided around the distressed member, further, a formwork is provided around the reinforcement cage, and consequently, the very narrow region is available to pour the concrete as a retrofitting material. In this narrow region, the complete efficiency of vibration to eliminate the air voids from the poured concrete is very difficult, therefore, a highly flowable concrete along with the superior strength and durability is essential to achieve efficient retrofitting performance.

To satisfy these requirements of a retrofitting material to strengthen the initially damaged beam column joint, a pre-requisite has been set; The developed HP-HFRC should exhibit the maximum flowability along with the 28 days strength more than 120 MPa. The higher

flowable HP-HFRC enables to flow in a narrow region and required less external energy to achieve the compaction. While a higher strength helps in minimizing the overlay thickness to retrofit the initial damage beam column joint simultaneously, maximum strength can be achieved. The higher strength and durability of HP-HFRC render the minimum thickness of the retrofitted layer to achieve the required seismic demand. Also, the higher durability increases the serviceability of the structure. It has been observed that the HP-HFRC prepared using trial and error method does not achieve the criteria as mentioned above.

Therefore, the Andreasen and Andersen (A&A) packing model is used to develop the HP-HFRC. The fresh, mechanical, durability, and microstructural properties are evaluated at 28 days. It has been found that the flow value achieves the pre-requisite; 84% flowability, 28 days compressive strength of the HP-HFRC is 125.4 MPa as well as excellent durability. The HP-HFRC developed using A&A packing model to achieve all the criteria and further used for retrofitting the beam column joint. Initially, the physical properties of the materials are tested before preparing the HP-HFRC mix and discuss in detail below;

3.2 MATERIAL

3.2.1 Cement

The Ultra Tech make OPC 53-grade cement is used to develop the HP-HFRC. The physical properties of the cement are shown in Table 3.1. The 7 and 28 days compressive strength of the cement is 39.5 MPa and 57 MPa, respectively. The scanning electron microscopy is conducted to characterize the morphological characteristics of cement and is shown in Fig. 3.1.

3.2.2 Pozzolanic Materials

The Elkem make grey color silica fume of grade 920U (un-condensed state), specific gravity 2.2, a mean particle size 0.15µm and, off-white colour highly reactive metakaolin are used as a mineral admixture (see Fig. 3.2 a-b). The white colour quartz powder procured from Jaipur, Rajasthan, is used to develop the HP-HFRC. The specific gravity of metakaolin and quartz powder is 2.50 and 2.65, respectively.

The other physical properties of silica fume, metakaolin, and quartz powder are shown in Table 3.2 - 3.4. The fly ash is procured from the Ropar thermal power plant, Punjab, for this study. The specific gravity of the fly ash is 2.28, as shown in Table 3.5. The morphology of the pozzolanic materials is shown in Fig. 3.3 – 3.6.

Table 3.1 Physical Properties of Cement

Sr No	Characteristics	Test values	Values specified by IS 12269-2013
1	Standard Consistency *(%)*	32	---
2	Fineness of cement as retained on 90-micron sieve *(%)*	0.7	---
3	Specific Gravity	3.12	3.15
4	Setting Time (*minutes*)		
	(a) Initial Setting time	116	30 min (minimum)
	(b) Final Setting Time	305	600 min (maximum)
5	Compressive Strength *(MPa)*		
	(a) 3 days	29	27
	(b) 7 days	39.5	37
	(c) 28 days	57	53

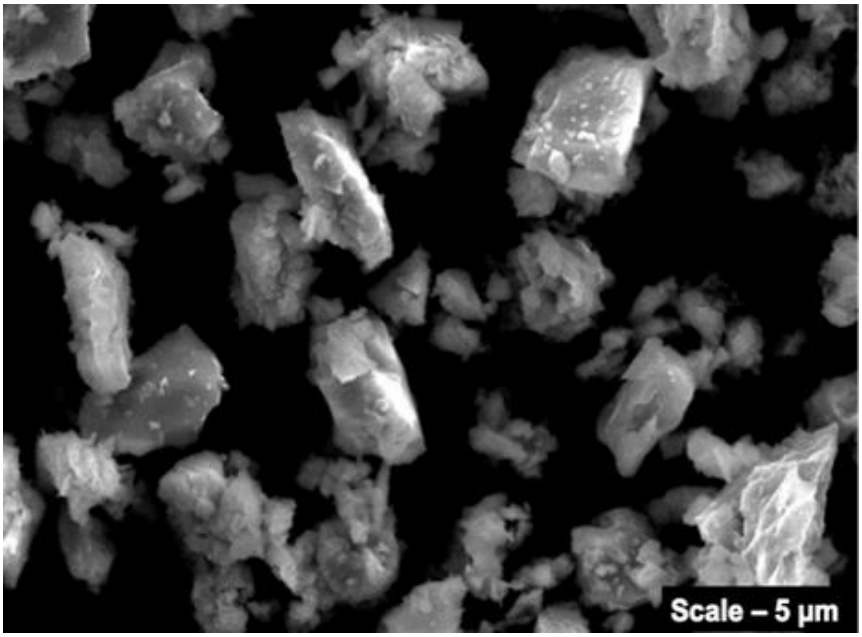

Fig. 3.1- Scanning Electron Microscopic (SEM) Image of OPC 53 Grade Cement

Fig. 3.2 - a) Un-Condensed Silica Fume; b) Metakaolin

Table 3.2 - Physical Properties of Silica Fume

Sr No	Characteristics	Test values
1	Color	Gray
2	Specific Gravity	2.2
3	Type	Uncondensed
4	Mean Particle size	0.15 micron

Table 3.3 - Physical Properties of Metakaolin

Sr No	Characteristics	Test values
1	Color	Off white
2	Specific Gravity	2.50
3	Mean Particle size	3 micron

Table 3.4 - Physical Properties of Quartz Powder

Sr No	Characteristics	Test values
1	Color	White
2	Specific Gravity	2.65
3	Particle shape	Sub-Angular

Table 3.5 - Physical Properties of Fly Ash

Sr No	Characteristics	Test values
1	Color	Whitish grey
2	Specific Gravity	2.28
3	Average particle size (µm)	6.92
3	Particle shape	Round

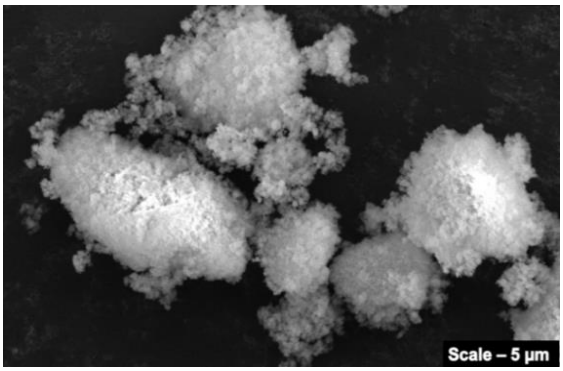

Fig. 3.3 - SEM Image of Uncondensed Silica Fume

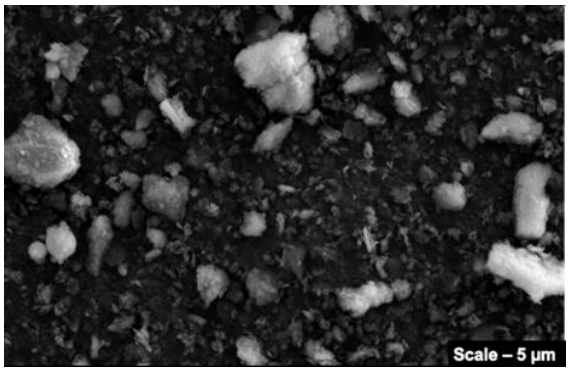

Fig. 3.4 - SEM Image of Metakaolin

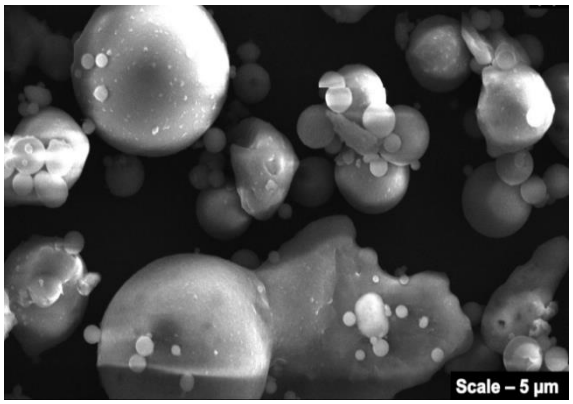

Fig. 3.5 - SEM Image of Fly Ash

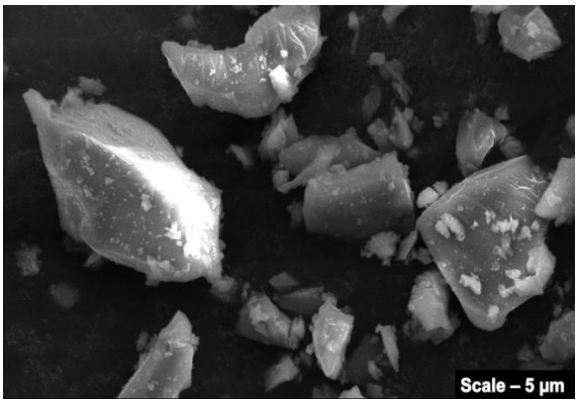

Fig. 3.6 - SEM Image of Quartz Powder

3.2.3 Fine Aggregates

The Ennore sand procured from Tamilnadu Minerals Ltd. (TAMIN) Tamilnadu is used as fine aggregates for the development of HP-HFRC. The ennore sand is available in three grades; grade I (particle size range 2 mm – 1mm), grade II (particle size range 1 mm - 500 micron), and grade III (particle size range from 500 micron - 90 micron) and is free from any organic impurities. The physical properties of ennore sand are shown in Table 3.6. The SEM

image of ennore sand shows that the shape of the particles is sub-angular, as shown in Fig. 3.7.

Table 3.6 - Physical Properties of Ennore Sand

Sr No	Characteristics	Test values
1	Color	Grayish White
2	Specific Gravity	2.64
3	Water Absorption	0.80 %
4	Particle Size Range	
(a)	Grade I	2 mm – 1 micron
(b)	Grade II	1 mm – 500 µm
(c)	Grade III	500 µm – 90 µm

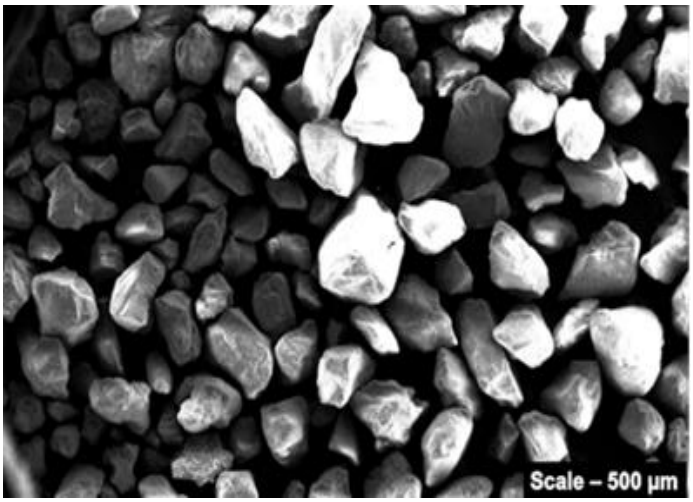

Fig. 3.7 - SEM Image of Ennore Sand

3.2.4 Fiber

Two types of fibers, crimped (15 mm x 0.6 mm) and hooked (60 mm x 0.75 mm), steel fiber, as shown in Fig. 3.8 are used in the present study. The aspect ratio and tensile strength of both the fibers are shown in Table 3.7. A multilevel reinforcement system is used in this study, the short crimped fibers having undulation along the length and hooked fibers with mechanically deformed hooks at both ends.

Fig. 3.8 - Crimped and Hooked Fibers

Table 3.7 Properties of Fibers

Type of fiber	Length (mm)	Diameter (mm)	Aspect ratio	Ultimate tensile strength (MPa)
Crimped steel fibers	15	0.6	25	1200
Hooked steel fibers	60	0.75	80	1200

3.2.5 Superplasticizer

The superplasticizers are used to reduce the water/binder ratio without compromising the flowability of concrete. The required flowability of the mix can be achieved by performing the number of initial trials. In the present study, the BASF make MASTER GLENIUM SKY 8855 polycarboxylic ether based superplasticizerare are used to obtain the flow properties of the mix.

3.2.6 Water

As per IS 456: 2000, the water used for curing of concrete should be free from chemical salt, oils, organic material, and other harmful substances. In the present study, the potable water is recommended for the production of concrete. The potable water available in the laboratory of the institute is used to prepare and cure the HP-HFRC specimens.

3.3 MIX DESIGN AND TESTING DETAILS

The HP-HFRC is developed using two methodologies. Firstly, a trial and error method is adopted to finalize the initial mix proportions, and these initial mix proportion are tested for flow, mechanical, and microstructural properties. Based on the obtained results of these trial mixes, further improvement in the properties of these mixes has been done using Modified Andreasen and Andersen model.

3.3.1 Scheme I

Initially, the trial mixes are prepared to develop the HP-HFRC. The trial mix has been done to evaluate the flowability and compressive strength. The sand/cement ratio, superplasticizer dosage, and water/binder ratio are varied, as shown in Table 3.8. To develop the HP-HFRC, the parameter is opted based on the following principal; a lesser amount of water/binder ratio helps in achieving the minimum air voids thus increase the density of matrix, the smaller maximum size of ingredients and use of pozzolanic materials improve the uniformity and property of interfacial transition zone. The optimum dosage of superplasticizer, along with the lowest amount of water/binder ratio, helps to maintain the initial slump without affecting the mechanical and durability property of concrete. The lower sand/cement ratio enables the binder to coat the surface of filler material efficiently *(Emmons 1993; Rossi 2002, Graybeal 2005, Parra-Montesinos 2005, Graybeal 2007, Graybeal 2006, Voort 2008; Alsadey 2015; Rangaraju et al., 2014).* The mix exhibited higher flowability and compressive strength in the phase I selected for the phase II study.

In phase II, the supplementary cementitious material (fly ash, metakaoline, silica fume, and quartz powder) has been used to prepare the HPC, and the fresh and hardened properties are assessed. Based on the higher flowability and compressive strength, the mix is further developed with the addition of hybrid steel fibers.

In the phase III study, the crimped fiber and hooked fiber is used. The crimped and hooked steel fibers have been added by 1% and 1.5% volume of concrete. This addition in HPC intends to evaluate the effect of fiber on the flow value and hardened properties. Short crimped fiber has undulation along the fiber length which provides mechanical anchorage of the fibers into the concrete and delays the opening of crack, and long length mechanically deformed hooked fiber enable to retard the propagation of a macro crack through the hooked end configuration and improve the post-peak response *(Kwon et al., 2013; Ganesan et al., 2014; Bentur and Mindess, 2006; Kim et al., 2011).* Therefore, to obtain the higher ductility

in HP-HFRC, the crimped fiber and hooked fiber in the hybrid state is used. The detail of the various mixes is shown in Table 3.8 – 3.10.

Table 3.8 - Detail of Various Mixes for HPC Formation (Phase I)

Designation	Cement	Sand/cement ratio (2mm - 1mm)	Sand/cement ratio (1mm-500 µm)	Sand/cement ratio (500 µm- 90 µm)	Total sand/cement ratio	Superplasticizer (%)	Water/Binder
TM-1	750	345	345	345	1035	0.50	0.25
TM-2	750	345	345	345	1035	1.5	0.25
TM-3	750	345	345	345	1035	2.53	0.25
TM-4	750	345	345	345	1035	0.50	0.225
TM-5	750	345	345	345	1035	1.5	0.225
TM-6	750	345	345	345	1035	2.53	0.225
TM-7	750	262.5	262.5	262.5	787.5	0.50	0.172
TM-8	750	262.5	262.5	262.5	787.5	1.5	0.172
TM-9	750	262.5	262.5	262.5	787.5	2.53	0.172

Table 3.9 - Detail of Various Mixes, Prepared with Pozzolanic Material for the HPC Formation (Phase II)

Ingredients	Cement	Ennore Sand	Silica Fume	Quartz Powder	Fly Ash	Metakaolin	Superplasticizer (%)	Water/Binder
HPC-1	1	1.05	0.25	0.10	-	0.15	2.53	0.172
HPC-2	1	1.05	0.25	-	0.10	0.15	2.53	0.172

Table 3.10 - Detail of Selected Mix Prepared for HP-HFRC with Hybrid Fiber (Phase III)

Ingredients	Cement	Ennore Sand	Silica Fume	Quartz Powder	Fly Ash	Metakaolin	Crimped Fiber (%) + Hooked Fiber (%)	Superplasticizer (%)	Water/ Binder
HP-HFRC1	1	1.05	0.25	0.10	-	0.15	1+1.5	2.53	0.172
HP-HFRC2	1	1.05	0.25	-	0.10	0.15	1 + 1.5	2.53	0.172

3.3.1. 1 Mix procedure and sample preparation of scheme I

The water/binder ratio and superplasticizer dosage are varied to achieve the maximum flowability along with the higher compressive strength. The procedure for preparing the HP-HFRC is explained hereafter;

- Initially, the cement and fine aggregates are mixed in the dry state in a mixer for 2 minutes (to obtain uniformity)
- The crimped hybrid fibers added in the mix
- 80% of water is added in the mix, and mixing has been done for 3 minutes.
- After 3 minutes, the water + Poly carboxylate ether based superplasticizer added in the mix and mixing is done for 8 minutes.
- The prepared mix is filled in a 70.5 x 70.5 x 70.5 mm size mould. The cubic specimens are de-moulded after 48 ± 1 hour and cured in water at 21° Celsius throughout the curing period.
- Three specimens of each mix are cast and tested at 3, 7, 28, and 90 days. The reported compressive strength of the sample for each mix is the average of three specimens.

3.3.2 Material Testing Methodology

3.3.2.1 Flow Behaviour

The flowability of all the mixtures is measured using Hagarman's mini slump cone. The frustum shape of mini slump cone having a base diameter of 70 mm, top diameter 60 mm, and height of 100 cm is used. Firstly, the concrete mix is poured in mini slump cone mould, then the mould is lifted, and the HPC mix was subjected to 15 strokes with a raise and drop of 15 mm. The diameter of the spread concrete was the average of two measurements, which was diametrically opposite. The mix exhibited a higher flowability and a maximum of 28 days compressive strength is used further to develop the HP-HFRC.

3.3.2.2 Compressive Strength Test

The compression testing machine of 500-ton load carrying capacity is used to find out the compressive strength of the mix. The loading rate was 140 kg/square cm/minute. The average of 3 tested specimens is reported as compressive strength. The cube sizes of 70.5 x 70.5 x 70.5 mm were used to evaluate the compressive strength, as shown in Fig. 3.9.

Fig. 3.9 – Test Setup used to Test the Compressive Strength of HPC/HP-HFRC

3.3.2.3 Axial Stress Strain Test

To measure the axial stress strain behaviour of the mix, the cylinder sizes of 150 mm x 300 mm were cast. The cast cylinders were cured in water for 28 days and 90 days. The extensometer is used to measure the 28 and 96 days of stress strain behaviour. Fig. 3.10 shows the test setup used to measure the axial stress strain behaviour of HPC/HP-HFRC.

Fig. 3.10 - Test Setup to Evaluate the Stress Strain Behaviour of HPC/HP-HFRC

3.3.2.4 Flexural Strength Test

The flexural strength of the prepared mix is measured as per EN: 196-1 (1994) guidelines. The specimens of sizes 40 x 40 x 160 mm were cast and tested at the age of 28 and 96 days. The rate of loading for the test is 50 ± 10 N/second, as per EN: 196-1 (1994) is adopted. The centre to centre of the support i.e., 120 mm, is taken as an effective length for calculating the flexural strength. The dial gauge is placed at the bottom of the beam to measure the deflection at the center. The test setup and arrangement of the dial gauge is shown in Fig. 3.11. The flexural strength under central point loading has been calculated using equation 3.1.

$$f_f = \frac{3\ x\ P\ x\ L}{2\ xB\ x\ D^2} \qquad (3.1)$$

Where f_f is the modulus of rupture (MPa)

P is the peak load (N)

L is the span length (mm)

B is the average width of the specimen at fracture (mm)

D is the average depth of the specimen at fracture (mm)

Fig. 3.11 – Three Point Bending Test Setup Arrangement

3.3.2.5 Scanning Electron Microscopy (SEM) and Electron Diffraction Spectroscopy (EDS)

The scanning electron microscopy (JSM-6510LV, JOEL, Ltd., Tokyo, Japan) was used to evaluate the microstructure of prepared HPC and HP-HFRC samples. The sample was

prepared in such a way so, that the fiber matrix interaction could be captured in SEM. The elemental analysis was conducted by energy dispersive spectroscopy using model INCA51-ADD0076, Oxford Instruments, Abingdon, UNITED KINGDOME.

3.3.2.6 X-Ray Diffraction (XRD)

The PANalyticalXpert PRO X-ray diffractometer with CuKα radiation (λ = 1.54 Å) was used to study the compound formation of HPC. The angle 2θ varies from 10° - 90°.

3.3.2.7 Differential Scanning Calorimetry (DSC) and Thermo-gravimetric Analysis (TGA)

The equipment of the NETZSCH model STA 449 F3 Jupiter was used for the thermal property evaluation. The Thermo-gravimetric (TG) and Differential Scanning Calorimetry (DSC) analysis of HP-HFRC paste were conducted to evaluate the mass loss and compound degradation. The heating rate of 5^{o} C/min from 25^{o} C to 1000^{o} C in a nitrogen atmosphere was adopted. The 10 mg sample was used for obtaining the DSC and TG curve of the sample.

3.4 RESULTS AND DISCUSSION

3.4.1 Flow behaviour of HPC/HP-HFRC

Fig. 3.12 shows the flow behaviour of trial mix (Phase I), high performance SCC contained mix (Phase II) and high performance hybrid fiber contained mix (Phase III). Initially, the flow value of each mix has been noted; thereafter the compressive strength of each mix has been evaluated. The mix exhibited the maximum flow along with the highest compressive strength is selected further to develop the HPC and HP-HFRC. The Hagerman's mini-slump cone has been used to assess the flow value of the prepared mix. The range of flow value i.e., 130 mm – 180 mm, is selected to develop the phase I mix to HP-HFRC. The cube of 70.5 mm size has been cast and tested as per the guidelines provided in C 1856 to evaluate the compressive strength. The results show that the flow value of TM-1, TM-2, and TM-3 increases by up to 146% with the increase of superplasticizer content from 0.50 to 2.53%. The flow value of TM-4, TM-5, and TM-6 shows the 98.63% improvement in flow value with the increase of superplasticizer content from 0.50 to 2.53%. Whereas, the flow value of TM-7, TM-8, and TM-9 shows the improvement in flow value by 90.78% for increased superplasticizer content from 0.50 to 2.53% (Fig. 3.13). The TM-6 and TM-9 show a similar flow value i.e. 145 mm and exhibited the strength of 70.31 MPa and 76 MPa, respectively. The same flow value of both the mix is obtained but the strength of TM-9 is higher than TM-6. The sand content in TM-9 reduced from 1.35 to 1.05 resulted in a lower surface area of

sand and required less water content. Also, the surface area of sand particles has been reduced resultant in the efficient coating of cement particles on the surface of the sand. Therefore, the compressive strength of TM-9 is higher than TM-6, as shown in Table 3.11. TM-9 is opted to develop the HPC mix (Phase II). Fig. 3.15 & Table 3.11 show the compressive strength of the Phase I mix. The supplementary material such as fly ash, silica fume, metakaolin, and quartz are used to improve the performance of the TM-9 mix. The total amount of supplementary material is 50% of cement in the Phase II mix. The comparison in flow value and compressive strength of HPC-2 (fly ash contained mix) and HPC-1 (quartz powder contained mix) has been done. The flow behaviour of HPC-1 and HPC-2 is 3.44 % and 11.72% higher than the TM-9 mix. The improvement in flow behaviour of HPC-2 is more than HPC-1 because of the presence of fly ash in HPC-2 (see Fig. 3.14). Fig. 3.7 shows the glassy texture and shape of the fly ash is spherical. These properties of fly ash reduce the inter-particle friction in HPC-2 as compared to the quartz powder contained HPC-1 mix *(Kondraivendhan and Bhattacharjee, 2015; Joshi and Nagaraj, 1990).* The HPC-2 revealed the higher flow and compressive strength as shown in Table 3.12. The improvement in both the mix has been done by the addition of hybrid steel fibers and properties are evaluated in phase III. In the phase III study, The HP-HFRC1 and HP-HFRC2 mix revealed 32.41% and 17.24% reduction in the flow value respectively as shown in Fig. 3.14. The addition of fiber drastically alters the flow behaviour of the mix. *Grünewald 2004; Markovic 2006* reported that the geometry, surface properties, and stiffness of the fiber are significantly differed than the crushed aggregate. Therefore the fiber generates the more surface area than aggregate at the same volume, and stiff fiber changes the particle arrangement while soft fiber fills the space of matrix, and bonding properties of the surface of fiber affects the overall behaviour of the concrete.

Phase- I (TM-1)

Phase –I (TM– 2)

Phase –I (TM– 3)

Phase-I (TM-4)

Phase-I (TM-5)

Phase-I (TM-6)

Phase-I (TM-7)

Phase-I (TM-8)

Phase-I (TM-9)

Phase – II (HPC- 1)

Phase – II (HPC- 2)

Phase- III (HP-HFRC-1)

Phase- III (HP-HFRC-2)

Fig. 3.12 - Flow Table Behaviour of Phase I, II and III

Table 3.11 - Flow Value and Compressive Strength of Trial Mixes (Phase I)

Designation	Flow Value (mm)	Compressive Strength (MPa)	
		7 days	28 days
TM-1	77	59.39	63.21
TM-2	120	53.927	62.23
TM-3	190	53.724	63.12
TM-4	73	71.33	73.67
TM-5	110	53.77	72.34
TM-6	145	50.76	70.31
TM-7	76	54.76	65.66
TM-8	115	50.37	63.4
TM-9	145	54.30	76

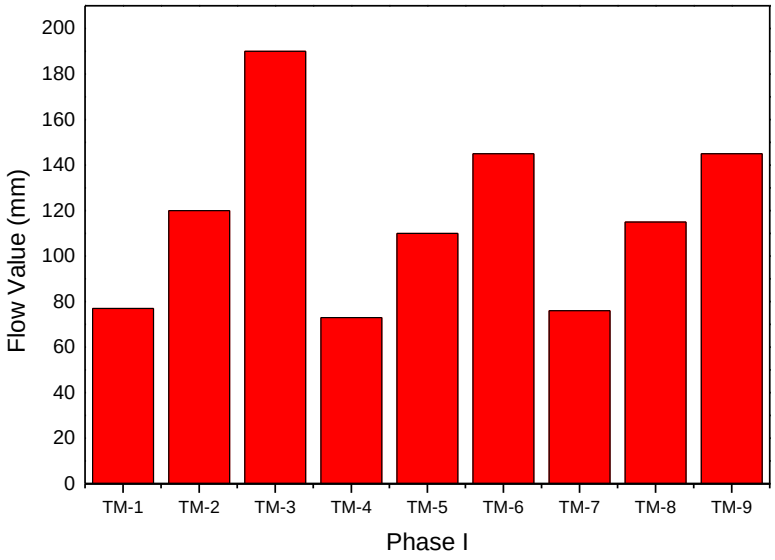

Fig. 3.13- Flow Behaviour of Phase I mix

Table 3.12 - Flow Value of SCM Contained HPC Formation (Phase II) and, Hybrid Fiber Contained HP-HFRC (Phase III)

Phase	Ingredients	Flow value (mm)
II	HPC-1	150
II	HPC-2	162
III	HP-HFRC1	98
III	HP-HFRC2	120

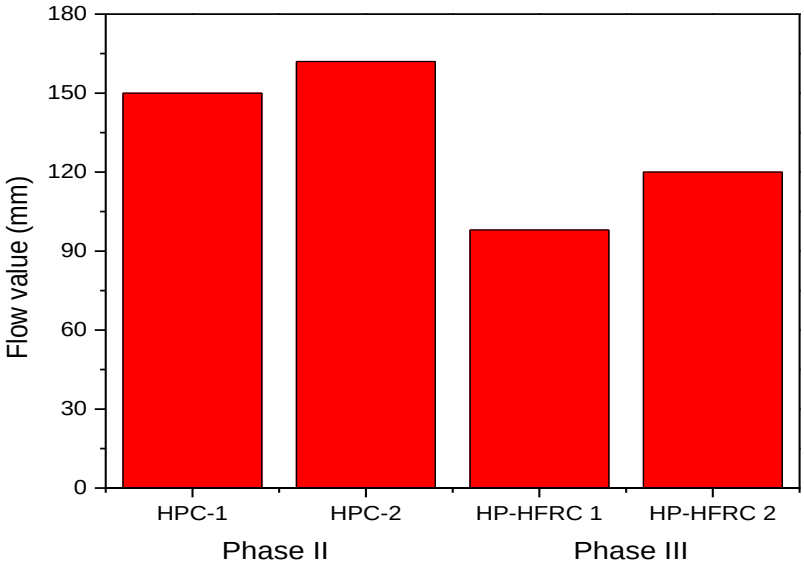

Fig. 3.14 - Flow value of Phase II and Phase III mix

3.5 MECHANICAL AND MICROSTRUCTURAL TESTING

3.5.1 Compressive Strength

Table 3.13 and Fig. 3.15 - 3.17 shows the compressive strength and axial stress-strain behaviour of best-performed sample results from each phase. The additions of finer size SCM i.e., fly ash, silica fume, and metakaolin in a mix TM-9, improve the 90 days compressive strength by 20.88%. Whereas the additions of quartz powder mix i.e., HPC-1 (Phase II) improves the compressive strength by 14.68% at 90 days as compared to mix TM-9. Due to the very low reactivity of quartz powder, the improvement in the strength of the quartz powder mix HPC is lower than the fly ash mix HPC *(Mohammad et al., 2013).* The filler effect and pozzolanic reaction of fly ash in HPC-2 (Phase II) enable the matrix to gain the compressive strength at the age of 90 days. In initial curing days, the fly ash particles act as a filler and later provide the additional nucleation sites on the surface for hydrates from the cement (called seeding effect). Therefore, the fly ash improves the denseness of the matrix by filler effect and pozzolanic activity *(Deschner et al., 2012; Rahhal and Talero, 2004; Baert et al., 2008; Fraay 1989).* Also, the usage of fly ash with silica fume improves the mechanical properties of HPC matrix *(Zhang 2017).*

The axial strain i.e., 0.00357, has been observed in HPC-2 (Phase II), which is the maximum ultimate strain in without fiber category samples. However, brittle failure is observed in sample TM-9 and HPC-2 (Phase II) at the ultimate failure stage, as shown in Fig. 3.15. The rapid loss of strength has been observed after the peak stress attainment of the specimen, consequently affects the post peak performance. The ductile post peak performance is significant for the field application of high performance concrete. To achieve the high strength and higher ductility, the steel fiber in the hybrid state has been added in the HPC matrix. The use of hybrid fiber along with supplementary material excels the performance at 90 days as compared to TM-9 mix. The maximum improvement in compressive strength is observed in HPHFRC-2 i.e. 58.22% as compare to TM-9. The HPHFRC-2 contained the small and large aspect ratio steel fiber. The small aspect ratio of fiber delay the opening of hairline cracks while the high aspect ratio bridge the large width crack hence these fiber improves the ultimate performance of the mix *(Grünewald 2004; Yu et al., 2015).* Therefore, the HPHFRC-2 exhibits the ultimate axial strain of 0.0089 and 0.0139 at the age of 28 and 90 days which shows the excellent improvement in axial stress strain post peak behaviour compared with TM-9 and HPC-2 (Phase II) (see Fig. 3.16).

The hybrid fiber contained matrix required higher energy to break the fiber and matrix bonding and therefore absorb the higher energy as compared to control samples. Based on the obtained axial stress strain behaviour of all the samples, the sequence of the sample in terms of excellent strain is HPHFRC-2 > HPC-2 >TM-9. Fig. 3.17 revealed the failure pattern of hybrid fiber contained matrix; it has been observed that the steel fiber bridge the large crack width at ultimate load and completely eliminate the brittle failure. This behaviour of HP-HFRC helps the structure to serve the design life and fulfill the serviceability criteria.

Table – 3.13 Compressive Strength of Phase I, II and Phase III mix

	Compressive Strength (N/mm^2)			
Particulars	3 Days	7 Days	28 Days	90 Days
TM-9 (Phase - I)	45	54.3	76	79
HPC-2 (Phase - II)	71.05	86.23	90.175	95.5
HPHFRC-2 (Phase - III)	70.05	82	93.33	125

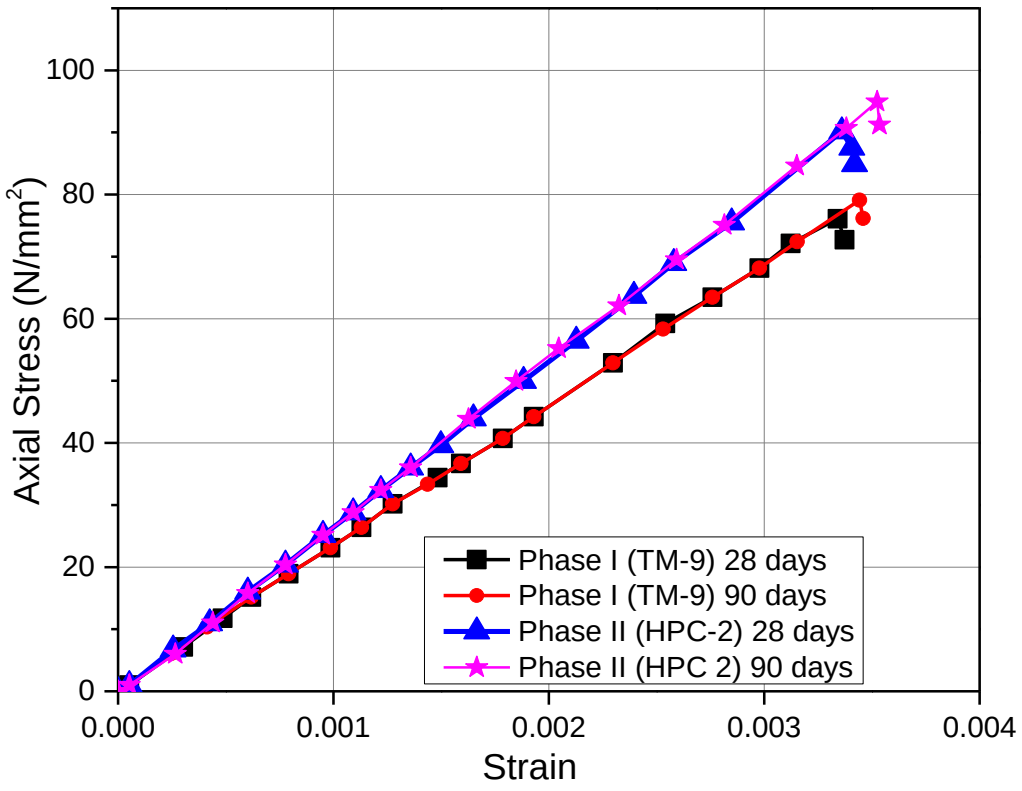

Fig. 3.15 - Axial Stress Strain Behaviour of Phase I and Phase II Sample

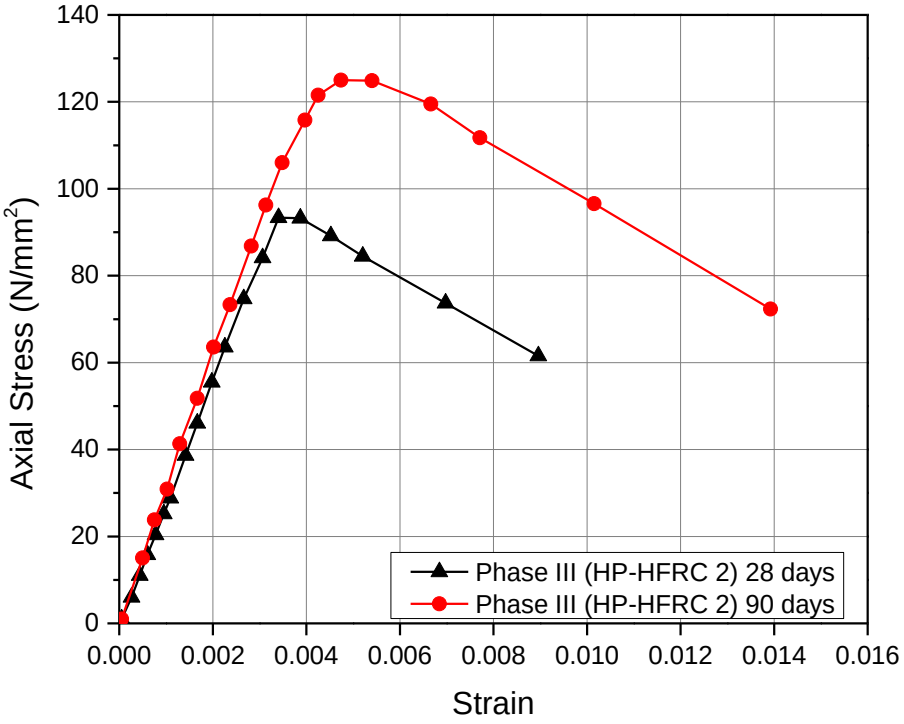

Fig. 3.16 - Axial Stress Strain Behaviour of Phase III Sample

Fig. 3.17 – Failure Pattern of 28 Days Cured HPHFRC-2 Sample (Phase- III)

3.5.2 Flexural Strength

The flexural strength of the specimen has been tested under three point bending test as per EN 196-1 (1995). The TM-9 exhibited the flexural strength of 6.94 MPa and 7.8 MPa at the age of 28 and 90 days, respectively. The 18.15% and 7.05% improvement has been observed

with the addition of supplementary cementitious material i.e., HPC-2, Phase II at the age of 28 and 90 days, respectively (Table 3.14). The TM-9 and HPC-2 exhibited linear pre peak behavior, whereas brittle failure has been observed in post peak region (Fig. 3.18a).

The excellent improvement in flexural strength has been observed in HP-HFRC2 (Phase III). The HP-HFRC-2 exhibit 12.68 MPa and 19.36 MPa at the age of 28 and 90 days, respectively. Also, the significant difference has been observed in post peak region between the plain HPC samples (TM-9, HPC-2) and hybrid fibers containing samples (UHPHFRC-2, Phase III). The hybrid fibers containing sample (HPHFRC-2) exhibited a higher load carrying capacity, then TM-9 and HPC-2 (Phase II) as shown in Fig. 3.18b. The presence of micro fiber and macro fiber improves the pre-elastic and post-elastic performance of the specimen *(Rossi et al., 1987)*. The presence of micro fibers retard the opening of micro crack hence improves the pre peak load deformation behaviour. Also, the delay in opening of macro cracks because of the presence of macro fibers improves the post-elastic deformation characteristics of the HPHFRC-2 consequently, imparts the ductility in the specimen. Also a large amount of energy absorption has been observed in post peak region of HPHFRC-2 specimen.

Table 3.14 - Flexural Strength of Trail, HPC, and HP-HFRC Mixes

Sr. No	Particulars	28 days flexural strength (MPa)	90 days flexural strength (MPa)
1	TM 9 (Phase I)	6.94	7.8
2	HPC-2 (Phase II)	8.2	8.35
3	HPC-HFRC2 (Phase III)	12.68	19.36

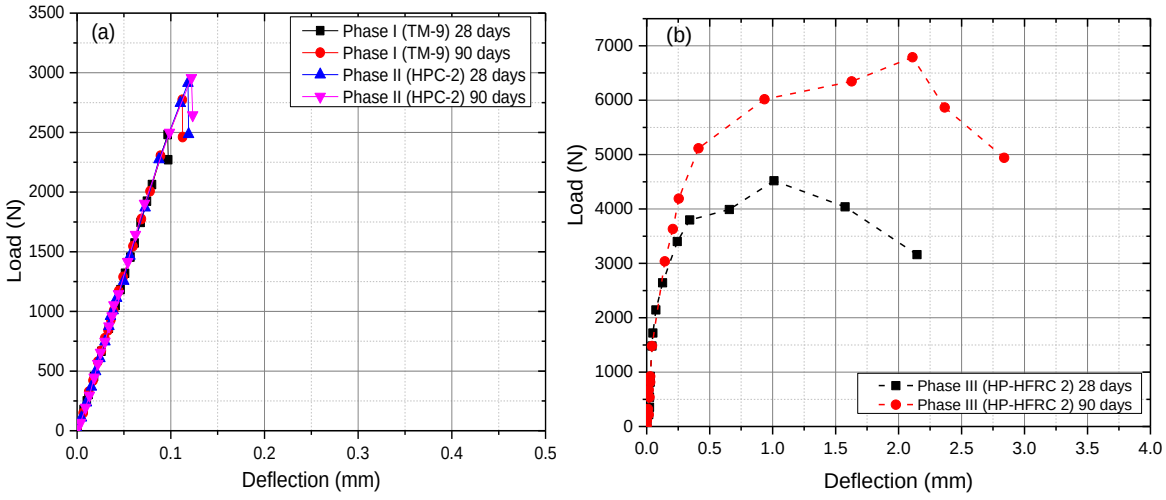

Fig. 3.18 - Load Deformation Behaviour of (a) Trial Mixes and HPC, (b) - HPHFRC - 2 (Phase III) Mix

3.6 MICROSTRUCTURE PROPERTY ASSESSMENT

3.6.1 Scanning Electron Microscopy/Energy Dispersive Spectroscopy

The scanning electron microscopy and elemental analysis by energy dispersive X-ray spectroscopy are conducted on HP-HFRC1 and HP-HFRC2 sample, and the results are compared. The images have been captured at a magnification level of x50, x150, x1500, and x4500 to study the microstructural changes near the fiber and matrix interface as shown in Fig. 3.19. The dense bonding has been observed between the fly ash contained matrix and steel fiber (Fig. 3.19a - d). It has also been observed that the presence of C-S-H enhances the bonding performance of the interface. Consequently, the prepared HP-HFRC1 resists the higher load and bond between the matrix and fiber enable the specimen to absorb higher energy. The supplementary cementitious material in the presence of water-cement ratio lesser than 0.20 develops the denser C-S-H formation and lesser $(Ca(OH)_2$. Although it can also be observed that the voids are present in the matrix, which indicates that the matrix can be improved by optimizing the amount of ingredient. Fig. 3.20 shows the maximum amount of calcium and silicon dioxide in the fly ash contained mix (HPHFRC-2). The presence of fly ash contributes to enhancing the calcium, which further reacts and improves the strength of concrete.

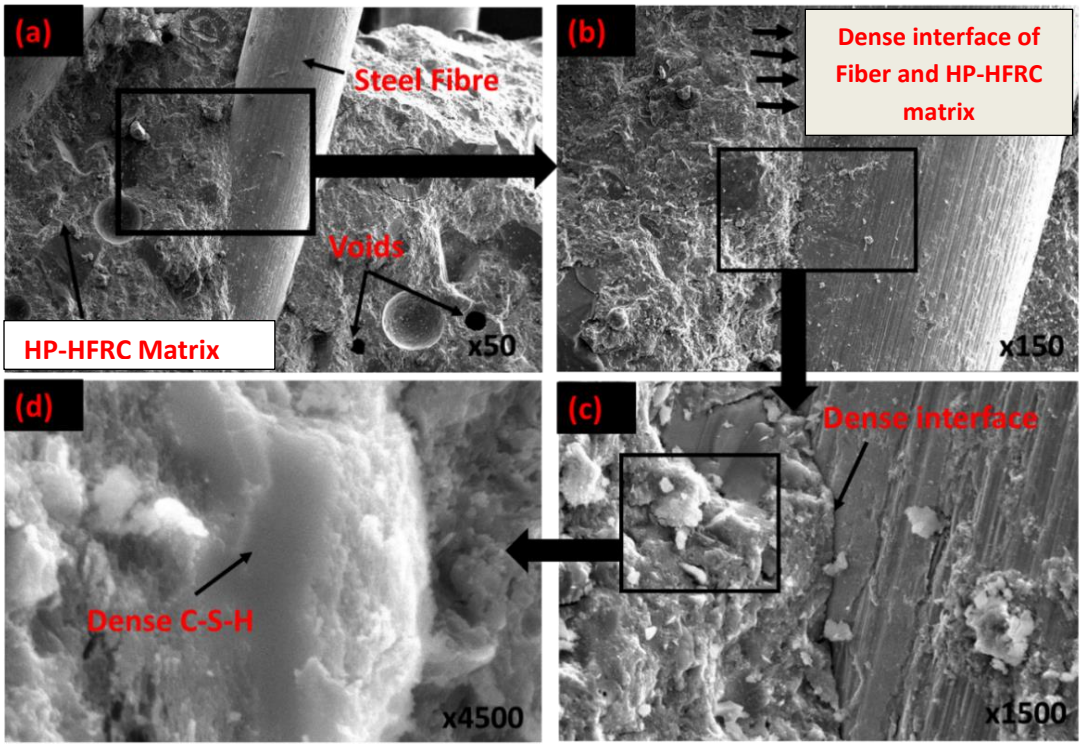

Fig. 3.19 - Morphology Evaluation of HPC - 2 (Phase III)

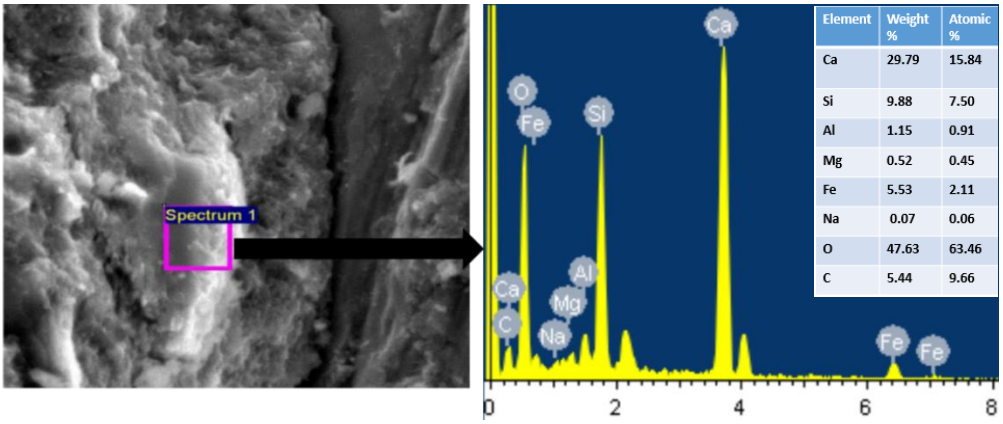

Element	Weight %	Atomic %
Ca	29.79	15.84
Si	9.88	7.50
Al	1.15	0.91
Mg	0.52	0.45
Fe	5.53	2.11
Na	0.07	0.06
O	47.63	63.46
C	5.44	9.66

Fig. 3.20 - EDS of HPHFRC - 2 (Phase III)

The microstructure property of mix HPHFRC-1 is also evaluated using SEM and EDS. Fig. 3.21 (a-d) shows the hairline crack in the matrix of HP-HFRC1. Fig. 3.22b shows the gap between the steel fiber and HP-HFRC1 matrix. Further, the fiber matrix interface analysed at a higher magnification level i.e., x1500, and it is confirmed that the bond between the matrix and fiber is weak, as shown in Fig. 3.21c. The reaction of quartz powder is lower than the fly ash and does not able to produce the dense matrix around the fiber however, the quartz in HP-HFRC matrix developed the dense C-S-H in a paste. Due to weak fiber matrix interaction, the performance of HP-HFRC1 is lower than HP-HFRC2. Fig. 3.22 shows the EDS of quartz powder contained HP-HFRC which revealed the silica 26.20% by weight which is higher than the HP-HFRC2

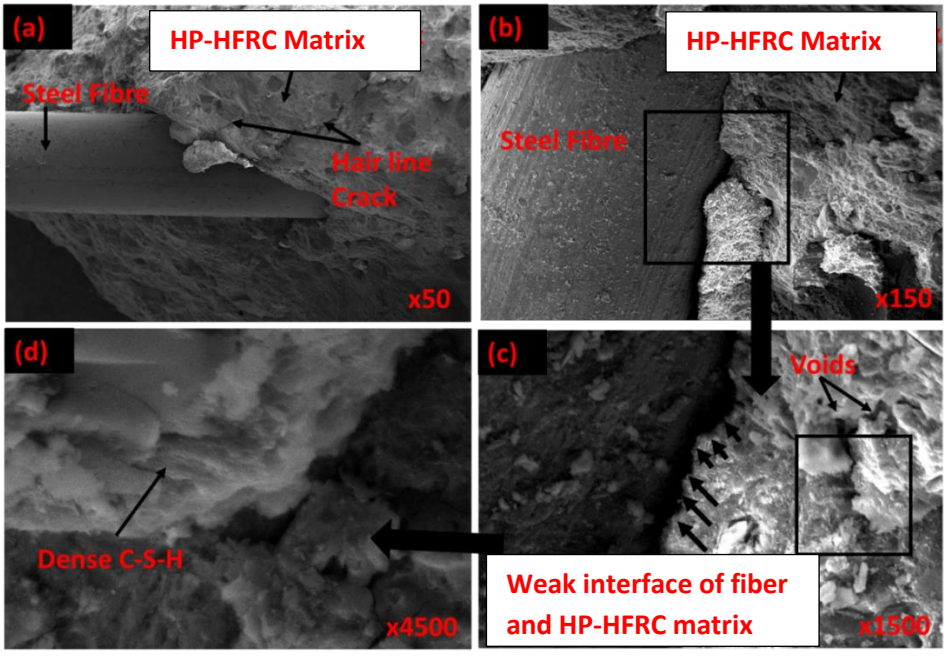

Fig. 3.21 - Morphology Evaluation of HPHFRC - 1 (Phase III)

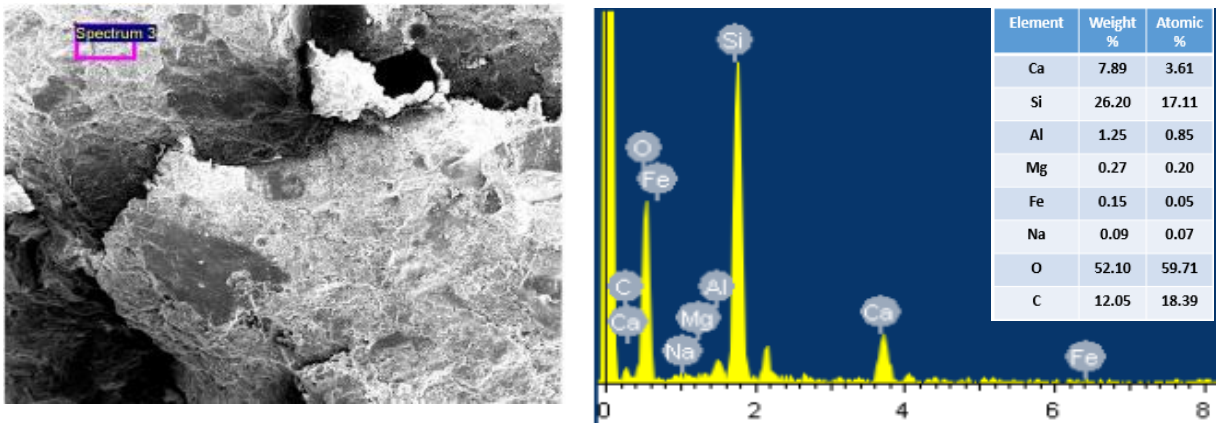

Element	Weight %	Atomic %
Ca	7.89	3.61
Si	26.20	17.11
Al	1.25	0.85
Mg	0.27	0.20
Fe	0.15	0.05
Na	0.09	0.07
O	52.10	59.71
C	12.05	18.39

Fig. 3.22 - EDS Analysis of HPHFRC - 1 (Phase III)

3.6.2 XRD Analysis

The compound formation of HP-HFRC1 and 2 has been evaluated using the XRD analysis. From Fig. 3.23, it has been observed that the quartz, portlandite, C-S-H, potassium calcium silicate, calcium aluminium iron oxide, tricalcium aluminate, and ettringite are present in the quartz powder contained mix. The higher peak of quartz revealed the unreacted particles and acted as a filler in the mix. The filler particle does not participate in forming a compound however decreases the void in the mix. The CSH shows the hydration product in the mix. Based on the observation mentioned above, it can be concluded that the higher amount of quartz powder does not contribute much in hydration product, but filler particles decrease the voids in the matrix. Therefore, the weak bond between the matrix and the fiber is observed

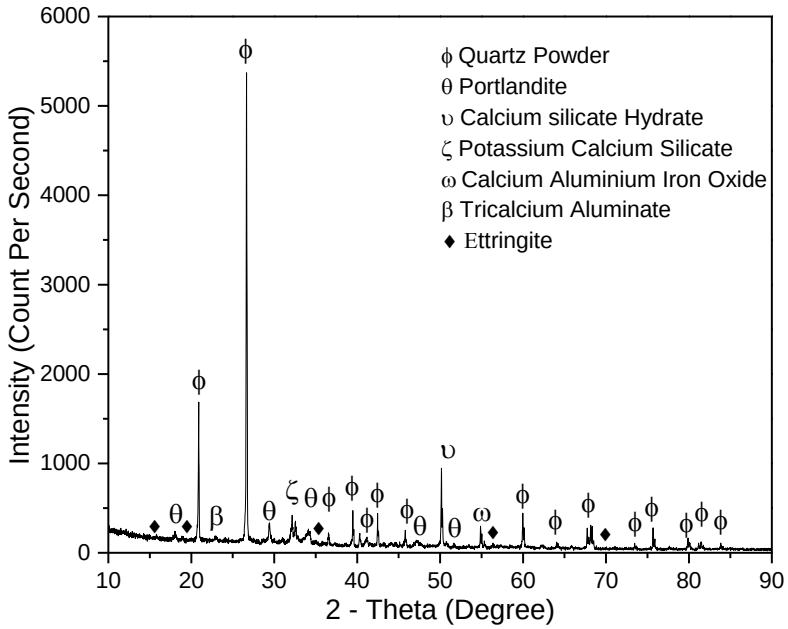

Fig. 3.23 - XRD of HPHFRC-1 (Phase III)

The compound formation of HP-HFR2 is also evaluated using XRD, the result of the same is shown in Fig. 3.24. It has been observed that the quartz, portlandite, C-S-H, potassium calcium silicate, calcium aluminium iron oxide, tricalcium aluminate, and ettringite are present in the quartz powder contained mix. The majority of crystalline phases of silica and calcium silicate hydrate are observed. It can be concluded that the silica and lime are present substantially in the fly ash consequently, the higher amount of CSH in HP-HFRC2 is observed than the HP-HFRC1.

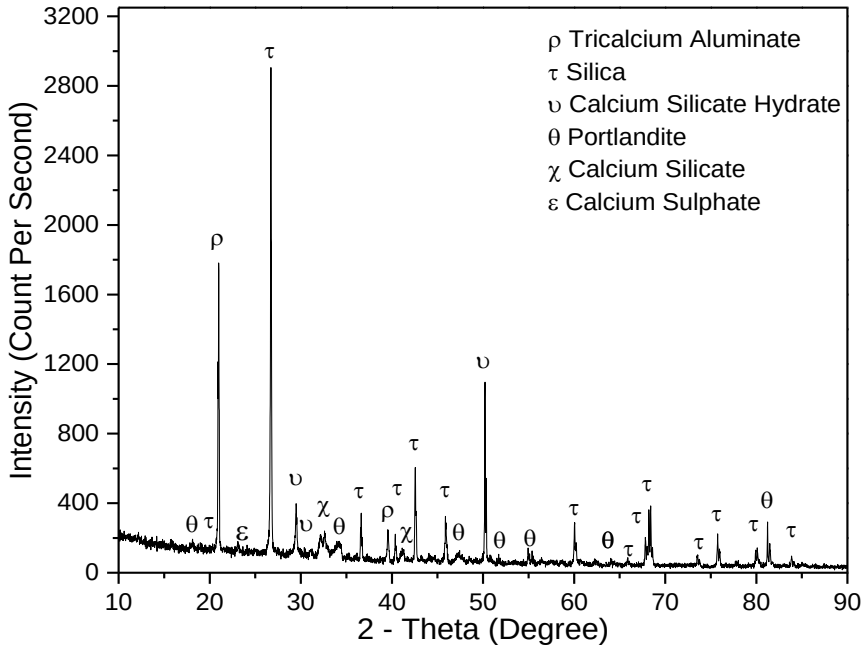

Fig. 3.24 - XRD of HPHFRC-2 (Phase III)

3.6.3 Thermal Property Analysis of HP-HFRC

The thermal property of HPHFRC-1 and HP-HFRC2 samples are evaluated using Differential scanning calorimetry (DSC) and Thermo-gravimetric analysis (TGA), as shown in Fig. 3.25-3.26. Fig. 3.25 shows a peak near 100 ^{o}C, 400 ^{o}C, 650 ^{o}C, and 850 ^{o}C. The peak near 100 ^{o}C represents the water evaporation; further part of the water bound in the particles escape in the range of 30 – 105 ^{o}C. Also, the water is eliminated at 120 ^{o}C *(Johari et al., 2012; Mohammed et al., 2014).* The temperature from 450^{o}C - 550 ^{o}C and 700 ^{o}C – 900 ^{o}C revealed the dehydroxilation of the $Ca(OH)_2$ and decarbonisation of calcium carbonate. *(Johari et al., 2012; Mohammed et al., 2014; Ollivier et al., 1995).* From Fig. 3.25, it has been observed that the peak around 450 ^{o}C and in the range of 700 ^{o}C – 900 ^{o}C are observed, which

represent the dehydroxilation of the $Ca(OH)_2$ and decarbonisation of calcium carbonate. The portlandite in the mix is revealed by XRD analysis.

The mass loss of both the mix has been plot and shown in Fig. 3.26. It has been observed that the mass loss pattern with respect to increased temperature is similar for both the sample. However, the quantity of percentage mass loss is different; this might be due to the reaction between the substance is different at a different temperature. The maximum amount of mass loss has been observed at 450 ^{o}C and 700 ^{o}C due to the decomposition of portlandite and calcium carbonate.

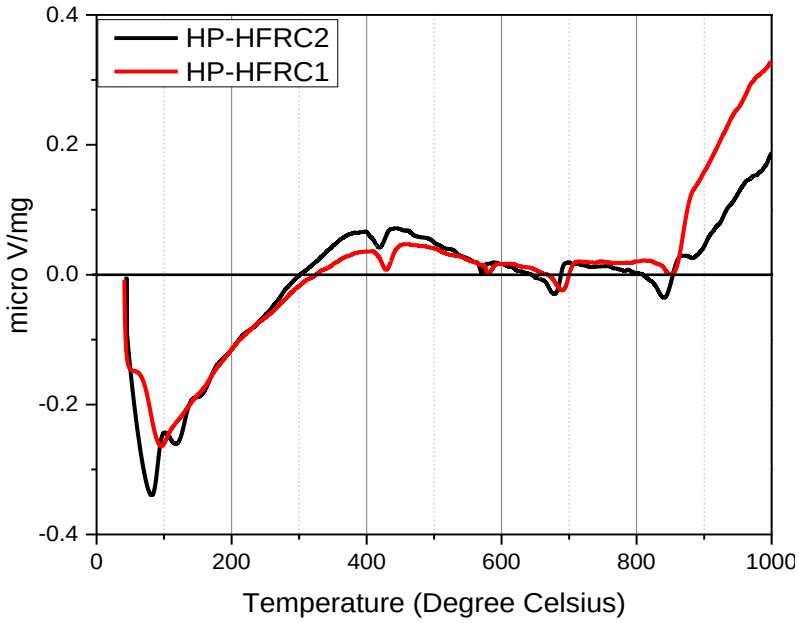

Fig. 3.25 - DSC Curve of HPC Paste at 90 Days of Hydration

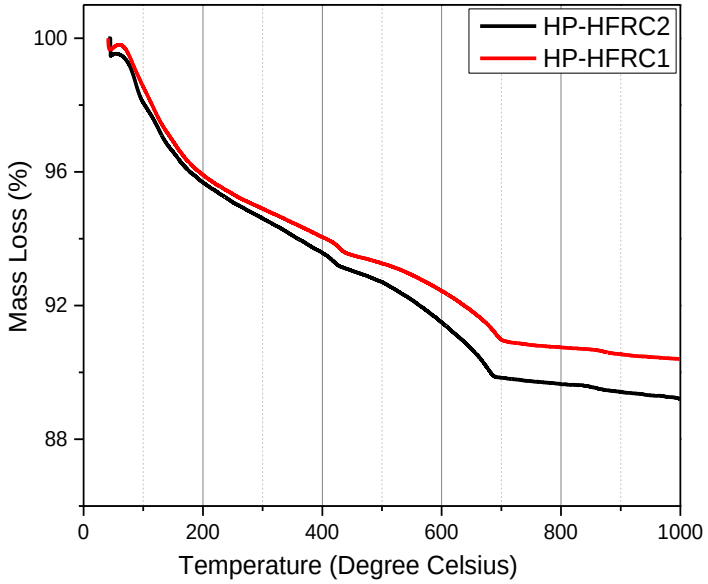

Fig. 3.26 - TG Curves of HPC Paste at 90 Days of Hydration

The HPC/HP-HFRC developed using error and trial method has been examined to assess the fresh, mechanical and microstructural property. It has been found that the material developed using different combination of sand/cement ratio, pozzolanic material, water/binder ratio, and fiber content is successfully achieved the strength around 100 MPa; the presence of fly ash lengthen the period of hydration and 125 Mpa strength has been achieved at the age of 90 days. This experiment intended to develop the HP-HFRC with the required flowability and rapid strength attainment i.e. more than 120 MPa in 28 days. The flowability has been achieved from the mix developed using error and trial method but the target strength has not been achieved.

The high performance materials along with high strength attainment property in 28 days water curing helps to minimize the retrofitting cost as well as the project duration. The durability offered by high performance concrete is the prime advantage to perform the structural element for the longer period of time.

In the context of these benefits, the Modified Andreasen and Andersen particle packing model has been used to again develop the high performance hybrid fiber reinforced concrete. The developed HP-HFRC tested to evaluate fresh, mechanical, microstructural and the most important durability property. The development of HP-HFRC is explained step-wise in the subsequent sections;

3.7 SCHEME II

3.7.1 Modified Andreasen and Andersen (A&A) Particle Packing Model

The particle packing has early introduced by Fuller and Thomsen 1907 revealed the impact of packing of ingredients on properties of concrete. The densely packed ingredients of concrete achieved the maximum strength and durability properties. Whereas, the same ingredients filled loosely is the source of voids and porosity in the matrix. In the series of the continue research based on the Fuller and Thompson 1907, the Andreasen and Andersen (A&A) 1930 work finally concluded that the minimal porosity can be theoretically achieved by an optimal particle size distribution (PSD) of all the ingredients of concrete. The eq. 3.2 is used to attain minimal porosity using optimal particle size distribution.

$$P\ (D) = \left(\frac{D}{D_{max}}\right)^{q} \qquad (3.2)$$

Where *D* is the particle size (μm)

P(D) is a fraction of the total particles smaller than the size "D"

D_{max} is the maximum size of the solid particle (μm)

q is the distribution modulus, and it determines the fraction between the fine and coarse particles in the mix.

However, in eq. 3.2, the minimum particle size is not considered, but in actual, there is a lower size limit, with which a more efficient particle packing model could be developed. That's why Funk and Dinger (2013) suggested a new model based on the A&A equation considering the lower size of the particle. It is based on the principle of attainment of optimum particle packing by a continuous grading of all the solid ingredients in the mix.

Therefore, a modified A&A particle packing model is used to develop the high performance hybrid fiber reinforced concrete. Since very fine materials were used in the mix design of HP-HFRC in the present study so, Mastersizer 3000 model using a laser diffraction technique had been used to determine the particle size distributions of the constituent materials.

$$P(D) = \frac{D^q - D_{min}^q}{D_{max}^q - D_{min}^q} \tag{3.3}$$

In equation 3.3, D_{max}, $D_{min,}$ and D represent maximum, minimum and particle size of the mix, respectively. P(D) is a fraction of the total solids being smaller than size D. The 'q' is the distribution modulus, which helps to finalize the proportion of fine and coarse particles in the matrix. The larger q value results in a coarser mix, and the lower value is suitable to produce fine particle contained mix. As the amount of fine particle in the mix is large, so, the value of 'q' in this experimental study is fixed as 0.25. After calculating the target curve using eq. 3.3, the proportions of the ingredients should be mix in such a manner that the laboratory mix reaches as close as possible to the target curve. To fix the proportions of the mix in a laboratory the following equation shall be used;

$$V_{total\ solid} = \sum_{k=1}^{m-2} V_{Solid,k} \tag{3.4}$$

and the volumetric proportions of each solid ingredients $V_{Solid,k}$ are defined as;

$$V_{Solid,k} = \frac{V_{solid,k}}{V_{total}} \quad \text{for K = 1,2,3……., m-2} \tag{3.5}$$

The $V_{Solid,k}$ is further used to calculate the combined sieve residue R_{mix} of the mix

$$R_{mix}(D_i^{i+1}) = \frac{\sum_{k=1}^{m-2} \frac{v_{sol,k}}{\rho_{sol,k}} Q_{sol,k}(D_i^{i+1})}{\sum_{i=1}^{n} \sum_{k=1}^{m-2} \frac{v_{sol,k}}{\rho_{sol,k}} Q_{sol,k}(D_i^{i+1})} \tag{3.6}$$

The 'm' represents the total ingredients of concrete mix excluding fibers. The m-2 represents the solid particles only as the air and liquid is not considered in this equation. The '$v_{sol,k}$' is the volumetric proportion of each solid material. In the present study the k_1, k_2, k_3, and k_4 are cement, ennore sand, silica fume and metakaolin respectively.

$Q_{sol,k}\ (Di^{i+1})$ is the sieve residual of material k on sieve i

$R_{mix}\ (Di^{i+1})$ is the computed sieve residue of the composed mix and,

$\rho_{sol,k}$ is the specific density of material k.

The total volume of solid $V_{total\ solid}$ per m^3 concrete can also be adjusted by the optimization algorithm. This value is not directly related to the target value as it is the case for the volumetric proportion of each solid ingredient$V_{Solid,k}$. The total volume of solids $V_{total\ solid}$ is only influenced by the constraints of the optimization algorithm. During optimization the following physical constraints are significant; non-negative constraints, i.e., a negative volumetric proportion of each solid ingredients $V_{Solid,k}$ as well as the negative total volume of solids $V_{total\ solid}$ per m^3 concrete is not a valid solution; The sum of the volumetric proportion of the granular ingredients cannot be higher than 1.

In this present study, all the constraints are taken care of using EMMA software offered by the ELKEM. The input of this software is the quantity of ingredients per meter cube, and based on that, the target and the optimized curve is the output. The output file in terms of PSD target and PSD optimized curve for the selected mix is presented in Annexure A. The

physical properties of material used to design the HP-HFRC by A&A model is shown in Table 3.15.

Table 3.15 - Physical Property of Materials Required for Mix Design

Characteristic	Value
Specific Gravity of Cement	3.12
Specific gravity of Indian standard sand	2.64
Specific gravity of Silica fume	2.20
Specific gravity of Metakaolin	2.50
Specific gravity of Superplasticizer	1.08

The particle size distribution curves of all the materials used in the design mix are prepared and shown in Fig. 3.27. The target curve is prepared using Andreasen and Andersen equation, and the actual curve is optimized by adjusting the volume of different materials in a mix to achieve the target curve (Fig. 3.28). The proportion of the various ingredients of the HP-HFRC, as obtained from the optimized curve, is shown in Table 3.16.

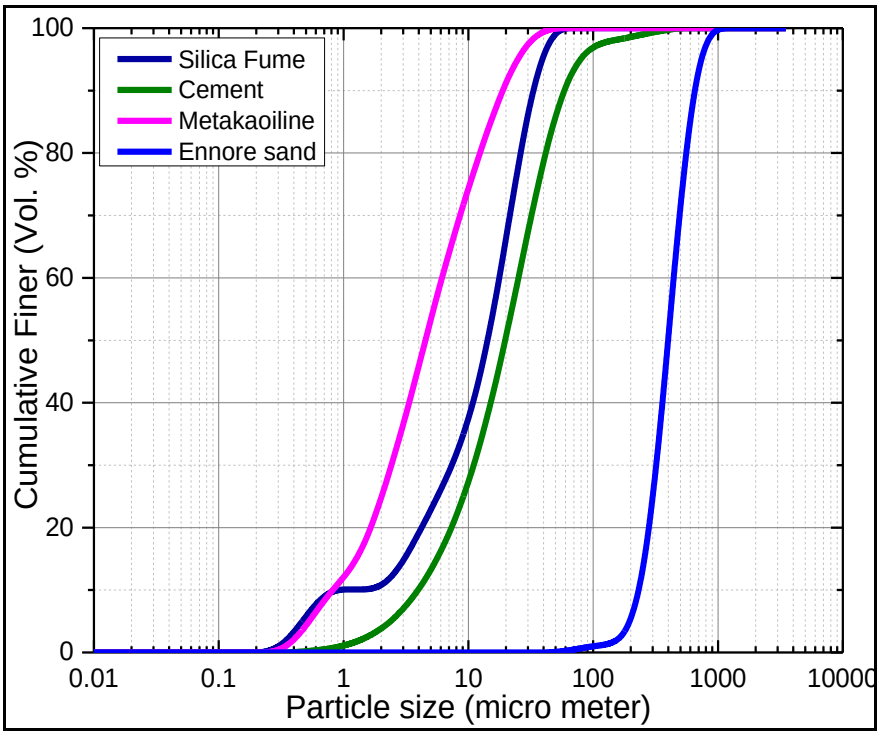

Fig. 3.27 - Particle Size Distribution Curve of All the Ingredients Used to Produce HP-HFRC

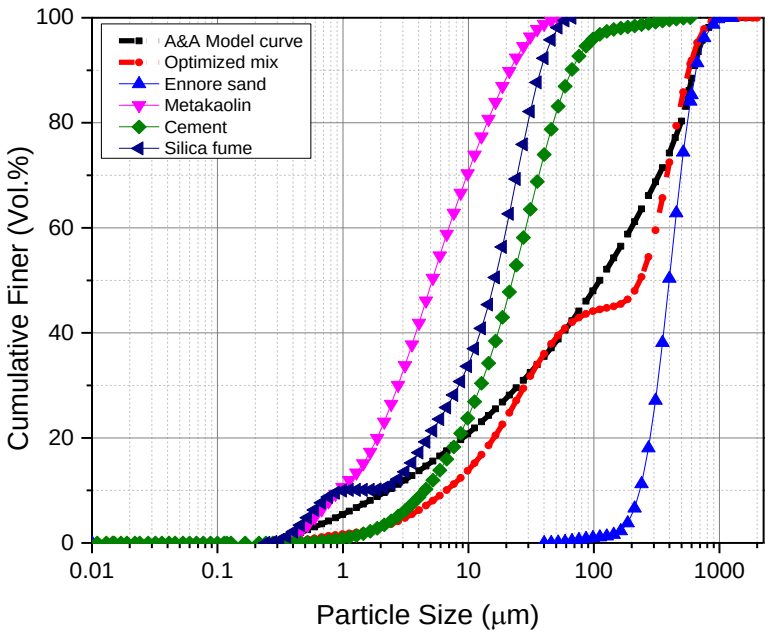

Fig. 3.28 - Particle Size Distribution Curve, Target Curve and Optimized Curve Used to Produce HP-HFRC

Table 3.16 - Design Mix of HP-HFRC

Ingredients	Type	Specific Density (kg/m^3)	Quantity Kg/m^3
Cement	OPC-53	3150	950
Ennore Sand	Ennore	2640	1050
Silica Fume	Uncondensed	2200	143
Metakaoline	-	2500	95
Superplasticizer	Polycarboxylic ether based	1050	23.75
Water	-	-	225
Crimped fiber	Steel	7800	78
Hooked Fiber	Steel	7800	117

3.7.2 Curing Strategies

The HP-HFRC has been developed using normal curing and steam curing. These different curing is adopted to check the effect of curing on the mechanical, microstructural, and durability properties of the HP-HFRC. The HPHFRC cured at room temperature for 28 days

and designated as HPHFRC-NC. The steam cured concrete developed using the following procedure;

- Samples de-mould after 24 hours of casting and cured in room temperature for 3 days.
- After the completion of 3 days of normal water curing, the sample placed in the steam curing chamber for 12 hours
- After the completion of 12 hours, the specimen is taken out and placed in open-air to achieve the room temperature
- Finally, the specimen cured in normal water for rest of the days to complete the 28 days curing

The specimen has been tested after 28 days of curing to assess the mechanical, durability and microstructural property.

3.7.3 Material Testing Methodology

3.7.3.1 Compressive Strength

The recently published guidelines regarding standard practice for fabricating and testing specimens of ultra high performance concrete by ASTM documented in C1856 is adopted for the compressive strength testing. The casted cylinders were demolded after 24 hours of curing and then cured at room temperature in normal water and another set of cast cylinders cured in steam to achieve the steam curing. The cylinder size of 75 mm diameter x 150 mm length is cast and the test set up is shown in Fig. 3.29. The stress rate on the specimens is adopted as 1 MPa/s. Three specimens are tested to report the average strength of the sample.

Fig. 3.29 - Compressive Strength Test Setup

3.7.3.2 Axial Stress Strain Curve

The detail of the setup and sample size is similar as used in evaluating the stress strain behaviour of the mix prepared using trial and error method. The details are given in section 1.3.2.3 in the present chapter.

3.7.3.3 Split Tensile Strength

The specimens of 150 mm x 300 mm (Diameter x Length) cylinders are prepared to test the split tensile strength. The guidelines given in IS 5816 are followed to prepare and test the specimen. The line contact for applying the axial load is prepared by placing the 10 mm plywood piece at the opposite ends. The rate of applied loading is 2 N/mm^2/minute. The equation 3.7 is used to calculate the indirect tensile strength.

$$F_t = \frac{2P}{\pi \, x \, l \, x \, D} \tag{3.7}$$

F_t is the split tensile strength of the cylinder in MPa

P is the applied load (kN)

l is the length of the cylinder (mm)

D is the diameter of the cylinder (mm)

3.7.3.4 Flexural Strength

The detail of the setup and sample size is similar as used in evaluating the flexure strength of the mix prepared using trial and error method. The details are given in section 1.3.2.4 in the present chapter.

3.7.3.5 Rapid Chloride Permeability Test (RCPT)

The 50 mm length slices are cut from 100 x 200 mm (Diameter x Length) cylindrical samples as specified in the ASTM C1202 – 12 to perform RCPT. To avoid the condition of the overflow of charge pass because of the same length of the specimen and the fiber, the specimens of HP-HFRC for RCPT is prepared without the steel fiber.

3.7.3.6 Sorptivity

The capillary suction during initial contact with water is the prominent action to measure the sorptivity. Therefore, to perform water sorptivity, 50 mm length slices are cut from 100 x 200 mm (Diameter x Length) cylindrical samples. The water sorptivity prepared of the prepared mix is evaluated as per the guidelines stated in C1585.

3.7.3.7 Sulphate Resistance

The HPHFRC-NC and HPHFRC-SC specimen of sizes 100 x 100 x 100mm are prepared. After 28 days of curing the specimen is poured into sodium sulphate (Na_2SO_4) solution having a concentration of 5%. The extent of deterioration is measured by visual inspection and compressive strength of both the sample after 180 days of sulphate curing.

3.7.3.8 Scanning Electron Microscopy (SEM)/ Electron Diffraction Spectroscopy (EDS) and Area Mapping

The complete detail of the machine used to evaluate the fiber-matrix interaction and elemental analyses is given in section 1.3.2.5 of the present chapter

3.8 RESULT AND DISCUSSION

3.8.1 Compressive Strength

Fig. 3.30 shows the compressive strength test results of HP-HFRC samples. The normal curing (HPHFRC-NC) and steam curing (HPHFRC-SC) specimens are tested at the age of 28 days curing. It has been observed that the 7 and 28 days strength of HPHFRC-NC exhibited 102.04 and 125.4MPa respectively. The HPHFRC-SC sample revealed higher compressive strength than normal cure HP-HFRC samples at 7 and 28 days of curing i.e. 114. 32 MPa and 129.36 Mpa respectively. After 3 days of normal curing, the 12 hours steam cured samples i.e. HP-HFRC, improves the 7 and 28 days strength by 12.03% and 3.15% respectively. The improvement in HPHFRC-SC could be attributed to the higher formation of C-S-H gel formation under steam curing as compare to HPHFRC-NC specimen. It has also been observed that the improvement in steam curing samples is higher in 7 days, and the rate of strength development is lower at later stages. The improvement in steam curing samples significantly depend upon the delay period of steam curing, as the delay period increases, the

strength improvement is affected. In the present study, the delay period is 3 days to develop the HPHFRC-SC mix.

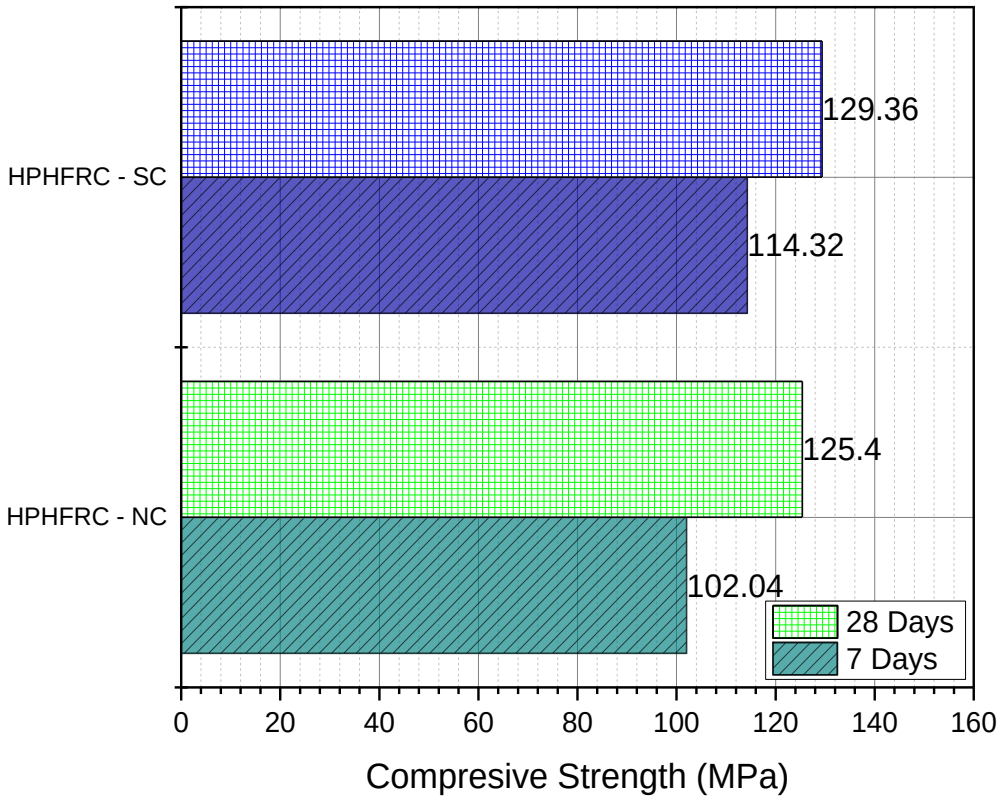

Fig. 3.30 - Compressive Strength of HP - HFRC Normal Cured and Steam Cured Samples

3.8.2 Axial Stress Stain Curve

The extensometer is used to evaluate the axial stress stain behaviour of HPHFRC-NC and HPHFRC-SC specimen subjected to axial compression. It has been observed that the linear strain is up to 0.00292, and then in the post elastic stage, the ultimate strain is reached at 0.0159 as shown in Fig. 3.31. The obtained strain of HP-HFRC normally cured specimen is much higher than normal concrete linear and ultimate stain i.e., 0.002 and 0.035, respectively. The higher axial deformation enables the material to release the higher energy and material sustained higher stresses. This behaviour is obtained because of the presence of hybrid fibers (hooked and crimped fiber), which hold the crack propagation through their fiber-matrix bond and higher modulus of elasticity of steel fiber geometry.

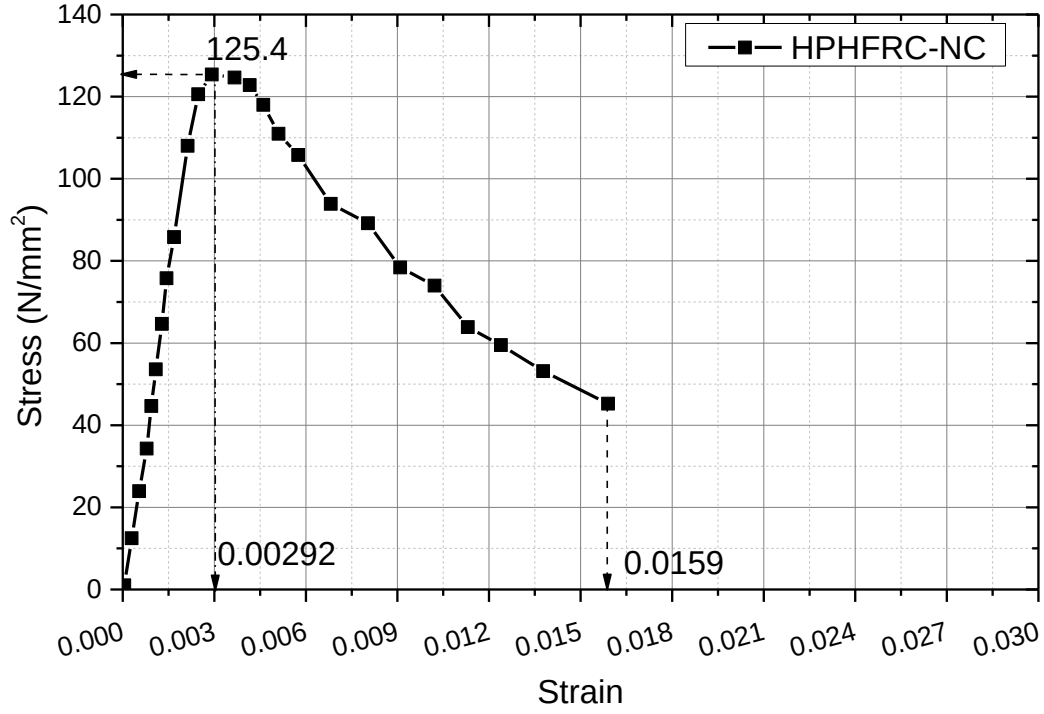

Fig. 3.31 - Axial Stress Strain Behaviour of Normally Cured HP-HFRC

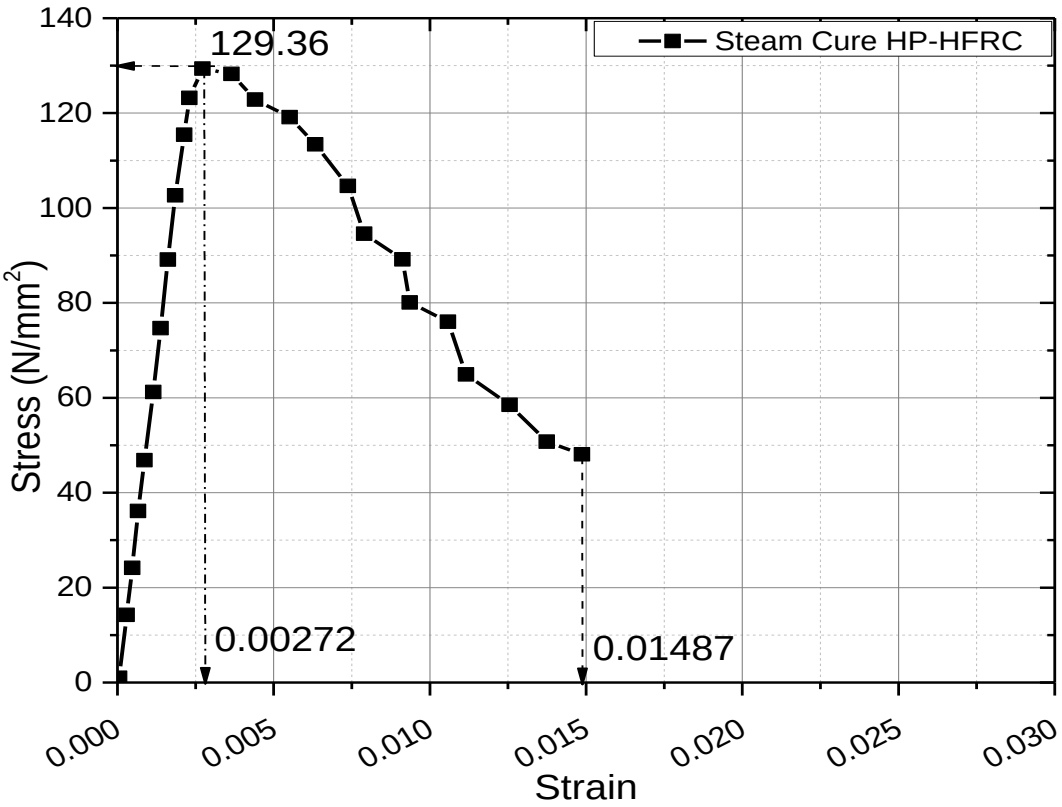

Fig. 3.32 - Axial Stress Strain Testing of Steam Cured HP-HFRC

The stress strain behaviour under axial compression of HPHFRC-SC is also observed. It has been observed that the linear strain exhibited up to 0.00272, and then in the post elastic stage, the ultimate strain is reached at 0.01487, as shown in Fig. 3.32. The obtained strain of HPHFRC-SC specimen is much higher than the normal concrete linear and ultimate stain. However, the ultimate strain of the steam cured specimen is lesser than the HPHFRC-NC. It may be due to the rapid degradation of the post elastic bond strength of the steam cure specimen also, it reflects the somewhat lesser ductility than HPHFRC-NC specimen.

3.8.3 Split Tensile Strength

The indirect tensile strength test is conducted to evaluate the tensile strength of HPHFRC-NC and HPHFRC-SC specimens. It has been observed that the steam cured sample (HPHFRC-SC) achieves the higher tensile strength i.e., 12.6 MPa than normal cure sample (HPHFRC-NC) as shown in Table 3.17. It has been observed that the specimens resist the growth of the cracks because of the presence of randomly oriented hybrid fibers. It has been observed that the rapid growth of crack is observed in HPHFRC-SC specimen.

Table 3.17 - 28 Days Split Tensile Strength of HPHFRC-NC and HPHFRC-SC

Sr. No	Particulars	28 days strength (MPa)
1	HPHFRC Normal curing (HPHFRC-NC)	10.3
2	HPHFRC Steam Curing (HPHFRC-SC)	12.6

3.8.4 Flexural Strength

The flexural strength of the HPHFRC-NC and HPHFRC-SC at 7 and 28 days is tested. It has been observed that the excellent flexural strength of both the mix is obtained. The flexural strength of HPHFRC-NC specimen at 7 and 28 days are 23.63 MPa and 33.38 MPa respectively. The flexural strength of HPHFRC-SC specimen at 7 and 28 days are 25.14 MPa and 35.69 MPa respectively. The HPHFRC-SC specimen revealed the higher flexural strength as compare to HPHFRC-NC specimen.

It can be interpreted from Fig. 3.33 that the initial stiffness of HPHFRC-SC is higher than the HPHFRC-NC specimen. The larger post peak plateau of HPHFRC-NC specimen exhibited higher ductility than the HPHFRC-SC specimen. The presence of micro fiber very efficiently delays the opening of crack also, the rate of propagation of crack at the macro stage is

controlled by hooked fiber (macro fiber). This property of hybrid fiber helps the HPHFRC to absorb higher energy, higher ductility, and excellent post peak performance. The large crack width of HPHFRC-NC specimen revealed the higher deflection and energy absorption. In addition, the absence of spalling at the ultimate failure stage is also observed in both the specimen as shown in Fig. 3.34 - 3.35.

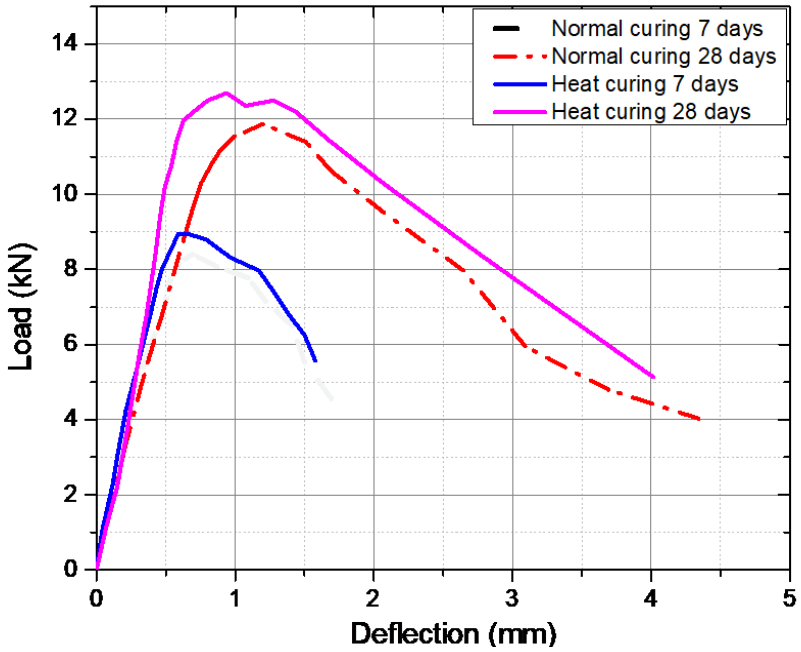

Fig. 3.33 – Flexural Strength of HPHFRC-NC and HPHFRC-SC Specimen at 7 and 28 Days

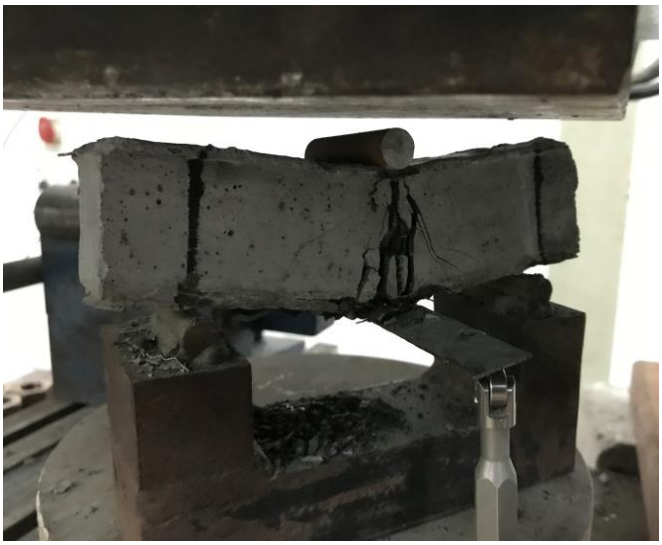

Fig. 3.34 - Large Crack Width of HPHFRC-NC Specimen Obtained during Flexural Testing

Fig. 3.35 - Ultimate Failure of HPHFRC-SC Specimen during Flexural Testing

3.8.5 Rapid Chloride Permeability Test

The specimen of size 50 mm x 100 mm (thickness x diameter) is used to determine the chloride permeability. The guidelines provided by *ASTM C1202-15* are followed to conduct the test. The length of the fiber is large and the specimen along with fiber used to measure the chloride permeability shows the overflow of charge passed at the onset of the experiment. So, this test is performed without the usage of fibers. The average test results of the 3 specimens each of HPHFRC-SS and HPHFRC-NS at 28 days are shown in Fig. 3.36.

It can be observed from the test results that both the specimen exhibited outstanding resistance against chloride ion transfer. The HPHFRC-NC and HPHFRC-SC specimen exhibited the 150, and 450 charge passed (Columbs) in 6 hours test duration. As per the limits provided by ASTM C1202-15, the value lies between the 100 – 1000 charge passed (Columbs) reflects very low ion penetration and values less than 100 Columbs shows negligible chloride ion penetration. In the present results, it can be concluded that the HPHFRC-NC and HPHFRC-SC lie in the range of very low ion penetration. It can be concluded that the steam curing developed the higher CSH gel in the matrix which occupies the space in-between the matrix ingredients and hence low permeability achieved.

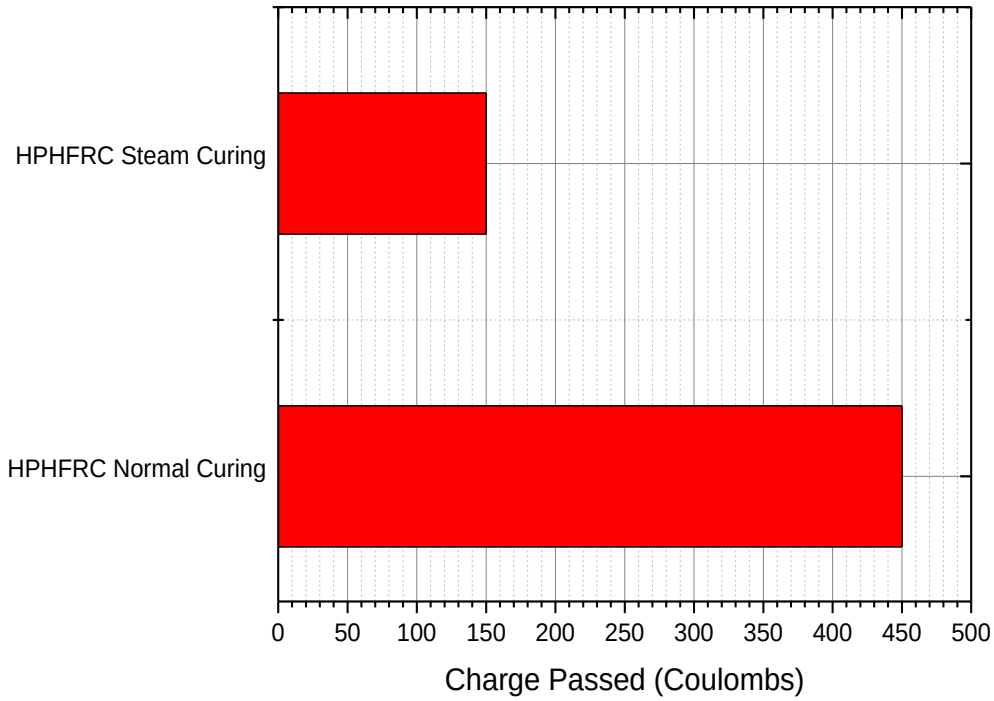

Fig. 3.36 - Rapid Chloride Permeability Test of HPHFRC-SC and HPHFRC-NC Specimen

3.8.6 Sorptivity

Sorptivity is the water intake through the pores by suction. The sorptivity is measured using the change in mass of the specimen divided by the product of cross-section of the specimen and the density of the water. The higher the sorptivity means higher the amount of water absorption consequently, higher the entrance of deteriorative substances carried by water into the concrete *(Ozer and Ozkul, 2017)*. The sorptivity of HPHFRC-NC and HPHFRC-SC specimens is measured after 28 days of curing. From Fig. 3.37, it can be observed that the HPHFRC-NC specimen exhibited the ultimate absorption of 0.475 mm whereas, specimen HPHFRC-SC absorption is 0.309 mm. After 3 days of the test, the sorptivity of HPHFRC-SC specimen is constant till the last day of the test. The absorption rate is constant in HPHFRC-NC specimen after 6 days of the test. It is noteworthy to mention here that the higher rate of initial sorptivity is observed in HPHFRC-NC specimen as compare to HPHFRC-SC specimen.

The absorption of steam cured HPHFRC exhibited lower absorption as compared to the HPHFRC-NC specimen. The refinement in the pore, additional C-S-H formation, and

pozzolanic reactivity due to the steam curing led to lower rate of absorptions in HPHFRC-SC specimen as compared to HPHFRC-NC.

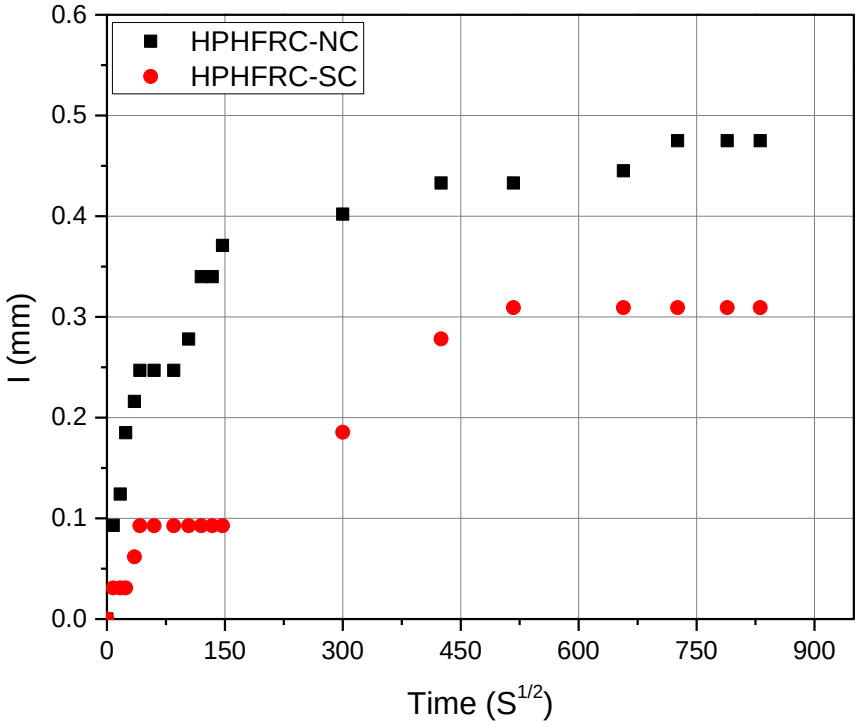

Fig. 3.37 - Water Absorption Curves as a Function of Time Measured for HPHFRC-NC and HPHFRC-SC Specimen

3.8.7 Sulphate Resistance

The concrete hydration and sulphate solution reaction mainly developed two chemical compounds i.e. gypsum and ettringite. The prime reactions taken place during sulphate attack on concrete are;

$$Na_2SO_4 + Ca(OH)_2 + 2\,H_2O \rightarrow CaSO_4.\,2H_2O + 2\,NaOH \qquad (3.9)$$

(Gypsum)

$$3CaO.\,Al_2O_3\,.12H_2O + 3(CaSO_4.\,2\,H_2O) + 13H_2O \Rightarrow 3CaO.Al_2O_3\,.3CaSO_4.31H_2O \qquad (3.10)$$

(Ettringite)

The excessive formation of these compounds leads to expansion and disrupts the cement paste; consequently, the fine cracks and disintegration of concrete occur (Saleh 2017). The aggressive chemicals contained water in the atmosphere easily penetrates in concrete once the

fine cracks developed. This process significantly affects the serviceability of concrete structures along with concrete durability.

The visual inspection of HPHFRC-NC shows the disintegration of concrete from all around the corners. The disintegration initially took place in corners and led to the three dimensions in each sample of HPHFRC-NC specimen, as shown in Fig. 3.38. The spots on the surface of the specimen are also observed after 180 days of sodium sulphate concentrated curing. HPHFRC-SC specimen exhibited minor disintegration on the corners and spots on the surface as shown in Fig. 3.39. It can be concluded that the steam curing specimen depicts the more resistance against sulphate attack as compared to the normal curing specimen.

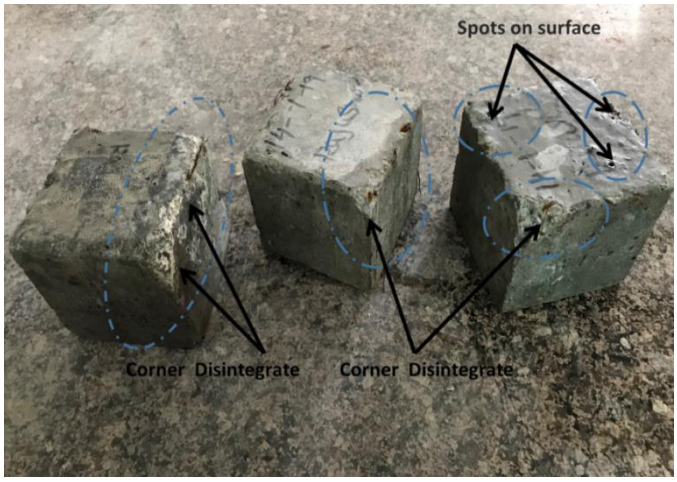

Fig. 3.38 - Visual Inspection of HPHFRC-NC Specimen after 180 Days Curing in Sodium Sulphate Solution

Fig. 3.39 - Visual Inspection of HPHFRC-SC Specimen after 180 Days Curing in Sodium Sulphate Solution

The strength of both the specimen is measured after 180 days of sodium sulphate curing. The 7.50% of strength loss has been found in HPHFRC-NC specimen. The strength loss in HPHFRC-SC is lesser than the HPHFRC-NC i.e., 4.23%. The improvement in gel and

internal structure of the steam curing specimen increases the resistance of concrete against the sulphate attack.

3.8.8 Scanning Electron Microscopy (SEM)/Electron Diffraction Spectroscopy (EDS) and Line Mapping

From Fig. 3.40 – 3.43, it has been observed that the pit near the fiber-matrix bond led to weaken the performance of HPHFRC-NC specimen. The bond between the fiber and matrix has captured at 50x, 150x, 1500x and 4500x for the normal water cured and steam cured HP-HFRC. A large number of voids with poor matrix fiber interface bond have been confirmed (see Fig. 3.43). However, a dense fiber-matrix interface has been observed in steam cured HP-HFRC, as shown in Fig. 3.44 - 3.47. The steam cured sample also shows the pit on the surface but it occurs away from the fiber-matrix interface. An excellent fiber-matrix bond, along with the dense matrix, has been observed, as shown in Fig. 3.47. The EDS results of HPHFRC-NC and HPHFRC-SC specimens are somewhat similar. However, the amount of calcium element is found higher in steam cured HP-HFRC than water cured HP-HFRC (see Fig. 3.48 – 3.50). The line mapping of both the specimen is conducted. The line is marked from the fiber surface to the matrix in both the specimen, as shown in Fig. 3.52 – 3.53. It has been observed from the line mapping that the lime, silica, and alumina exhibited the consistent intensity in the matrix in normal water cured HP-HFRC and steam cured HP-HFRC. The intensity of iron is maximum on the steel fiber but as the line approach to the matrix phase, the percentage of iron is negligible in both the samples (Fig. 3.54 & 3.55). So, it can be concluded that the distribution of elements is uniform in both types of specimen. However, the dense formation of gel and fiber matrix interaction as illustrated in SEM images significantly depends upon the curing.

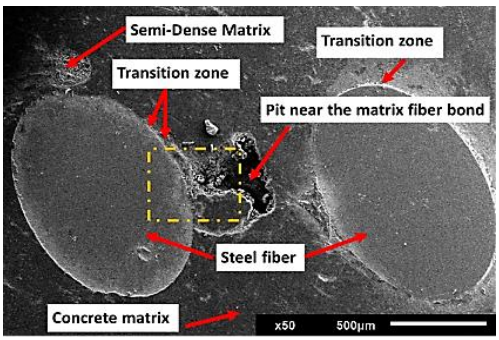

Fig. 3.40- Morphology Evaluation of Normal Cured HPHFRC - NC at x 50 Magnification Level

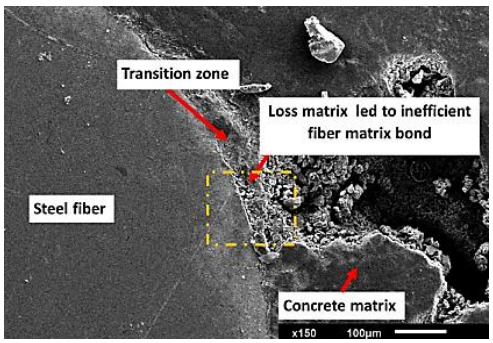

Fig. 3.41- Morphology Evaluation of Normal Cured HPHFRC - NC at x 150 Magnification Level

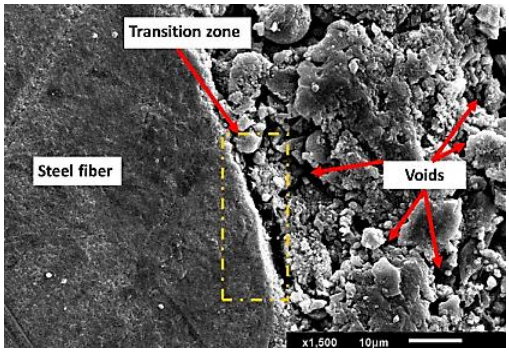

Fig. 3.42- Morphology Evaluation of Normal Cured HPHFRC - NC at x 1500 Magnification Level

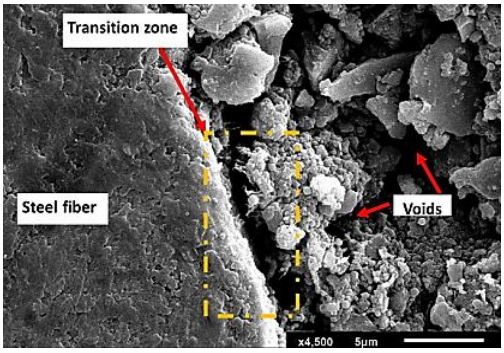

Fig. 3.43- Morphology Evaluation of Normal Cured HPHFRC - NC at x 4500 Magnification Level

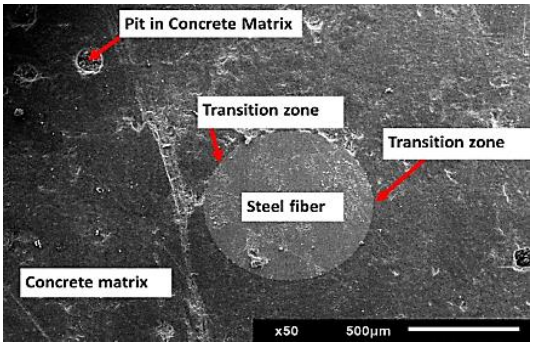

Fig. 3.44 - Morphology Evaluation of Steam Cured HPHFRC -SC at x 50 Magnification Level

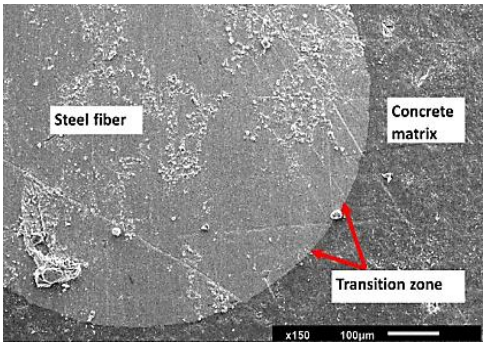

Fig. 3.45 - Morphology Evaluation of Steam Cured HP-HFRC - SC at x 150 Magnification Level

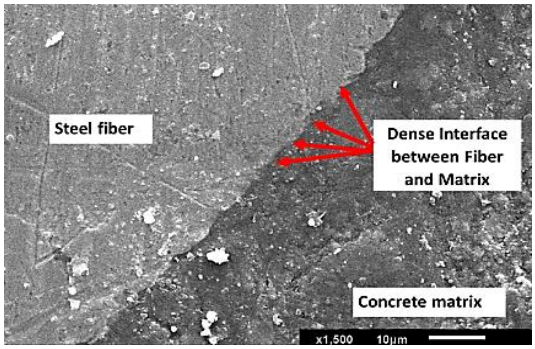

Fig. 3.46 - Morphology Evaluation of HPHFRC-SC at x 1500 Magnification Level

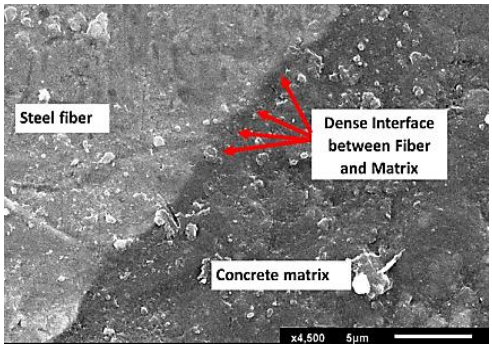

Fig. 3.47 - Morphology Evaluation of HPHFRC-SC at x 4500 Magnification Level

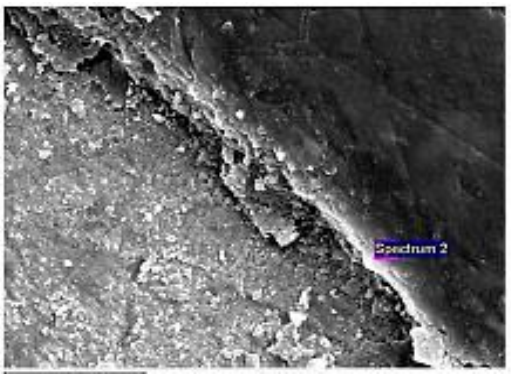

Fig. 3.48 - Location for EDS Analysis of HPHFRC-NC Specimen

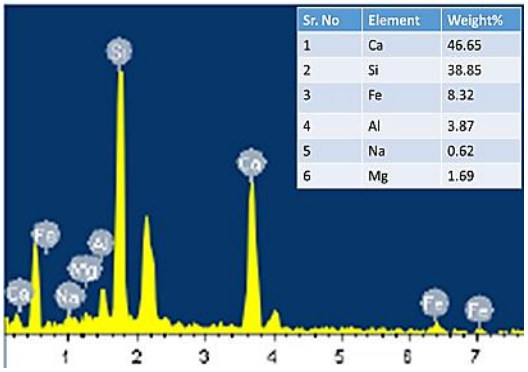

Fig. 3.49 - Elemental Analysis using EDS of HPHFRC-NC Specimen

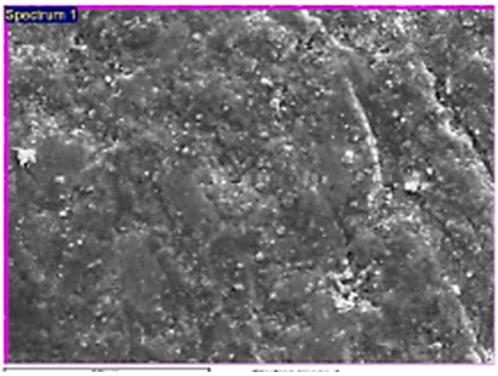

Fig. 3.50 - Location for EDS Analysis of HPHFRC-SC Specimen

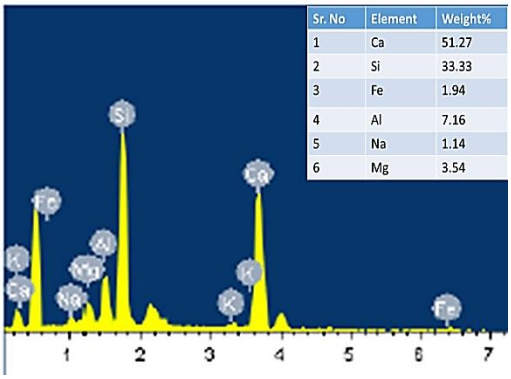

Fig. 3.51 - Elemental Analysis using EDS of HPHFRC-SC Specimen

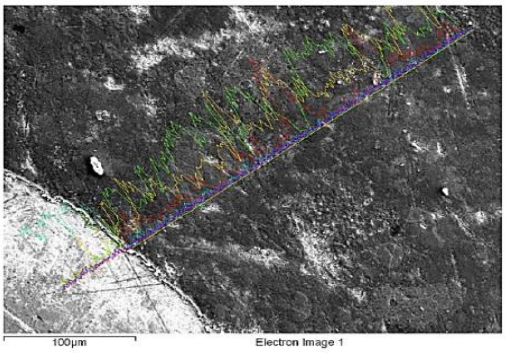

Fig. 3.52 - Location for Line Mapping Analysis of HPHFRC-NC Specimen

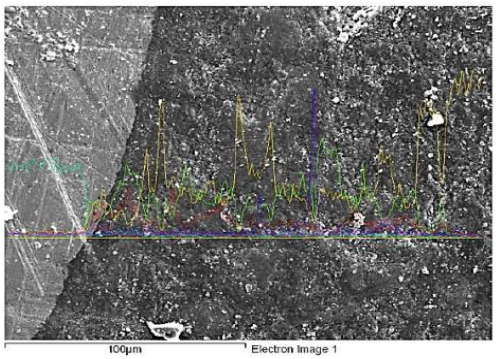

Fig. 3.53 - Location for Line Mapping Analysis of HPHFRC-SC Specimen

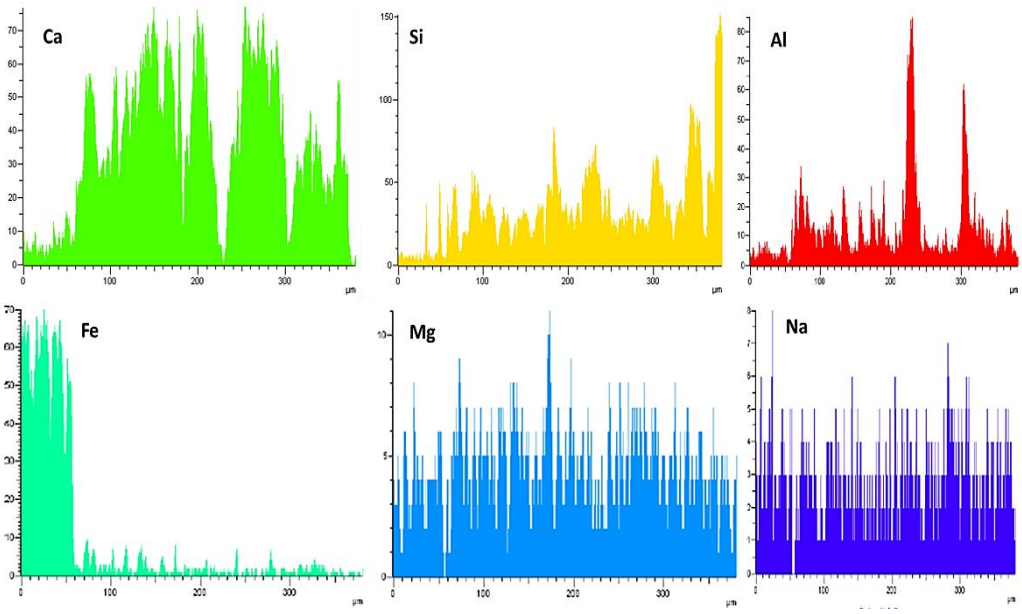

Fig. 3.54 - Line Mapping Analysis of HPHFRC - NC Specimen

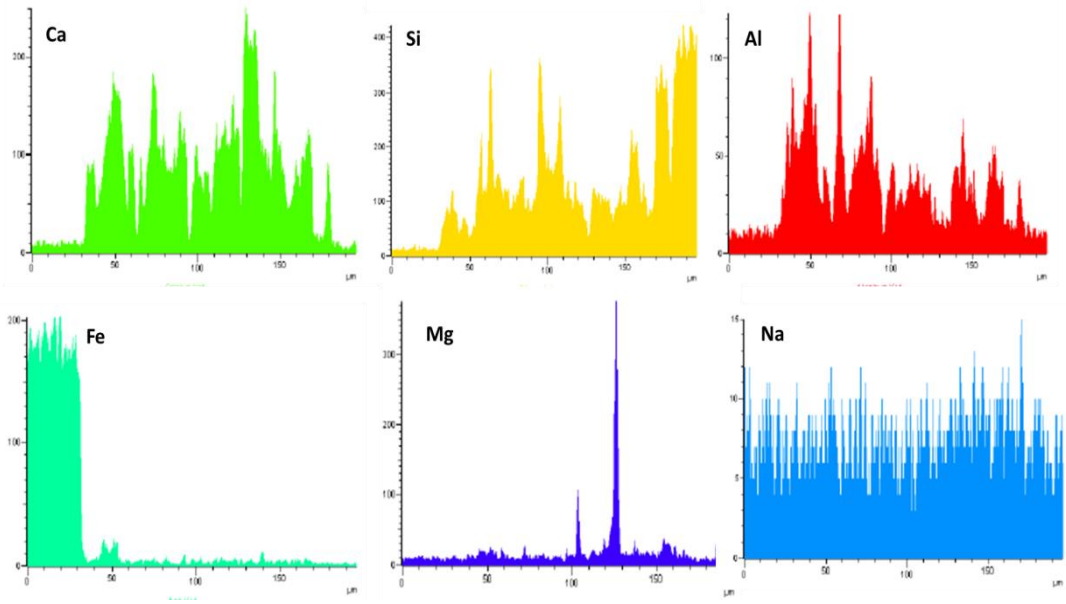

Fig. 3.55 - Line Mapping Analysis of HPHFRC - SC Specimen

HPHFRC-NC and HPHFRC-SC exhibited excellent mechanical, durability, and microstructure property. The development of HPHFRC using normal curing and steam curing intends to apply for the retrofitting of the initially damaged beam column joint. The normal curing is feasible and cheap as compare to steam curing for field application; therefore, HPHFRC-NC is opted for retrofitting the initially damaged beam column joint.

CHAPTER 4
EXPERIMENTAL PROGRAM

4.1 GENERAL

This part of the dissertation aims to evaluate the physical properties of the ingredients used to prepare the M20 grade concrete and steel used as reinforcement to cast the beam column joint specimens. Also, the strategies adopted to retrofit the initially damaged beam column joints are explained in detail in this chapter. Total sixteen beam column joint specimens have been cast, out of these sixteen specimens, eight specimens (two for each damage level) are retrofitted using confined HP-HFRC, and the other eight are retrofitted by wire mesh confined HP-HFRC. The two specimens initially tested as control specimens under quasi static reverse cyclic loading to measure the ultimate load carrying capacity of the specimen to prepare the load displacement hysteresis.

From the obtained load displacement hysteresis of control specimen, the Park and Ang damage indices model is used to quantifying the four distinct damage states i.e., complete damage, severe damage, moderate damage, and slight damage.

Further, the set of two specimens have been initially damaged under quasi static reverse cyclic loading to obtain the each calculated damage state. These damaged specimens are further retrofitted using HP-HFRC and HP-HFRC confined with wire mesh.

The retrofitted specimens under both the retrofitting scheme are tested under quasi static reverse cyclic loading and their behaviour is compared with the control specimen.

4.2 MATERIALS

4.2.1 Binder

UltraTech makes 43 grade Ordinary Portland cement is used as a binder for preparing M20 grade concrete. Before use, the cement is tested in the laboratory as per the BIS standards IS: 8112. The physical properties of cement are shown in Table 4.1.

Table 4.1 - Physical Properties of Cement

Sr No	Characteristics	Test values	Values specified by IS 8112 – 2013
1	Standard Consistency (%)	32	----
2	Fineness of cement as retained on 90 micron sieve (%)	2	----
3	Specific Gravity	3.11	3.15
4	Setting time:		
	a) Initial Setting time(minutes)	125	30 *(minimum)*
	b) Final Setting Time(minutes)	333	600 *(maximum)*
6	Compressive Strength, MPa:		
	a) 3 days	25.5	23*(minimum)*
	b)7 days	35	33*(minimum)*
	c) 28 days	45	43*(minimum)*

4.2.2 Aggregates

Two types of aggregates i.e., fine aggregates and coarse aggregates, are used. The physical properties of fine aggregates are experimentally evaluated as per the guidelines provided in IS 2386Part 1: 1963 and IS 383: 1970. The various properties of fine aggregates are presented in Table 4.2 – 4.3. The experimentally obtained cumulative particle size distribution curve, upper and lower limits of sand lie in zone III, is plotted in Fig. 4.1. The 20mm nominal size coarse aggregates are used. The experimental tests are conducted to evaluate the physical properties of coarse aggregate, and the obtained values are presented in Table 4.4 and 4.5. The cumulative particle size distribution curve of the coarse aggregate is shown in Fig. 4.2.

Table 4.2 - Physical Properties of Fine Aggregates

Sr. No.	Characteristics	Test values
1	Type	Natural Sand
1	Specific Gravity	2.65
2	Water Absorption	1.02 %
3	Particle Size Range	0.15 mm – 4.75 micron
4	Fineness Modulus	2.22

Table 4.3 - Fineness Modulus of Fine Aggregates

Sieve Size (mm)	Weight Retained (gram)	Weight retained (%)	Cumulative weight retained (%)	Percentage passing	Limit described in IS 383 :1970 for Zone III
4.75	34	0.34	0.34	99.66	90 -100
2.36	64.9	6.49	6.83	93.17	85 - 100
1.18	157.4	15.74	22.57	77.43	75 - 100
600	166.9	16.69	39.26	60.74	60 - 79
300	237.2	23.72	62.98	37.02	12 - 40
150	274	27.4	90.38	9.62	0 - 10
Pan	65.6		Σ = 222.36		

$$\text{Fineness Modulus} = \frac{222.36}{100} = 2.22$$

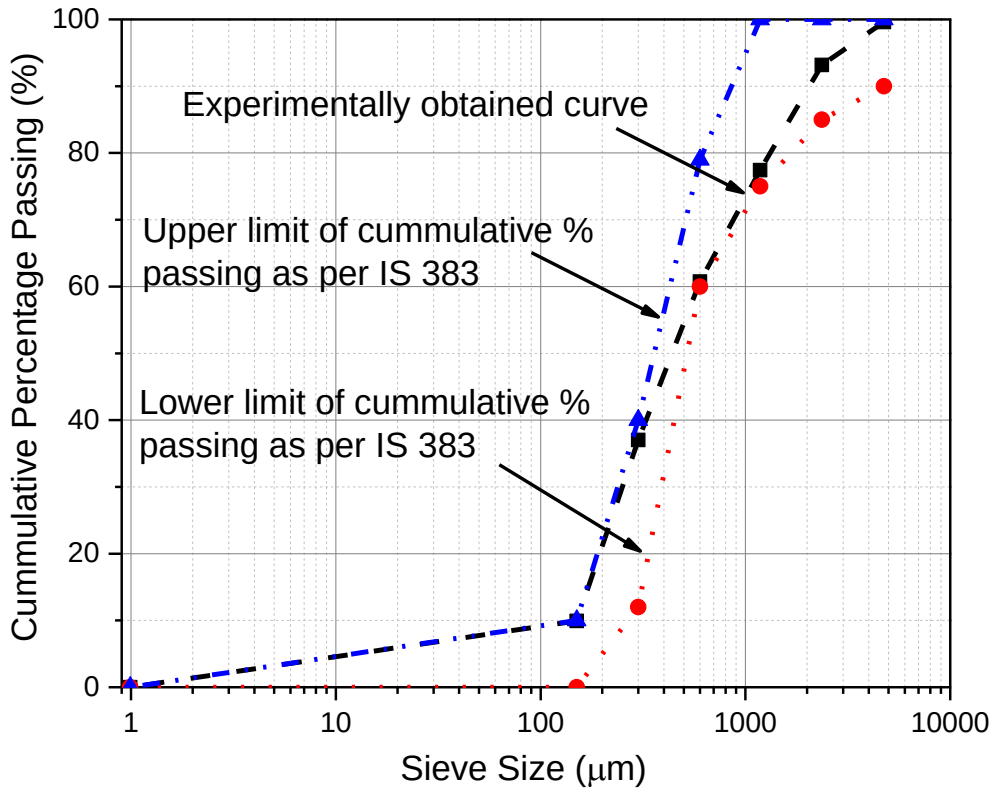

Fig. 4.1- Particle Size Distribution Curve of Fine Aggregate

Table 4.4 - Physical Properties of Coarse Aggregate

Sr No	Characteristics	Test values
1	Type	Crushed
1	Particle Size	20 mm
2	Specific Gravity	2.60
3	Water Absorption	1.90 %
4	Fineness Modulus	6.87

Table 4.5 - Fineness Modulus of Coarse Aggregate

S.No.	Sieve Size (mm)	Weight retained (gram)	Weight retained (%)	Cumulative weight retained (%)	Percentage Passing,
1	80 mm	0	0	0	100
2	40 mm	0	0	0	100
3	20 mm	0	0	0	100
4	10 mm	2648	88.26	88.26	11.74
5	4.75 mm	324	10.80	99.06	0.94
6	pan	28	0.94	Σ=187.32	-

$$F.M = \frac{187.32+500}{100} = 6.87$$

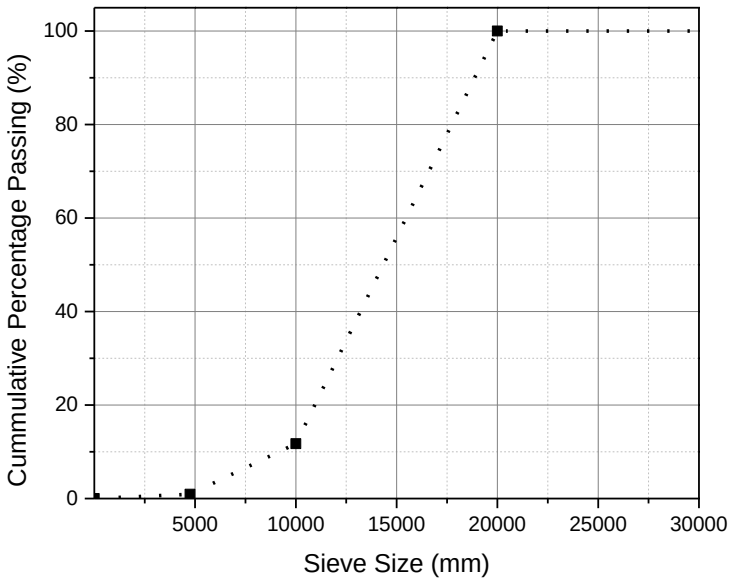

Fig. 4.2 - Particle Size Distribution Curve of Coarse Aggregate

4.2.3 Reinforcement

The HYSD-TMT steel, 8 mm, and 10 mm diameter bars, of grade Fe-415 confirming to IS: 1786-1985 is used as reinforcement in beam column joint specimens. The reinforcement is tested using a Universal Testing machine of 1000kN capacity. The arrangement of testing and mode of failure of reinforcement bars at the ultimate load is shown in Fig. 4.3, and 4.4. The yield strength and ultimate tensile strength of 10 mm and 8 mm diameter bars have been found out to be 455 MPa, 418 MPa, and 555 MPa, 525 MPa, respectively.

Fig. 4.3 - Testing Arrangement of Reinforcement

Fig. 4.4 - Ultimate Fracture of Reinforcement

4.2.4 Wire Mesh

The galvanized wire mesh of 0.48mm-0.49mm diameter bars and 10mm x 10mm opening size is used to retrofit the beam column joint. The uniaxial tensile strength of mesh is conducted in a universal testing machine of 1000 kN capacity as per ACI 549.1R-1999. The yield strength and ultimate strength of wire mesh has been found out to be 630 MPa and 715 MPa, respectively

4.2.5 Bonding Agent

The Fosroc make Nitobond EP STD, base and hardener are used to generate the efficient bond between the old and new concrete. The base and hardener are mixed in a ratio of 1: 0.5 and stirred properly before applying. Fig 4.5 shows the bonding agent used in the present study. The mechanical properties of the bonding agent (as provided by the manufacturer) are shown in Table 4.6.

Fig. 4.5 - Nitobond EP STD used for Offering the Efficient Bond between Old and New Concrete

Table 4.6 - Properties of Nitobond EP STD

Sr. no.	Properties	Value
1	Pot life	Min. 120 minutes @ 350^{o} C
2	Full hardness	24 hours
3	Overlay time	Up to 3 hrs.
4	Compressive Strength as per BS 6319 Part 2	40 N/mm^2
5	Tensile Strength as per BS6319 Part 7	15 N/mm^2
6	Flexural Strength as per BS 6319 Part3	25 N/mm^2
7	Bond strength as per ASTM C881	11N/mm^2

4.3 DESIGN MIX DETAIL AND CASTING OF BEAM COLUMN JOINT

4.3.1 Design Mix

To study the behaviour of beam column joints retrofitted using HP-HFRC and wire mesh confined HP-HFRC, external beam column joint specimens are cast using M20 grade concrete. The M20 grade concrete mix is designed by adopting the design procedure described in IS 10262:2009, and final mix proportions are shown in Table 4.7. The concrete cylinders of size 150 x 300 mm are cast and tested as per ASTM C39 to assess the

compressive strength of concrete. The 7 and 28 days compressive strength of the concrete cylinder are shown in Table 4.7. The axial stress-strain curve of the concrete design mix, after 28 days of curing, is plotted and shown in Fig. 4.6. It can be observed from the stress-strain curve that the stress-strain is almost linear up to a strain level of 0.0013, and afterward, the post peak strain reaches up to .00286.

Table 4.7 - Mix Design of M20 Concrete as Per Indian Standard Code 10262: 2009

Particulars	Cement(Kg/m^3)	Sand(Kg/m^3)	Coarse aggregate(Kg/m^3)	Water(Kg/m^3)	7 days strength (MPa)	28 days strength (MPa)
Quantity	394	637	1142	197	18.36	25.6

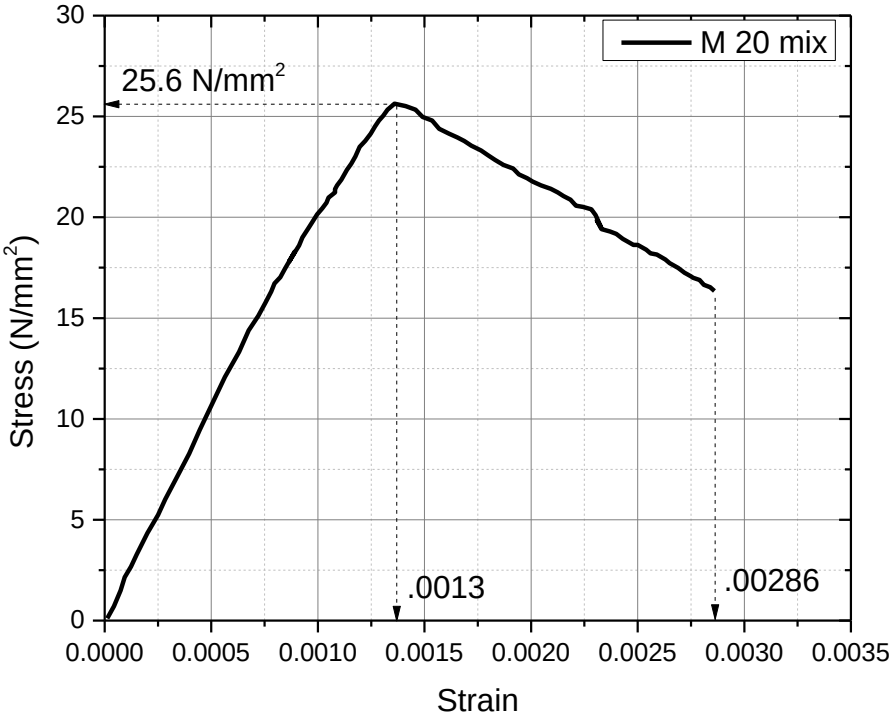

Fig. 4.6 - Axial Stress Strain Curve of Control Concrete

4.3.2 Casting of Beam Column Joint Specimens

The casting of beam column joint specimens is done using MS moulds. The mould used for casting the BCJ is oiled properly before the casting, to facilitate easy de-moulding. The cover blocks of 25mm thickness are placed between the shuttering and reinforcement cage of BCJ

to provide the nominal cover all around the cage of beam column joint (see Fig. 4.7). The concrete mix is prepared using a tilting type mixture. The prepared concrete is filled in two layers in the mould; each layer is vibrated using a 60 mm diameter needle. The internal vibrator mechanism is used to eliminate the voids from the fresh concrete. The vibrator placed inside the concrete at an angle of 90^{o} for achieving efficient compaction (see Fig. 4.8).

During the casting of BCJ specimens, concrete cylinders are filled and tested after 28 days (see Fig 4.9). After one day of curing, the vertical sides of mould are removed, and the surface is covered with wet jute bags (see Fig. 4.10).

Fig. 4.7 – BCJ Reinforcement Cage is Placed Inside of the Mould

Fig. 4.8 - Internal Type Vibrator used for Compaction

Fig. 4.9 - Cubes and Cylinders Filled for 28 Days Compressive Strength Testing

Fig. 4.10 - BCJ Surface Cover with Wet Jute Bags for Curing

4.4 BEAM–COLUMN JOINT SPECIMEN AND TEST SETUP

The dimensions and reinforcement details of beam column joint specimens are shown in Fig. 4.11. As shown in the Figure 4.11, three bars of 10 mm diameter is provided at the top, and

two bars of 8 mm diameter is provided at the bottom of the beam, whereas, 8mm diameter 2L- stirrups @ 100 mm centre to centre are provided as shear reinforcement. In a column, four bars of 10 mm diameters are provided as the main reinforcement, and 8mm diameter rings @ 100 mm centre to centre are as lateral reinforcement. The detailing of reinforcement is done as per the guidelines provided in IS 456: 2000 for ordinary moment resisting frame, which is not intended to meet the special detailing as per IS 13920 for obtaining the ductile behaviour during non-linear rotation.

The specimen is tested in the loading frame with the help of double acting jack of capacity 300 kN. The displacement control quasi-static reverse cyclic loading is used to test the beam column joint and the test set-up is shown in Fig. 4.12. The steel I section of 1000 mm depth is used as a reaction wall. The quasi static reverse cyclic loading jack and assembly are fixed through nut and bolt arrangement on the reaction wall to apply the lateral loading on the beam portion. In the test set-up, the column is placed horizontally on the strong base and beam held vertically at an angle of 90° to the base. The 16 mm diameter nut bolt system is used to fix both ends of the column at a distance of 100 mm from each end. The roller support is also placed at 100 mm away from the column end. The horizontal moment and P - Δ effect of the column is restricted through this arrangement as this study is focused on the joint behaviour through beam rotation. The axial force in the column is applied with the help of hydraulic jack on one end of the column and keeping the other end of the column supported by fix welded steel angle to produce the equal reaction.

The adopted load displacement history is shown in Fig. 4.13. The quasi static reverse cyclic loading onset with an initial displacement of 5 mm and then increment of 5mm till failure (each step consisting of two cycles of the same displacement) has been applied to achieve the complete strength and stiffness degradation of the BCJ. The two linear variable differential transducers (LVDT) are placed (one on the left side of the beam and one on the right side of the beam) on the same axis of applied loading to measure the lateral deformation of the beam. The least count and maximum displacement capacity of the LVDT are 0.001 and 50 mm, respectively. The LVDTs are attached to the data logger to receive the response of the beam column joint. The data logger contained two channels for load, three channels for LVDTs, and eight channels to record the strain. Before starting the test, an initial displacement of 1mm is applied to check the working status of the load cell and LVDTs. Once the working condition of load cell and LVDTs are confirmed through the signal received in the data logger, the test is proceeded to obtain the complete response.

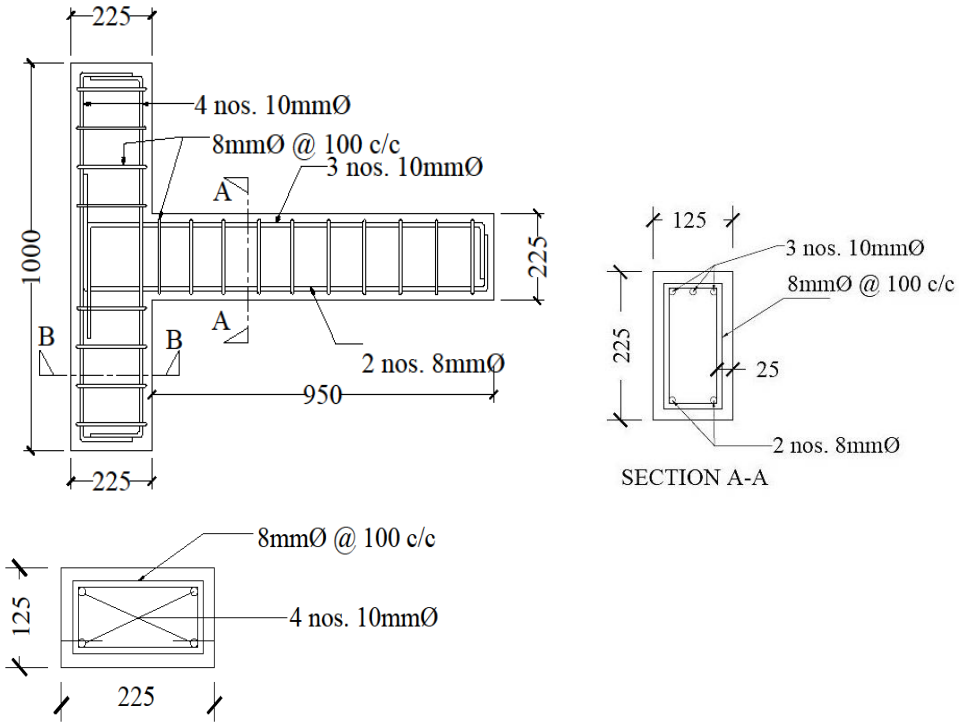

Fig. 4.11 - Reinforcement Detail of RC Exterior Beam Column Joint

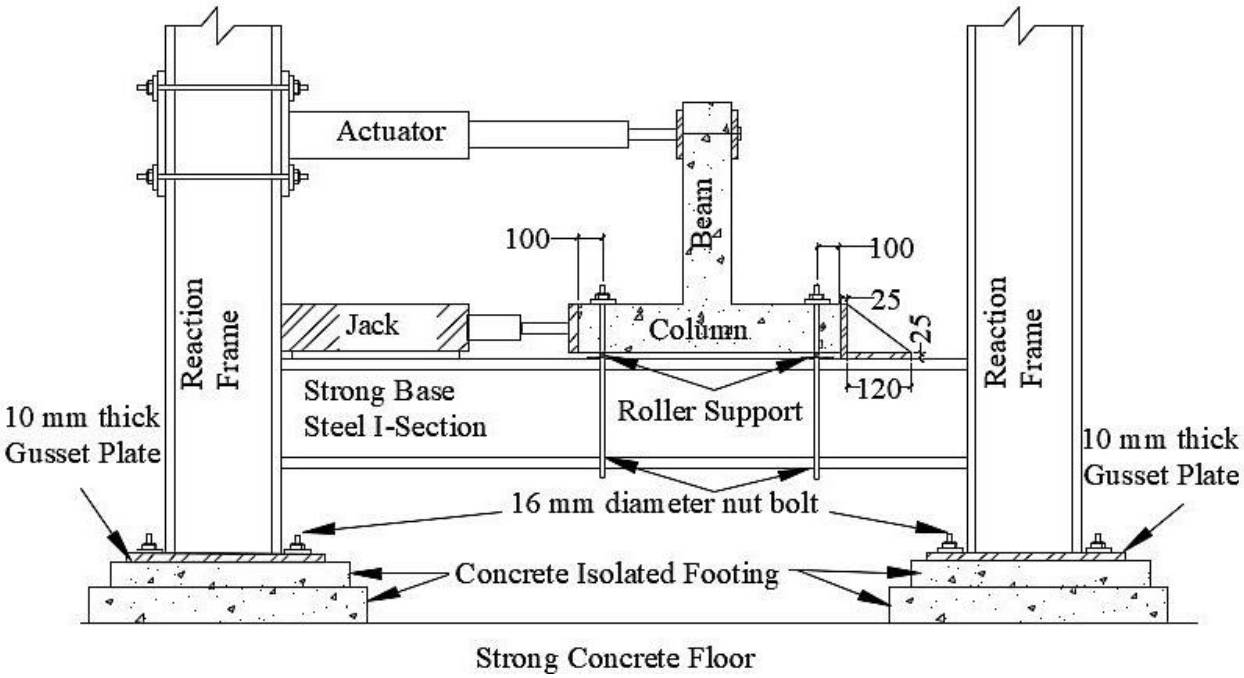

Fig. 4.12 - Detail of Experimental Setup and Geometric Dimensions of the Beam Column Joint

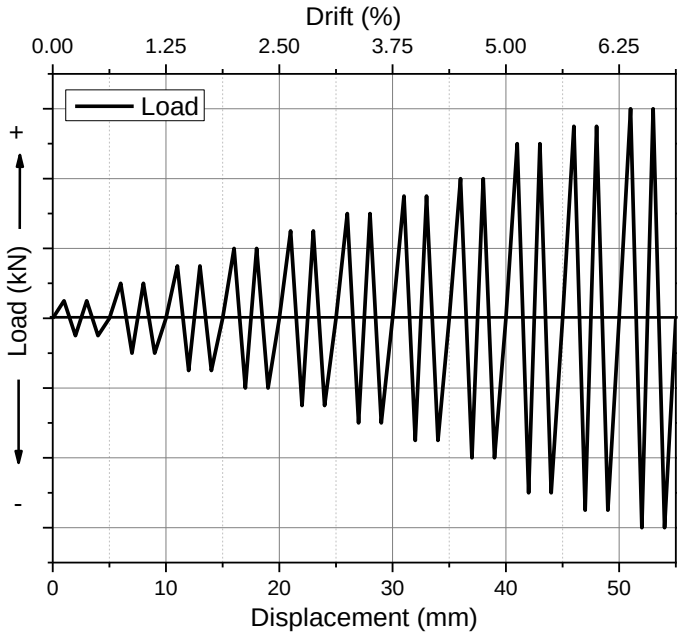

Fig. 4.13 - Cyclic Loading History for Testing the Beam Column Joint

4.5 DAMAGE LEVEL OF BCJ SPECIMENS

Firstly the control specimen is tested under quasi-static reverse cyclic loading till failure. Based on the obtained load displacement hysteresis of the controlled specimen, the damage indices were calculated using the park and Ang index model. The equation used to calculate the damage index is as follows.

$$D = \frac{\delta_M}{\delta_u} + \frac{\beta}{F_y \delta_u} \int dE \qquad (5.1)$$

In the above equation, δ_u is the maximum displacement experienced by the structure i.e., 35 mm and δ_M is the maximum displacement of the cycle considered i.e., 5mm, 10mm, 15mm, 20mm, 25mm, 30mm, and 35mm. The integral part contained the hysteretic energy dissipation of the cycle understudy, and F_y is the yield strength of the structure, calculated from the load hysteresis curve of the control specimen. Factor "β" is a strength degradation parameter depends upon volumetric transverse ratio, shear span to depth ratio, normalized axial force, and tensile force, who's value is taken as 0.1 in the present study. The damage index 'D' is a dimensionless parameter. Under the elastic conditions, the value of damage index "D" will be zero. However, equation 5.1 gives a very small non zero value of "D" in the elastic range. Whereas, the value of D ≥ 1.0 indicates that the structural element is collapsed or totally damaged. The theoretical range of damage indices i.e. ≥1 (Complete damage), 0.6 – 0.8 (Severe damage), 0.4 – 0.6 (Moderate damage), 0.2 – 0.4 (Slight damage) are taken to define the damage state *(Park and Ang, 1985, 1987)*. Based on the load

displacement hysteresis of control specimens, the damage indices are calculated in such a way that they lie in the range of complete damage, sever damage, moderate damage, and slight damage. Now depending upon the value of the calculated damage index, the damage can be defined as complete damage (DI - 1), severe damage (DI - 0.80), moderate damage (DI - 0.45), and slight damage (DI - 0.30) as shown in Table 4.8. It is noteworthy to mention that each calculated damage index is obtained in the specimen by applying the fraction of quasi static reverse cyclic loading from the complete load displacement history of the control specimen. As the fraction of displacement from the complete load displacement history is applied, the fraction of energy is released and the specimen reached its particular damage level. Therefore, the specimens are subjected to cyclic loading to obtain the complete damage, severe damage, moderate damage, and slight damage based on their calculated damage index from the load displacement hysteresis obtained from the testing of the control specimens. The initially damaged specimens designated as C-CD, C-SED, C-MD, and C-SD is prepared for retrofitting.

Table 4.8 - Calculated Damage Index of the Specimens

Sr. No	Specimen Identification	Damage Level	Damage Index	Calculated damage index
1	Control Complete Damage (C-CD)	Complete Damage	Equal/greater than 1	1
2	Control Severe Damage (C-SED)	Severe Damage	0.6 to 0.8	0.80
3	Control Moderate Damage (C-MD)	Moderate Damage	0.4 to 0.6	0.45
4	Control Slight Damage (C-SD)	Slight Damage	0.2 to 0.4	0.30

4.6 RETROFITTING USING HP-HFRC

The concrete cover/damaged concrete from all the initially damaged specimen is chipped off, and the loose material is removed with the help of a blower (Fig. 4.14). The dimensions of removed concrete up to the cover from the periphery of the BCJ specimen are illustrated in Fig. 4.15. The ends of chipped surfaces of tested BCJ specimen are chamfered at the slope of 1:8 to avoid the abrupt change of plane between the old concrete (M20 grade) and HP-HFRC (4.16a). The surface is cleaned and bonding agent i.e., Nitobond EP-STD, is applied on the chipped cleaned surface. The Nitobond base and hardener are mixed in the ratio of 1: 0.5. The bonding agent is used to avoid the bonding failure of new and old concrete; otherwise, de-bonding promotes the premature failure of the old and new concrete bonding plane (Fig.

4.16b). After the application of the bonding agent, the specimen is placed in formwork. Alongside this, the HP-HFRC is prepared to retrofit the damaged BCJ specimen. The prepared HP-HFRC is poured on the chipped area of beam column joint, and the vibrator consisted of a 25 mm size needle is used to eliminate the voids from the HP-HFRC (Fig. 4.16c). The procedure to retrofit the initially complete damage (CCD) specimen is shown in Fig. 4.16a-c. After 24 hours, the side face of the formwork is removed, and the specimen is covered by wet gunny bags. After 7 days of casting, the bottom formwork is removed, and the specimen is covered from all sides with wet gunny bags for curing till testing. The nomenclature for retrofitted initially damage specimens concerning their initial damage index i.e., 1 (complete damage), 0.80 (severe damage), 0.45 (moderate damage), and 0.30 (slight damage) are described in Table 4.9.

Fig. 4.14 - Specimen Chipped Off for the Retrofitting

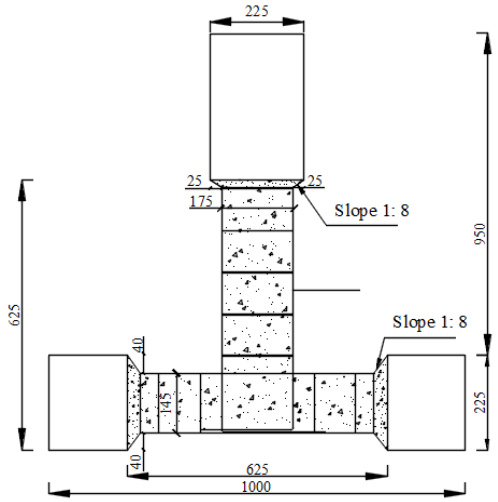

Fig. 4.15 - Schematic Illustration of Geometrical Dimensions of the Chipped Area to Retrofit the Specimen

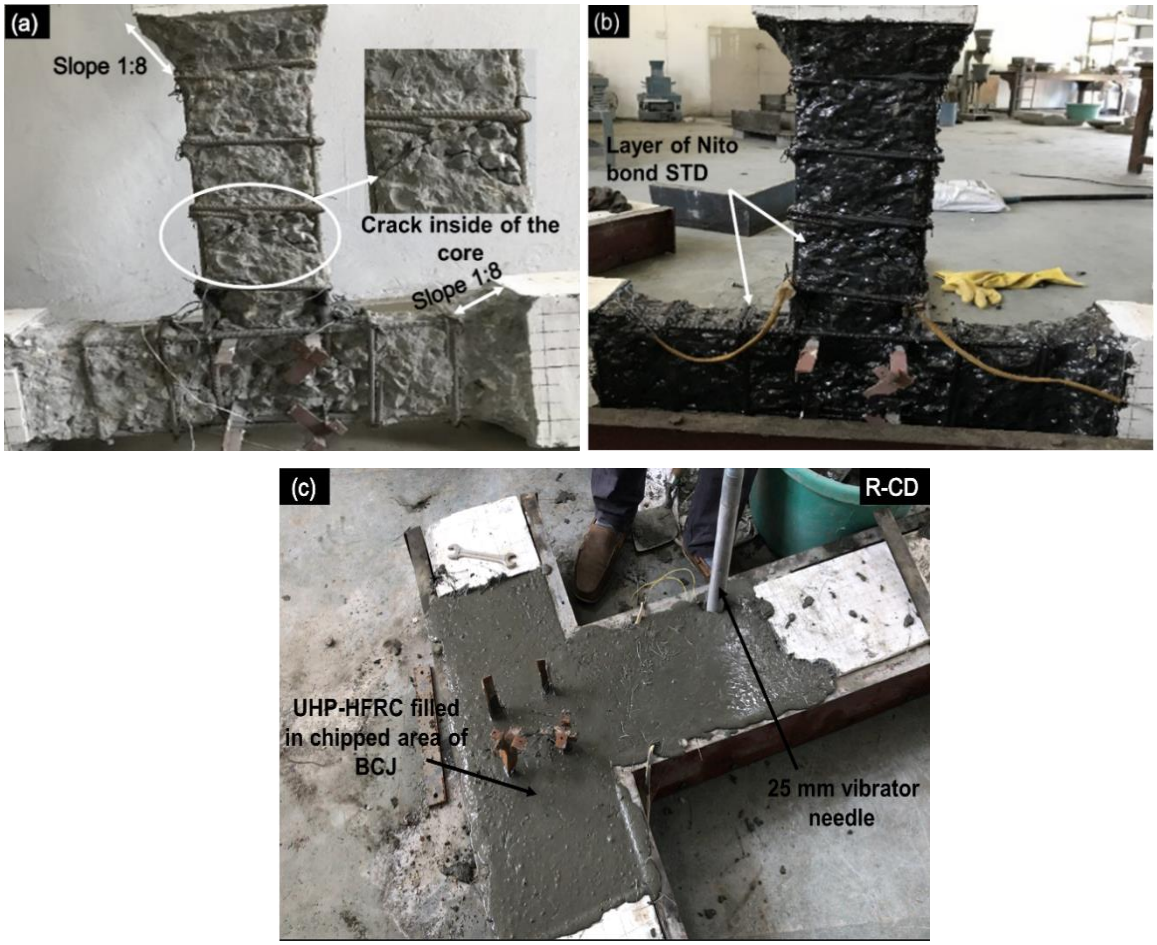

Fig. 4.16 - (a) Concrete Chipped up to Cover, (b) Layer of Nitobond STD on the Chipped Surface of Beam Column Joint, (c) HP-HFRC Poured in Formwork Consisted of Chipped Beam Column Joint

Table 4.9 - Configuration of the Retrofitted Specimen

Sr. No	Specimen Identification	Initial damage level for retrofitting	Corresponding damage index	Number of Specimen
1	Retrofitted Complete Damage (R-CD)	Complete Damage	1	2
2	Retrofitted Severe Damage (R-SED)	Severe Damage	0.80	2
3	Retrofitted Moderate Damage (R-MD)	Moderate Damage	0.45	2
4	Retrofitted Slight Damage (R-SD)	Slight Damage	0.30	2

4.7 RETROFITTING USING WIRE MESH CONFINED HP-HFRC

The process of chipping, cleaning, and application of nitobond on the clean chipped surface of initially damaged beam column joint are similar, as described in section 4.6. In the present

retrofitting technique, after the application of nitobond, the layers of wire mesh are used to wrap the chipped surface of the initially damaged beam column joint. The different configurations of wire mesh used to retrofit the initial damage beam column joint are numerically labeled as shown in Fig. 4.17. The sequence of wrapping of the wire mesh on the chipped area of initially damage beam column joint is illustrated in Fig. 4.17 and explained stepwise procedure as follows;

- The beam, column, and chipped portion of beam column joint are designated as 1, 2, and 3, respectively. L shape wire mesh 4 apply on the beam top, and adjacent column chipped portion above the beam 2 (see Fig 4.17 - 4.18a).
- L shape wire mesh 5 applies on the beam bottom, and adjacent column chipped portion below the beam 2.
- A U shaped wire mesh 6 placed on the chipped surface of joint and adjacent chipped portion of the beam on both sides faces.
- Wires mesh 7 wraps over the 4, 5 and 6 and finally tighten the wire mesh 7 with binding wire.
- Place the 8 and 9 wire mesh on side faces of the chipped column portion and wrap the 8 and 9 with 10 and 11, and then 10 and 11 tightened, further, with binding wire (see Fig. 4.18b)
- The HP-HFRC is so poured that it covers the gap between the old concrete and wire mesh and further, the provided wire mesh also gets 25 mm concrete cover i.e., the wire mesh is sandwiched between HP-HFRC. The poured concrete on the wire mesh wrapped surface of beam column joint is vibrated using plate vibrator and then leveled finely.
- The old core concrete confined with wire mesh and HP-HFRC produces the confinement effect.
- The retrofitted member is a cure in water for at least 28 days to attain sufficient strength and then prepared for testing (see Fig. 4.18c).

The nomenclature used for the wire mesh confined retrofitted initially damaged specimens is wire mesh confined retrofitted complete damage (WC-RCD), wire mesh confined retrofitted moderate damage (WC-RMD), wire mesh confined retrofitted severely damage (WC-SED) and wire mesh confined retrofitted slight damage (WC-RSD)as shown in Table 4.10.

The limitation of this scheme is that the HP-HFRC prepared using coarse aggregate cannot spread uniformly in the chipped area because of the limited size of the wire mesh opening size. The limited opening size of wire mesh may hinder the uniform flow of the ingredient of HP-HFRC in the narrow and tight region consequently;, it may lead to the poor performance of retrofitted specimens. The alternative can be the selection of wire mesh with large size opening, which reduces the hindrance of large size ingredients in the mix; therefore, the uniform distribution of ingredients and improved performance can be achieved.

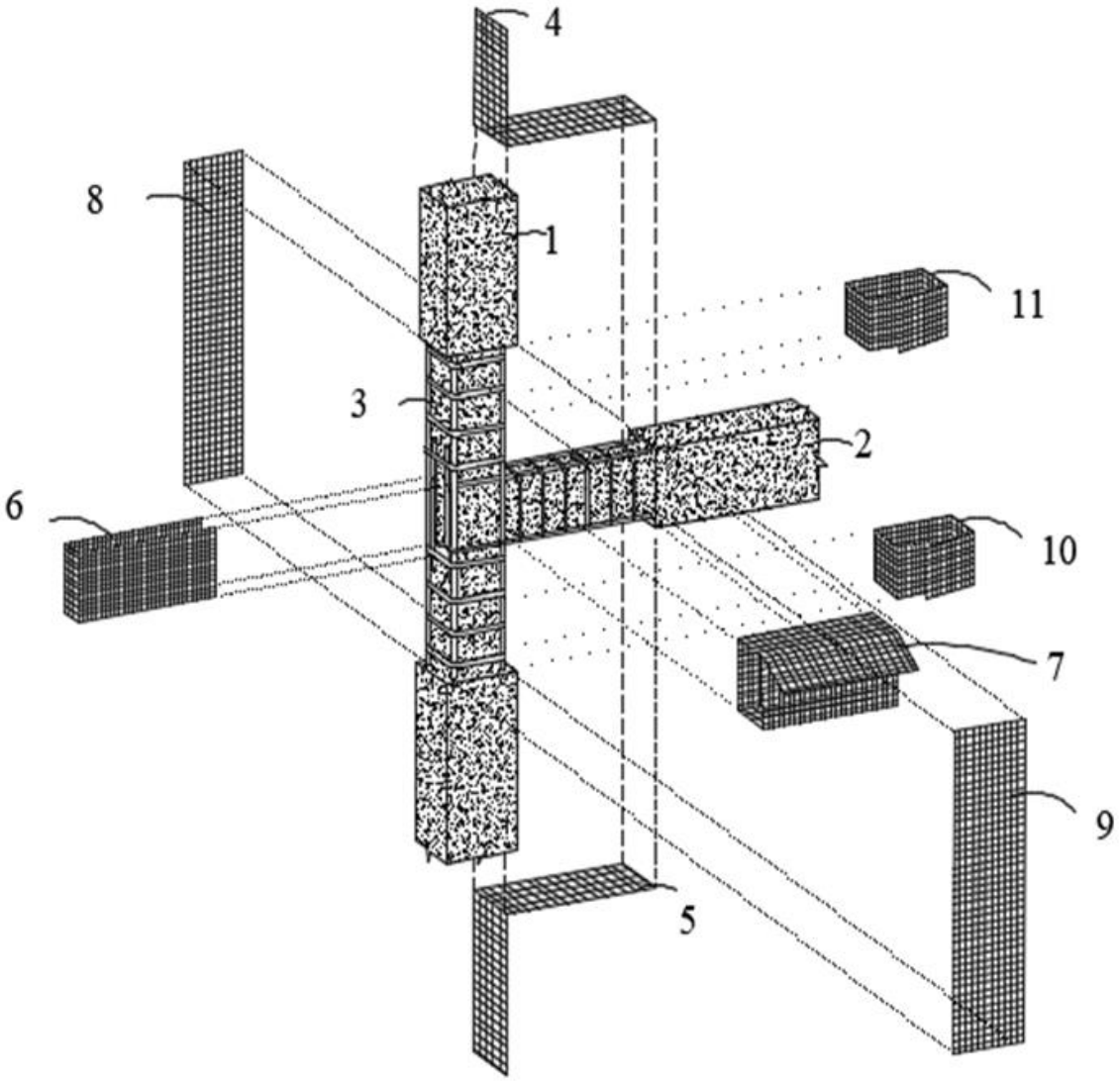

Fig. 4.17 - Schematic Description of the Process of Wire Mesh Confined HP-HFRC Retrofitting Strategy on the Initially Damage BCJ

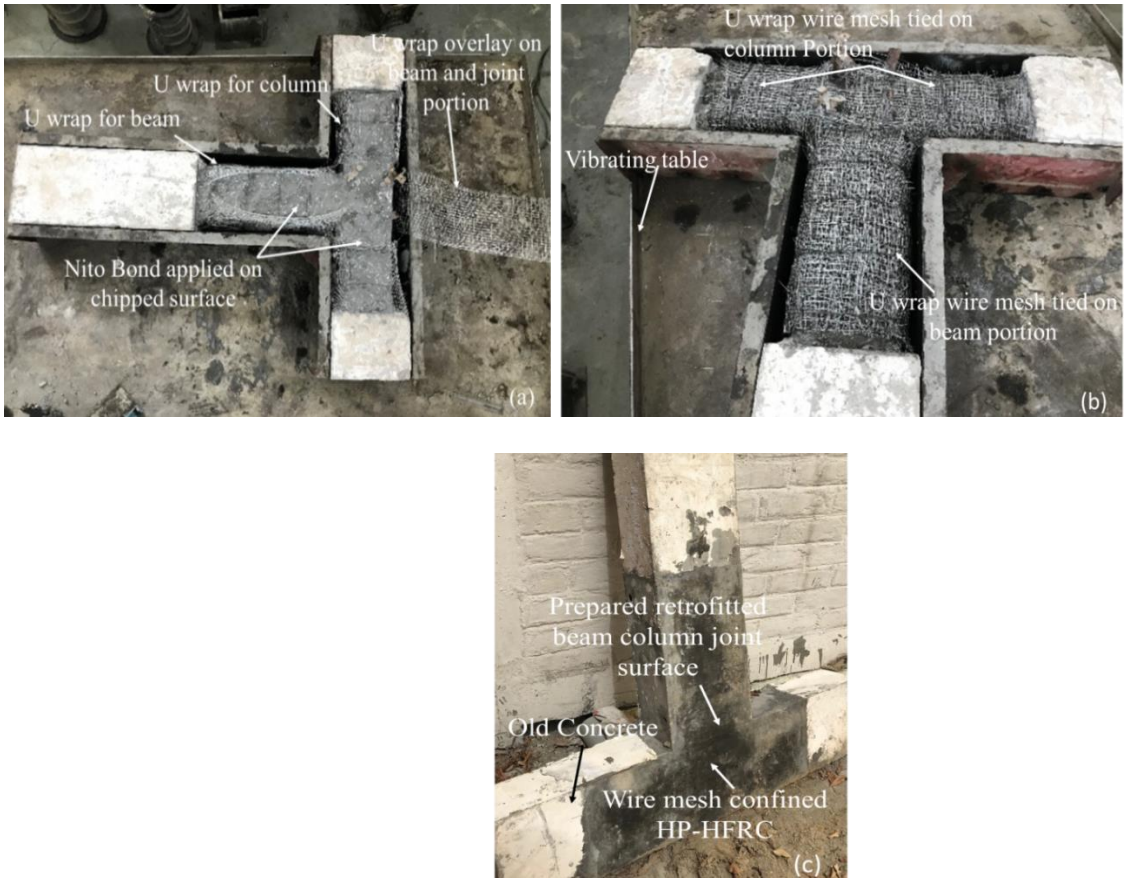

Fig. 4.18 - (a) Application of Nitobond on Chipped Surface of BCJ; (b) Wire mesh Tied on Chipped Portion and Ready for HPC-HFRC Pouring; (c) Retrofitted Specimen after Casting

Table 4.10 - Identification of Different Initial Damage Level Specimens and Retrofitted Specimens

Sr. No	BCJ identification before retrofitting	Selected initial Damage level	Range of Damage index	Obtained damage index corresponding to initial damage level	BCJ identification after retrofitting	Number of Specimen
1	Control Complete Damage (CCD)	Complete Damage	Equal/greater than 1	1	Wire mesh confined retrofitted complete damage (WC-RCD)	2
2	Control Severe Damage (CSED)	Severe Damage	0.6 to 0.8	0.80	Wire mesh confined retrofitted moderate damage (WC-RMD)	2
3	Control Moderate Damage (CMD)	Moderate Damage	0.4 to 0.6	0.45	Wire mesh confined retrofitted severely damage (WC-SED)	2
4	Control Slight Damage (CSD)	Slight Damage	0.2 to 0.4	0.30	Wire mesh confined retrofitted slight damage (WC-RSD)	2

In brief, a total of sixteen beam column joint specimens is cast, out of which, a set of eight specimens were retrofitted using HP-HFRC and other eight retrofitted using wire mesh

confined HP-HFRC. The set of eight specimens is distributed in four categories for HP-HFRC retrofitting strategy. The four categories are divided i.e., complete damage, severe damage, moderate damage, and slight damage level. A set of two specimens are tested under each damage level. So, a total of eight specimens are tested in HP-HFRC retrofitting strategy, and likewise, eight specimens have been tested for wire mesh confined HP-HFRC retrofitting.

CHAPTER – 5

RETROFITTING OF BEAM COLUMN JOINTS USING HIGH PERFORMANCE HYBRID FIBRE REINFORCED CONCRETE

5.1 GENERAL

In this part of the dissertation, an experimental investigation is carried out to evaluate the efficacy of high performance hybrid fiber reinforced concrete (HP-HFRC) in retrofitting. Further, the effect of initial damage on the performance of HP-HFRC retrofitted exterior beam column joint is also presented and discussed. To achieve the objectives, firstly, the control specimens (set of two beam column joints) are tested to obtain the complete load hysteresis behaviour, when subjected to quasi static reverse cyclic loading. Based on the obtained load displacement hysteresis of control specimen, the different damage levels viz., slight, moderate, severe, and complete have been calculated using Park and Ang model. The procedure for calculating the initial damage level is described in Chapter 4. Further, a total of eight beam column joints have been initially damaged to achieve the slight, moderate, severe, and complete damage levels; each damage level contained a set of two specimens. After that, the initially damaged specimens have been retrofitted using high performance hybrid fiber reinforced concrete.

The retrofitted initially damaged, i.e., retrofitted complete damage (R-CD); retrofitted severe damage (R-SED); retrofitted moderate damage (R-MD) and retrofitted slight damage (R-SD) specimens are tested again under quasi static reverse cyclic loading to study the seismic performance of the retrofitted specimens. The seismic performance of HP-HFRC retrofitted beam column joints have been measured in terms of load displacement behaviour, displacement ductility, energy dissipation, stiffness, strength degradation, and principal tensile stress. The obtained results of the controlled specimen and retrofitted beam column joints are analysed and discussed in the subsequent sections.

5.2 CYCLIC BEHAVIOUR OF CONTROLLED SPECIMEN

5.2.1 Cyclic Behaviour of Control Complete Damage (C-CD) Specimen

The control beam column joint specimen (C-CD) is tested under quasi-static reverse cyclic loading till failure; the response of the same is shown in Fig. 5.1. From the response curve, it

can be observed that the specimen C-CD exhibited a different peak load capacity during positive and negative displacement. The specimen resists the lateral loading up to 15 mm displacement in the compression zone, whereas, in tension, the specimen resists lateral loading till 25 mm displacement. After that, the load in positive and negative lateral displacement starts decreasing. The cycle peak load starts decreasing from the lateral displacement of 15 mm for the positive displacement and 25 mm for the negative displacement. A sudden drop in cycle peak load is observed at a positive displacement of 30 mm. The drop in peak load is indicating the degradation in the bond between concrete and reinforcement, yielding of the steel reinforcement and formation of severe cracks. The complete failure of the joint has occurred at 35 mm positive displacement, which can be attributed due to the higher rate of bond degradation on the compression face of the beam due to the unequal amount of reinforcement (2 – 8 mm diameter on compression phase and 3 – 10 mm diameter on tension face).

The onset of hairline cracks has been observed in the compression face and tension face of the beam column joint at 5 mm and 10 mm lateral displacement, respectively. The cracks began early in the compression face (5mm lateral displacement) as compare to the tension face of the beam. During testing, it has been observed that the cracks initiate from the compression face of the beam and start to propagate rapidly towards the tension face of the beam and joint areas as the increment in cyclic displacement applied. During testing, it has also been observed that the cracks always propagate when the incremental displacement applied. The second cycle of n^{th} lateral displacement has been responsible for crushing the concrete at the crack opening region and moderate peak load degradation in compression as well as in the tension face of the beam. The wide cracks at the joint interface and principal tensile diagonal cracks in the joint panel occurred when the lateral displacement increased from 20 mm to 25 mm. As the lateral displacement increased from 25 mm to 35 mm the following observation has been made;

- Flexure cracks occur in the beam portion,
- Principal tensile diagonal tension cracks extended in joint region and width of the cracks in compression face and interface of the joint is significantly increased,
- From the joint interface, the number of cracks propagates towards the joint area and tension face of the beam.

The crack pattern of control specimen shows the complete degradation of bond; consequently, a chunk of concrete felled out from the compression face and reinforcement

buckled at ultimate lateral drift, i.e., 35 mm in both the controlled specimen (see Fig. 5.2&5.3). Normally, the beam under gravity loading is designed with the methodology that the cross-sectionn above the neutral axis is offering the resistance to compressive force, whereas steel reinforcement below the neutral axis resists the tensile stresses; the tensile strength of the concrete below the neutral axis is generally neglected. However, during the reverse cyclic loading, both top and bottom face of the beam is subjected to compression as well as tension. The compression face is designed to resist the compressive stresses but due to the cyclic lateral force, the same face of the beam is subjected to tension also. Nevertheless, the C-CD specimen compression face resists the force till 15 mm lateral displacement, but afterward, the degradation in peak load is observed and sudden drop has been observed at 30 mm lateral drift. The complete yielding of 8 mm diameter reinforcement resulted in premature failure in the whole beam column joint, and the spalling of concrete is started. The test is stopped at the stage of complete failure of the beam column joint. The cause of complete failure is the failure of the compression face of beam column joint at ultimate drift however, sufficient residual stresses is left on the tension side. The structure subjected to this type of failure does not mobilize the complete efficiency of the structure during the earthquake and lead to local failures.

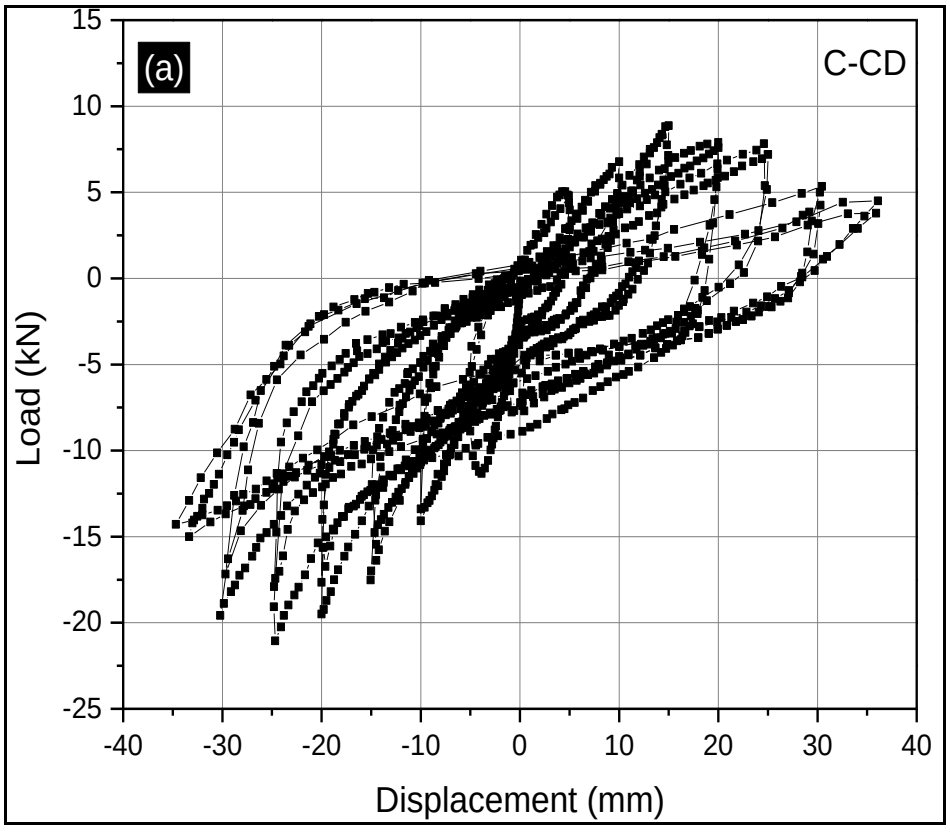

Fig. 5.1 - Load versus Displacement History of Control Complete Damage (C-CD) Specimen

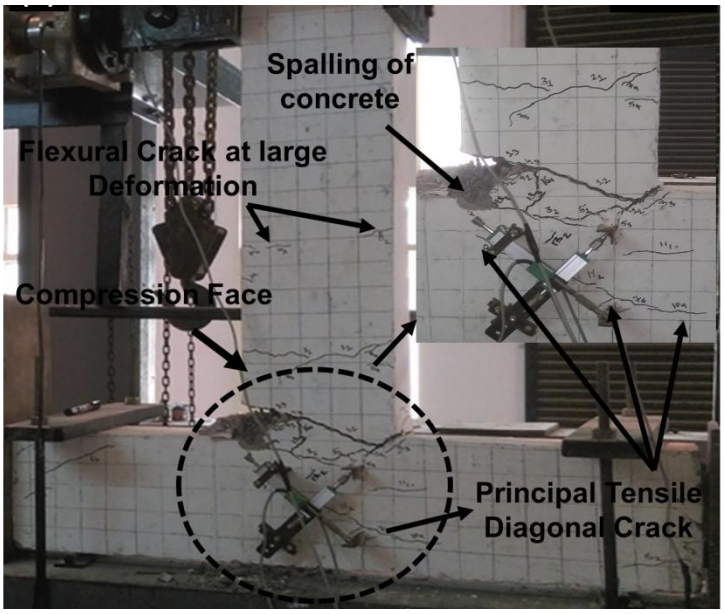

Fig. 5.2 - Crack Pattern of Control Complete Damage (C-CD) Specimen I

Fig. 5.3 - Crack Pattern of Control Complete Damage (C-CD) Specimen II

Using Park and Ang method, four damage indices, i.e., complete (C-CD), severe (C-SED), moderate (C-MD), and slight damage (C-SD) are calculated from the load displacement hysteresis of control specimen.

Further, each specimen is damaged under quasi static reverse cyclic loading to achieve the different damage states corresponding to their respective damage indices.

5.2.2 Cyclic Behaviour of Control Severe Damage (C-SED) Specimen

The severe damage state is obtained by applying the fraction of complete load history. The lateral displacement up to 25 mm is applied to obtain the severe damage state. The load displacement hysteresis of severe damage specimen is shown in Fig. 5.4. It has been observed that the initially hairline cracks occurred at 5 and 10 mm positive and negative lateral displacement, respectively. At higher lateral displacement, the width of the cracks increased, and crack propagate at joint interface, joint area, and later on the flexural cracks on the beam portion are also observed.

The crack patterns of C-SED shows the crack at three locations viz. (a) the face of the joint; (b) joint area; (c) column areas (see Fig. 5.5 and 5.6). The extent of the crack is lesser in C-SED than C-CD specimens as the damage level shifts from complete to severe.

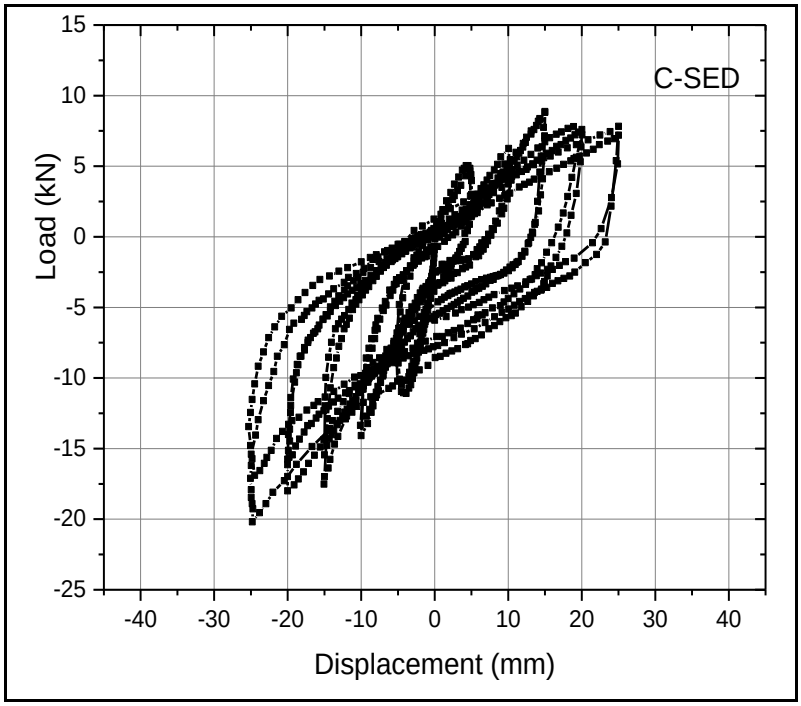

Fig. 5.4 - Load versus Displacement History of Control Severe Damage (C-SED) Specimen

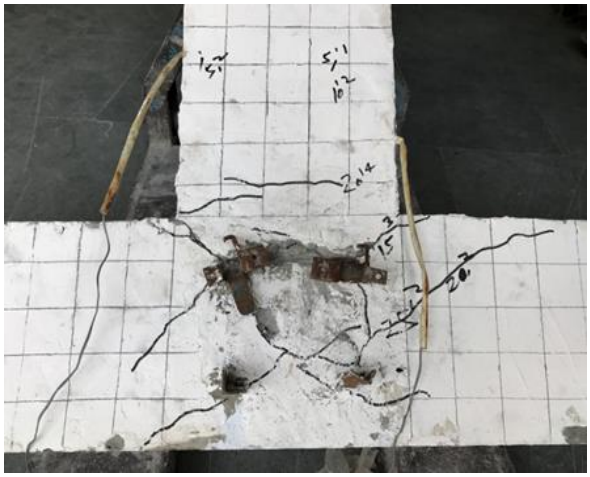

Fig. 5.5 - Crack Pattern of Control Severe Damage (C-SED) Specimen I

Fig. 5.6 - Crack Pattern of Control Severe Damage (C-SED) Specimen II

5.2.3 Cyclic Behaviour of Control Moderate Damage (C-MD) Specimen

The moderately damaged specimen C-MD is subjected to lateral displacement of 15 mm; load hysteresis response has been plotted and shown in Fig. 5.7. It has been observed that the resistance of load has not been decreased till 15 mm displacement as the control specimen has a sufficient load resistance capacity at 15 mm and 25 mm positive and negative displacement, respectively, as shown in Fig. 5.1. At the moderate damage state, the specimen has a higher amount of residual stresses as compare to C-CD and C-SED specimens. The

cracks appear on the beam column joint interface from the compression face of the beam, and as the lateral displacement increased, the crack propagates towards the tension face of the beam. It has also been observed that at the 15 mm lateral cyclic displacement, the crack propagate in the joint area in all the direction and width of crack increased at the joint interface (Fig. 5.8 & 5.9).

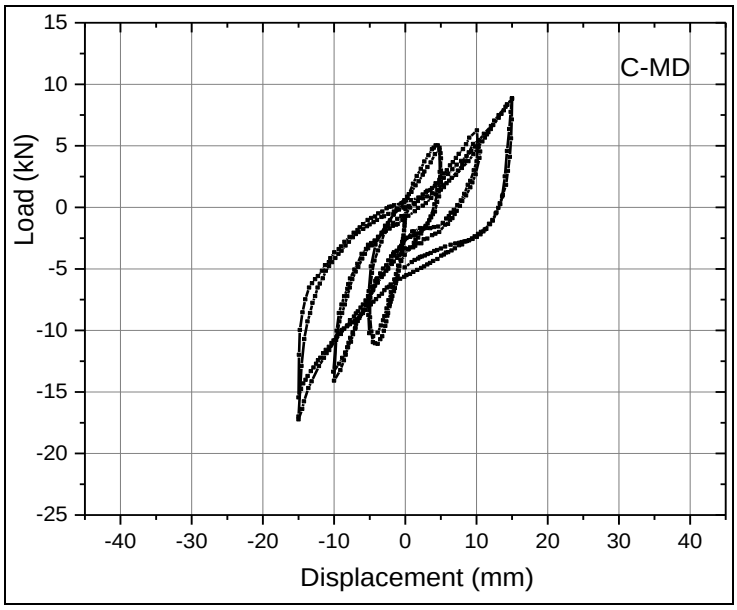

Fig. 5.7 - Load versus Displacement History of Control Moderate Damage (C-MD) Specimen

Fig. 5.8 - Crack Pattern of Control Moderate Damage (C-MD) Specimen I

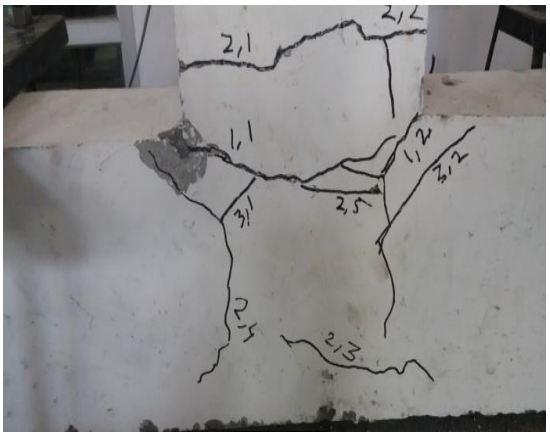

Fig. 5.9 - Crack Pattern of Control Moderate Damage (C-MD) Specimen II

5.2.4 Cyclic Behaviour of Control Slight Damage (C-SED) Specimen

The slight damage state has been achieved by applying the lateral displacement of 10 mm. The load displacement hysteresis of C-SD specimen is shown in Fig. 5.10. The crack appears

only at the interface of joint in C-SD, as this specimen is only subjected to 10 mm lateral displacement. The single crack at the interface and in the beam portion is observed, as shown in Fig. 5.11 & 5.12. It can be concluded from the crack pattern that the extent of cracks in the slightly damaged specimen (C-SD) is least among all the damage state. It is also worth mentioning here that the extent of cracks is the reflection of the magnitude of residual stresses left in an initially damaged beam column joint. The amount of residual stresses significantly depends upon their respective initial damage level and also affects the seismic performance of initially damaged specimens after retrofitting. The all damaged specimens are retrofitted using HP-HFRC, the adopted procedure for retrofitting is explained in Chapter 4, and water cured for 28 days. The matured retrofitted specimens are tested under quasi static reverse cyclic loading to study the effect of initial damage level on the performance of the retrofitted beam column joint.

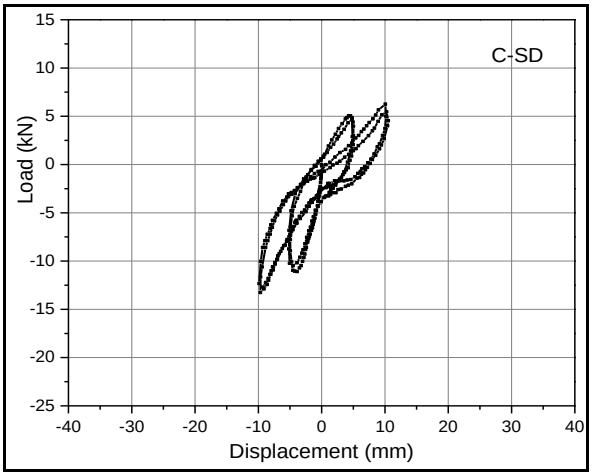

Fig. 5.10 - Load versus Displacement History of Control Slight Damage (C-SD) Specimen

Fig. 5.11 - Crack Pattern of Control Slight Damage (C-SD) Specimen I

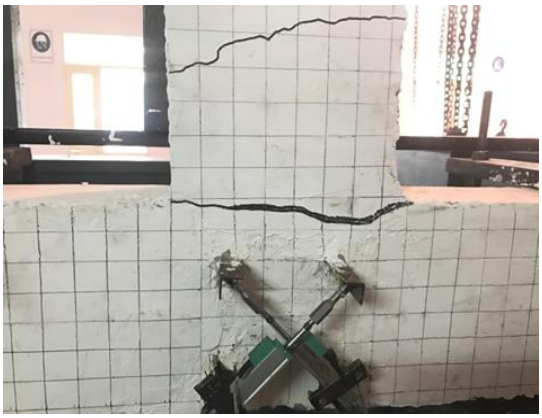

Fig. 5.12 - Crack Pattern of Control Slight Damage (C-SD) Specimen II

5.3 CYCLIC BEHAVIOUR OF HP-HFRC RETROFITTED BEAM COLUMN JOINT SPECIMENS

5.3.1 Cyclic Behaviour of Retrofitted Initially Complete Damaged (R-CD) Specimen

The load displacement hysteresis of retrofitted initially complete damaged (R-CD) specimen is the plot and shown in Fig. 5.13. From the load displacement plots, it can be observed that the HP-HFRC retrofitting material contributes to the improvement of the lateral load-carrying capacity of initially complete damage specimen. Also, the lateral load carrying capacity has been continuously increased up to 10 mm and 25 mm lateral positive and negative lateral displacement, respectively. The R-CD specimen achieved the same peak load as C-CD in positive displacement (compression face), whereas, in the negative displacement (tension face) the peak load is higher in comparison to C-CD. This behaviour is attributed to the higher mechanical properties offered by the HP-HFRC retrofitted material; consequently higher initial strength has been obtained. The sudden drop in cycle peak load is observed after 10 mm positive displacement; however, the performance in the tensile zone is excellent at this lateral displacement level.

This happened due to the pre-yielded compression face reinforcement and damage of core concrete during initial damage. The initially complete damage specimen has minimal residual stress and crack onset on the retrofitted layer of HP-HFRC at a 5mm displacement level. The opening of micro cracks developed in HP-HFRC due to the failure/ slippage of micro fibers. From this point, onwards, macro fibers present in the HP-HFRC start offering resistance against the crack opening. However, the severe crack at 10 mm displacement shows the negligible contribution of pre-yield compression face reinforcement, and severe cracks appears.

The HP-HFRC improves the hysteresis behaviour of R-CD specimens and contributes to sustaining the load in positive displacement even after the complete yielding of reinforcement. Nevertheless, the ultimate failure of the R-CD specimen is governed by the positive displacement as in C-CD specimen (see Fig. 5.13). At a positive displacement of 25 mm, the macro fibers slipped from the matrix, and confinement provided by HP-HFRC to the beam-column joint core becomes ineffective and resulting in the failure of the joint.

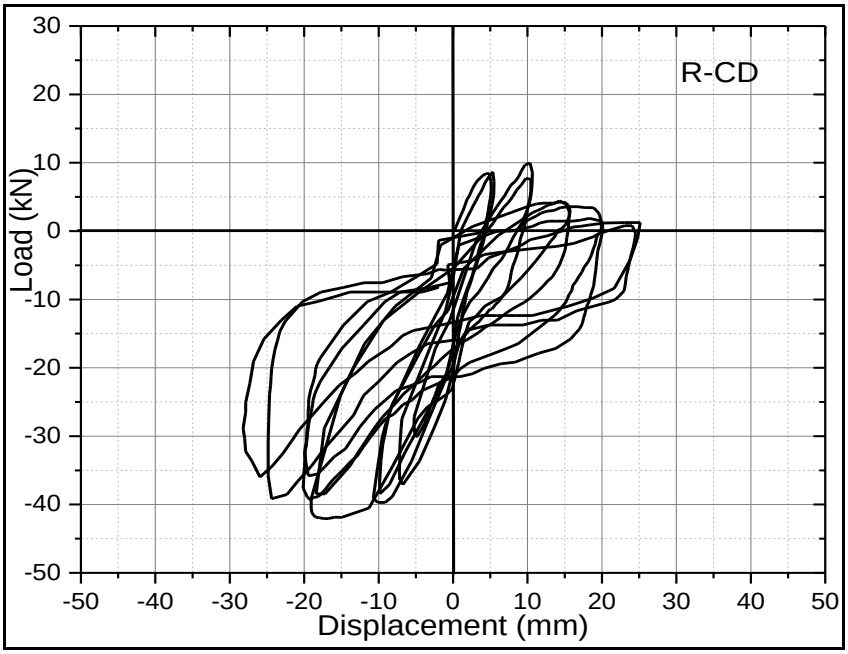

Fig. 5.13 - Load versus Displacement History of Retrofitted Complete Damage (R-CD) Specimen

5.3.2 Cyclic Behaviour of Retrofitted Initially Severe Damaged (R-SED) Specimen

The load displacement hysteresis of retrofitted initially severely damaged (R-SED) specimen is the plot and shown in Fig. 5.14. From the load displacement plots, it can be observed that the HP-HFRC retrofitting material significantly improves the lateral load carrying capacity of the initially severely damaged specimen. The specimen resists the lateral load effectively up to 15 mm lateral displacement; after that, the degradation in peak load has been started. It can be concluded that the presence of hybrid fiber in HP-HFRC resists the opening of crack at the initial lateral displacement consequently, the retrofitted specimen initially regains the strength and stiffness. The crack has been observed at the interface of the joint and extends towards the tension face of the joint as the lateral displacement increased. A sudden drop in cycle peak load is observed after a positive displacement of 25 mm in the R-SED specimen however the same drop has been observed at 10 mm in the R-CD specimen (see Fig. 5.13 & 5.14). The level of initial damage is severe in R-SED specimen; as a result, the reinforcement in the compression face of the beam is partially yielded. Also, the level of damage in tension reinforcement is somewhat lower than the compression face reinforcement. Therefore, at the higher lateral displacement when the severe crack/higher stresses in HP-HFRC layer approach the core concrete during quasi static reverse cyclic loading, the core concrete in the presence of partially yielded reinforcement could not able to sustain those higher stresses and sudden drop in load carrying capacity has been observed. At this stage, the crack penetrates from HP-HFRC retrofitted layer to core concrete. As a result, the higher stresses are transfer

from HP-HFRC layer to core control concrete, and severe bond degradation and reinforcement yielding start. The strength of core concrete is lesser than the HP-HFRC layer, and the absence of confinement (severe cracks in HP-HFRC layer) led to a higher rate of propagation of cracks. The ultimate failure in the specimen has been observed at 35 mm lateral displacement. The specimen ultimate failure is completely governed by the positive lateral displacement; the lower rate of degradation in peak load has been observed in negative lateral displacement (see Fig. 5.14).

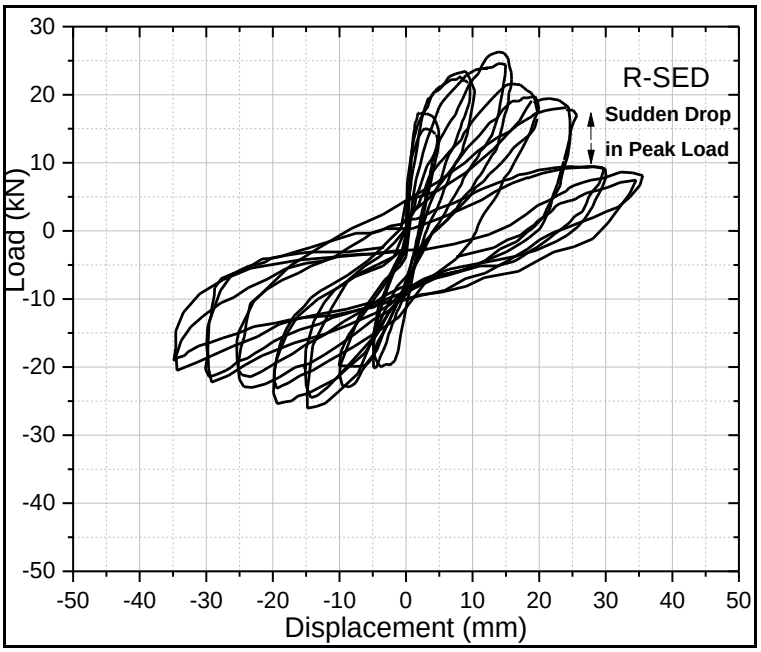

Fig. 5.14 - Load versus Displacement History of Retrofitted Severe Damage (R-SED) Specimen

5.3.3 Cyclic Behaviour of Retrofitted Initially Moderate Damaged (R-MD) Specimen

The hysteresis behaviour of retrofitted initially moderate damaged (R-MD) specimen is plotted and shown in Fig. 5.15. The significant improvement in positive and negative lateral load carrying capacity is observed. The maximum peak load is 26.62 kN at 10 mm lateral displacement in positive displacement whereas, the maximum peak load is 26.12 kN at 15 mm negative displacement. Also, a sudden drop in cycle peak load in positive displacement is not observed; a sudden drop in cyclic positive peak load is the governing mode of failure in specimen R-CD and R-SED. The retrofitting using HP-HFRC at an initial moderate level of damage in beam column joint eliminates the possibility of premature failure in positive displacement, as shown in Fig. 5.15. This is attributed to the efficient bond between the initially yielded compression face reinforcement with the HP-HFRC. The sufficient residual stresses are left in the compression face steel and core control concrete of beam column joint

during initial damage; consequently, the bond between the reinforcement and newly laid retrofitted layer of HP-HFRC significantly controls the governing mode of failure.

An appreciable improvement in ultimate lateral displacement capacity and post peak behaviour is observed in the retrofitted specimens. It has been observed that the rate of post peak strength degradation is lower in specimen R-MD as compare to R-CD and R-SED specimen. These improvements could be due to the addition of hybrid fiber in retrofitting material, which contributes to delaying the opening of crack at micro level, sustain the crack width at macro level during incremental lateral displacement and, improve energy dissipation capacity.

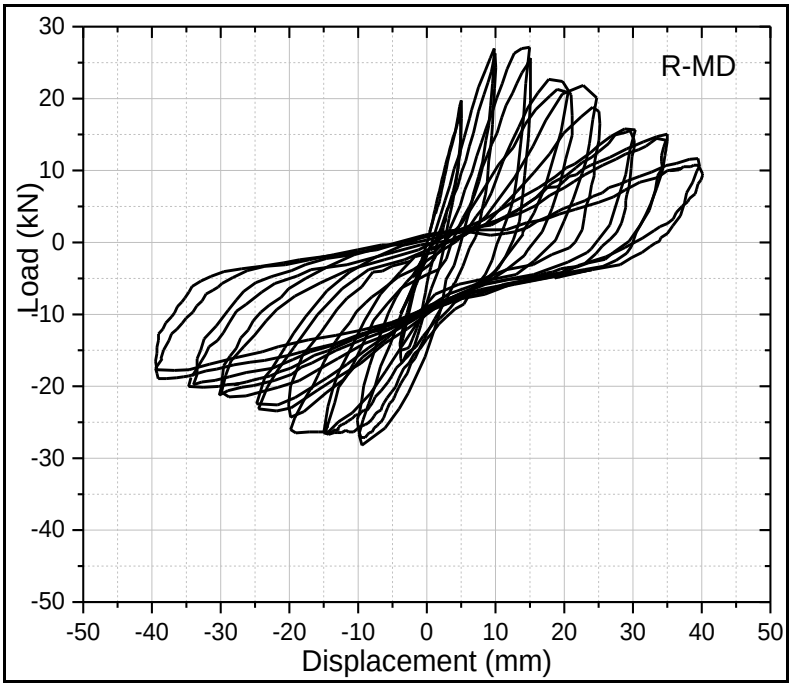

Fig. 5.15 - Load versus Displacement History of Retrofitted Moderate Damage (R-MD) Specimen

5.3.4 Cyclic Behaviour of Retrofitted Initially Slight Damaged (R-SD) Specimen

The initially slightly damaged and then retrofitted specimen (R-SD) is tested under cyclic loading, and load displacement graph has been plotted. The improvement in peak load and lateral displacement are very similar to the R-MD specimen. The peak loads in positive and negative displacement are 26.2 kN and 30.1 kN, respectively. The lateral displacement capacity of the R-SD specimen is 40 mm, which is similar to the R-MD specimen. It has been observed from Fig. 5.16 that the sudden drop in load during positive displacement as observed in R-CD and R-SED specimen has not been found in the R-SD specimen. The reason could be the efficient bond between the newly laid HP-HFRC layer and reinforcement.

The residual stresses are higher in the reinforcement also, the core concrete is undamaged during initial damage consequently, the retrofitted element performs like a composite element. As the crack approach to the core concrete, the core concrete enables to resist the stresses transfer from the HP-HFRC and does not exhibit a sudden drop in peak load during positive displacement.

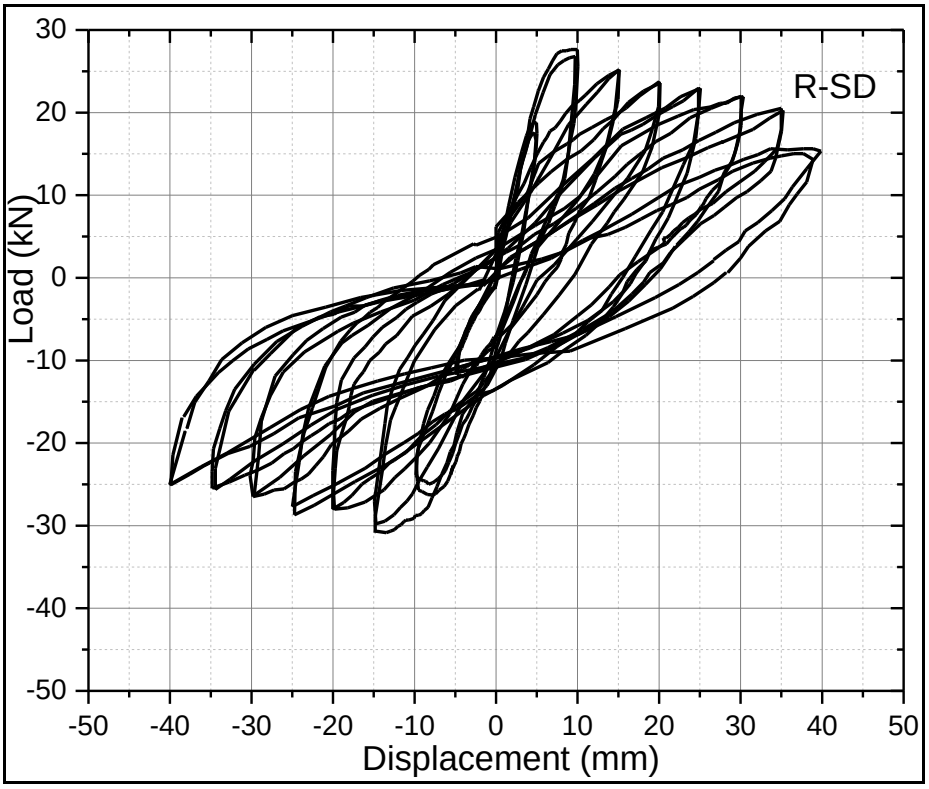

Fig. 5.16 - Load versus Displacement History of Retrofitted Slight Damage (R-SD) Specimen

It can be concluded from the observed performance of R-CD, R-SED, R-MD, and R-SD that the ultra high strength of retrofitted material significantly improves the pre-peak and post peak performance in term of peak load capacity and ultimate lateral drift capacity. The presence of hybrid fiber effectively participates in delaying the crack opening and resisting the width of crack at the higher lateral displacement.

The dense microstructure of HP-HFRC increases the bond between the hybrid fiber and matrix which imparts the ductility in the behaviour of retrofitted specimens under cyclic loading. It can also be concluded that the lower damage indices of BCJ empowering the efficiency of hybrid fiber, therefore, delaying or even eliminate the sudden drop in cycle peak load, which could be beneficial for the performance of the structure during an earthquake.

The significant participation of HP-HFRC is the contribution in enhancing the performance of the compression zone of the beam at the joint interface. The compression zone of the beam

is generally not designed to resist the tensile forces. However, this face also subjected to tensile forces during cyclic loading. Therefore a premature failure is observed at the compression face of C-CD specimen which led to failing the whole beam column joint. However, the retrofitted material i.e., HP-HFRC exhibited excellent tensile resistance property due to the strong bond between hybrid fiber and matrix. Therefore, the application of HP-HFRC in the compression zone of the beam contributes to resisting the crack opening and delaying the growth of crack width during lateral displacement. As a result, the premature compression zone failure of the beam is avoided, and overall performance of HP-HFRC retrofitted specimen is significantly improved

5.4 EFFECT OF INITIAL DAMAGE LEVEL ON THE DUCTILITY OF RETROFITTED BCJ SPECIMEN

"Ductility can be described as the ability of the structure or its components, or of the materials used to offer resistance in the inelastic domain of response. It includes the ability to sustain large deformations, and a capacity to absorb energy by a hysteretic behaviour" (Paulay and Priestley 1992; Le-Trung et al, 2010. The large post elastic deformation/rotation enables the structural elements to utilize the inelastic strength, as a result, the large post elastic plateau is obtained. The large post elastic plateau with the lower strength degradation exhibits the higher ductility.

In the present work, the displacement ductility is calculated to evaluate the performance of the retrofitted specimen. The displacement ductility is defined as the ratio of ultimate displacement to the yield displacement, as shown in equation 5.1. The specimen is considered a complete failure at the 80% drop of peak strength; the displacement corresponding to complete failure on the backbone curve is considered as an ultimate displacement. A horizontal line is drawn parallel to the x-axis from the point of ultimate displacement and meets the y-axis. Further, a point is located on the backbone curve, which represents the 50% drop in the peak load. The yield displacement is found by drawing a tangent from the origin and pass through the 50% drop of the peak load of the backbone curve to the point where the tangent meets to the horizontal line representing the 80% drop of peak strength parallel to the x-axis. The procedure to calculate the ductility is shown in Fig. 5.17.

The comparison of ductility between control and all retrofitted specimen is calculated and compares with the control specimen in the below sections.

$$\text{Displacement ductility } (\mu) = \frac{\Delta_{u1+\Delta u2}}{\Delta_{y1+\Delta y2}} \quad (5.1)$$

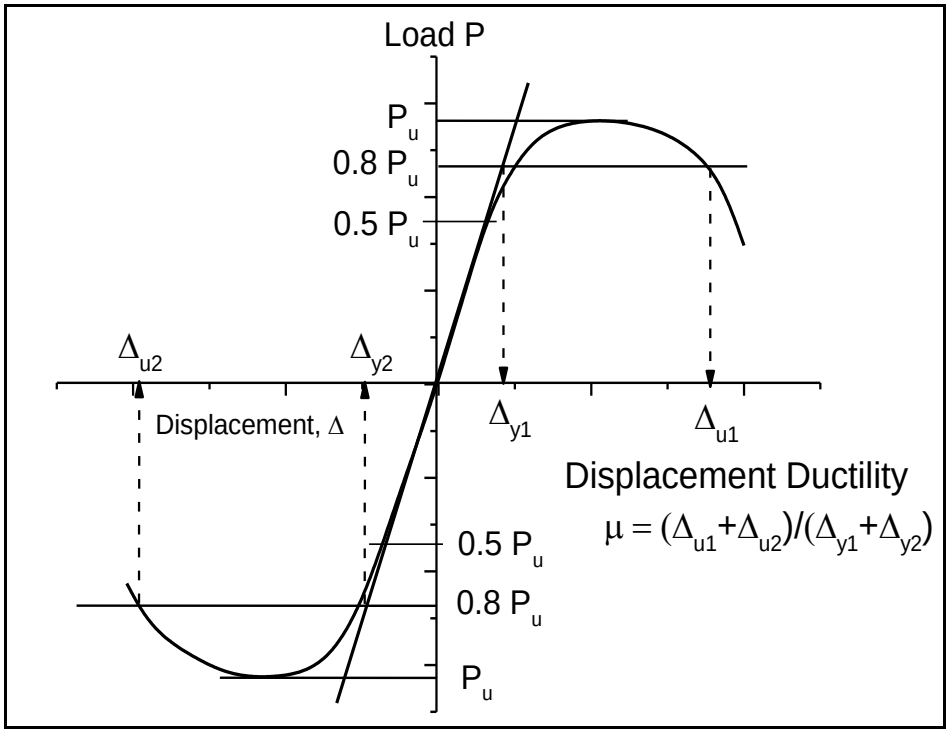

Fig. 5.17 - Procedure Adopted to Calculate the Displacement Ductility *(Chidambaram and Agarwal, 2015)*

5.4.1 Comparison between Control Specimen and Retrofitted Specimens

The procedure, as explained in Fig 5.17, is used to calculate the displacement ductility of control (C-CD) and the retrofitted complete damage specimen (R-CD). The load displacement backbone hysteresis curve of C-CD and R-CD is prepared and shown in Fig 5.18. The analysis of R-CD specimen from the load displacement backbone hysteresis curve can be done in two parts; 1) pre peak performance; 2) post peak performance. It has been observed that the stiffness is significantly improved in pre peak zone however in post peak region, due to the occurrence of micro and macro cracks the peak starts degrading. The yield positive and negative displacement of C-CD and R-CD specimen is calculated. The ductility of C-CD and R-CD specimens is 3.4 and 4.09, respectively.

It has been observed that the ductility improved by 20.30% in R-CD specimen, which reflects the capability of HP-HFRC to impart the inelastic rotational capacity even if the member is initially completely damage.

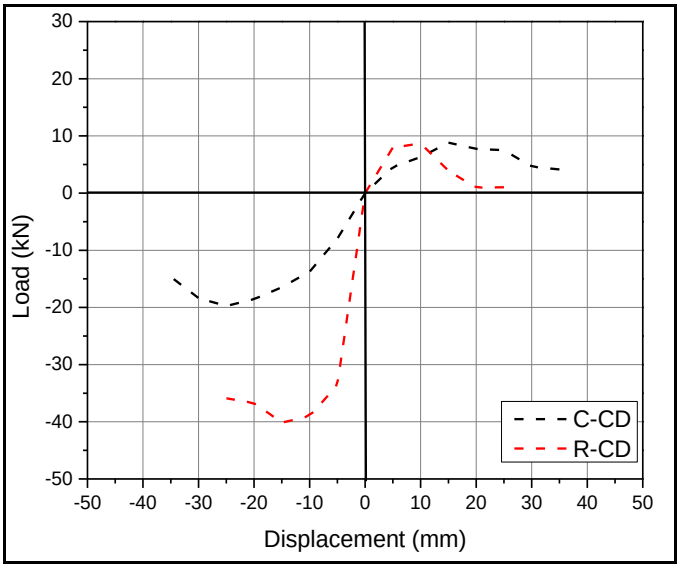

Fig. 5.18 - Backbone Hysteresis Curve of C-CD and R-CD Specimen

The backbone hysteresis curve of the R-SED specimen is prepared and compare with the C-CD response; the response of the same is shown in Fig. 5.19. The initial stiffness of HP-HFRC offers a significant improvement in pre-elastic and post-elastic region. It is noteworthy to mention here that the specimen R-SED achieves the original lateral displacement capacity i.e., 35mm. This behaviour is attributed to the presence of hybrid fiber in the HP-HFRC and the remaining residual stresses after obtaining the initial damage level. It has been observed that the presence of residual stress in reinforced concrete beam column joint offers the resistance

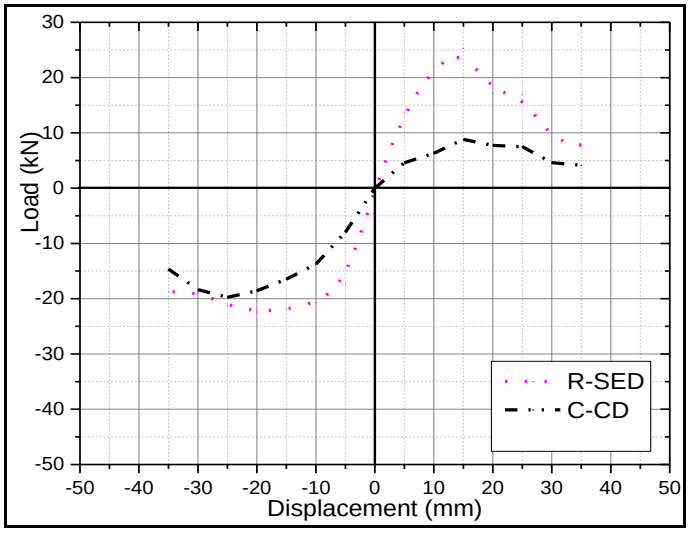

Fig. 5.19 - Backbone Hysteresis Curve of C-CD and R-SED Specimen

against lateral loading once the HP-HFRC fails, which helps in lengthen the plateau of the backbone hysteresis curve. The ductility of the R-SED specimen is 4.12, which is 21.17% enhancement over the C-CD specimen.

The response of R-MD is somewhat similar to the R-SED specimen but significantly better than the R-CD specimen. Also, the major improvement in the post elastic region has been observed, as shown in Fig. 5.20. It can be observed that the slope of post elastic region is decreased as the initial damage level shift from complete to moderate. The ductility of C-MD is 4.77, which is 40.29% higher than the C-CD specimen. The reason for the improvement in ductility is the lesser post elastic strength degradation and higher lateral displacement capacity.

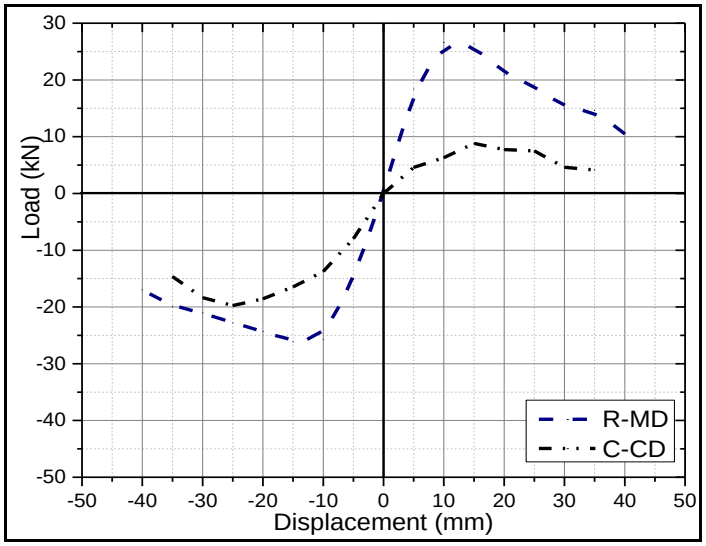

Fig. 5.20 - Backbone Hysteresis Curve of C-CD and R-MD Specimen

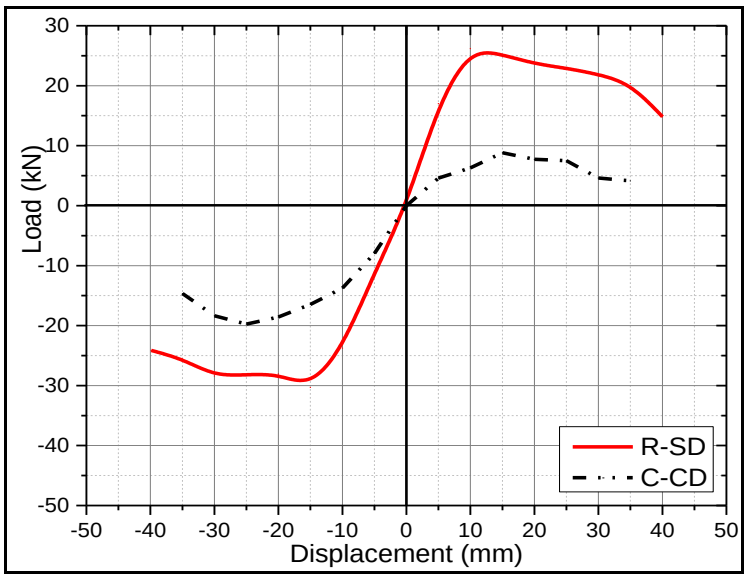

Fig. 5.21 - Backbone Hysteresis Curve of C-CD and R-MD Specimen

The load displacement backbone hysteresis curve is of R-SD is shown in Fig. 5.21. The pre-elastic and post elastic performance of the R-SD shows the higher initial stiffness and lower strength degradation, respectively. As the damage level shift from complete to slight, the bond between retrofitted matrix and reinforcement effectively sustain the higher lateral stress; also the contribution of reinforcement and core concrete helps to lengthen the post elastic plateau. The ductility of the R-SD specimen is 4.94, which is 45.29% improvement over the C-CD specimen.

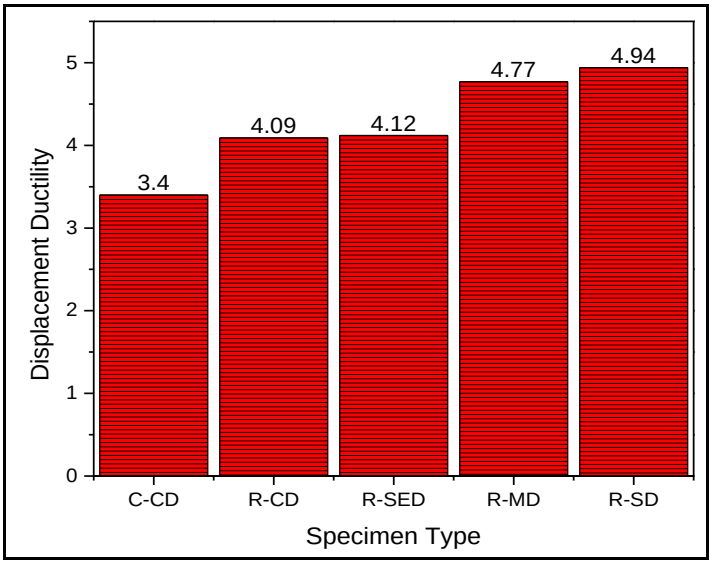

Fig. 5.22 –Ductility of Control and Retrofitted Specimens

Table 5.1 - Calculation of Displacement Ductility of Control and Retrofitted Specimen

Specimen name	Maximum				Ultimate				Displacement (D)		
	Positive		Negative		Positive		Negative		Yield D	Ultimate D	Ductility UD*/YD**
	Pm max (kN)	Dm (mm)	Pm max (kN)	Dm (mm)	Pu max (kN)	Du (mm)	Pu max (kN)	Du (mm)			
C-CD	8.83	15	19.74	25	4.14	35	14.60	35	17.4	59.2	3.40
R-CD	8.68	10	40.16	15	1.01	25	35.89	25	9.03	37	4.09
R-SED	25.26	15	22.4	20	7.78	35	18.72	35	13	53.62	4.12
R-MD	26.62	10	26.12	15	10.51	40	16.98	40	10.83	51.73	4.77
R-SD	26.2	10	30.31	15	14.82	40	24.13	40	15.27	75.41	4.94

*UD- Ultimate Displacement; **YD – Yield Displacement

It can be concluded from the analysis of backbone hysteresis curve of C-CD, R-CD, R-SED, R-MD and, R-SD is that the rate of degradation of the curve in post peak region starts decreasing as the initial damage level (complete, severe, moderate, and slight damage) of retrofitted BCJ shifts from complete to slight. The improvement in the plateau of post peak region reflects the enhancement in the ductility of retrofitted specimens as compare to C-CD specimen. The ductility of R-CD, R-SED, R-MD, and R-SD specimen improved by 20%, 21.17%, 40.29%, and 45.29%, respectively, in comparison to C-CD specimen as presented in Fig 5.22 and Table 5.1. The maximum and minimum improvement of ductility is observed in the R-SD and R-CD specimens, respectively. The decrease in the slope of the post peak region of R-SD, R-MD, and R-SED revealed the improvement in the performance of specimen imparts by HP-HFRC. The presence of hybrid fibers delays the growth of opening of cracks and improve the post peak performance.

5.5 STIFFNESS DEGRADATION

The peak to peak stiffness of control and retrofitted initially damage specimen tested under quasi-static reverse cyclic loading is calculated for each drift ratio. The slope of the line joining the peak point reached on positive and negative directions in a loading cycle is defined as peak to peak stiffness *(Zohrevand and Mirmiran, 2012)*. The procedure for the calculation of stiffness is shown in Fig. 5.23.

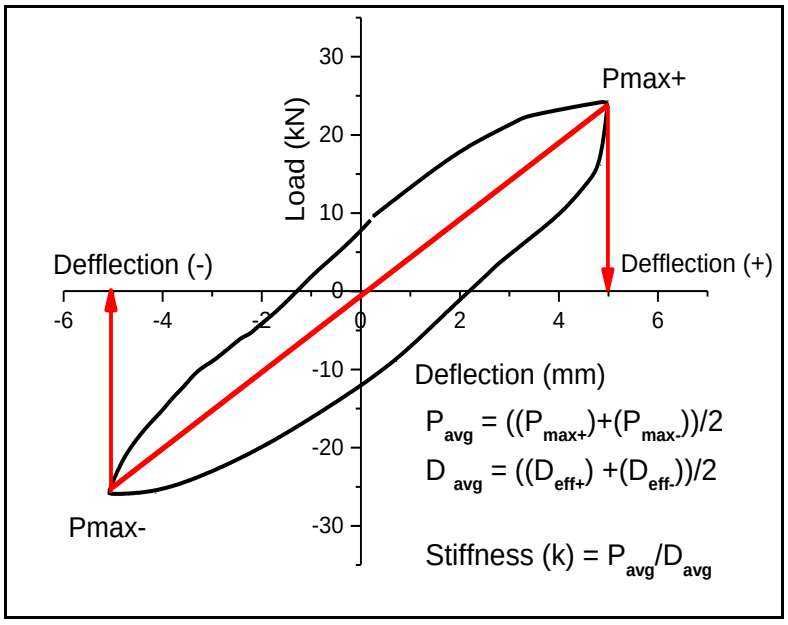

Fig. 5.23 - Procedure Adopted to Calculate the Stiffness

5.5.1 Comparison between Control Specimen and Retrofitted Specimens

The peak to peak stiffness of C-CD and R-CD specimen is calculated for each cycle and shown in Fig. 5.24. It can be observed that the initial stiffness of the R-CD specimen is significantly higher than the control specimen however the lateral displacement capacity is reduced by 28.57%. The rapid rate of stiffness degradation has been observed as the lateral displacement increased. The rapid rate of stiffness degradation has been observed up to 1.87% drift after that, the slower rate of degradation is observed till failure. The magnitude of stiffness at the failure of the R-CD specimen is 43.98% higher than the C-CD specimen. The initial higher stiffness helps the specimen to resist a moderate earthquake, whereas if the longer duration of seismic ground motion is the encounter with this type of retrofitted structure element, the rapid deterioration will be obtained along with the minimal residual stiffness at ultimate failure.

The peak to peak stiffness of the R-SED specimen is 2.90 times higher than C-CD. It has been observed from Fig. 5.24 that the rate of stiffness degradation is rapid up to 2.5% drift. Thereafter, the slope of stiffness degradation is decreased and, the lower rate of degradation is obtained. In addition, the stiffness is getting lower with the increase of drift capacity. The participation of mono fiber resists the growth of the opening of crack, and macro fiber effectively participates in bridging the large width crack with the increase of lateral drift. Therefore, the higher lateral load is required to attain the lateral deformation in R-SED as compare to R-CD and C-CD specimens. It is worth mentioned here that the R-SED specimen regains the original lateral drift capacity, and still, the residual stiffness at failure remains higher than the C-CD specimen.

It has been observed that the specimen R-MD exhibited the stiffness 3.15 times over the C-CD specimen. The pattern of stiffness degradation is somewhat similar to C-SED however, the magnitude differs at each drift ratio. From Figure 5.24, it has been observed that the rate of stiffness degradation is rapid up to 2.5% drift. Thereafter, the slope of stiffness degradation is decreased and, the lower rate of degradation is obtained. The retrofitting strategy significantly improves the ultimate displacement capacity of R-MD specimen. The 14.28% ultimate displacement capacity is increased over the C-CD specimen, which is the potential evidence of improvement in the performance of R-MD. Also, the role of residual stress plays a significant role in sustaining the stiffness once the HP-HFRC retrofitted layer is failed. It has also been observed that the stiffness at the collapse of the R-MD specimen is slightly higher than the C-CD stiffness value obtained at the collapse state.

The performance of the R-SD specimen is very much similar to the R-MD specimen, as shown in Fig. 5.24. The improvement in stiffness is 3.15 times over the C-CD specimen.

However, the rapid reduction in stiffness degradation in the R-SD specimen is observed up to 1.87 % drift ratio, and afterward, the rate of degradation is decreased. Like in the R-MD specimen, the ultimate displacement capacity of the R-SD specimen is increased up to 14.28% over the C-CD specimen.

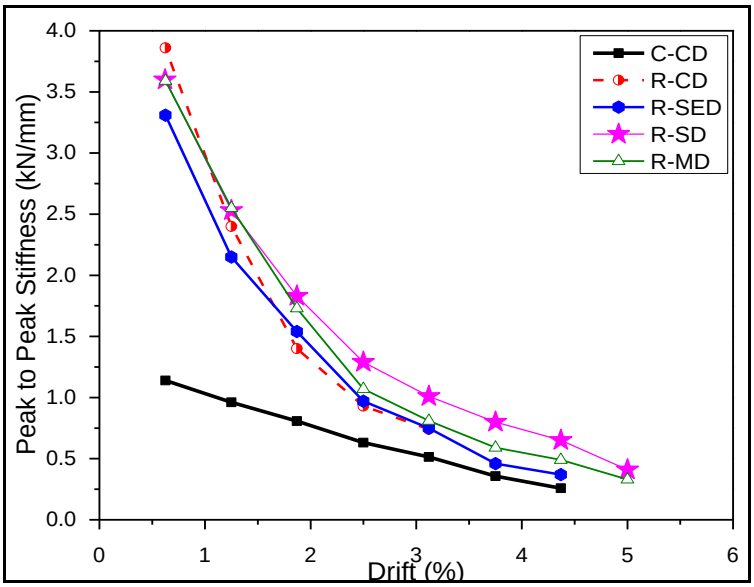

Fig. 5.24 - Stiffness versus Drift Ratio of Control and Retrofitted Specimen

It can be concluded that the peak to peak stiffness of all the specimens retrofitted using HP-HFRC is 2.90 to 3.38 times higher than that of the control specimen (C-CD). Further, it is also observed that the drift ratio at which initially slightly and moderately damaged specimen loses its stiffness increases after retrofitting. The specimens which are initially fully damaged or severely damaged and then retrofitted do not show any improvement in a higher drift ratio. However, the R-SD and R-MD specimens show the superior post-yield lateral stiffness due to confinement provided by the HP-HFRC. The peak to peak stiffness of control and the retrofitted specimen is shown in Table 5.2.

Table 5.2 - Peak to Peak Stiffness of Control and Retrofitted Specimen

Drift (%)	Peak to peak stiffness (C-CD) (kN/mm)	Drift (%)	Peak to peak stiffness (R-CD) (kN/mm)	Drift (%)	Peak to peak stiffness (R-SED) (kN/mm)	Drift (%)	Peak to peak stiffness (kN/mm)(R-MD)	Drift (%)	Peak to peak stiffness (R-SD) (kN/mm)
0.625	1.14	0.625	3.86	0.625	3.31	0.62133	3.59	0.625	3.6
1.25	0.961	1.25	2.4	1.25	2.15	1.25	2.55	1.25	2.53
1.87	0.808	1.87	1.4	1.87	1.54	1.87	1.73	1.87	1.83

2.5	0.631	2.5	0.93	2.5	0.97	2.5	1.07	2.5	1.29
3.12	0.514	3.12	0.74	3.12	0.75	3.12	0.81	3.12	1.01
3.75	0.357	--	--	3.75	0.46	3.75	0.8	3.75	0.59
4.37	0.258	--	--	4.37	0.37	4.37	0.65	4.37	0.49
--	--	--	--	--	--	5	0.41	5	0.33

5.6 STRENGTH DEGRADATION

The evaluation of performance in terms of strength degradation from the complete load displacement hysteresis is very much difficult and laborious; therefore, extraction of data from the complete load hysteresis behaviour to calculate strength degradation helps to analyze the strength behaviour of beam column joint specimen. In the present study, the change in peak load in consecutive cycles of the same directional drift is used to calculate the strength degradation *(Sasmal et al, 2013)*. The comparison of all the retrofitted specimen with a control specimen has been done in subsequent sections;

5.6.1 Comparison between Control Specimen and Retrofitted Specimens

The strength degradation of C-CD and R-CD specimen is calculated from the complete load displacement hysteresis response and shown in Fig. 5.25. The strength degradation of the specimen is measured for the negative and positive displacement both. Due to the different area of reinforcement placed in the tension and compression face of the beam, the strength degradation of both the faces is significantly different. It has been observed that the strength degradation (SD) of the C-CD specimen is started from 1.87% drift, whereas in tension zone, the SD has been started from 3.12%.

It has been seen that due to the dissimilar amount of reinforcement on both faces of the beam the strength degradation is started early from the lesser amount of reinforcement contained face i.e., compression face. Afterward, the rate of degradation and maximum strength degradation in both the face of beam column joint is different. The maximum strength degradation of 53.11 % and 25.83% has been obtained in the compression and tension face of the C-CD specimen, respectively.

The specimen R-CD exhibited the rapid rate of strength degradation during positive displacement as compare to C-CD. The strength reduction during positive and negative displacement has been onset at 1.25% and 1.87% positive and negative displacement, respectively. Under maximum positive and negative displacement, 88.36% and 10.62% reduction in strength is observed at the ultimate drift ratio, i.e., 3.12%, as shown in Fig. 5.25.

The higher percentage of strength reduction during positive displacement indicates the premature failure of the specimen.

The Specimen R-SED shows the improved performance as compared to C-CD and R-SED specimen, as shown in Fig. 5.25. The reduction in strength has been onset at 1.87% and 2.5% positive and negative displacement, respectively. The larger amount of strength reduction i.e. 32.02% during positive displacement is observed in the first cycle of R-SED specimen, which is 2.5 times higher than the C-CD specimen. However, under negative displacement, only 5.49% reduction in strength is observed in the first cycle. At ultimate drift, total of 69.2% and 16.42% strength reduction during negative and positive displacement is observed respectively in R-SED specimen, as shown in Table 5.3. The R-SED specimen initially severely damaged, irrespective of that, after retrofitting, the specimen sustains the original drift capacity.

The comparison between R-CD and R-SED specimen revealed at similar drift, the onset of strength reduction has been started in both the specimen, however, the reduction of strength is higher in the R-CD specimen.

The lower rate of strength degradation in the R-MD specimen is observed as compared to the C-CD specimen, as shown in Fig. 5.23. From Table 5.3, It can be observed that the 60.51% and 34.99% is the net reduction in strength is obtained at the ultimate drift ratio i.e., 5%. The lower rate of strength degradation along with higher drift capacity brings the slope of the strength degradation flatter than the C-CD specimen. Also, the performance of the R-MD specimen is better than R-CD and R-SED specimens.

The reduction in the slope of the strength degradation curve of the R-SD specimen revealed the improvement in seismic performance, as shown in Fig. 5.25. It can also be concluded that the maximum strength reduction in positive and negative displacement is 43.43% and 20.38%, respectively, which is 18.22% and 21.09% lower than the C-CD specimen, as shown in Table 5.3. Also, the lateral drift capacity increased by 28.57% as compared to the C-CD specimen. Therefore it can be concluded that the maximum improvement is observed as the damage level shifts from complete to slight. The presence of hybrid fiber plays a significant role in improving the strength degradation property; the delaying in the occurrence of hairline crack shift the drift ratio at which the degradation is the onset and the macro fiber helpful in bridging the crack at higher ultimate drift ratio. Therefore, the performance of the initially damaged specimen significantly improved after retrofitting.

The strength degradation of all the retrofitted specimens is calculated for both positive and negative drift, and it has been found that retrofitting using HP-HFRC improves the strength degradation at a larger drift ratio. The efficiency of the BCJ increases with a decrease in the

initial damage level in the specimen, as shown in Table 5.3. The R-SD specimen exhibited 44.43% and 20.23% strength degradation at 5% negative and positive drift, respectively, which is lowest amongst all the retrofitted specimens (see Fig. 5.25). To perform excellent under moderate earthquake, the RC framed structure should exhibit the lower rate of strength degradation, and damage to non-structural elements up to some extent is permitted. But the structural element capable enough to retain its elasticity; therefore no damage would occur *(Sasmal et al., 2013)*. The improvement in the lower rate of strength degradation improves the behaviour of BCJ during an earthquake.

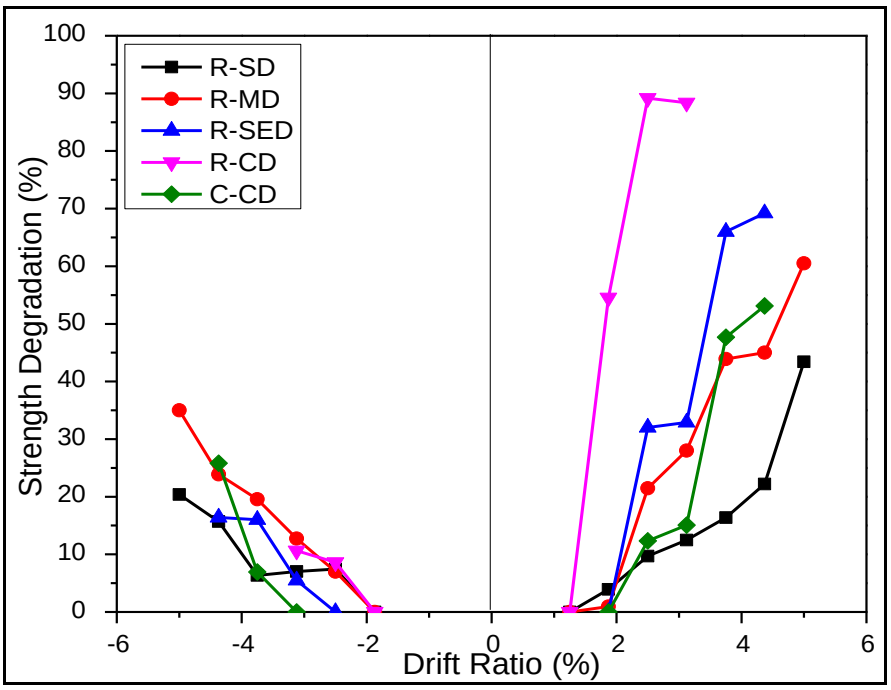

Fig. 5.25 - Strength Degradation versus Drift Ratio of Control and Retrofitted Specimen

Table 5.3 - Strength Degradation of Control and Retrofitted Specimen

Drift (%)	Strength Degradation (C-CD) (%)	Drift (%)	Strength Degradation (R-CD) (%)	Drift (%)	Strength Degradation (R-SED) (%)	Drift (%)	Strength Degradation (R-MD) (%)	Drift (%)	Strength Degradation (R-SD) (%)
4.37	53.11	3.12	88.36	4.37	69.2	5	60.51	5	43.43
3.75	47.67	2.5	89.17	3.75	66	4.37	45	4.37	22.22
3.12	15.06	1.87	54.53	3.12	32.89	3.75	43.91	3.75	16.37
2.5	12.34	1.25	0	2.5	32.02	3.12	28.02	3.12	12.48
1.87	0	0.625	--	1.87	0	2.5	21.48	2.5	9.69
1.25	--	--	--	1.25	--	1.87	0.93	1.87	3.93
0.625	--	-	--	0.625	--	1.25	0	1.25	0
		0.625							
--	--	-1.25	--	--	--	0.625	--	0.625	--
-0.625	--	-1.87	0	-0.625	--	--	--	--	--
-1.25	--	-2.5	8.61	-1.25	--	-0.625	--	-0.625	--

-1.87	--	-3.12	10.62	-1.87	--	-1.25	--	-1.25	--
-2.5	--	--	--	-2.5	0	-1.87	0	-1.87	0
-3.12	0	--	--	-3.12	5.49	-2.5	7	-2.5	7.45
-3.75	6.94	--	--	-3.75	16.02	-3.12	12.74	-3.12	7.02
-4.37	25.83	--	--	-4.37	16.42	-3.75	19.56	-3.75	6.33
--	--	--	--	--	--	-4.37	23.88	-4.37	15.7
--	--	--	--	--	--	-5	34.99	-5	20.38

5.7 ENERGY DISSIPATION

The energy dissipation of beam column joint is a significant parameter for the efficient structural response during an earthquake. The energy dissipation is calculated as the area enclosed in the load displacement hysteresis loop at different drift ratio *(Sasmal et al., 2013; Bindhu et al., 2009)*. The procedure adopted in this study to calculate the energy dissipation is shown in Fig. 5.26.

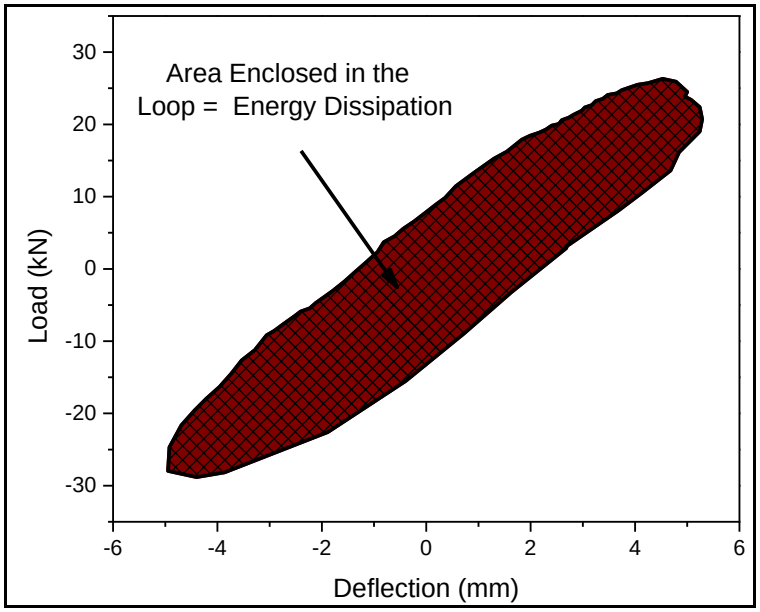

Fig. 5.26 - Calculation Procedure of Energy Dissipation for i^{th} Loop

5.7.1 Comparison between Control Specimen and Retrofitted Specimens

The energy dissipation of C-CD and R-CD specimen is calculated using the method illustrated in Fig. 5.26. It has been observed that the performance of R-CD is significantly better than C-CD. The comparison of energy dissipation at the ultimate drift ratio of C-CD and R-CD revealed that the R-CD specimen exhibited 1.71 times more energy than the C-CD specimen, as shown in Fig. 5.27. The retrofitted layer of HP-HFRC exhibited higher mechanical property, and the presence of fiber helps to dissipate the energy higher than C-CD at each cycle. However, the specimen R-CD failed earlier than the C-CD specimen.

The comparison in cumulative energy dissipation (CMD) is shown in Fig. in 5.28. It has been observed that the energy dissipation increased consecutively until the ultimate failure of the specimen. The CMD of R-CD specimen is higher than C-CD at all the drift ratio, which reflect the capacity of the initial damage than retrofitted specimen to sustain during strong ground motion.

The energy dissipation of the R-SED specimen shows improved performance than the C-CD specimen. It has been observed that the sudden increment and drop in energy dissipation at the 8^{th} cycle and 11^{th} cycles, respectively. It reflects the crack bridging phenomenon of hybrid fibers. This is might be due to the slippage in micro fiber starts from the 8^{th} cycle onwards, and then the stresses are transfer on macro fiber. At this stage, the macro fiber solely resists the crack opening, and then the slippage in macro fiber has been started from 11^{th} cycle onwards. After that, the specimen resists the forced through the core concrete and reinforcement and dissipates the energy up to 14^{th} cycle.

Likewise, the cumulative energy dissipation of both the specimen has been prepared and shown in Fig. 5.28. It has been observed that as the cycle increased the energy dissipated by the R-SED specimen is far better than the C-CD specimen. It is also observed that the specimen R-SED regains the original drift capacity. Therefore, it can be concluded that the retrofitting on initially severe damage specimen sustain the strong ground motion for the longer duration.

From Fig. 5.27, it has been observed that the specimen R-MD dissipate 2.23 time higher energy than C-CD specimen at ultimate failure. The capacity of sustaining the lateral cycle of the R-MD specimen also increased by 28.57% as compared to the C-CD specimen. The consistent increase in energy dissipation of the R-MD specimen revealed the effective contribution of higher mechanical property of retrofitted material and also the presence of hybrid fiber significantly controls the opening and widening of crack at both the level i.e. micro and macro level.

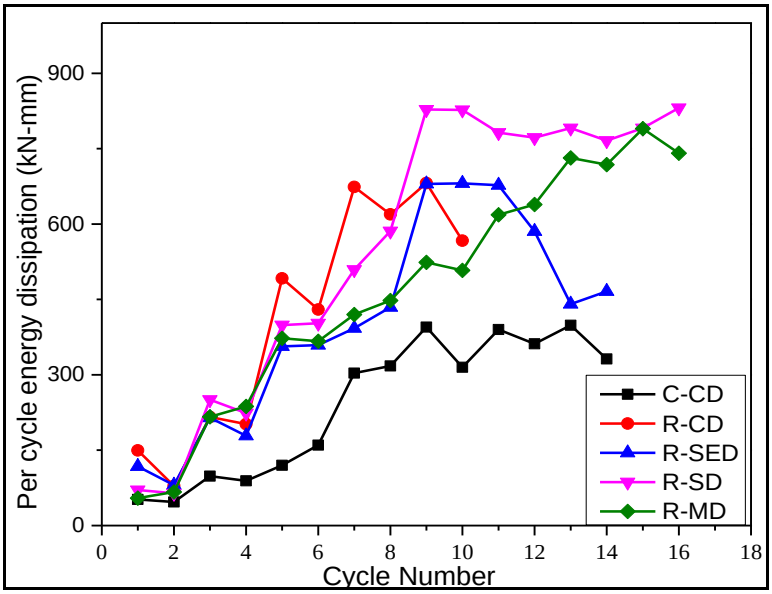

Fig. 5.27 – Per Cycle Energy Dissipation versus Cycle Number

The exponential growth is observed in the CED of R-MD specimen when compared to the C-CD specimen, as shown in Fig. 5.28. This growth of the CED parameter reflects the capability of the retrofitted specimen to sustain the seismic loading for a longer duration.

The specimen R-SD exhibited 2.50 times higher per cycle energy dissipation than the C-CD specimen. From Fig. 5.27, it is observed that the pattern of energy dissipation of the R-SD specimen is very much similar to the R-MD specimen; however, the magnitude of per cycle dissipated energy is higher than the R-MD. The steep rise in energy dissipation at 8^{th} cycle has been found, and then drop has been observed at the 11^{th} cycle. From Fig. 5.28, it can be seen that the growth pattern in CED is exponential up to the ultimate drift ratio i.e., 5%. It is the maximum improvement impart by the retrofitting strategy among all the specimens.

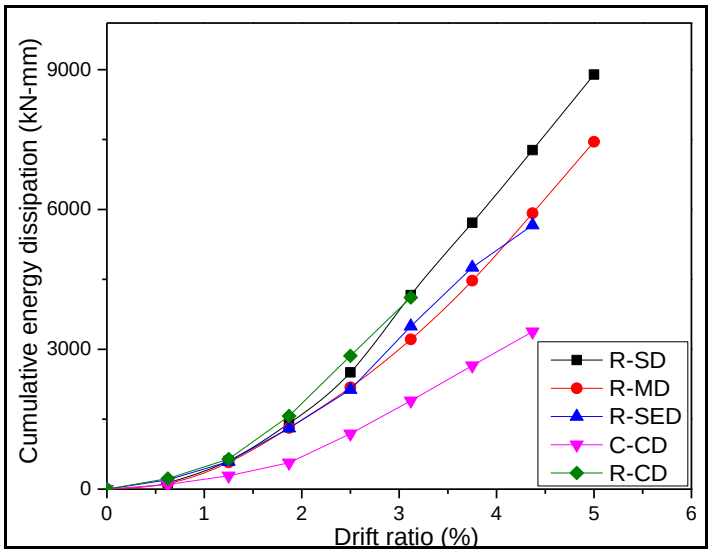

Fig. 5.28 Cumulative Energy Dissipation versus Drift Ratio

Table 5.4 - Cumulative Energy Dissipation of Control and Retrofitted Specimen

Drift Ratio (%)	C-CD (kN-mm)	Drift Ratio (%)	R-CD (kN-mm)	Drift Ratio (%)	R-SED (kN-mm)	Drift Ratio (%)	R-MD (kN-mm)	Drift Ratio (%)	R-SD (kN-mm)
0	0	0	0	0	0	0	0	0	0
0.625	98.81	0.625	228.47	0.625	198.24	0.625	121.35	0.625	135
1.25	286.13	1.25	646.47	1.25	591.4	1.25	574.97	1.25	609.35
1.87	566.13	1.87	1568.47	1.87	1307.13	1.87	1314.61	1.87	1411.05
2.5	1187.26	2.5	2861.77	2.5	2134.43	2.5	2182.43	2.5	2506.355
3.12	1897.26	3.12	4110.21	3.12	3495.48	3.12	3214.12	3.12	4161.35
3.75	2648.86	3.75	--	3.75	4758.25	3.75	4471.42	3.75	5715.355
4.37	3379.1	4.37	--	4.37	5665.03	4.37	5921.08	4.37	7272.35
--	--	--	--	--	--	5	7452	5	8894.355

The per cycle energy dissipation and cumulative energy dissipation of tested BCJ specimens are plotted in Fig. 5.27 & 5.28. It can be observed from the curves that under reverse cyclic load testing, all retrofitted specimens dissipate higher energy in each cycle than C-CD specimen; however, the ultimate displacement cycle sustained by R-CD is lower than C-CD, due to initially yielded reinforcement. Further, with a decrease in damage level from severe to slight, the ultimate displacement of R-MD and R-SD increases as compared to C-CD specimen, consequently the energy dissipation is increased, as shown in Table 5.3. The ability of R-MD and R-SD to dissipate the higher energy at the larger drift indicates the resisting of growth of crack opening by hybrid fiber at the micro and macro level (see Fig. 5.27).

The cumulative energy dissipation describes the response of the structure for the complete span of the earthquake. From Fig. 5.28, it can be observed that the specimen C-CD dissipates the energy till drift ratio of 4.37%, whereas, the R-CD specimen, due to complete pre-yielding of reinforcement, dissipate the energy only up to 3.12% drift ratio which is 28.60% lesser than the C-CD. The maximum improvement in cumulative energy dissipation is exhibited by R-SD followed by R-MD, RSE-D, R-CD, and C-CD, which shows that the performance of retrofitted specimens is much better than that of the control specimen in terms of energy dissipation and ductility.

5.8 JOINT PRINCIPAL TENSILE STRESS

The ability to sustain the higher principle tensile stress at the BCJ leads to the improvement of the performance during cyclic loading. *Priestley 1997* suggested the equations to calculate

the principal tensile stress (see equation 5.1 – 5.3). The joint principal tensile stress is calculated for control and all retrofitted initially damage specimen as follows;

$$\tau_{jh} = \frac{P}{A_{h\ core}}\left(\frac{L_b}{d_b} - \frac{L_b + 0.5\ D_c}{L_c}\right) \tag{5.1}$$

$$\sigma_t = \frac{\sigma_p}{2} + \sqrt{\frac{{\sigma_p}^2}{4} + {\tau_{jh}}^2} \tag{5.2}$$

$$\sigma_p = (N_c + P)/(b_c h_c) \tag{5.3}$$

Where the applied cyclic load (P) at the end of the beam is obtained from the experimental load displacement hysteresis curve (peak of each cycle). The length of the beam (L_b), the length of the column (L_c), the total depth of the beam (D_c) and the effective depth of the beam (d_b) is taken from the beam column joint geometrical dimension. The horizontal cross-sectional area (Ah core) of the joint core is calculated by using the cross sectional area participating in resisting the horizontal shear force. Where τ_{jh}, σ_t,σ_p and Nc is the joint horizontal shear stress, principle tensile stress, axial compressive stress and axial compressive load applied using a hydraulic jack, respectively. The equation 5.1-5.3 is used to calculate the principal tensile stress of control and retrofitted specimen.

5.8.1 Comparison between Control Specimen and Retrofitted Specimens

It has been observed that the specimen C-CD resist the principal tensile stress up to 1.87% and 3.12% drift ratio in positive and negative displacement respectively; whereas, the specimen R-CD resist the tensile stress up to 1.25% and 1.87% in positive and negative displacement respectively. It has been observed from Fig. 5.29 that the significant improvement in the principal tensile resistance capacity of the R-CD specimen is observed, but the degradation in the resistance capacity starts early as compared to the C-CD specimen. This is attributed to the completely pre-yielded reinforcement that could not enable to offer resistance with the increased lateral drift. In the initial lateral drift, the specimen resists the stresses because of the presence of the HP-HFRC layer, but after the failure of HP-HFRC, the specimen starts losing the resistance rapidly because of the lower residual stresses in the pre-yielded reinforcement and core concrete.

The specimen R-SED resist tensile stress up to 1.87% and 2.5% drift ratio in positive and negative displacement whereas, specimen C-CD resist the principal tensile stress up to 1.87% and 3.12% drift ratio in positive and negative displacement respectively. It has been observed that the resistance capacity degradation has been started at a similar drift ratio in positive displacement but starts early in negative displacement, as shown in Fig. 5.29. However, the maximum principal resistance capacity of R-SED increased 1.58 times than the C-CD specimen, which reflects the efficiency of the retrofitting strategy on the initial severely damaged specimen. The R-MD specimen resists the principal tensile stresses up to 1.25% and 1.85% positive and negative drift, respectively; after that, the degradation in resistance capacity starts degrading as shown in Fig. 5.29. At the ultimate drift ratio (5%), the principal tensile resistance capacity is 2.47 MPa and 3.58 MPa under positive and negative displacement, respectively, which is 8.20% and 10.76% higher than C-CD specimen resistance capacity. The post elastic performance of the R-MD specimen is significantly improved as compared to R-CD and R-SED specimens also.

The improvement in post elastic performance reflects the effective utilization of the strong bond of fiber-matrix interaction. The maximum improvement in principal tensile capacity is observed in specimen R-SD. From Table 5.5, it can be observed that the 1.76 and 1.33 times improvement in peak tensile resistance capacity of the R-SD specimen during positive and negative displacement over the C-CD specimen is obtained. The slope of degradation is also getting reduced as compare to the C-CD specimen, as shown in Fig. 5.29. The lower degradation of principal tensile resistance capacity of R-SD specimen as compare to the C-CD specimen reflects the significant improvement in post elastic/post rotational capacity.

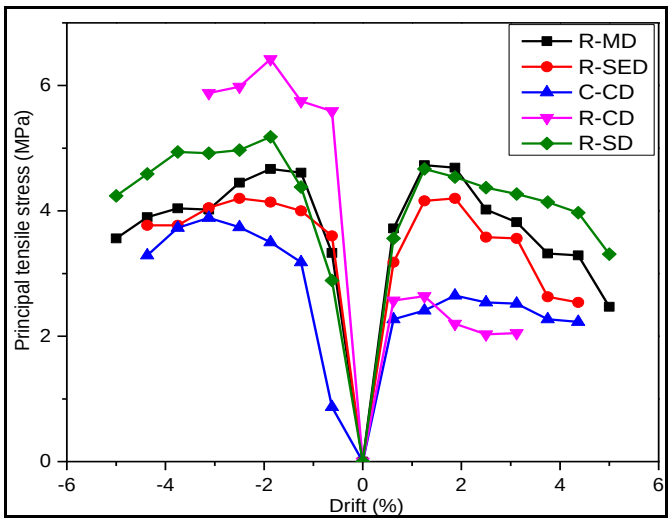

Fig. 5.29 - Principal Tensile Stress of Control and Retrofitted Specimen

It is observed from Fig. 5.29 that the retrofitted specimens can sustain the higher principal tensile stresses as compared to C-CD specimens in positive and negative drift. In R-CD, the developed initial joint stresses are completely resisted by the HP-HFRC retrofitting material. The matrix of retrofitting material (HP-HFRC) holds the stresses up to 1.25 % drift and then starts degrading. Further, the performance of R-SED, R-MD, and R-SD is better than C-CD in terms of sustaining the principal tensile stress at larger drift. The HP-HFRC significantly enhances the principal tensile stress carrying capacity in R-MD and R-SD specimens, specifically, in positive displacement as this phase is designed as a compression face. It meant that hybrid fiber with high strength increases the tension carrying capacity of the compression designed face of beam column joint and controls the crack and strength degradation against diagonal crushing on the post elastic stage.

Table 5.5 - Principal Tensile Stresses of Control and Retrofitted Beam Column Joint

Drift (%)	Principal tensile stress C-CD (MPa)	Drift (%)	Principal tensile stress R-CD (MPa)	Drift (%)	Principal tensile stress R-SED (MPa)	Drift (%)	Principal tensile stress R-MD (MPa)	Drift (%)	Principal tensile stress R-SD (MPa)
4.37	2.23	3.12	2.05	4.37	2.54	5	2.47	5	3.31
3.75	2.27	2.5	2.03	3.75	2.63	4.37	3.29	4.37	3.97
3.12	2.52	1.87	2.2	3.12	3.56	3.75	3.32	3.75	4.14
2.5	2.54	1.25	2.64	2.5	3.58	3.12	3.82	3.12	4.27
1.87	2.65	0.625	2.57	1.87	4.2	2.5	4.02	2.5	4.37
1.25	2.41	0	0	1.25	4.16	1.87	4.69	1.87	4.54
0.625	2.27	-0.625	5.59	0.625	3.18	1.25	4.73	1.25	4.67
0	0	-1.25	5.75	0	0	0.625	3.72	0.625	3.56
-0.625	0.872	-1.87	6.42	-0.625	3.6	0	0	0	0
-1.25	3.18	-2.5	5.98	-1.25	4	-0.625	3.33	-0.625	2.89
-1.87	3.5	-3.12	5.88	-1.87	4.14	-1.25	4.61	-1.25	4.38
-2.5	3.74	3.12	2.05	-2.5	4.2	-1.87	4.67	-1.87	5.18
-3.12	3.89	2.5	2.03	-3.12	4.05	-2.5	4.45	-2.5	4.97
-3.75	3.73	--	--	-3.75	3.77	-3.12	4.02	-3.12	4.92
-4.37	3.29	--	--	-4.37	3.77	-3.75	4.04	-3.75	4.94
--	--	--	--	--	--	-4.37	3.9	-4.37	4.59
--	--	--	--	--	--	-5	3.56	-5	4.24

5.8 CRACK AND FAILURE ANALYSIS

The failure pattern of control and retrofitted initially damage beam column joint is shown in Fig. 5.2 - 5.3 & Fig. 5.30 – 5.39, respectively. The different failure pattern of retrofitted specimens as compared to the control specimen is observed. In C-CD, the concrete at the compression face of the joint started to spell out in wedge shape at ultimate drift, as shown in Fig 5.2 – 5.3. It is observed that the number of cracks appeared on the compression face of C-CD specimen because of the compression face reinforcement started to yield in early displacement levels. Whereas, the tension face beam reinforcement yielding started in later displacement levels. In addition, the initiated cracks from the compression face of BCJ propagate towards the joint area at the higher lateral displacement and premature failure has been observed. The crack pattern of the control specimen is discussed thoroughly in section 5.2.

The failure of the R-CD specimen is governed by compression face as the reinforcement is completely pre yielded during initial damage, but the presence of hybrid fiber in HP-HFRC controls the spalling of concrete at the ultimate drift. It has been observed that the long length fiber holds the crack width during higher lateral drift. Consequently, the brittle collapse of the joint is avoided (see Fig. 5.30 – 5.33). The observed failure mode and failure pattern of R-SED, R-MD, and R-SD are significantly different from than C-CD specimen. The governing failure mode in C-CD and R-CD is the compression face of beam column joint, which is not observed in R-SED, R-MD and R-SD (see Fig 5.34 – 5.39). In R-SED, R-MD, and R-SD specimens, the rotation is localized at the beam column joint face, and energy started dissipated through this rotation till the ultimate lateral displacement.

Consequently, the wider cracks are observed at the face of beam column joint of R-SED, R-MD, and R-SD beam column joint, and hairline cracks are observed in the joint area, which represents the strong column-weak beam mechanism.The growth of hairline crack is bridged by micro fiber, and widened cracks at ultimate drift are bridged by macro fiber (see Fig. 5.38). This property is also very much required for the compression face of beam column joint as this face is designed for compression forces but in case of strong ground motion, the compression face of the beam is also subjected to tension forces.

The confinement offered by HP-HFRC in the joint area increased the tensile strength capacity of joint, so no diagonal cracks are observed in the joint region. The flexural strength of the beam is completely utilized before the shear failure at the joint in R-SED, R-MD and R-SD specimen. The formation of the plastic hinge in the beam portion reflects the large deformability, avoids the rapid shear deterioration of the joint area, and generally acceptable

for earthquake resistance design philosophy *(Park et al., 2012)*. Therefore, HP-HFRC concrete is a feasible retrofitting material for non-seismically designed structural elements.

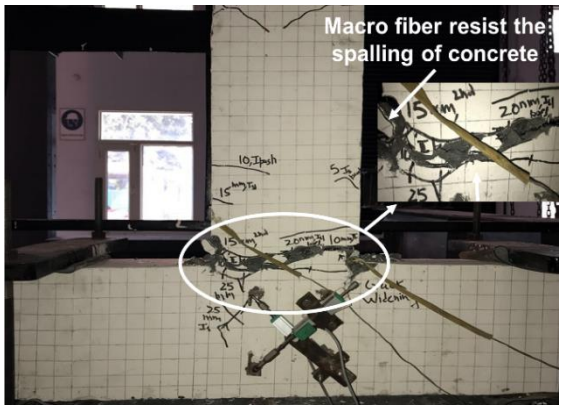

Fig. 5.30 - Failure of R-CD at Ultimate Lateral Displacement (Specimen 1)

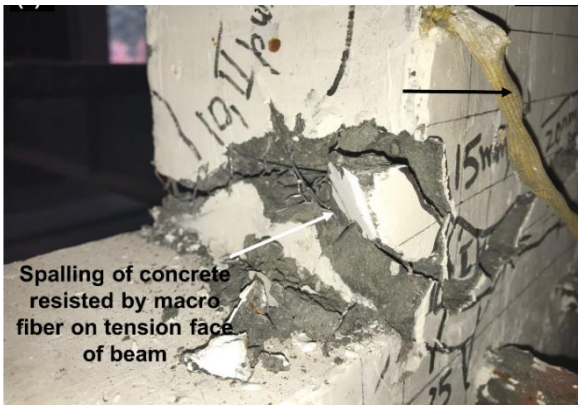

Fig. 5.31 - Enlarge View of Roll of Fiber to Control the Spalling of Concrete at Tension Face of R-CD at Higher Ultimate Displacement (Specimen 1)

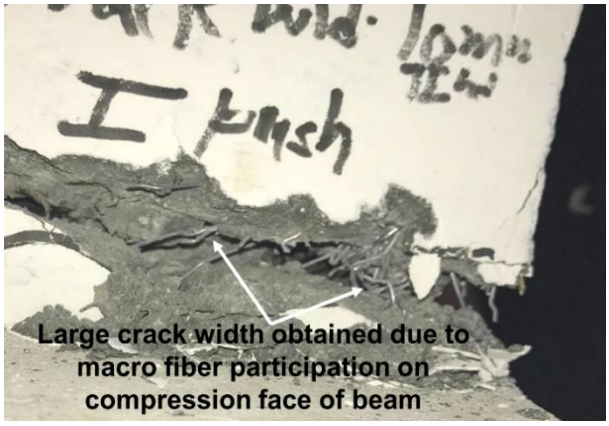

Fig. 5.32 - Enlarge view of Bridging the Crack by Fiber at Ultimate Displacement in R-CD (Specimen 1)

Fig. 5.33 - Failure of R-CD at Ultimate Lateral Displacement (Specimen 2)

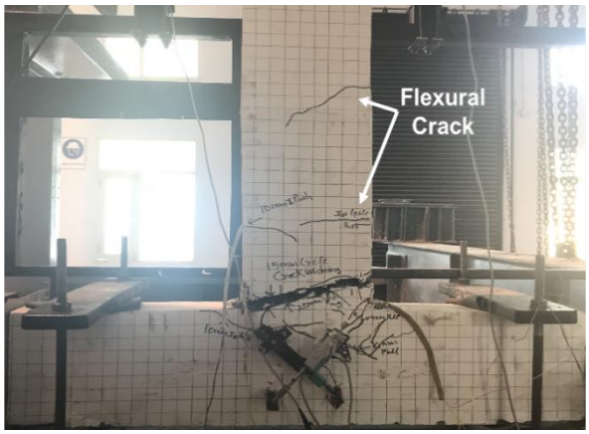

Fig. 5.34 - Failure Pattern of R-SED at Ultimate Lateral Displacement (Specimen 1)

Fig. 5.35 - Failure Pattern of R-SED at Ultimate Lateral Displacement (Specimen 2)

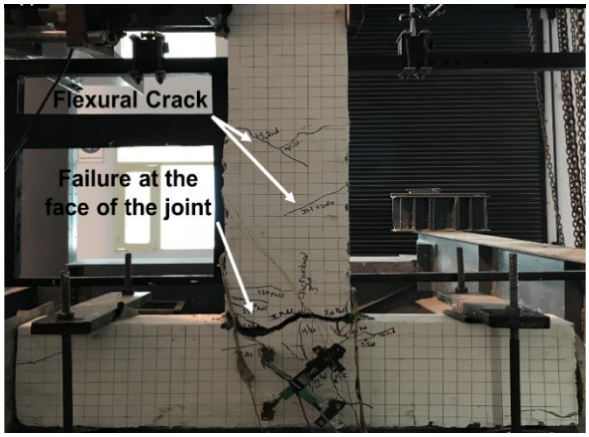

Fig. 5.36 - Failure Pattern of R-MD at Ultimate Lateral Displacement

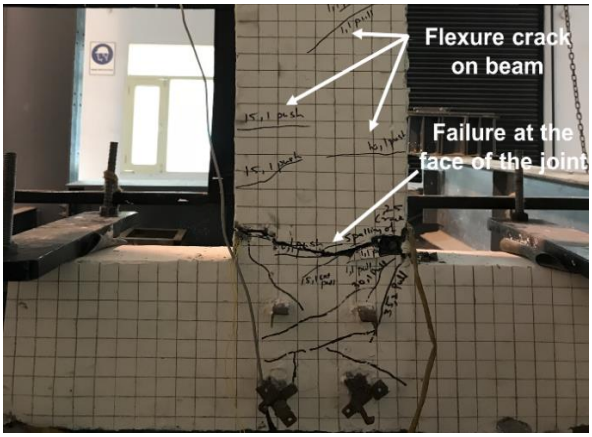

Fig. 5.37 - Failure Pattern of R-SD at Ultimate Lateral Displacement (Specimen 1)

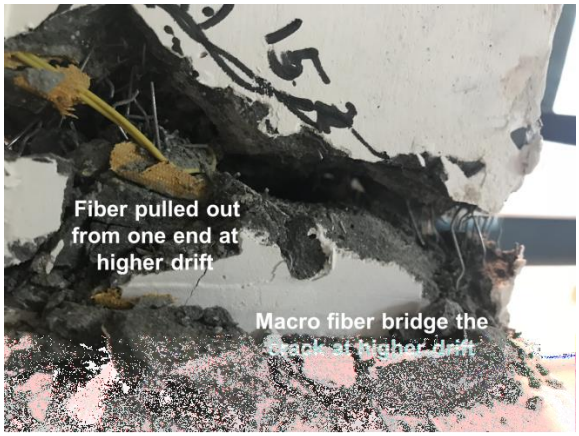

Fig. 5.38 - Enlarge View of Roll of Macro Fiber to Sustain the Higher Lateral Displacement in R-SD (Specimen 1)

Fig. 5.39 - Failure Pattern of R-SD at Ultimate Lateral Displacement (Specimen 2)

CHAPTER - 6

RETROFITTING OF BEAM COLUMN JOINT USING WIRE MESH CONFINED HIGH PERFORMANCE HYBRID FIBER REINFORCE CONCRETE

6.1 GENERAL

In this chapter of the dissertation, the seismic performance of initially damage specimen retrofitted using wire mesh confined HP-HFRC is reported. Firstly, as explained in the previous chapter, the control specimen is damaged under quasi static reverse cyclic loading to obtain the load hysteresis response. The four initial damage states viz., complete damage, severe damage, moderate damage, and slight damage, are calculated, using Park and Ang damage indices model from the load displacement hysteresis plot of the control specimen. Thereafter, the eight beam column joints, as a set of two each, are initially damaged using quasi static revers cyclic loading to achieve their respective damage level. These the initially damaged specimens are retrofitted using wire mesh confined HP-HFRC adopting procedure, as explained in detail in chapter 4.

The retrofitted specimens viz. retrofitted complete damage (RCD), retrofitted severe damage (RSED), retrofitted moderate damage (RMD), and retrofitted slight damage (RSD) are cured for 28 days and again tested under quasi static reverse cyclic loading. The response of retrofitted specimens is measured in terms of load displacement hysteresis, ductility, stiffness and strength degradation, energy dissipation, and principal tensile stresses. The effect of initial damage level on the efficacy of the retrofitted material, i.e., wire mesh confined HP-HFRC is also evaluated. Also, the comparison between the seismic performance of confined HP-HFRC retrofitted initially damaged beam column joint and wire mesh confined HP-HFRC retrofitted initially damaged specimens is presented in this chapter.

6.2 CYCLIC BEHAVIOUR OF CONTROLLED SPECIMEN

6.2.1 Cyclic Behaviour of Control Complete Damage (CCD) Specimen

Fig. 6.1 shows the load displacement hysteresis performance of control beam column joint sub-assemblage (CCD) tested under quasi static reverse cyclic loading. It has been observed that the peak load capacity of CCD is significantly higher during positive displacement as compared to the peak load capacity in negative displacement. The load carrying capacity of the specimen increased till the 15 mm positive displacement afterward, the peak load starts

decreasing. The same pattern of load resistance is also observed during negative displacement; however, the peak load is observed at 25 mm lateral displacement, and after that, the degradation in peak load has been started. The drop in peak load/strength is observed between 15 mm - 25 mm positive and negative lateral displacement, respectively. The CCD positive displacement shows the slower rate of load degradation between 15 mm -25 mm; further, the increment in positive lateral displacement revealed the drop in load at 30 mm. The drop in lateral load resistance capacity of CCD specimen is indicating the yielding of steel reinforcement and severe crack propagation in concrete. The complete failure of the joint occurred at 35 mm positive displacement, which could be attributed to the higher rate of bond degradation on the compression face due to the unequal amount of reinforcement (2 – 8 mm diameter on the compression phase and 3 – 10 mm diameter on tension face). The failure in compression face at 35 mm positive displacement is recognized as a premature failure because minor lateral load capacity of the specimen is degraded at the tension face of the beam.

It has been observed that the micro cracks initiate from the compression face at 5 mm lateral displacement and propagates as the lateral displacement increased. The onset of micro cracks has been observed in tension face at 10 mm lateral displacement. The cracks from the compression face propagated towards the joint area and tension face of the beam as the lateral displacement reached 15 mm. The severe degradation in strength capacity during positive displacement is observed between 20 – 30 mm lateral displacements because, the bond degradation has been started at 20 mm and, at 25 mm, spalling of concrete initiated in the compression face and, severe bond degradation resulted in a separation of a big chunk of concrete at 30 mm lateral displacement. The disintegration of the bond between the concrete and reinforcement at this stage in both the control complete damage specimen imparts the higher stress concentration on the longitudinal steel placed at the compression face of the joint, and thus, complete reinforcement yielding can be visualized in Fig. 6.2 - 6.4. At the collapse state of beam column joint, the following locations are identified to distinguish the severe, moderate, and minor cracks.

- Compression face of the beam exhibited the severe cracks; alternatively means maximum energy of the beam column joint is dissipated through this location,
- Joint interface exhibited severe cracks,
- Joint panel exhibited moderate cracks and,

- Beam portion exhibited the flexure crack at higher lateral displacement, identified as a minor crack location.

From the obtained load-displacement hysterics of the control specimen, four damage levels were calculated using Park and Ang damage indices model. Then control specimens (set of two) are damaged under quasi static reverse cyclic loading to obtain the distinct damage level of beam column joint.

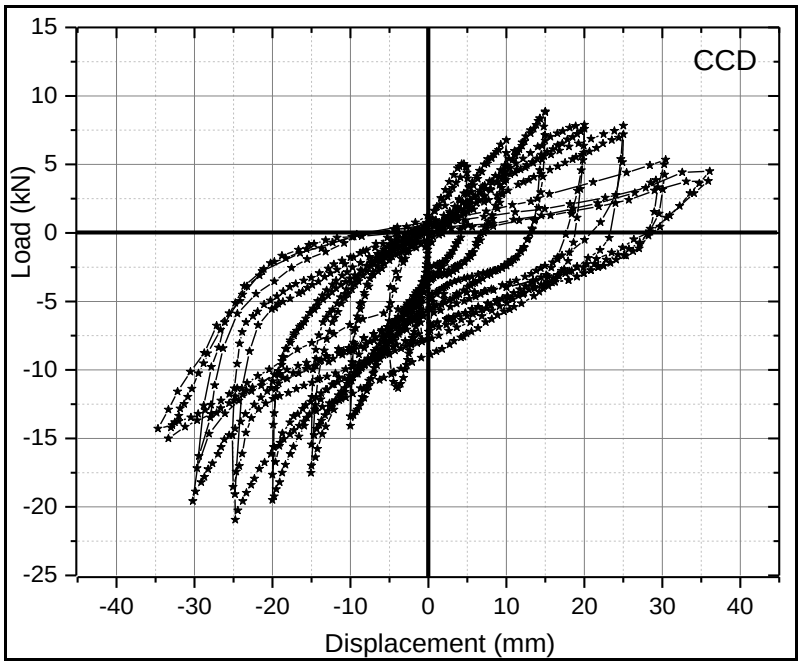

Fig. 6.1 - Hysteresis Behaviour of Control Complete Damage Specimens (CCD)

Fig. 6.2 - Crack Pattern of Control Complete Damage (CCD) Specimen I

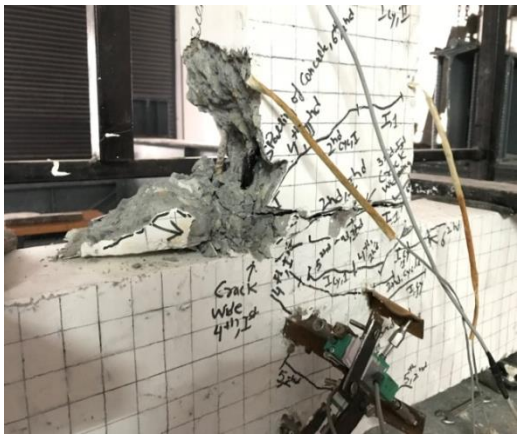

Fig. 6.3 - Concrete Spalling at the Ultimate Lateral Displacement of Control Complete Damage (CCD) Specimen I

Fig. 6.4 - Crack Pattern at 25 mm Lateral Displacement of Control Severe Damage (CCD) Specimen II

6.2.2 Cyclic Behaviour of Control Severe Damage (CSED) Specimen

A set of two specimens is tested to obtain the control sever damage state load displacement hysteresis response and shown in Fig. 6.5. The 25 mm lateral displacement is applied to obtain the severe damage state as calculated using Park and Ang's method. It is observed from Fig 6.5 that, at the initial cycles, 5 and 10 mm positive and negative lateral displacement the hairline cracks occurred around the joint panel. It has been observed that the crack width is increased as the lateral displacement increased. The width of the crack at 25 mm lateral displacement is higher in the compression face of the beam column joint as compared to the tension face (see Fig. 6.6 - 6.7). In addition, the crack propagates at the interface of the joint, joint panel, and, at 25 mm lateral displacement, the flexural cracks on the beam portion has also been observed (see Fig. 6.8). The crack network in CSED specimens affects the face of the joint, joint area, and column area; alternatively, the energy is dissipated through this location during the specimen subjected to cyclic loading. The extent of the crack is lesser in CSED than CCD specimens as the damage level shifts from complete to severe.

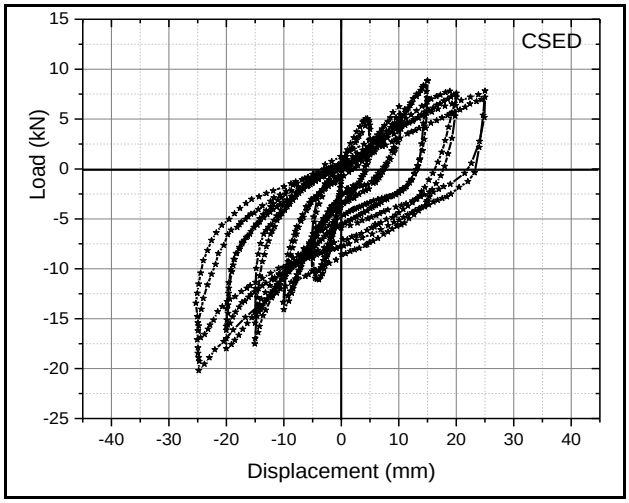

Fig. 6.5 - Hysteresis Behaviour of Control Severe Damage Specimen (CSED)

Fig. 6.6 - Crack Pattern of Control Severe Damage (CSED) Specimen I

Fig. 6.7 - Side View of the Crack Pattern of Control Severe Damage (CSED) Specimen I

Fig. 6.8 - Crack Pattern of Control Severe Damage (CSED) Specimen II

6.2.3 Cyclic Behaviour of Control Moderate Damage (CMD) Specimen

The 15 mm lateral displacement has been applied to obtain a moderate damage state. The load displacement hysteresis behaviour is shown in Fig. 6.9. It has been observed that the resistance of load has not been decreased till 15 mm displacement as the control specimen has a sufficient load resistance capacity at 15 mm and 25 mm positive and negative lateral

displacement, respectively, as shown in Fig. 6.9. The hairline cracks at the joint interface and in the beam portion have been appeared at 15 mm lateral displacement (see Fig. 6.10 – 6.13). The higher residual stresses are left in CMD specimens as compared to CCD and CSED specimens.

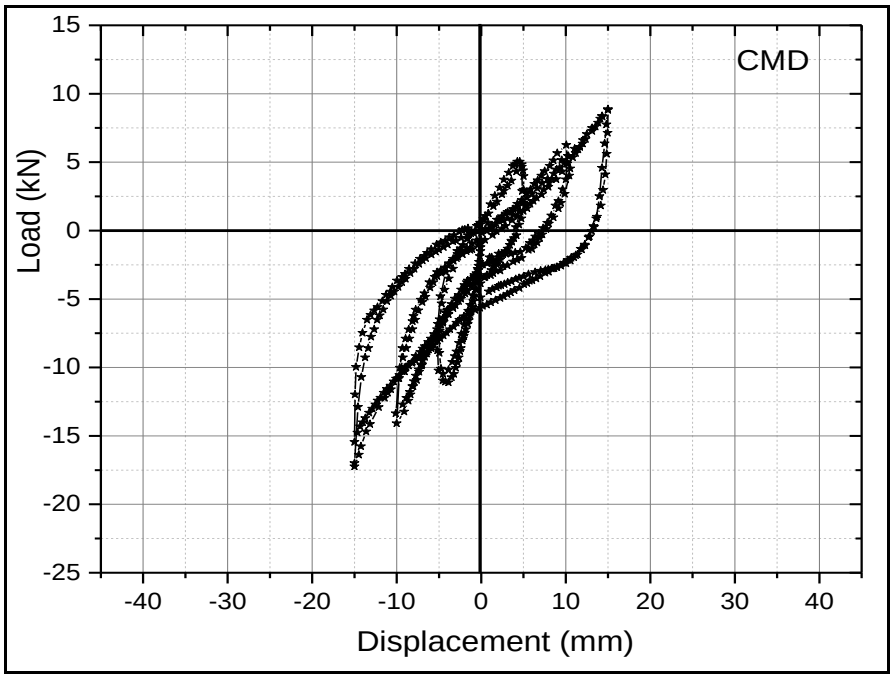

Fig. 6.9 - Hysteresis Behaviour of Control Moderate Damage Specimen (CMD)

Fig. 6.10 - Crack Pattern of Control Moderate Damage (CMD) Specimen I

Fig. 6.11 - Side View of the Crack Pattern of Control Moderate Damage (CMD) Specimen I

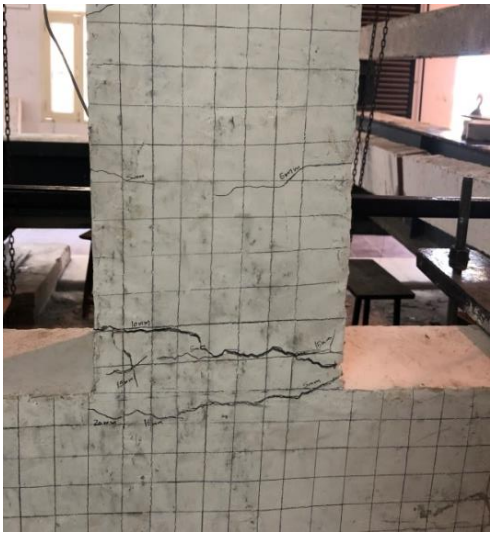

Fig. 6.12 - Crack Pattern of Control Moderate Damage (CMD) Specimen II

Fig. 6.13 - Side View of the Crack Pattern of Control Moderate Damage (CMD) Specimen II

6.2.4 Cyclic Behaviour of Control Slight Damage (CSD) Specimen

The response of the CSD specimen in terms of load displacement hysteresis is prepared and shown in Fig. 6.14. The 10 mm lateral displacement is applied to obtain a slight damage state. It has been observed that the crack appears only at the interface of joint in CSD as this specimen is only subjected to 10 mm lateral displacement; also the crack width is not severe. The single crack at the interface and in the beam portion is observed, as shown in Fig. 6.15-6.16. It can be concluded from the crack pattern that the extent of cracks in the slightly damaged specimen (C-SD) is least among all the damage state.

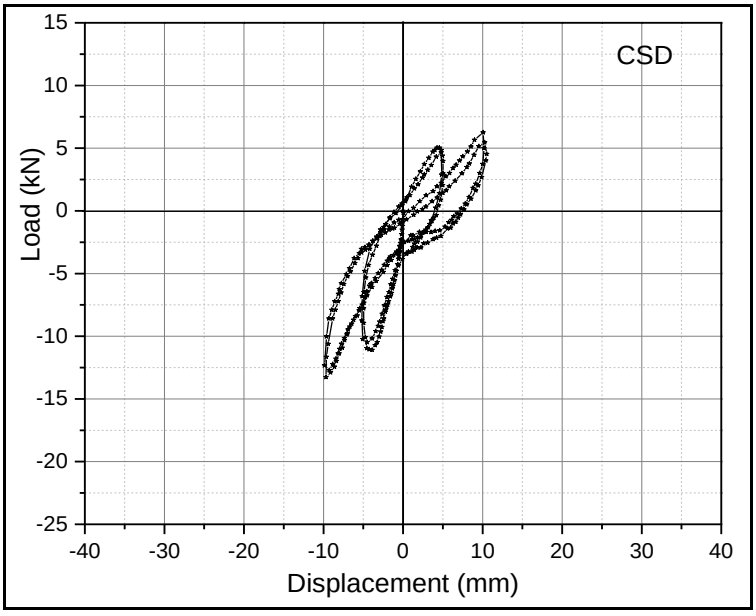

Fig. 6.14 - Hysteresis Behaviour of Control Slight Damage (CSD) Specimen

Fig. 6.15 - Crack Pattern of Control Slight Damage (CSD) Specimen I

Fig. 6.16 - Crack Pattern of Control Slight Damage (CSD) Specimen II

It can be interpreted that the extent of crack formation directly depends upon the damage level. As the initial damage level reduces from complete to slight damage, the lesser crack formation, crack length, crack width, and depth of the crack is observed. After applying the required level of the cycle of loading, the maximum residual stress is left in the slight damage specimen (CSD). Alternatively, it can be concluded that the lesser the initial damage level of beam column joint specimen higher the residual stresses in the beam column joint specimen. Further, the initially damaged specimen is processed for the retrofitting, as explained in Chapter 4. After retrofitting, the specimen is cured in water for 28 days and tested to assess the seismic performance of the wire-mesh confined HP-HFRC retrofitted beam column joint. The nomenclature of the retrofitted specimen is wire mesh confined HP-HFRC retrofitted initially complete damage (WC-RCD), wire mesh confined HP-HFRC retrofitted initially severe damage (WC-RSED), wire mesh confined HP-HFRC retrofitted initially moderate damage (WC-RMD) and wire mesh confined HP-HFRC retrofitted initially slight damage specimen (WC-RSD).

6.3 CYCLIC BEHAVIOUR OF WIRE MESH CONFINED HP-HFRC RETROFITTED BEAM COLUMN JOINT SPECIMENS

The initially damaged specimens (CCD, CSED, CMD, and CSD) are retrofitted using wire mesh confined HP-HFRC. All wire mesh confined retrofitted specimens (WC-RCD, WC-RSED, WC-RMD, and WC-RSD) are subjected to water curing for 28 days. The matured

retrofitted specimens are subjected to quasi static reverse cyclic loading. The effects of initial damage levels on the performance of wire mesh confined HP-HFRC retrofitted beam column joint specimens are analyzed and presented in subsequent sections.

6.3.1 Cyclic Behaviour of Wire Mesh Confined Retrofitted Initial Complete Damaged (WC-RCD) Specimen

The load displacement hysteresis of wire mesh confined retrofitted initially complete damaged (WC-RCD) specimen is plotted and shown in Fig. 6.17. The load displacement behavior of WC-RCD revealed the improvement over CCD specimen. It has been observed that the retrofitting using wire mesh confinement along with HP-HFRC render the post elastic rotation and, eventually, improve the ductile behavior. The WC-RCD specimen attained the peak load at 10 mm and 30 mm positive and negative lateral displacement, respectively as shown in Fig. 6.17. The peak load 22.021 kN in positive displacement and 33.578 kN in negative displacement has been observed whereas, the original CCD exhibited the 8.83 kN in positive displacement and 19.743 kN in negative displacement, which reflects the significant improvement in terms of peak load carrying capacity in WC-RCD specimen. The onset of the drop in peak load has been observed at 15 mm positive displacement because of the opening of micro cracks in HP-HFRC. At this stage, the micro fibers control the crack opening due to which a higher load is required to open the same crack width, which was occurred in CCD at a lower lateral load. Further, the increment in lateral displacement led to increases in the stress in the joint and micro crack propagate on the joint interface. At this moment, the conversion of micro cracks into macro cracks reflects the load degradation between the 15 mm - 25 mm positive lateral displacement. The presence of micro and macro fiber delays the opening of cracks between the 15 mm - 25 mm lateral displacement. However, the slippage of micro-fiber at higher drift transfers the stresses to the macro fiber-matrix bond and reinforcement concrete bond. The opening of macro cracks in the HP-HFRC utilized the efficiency of macro fiber matrix bond, and the approach of cracks toward the layer of wire mesh reduces the effect of wire mesh confinement. This is the second conversion stage of the failure in which the macro fibers slipped out from the matrix, and resistance of retrofitted specimen is solely offered by the wire mesh confined reinforced concrete core. Further, the sudden drop in load has been observed after 25 mm displacement due to the rupture of wire mesh during positive displacement. The higher lateral displacement increases the shear, and flexural stresses on the wire mesh confined area of the retrofitted specimen and the major share of the resistance are offered by the wire mesh at this stage resulted in the fracture of

mesh. Afterward, the pre-yielded reinforcement (8 mm diameter at positive displacement side) unable to sustain the lateral displacement and specimen collapse at 35 mm lateral displacement, which implies that the initial damage specimen retrofitted with wire mesh confinement and HP-HFRC regain the original ultimate lateral displacement. The residual stresses are left minimal in the initially complete damage specimen; therefore, the failure of retrofitted material resulted in a collapse of the beam column joint.

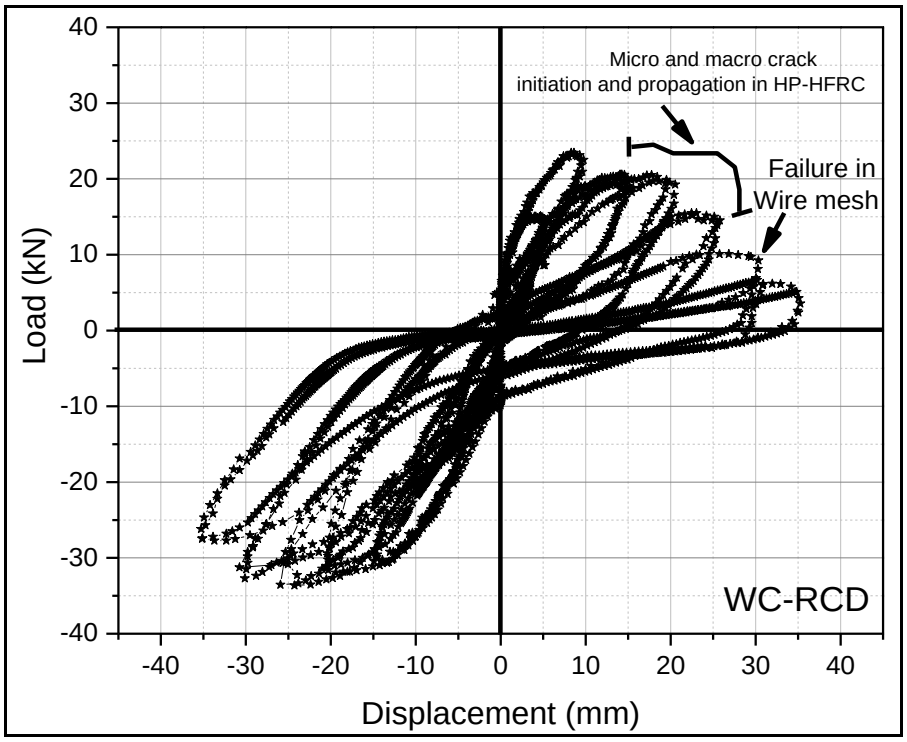

Fig. 6.17 - Hysteresis Behaviour of Wire Mesh Confined HP-HFRC Retrofitted Initially Complete Damage Specimen (WC-RCD)

6.3.2 Cyclic Behaviour of Retrofitted Wire Mesh Confined Initially Severe Damaged (WC-RSED) Specimen

The load displacement hysteresis response of initial severe damage than retrofitted specimen (WC-RSED) is plotted and shown in Fig. 6.18. It can be concluded from the load displacement hysteresis response that the wire mesh confined HP-HFRC retrofitting strategy significantly improve the seismic response of the specimen. The pre-peak response of WC-RSED exhibited higher stiffness, and continually the lateral load carrying capacity is increased up to 15 mm lateral displacement level. The micro-cracks appear on the joint interface from 10 mm lateral displacement onwards, and peak load is observed at 15 mm lateral displacement. The maximum peak load is 31.23 kN at 15 mm positive lateral displacement whereas, 37.54 kN maximum peak load is obtained at 20 mm negative lateral

displacement. Further increment in lateral displacement from 15 mm – 20 mm led to increasing the stresses in the joint, which results in the conversion of micro cracks into macro cracks. As the far most plane of the beam from the neutral axis is subjected to the highest bending stresses, therefore the width of cracks always increased either from the compression face or tension face of the beam. However, the tension face contained the designed reinforcement but, the compression face contained only hanger bars; therefore, the severity of cracks observed at the compression face of the beam. At this stage, the fibers retard the crack opening; consequently, the lower rate of load degradation and delay in the opening of cracks is observed. However, the drop in load at 25 mm positive displacement has been observed in the WC-RSED specimen. This is due to the penetration of crack from the HP-HFRC retrofitted layer to wire mesh. The higher stresses at the interface of joint impart the bending and shear tension on the wire mesh; consequently, the fracture is observed. It can be interpreted from the discussion that the fiber being completely pulled out from the matrix once the wire mesh got a fracture. Afterward, the partially pre-yielded reinforcement (8 mm diameter in compression face and 10 mm diameter in tension face of the beam) sustain the lateral displacement up to 40 mm which implies that the initial damage specimen retrofitted with wire mesh confinement along with HP-HFRC improve the 14.28% higher lateral displacement capacity than CCD and WC-RCD specimen.

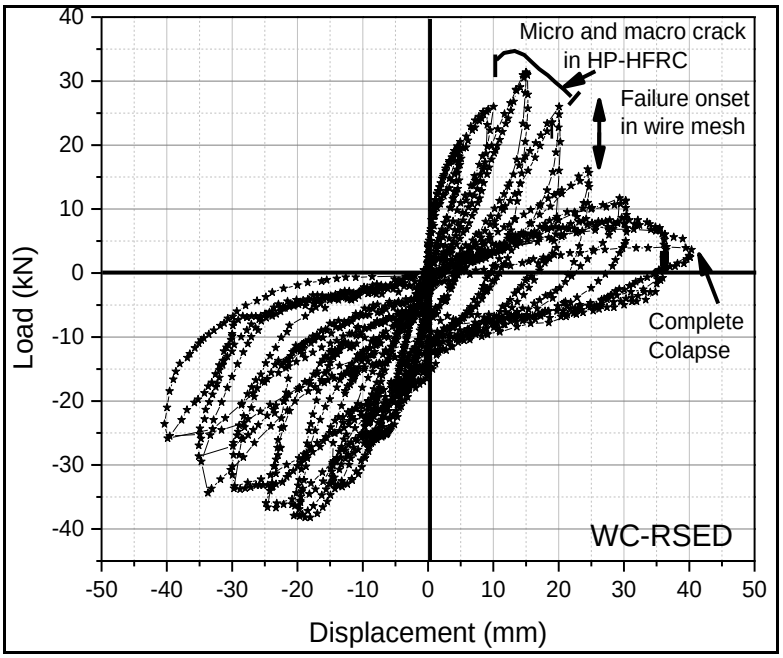

Fig. 6.18 - Hysteresis Behaviour of Wire Mesh Confined HP-HFRC Retrofitted Initially Severe Damage Specimen (WC-RSED)

6.3.3 Cyclic Behaviour of Wire Mesh Confined Retrofitted Initially Moderate Damaged (WC-RMD) Specimen

The hysteresis behavior of wire mesh confined retrofitted initial moderate damage specimen is plotted and shown in Fig. 6.19. The significant improvement in positive and negative lateral load carrying capacity is observed in the WC-RMD specimen. The maximum peak load is 35.06 kN at 25 mm positive displacement is observed. During negative displacement, the peak load i.e., 39.22 kN, is obtained at 25 mm. The initiation of micro cracks starts during 10 mm positive displacement. It has been observed that the crack onsets from the compression face and propagate towards the tension face. The presences of hybrid fibers bridge the cracks between10 mm -25 mm lateral displacement. It has been observed that the cracks initiate from the wire mesh confined HP-HFRC retrofitted layer and increases as the lateral displacement increases. The onset of micro cracks, the effectiveness of micro fibre to resist the hairline cracks, conversion of micro cracks into macro cracks, slippage of microfiber during the opening of hairline cracks and slippage of macro fibers from the matrix is observed in between 10 mm -25 mm lateral displacement.

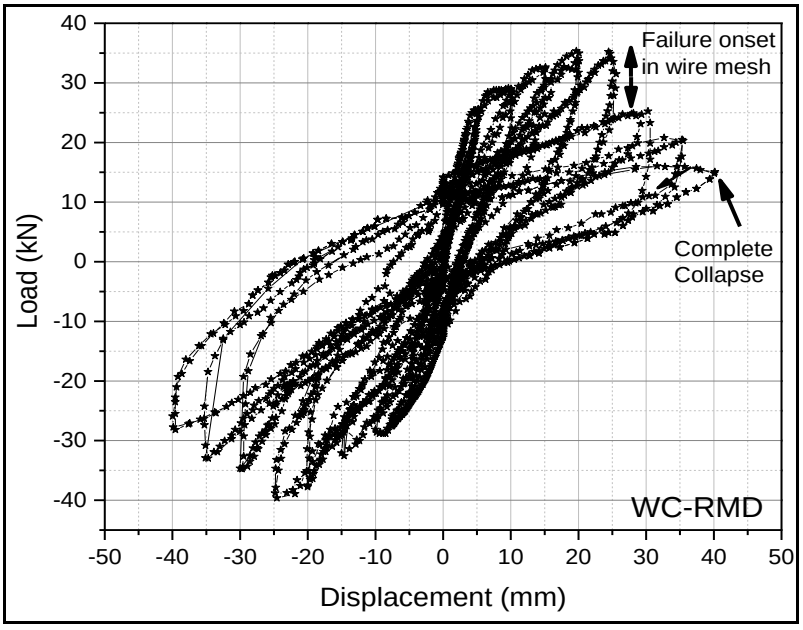

Fig. 6.19 - Hysteresis Behaviour of Wire Mesh Confined HP-HFRC Retrofitted Initially Moderate Damage Specimen (WC-RMD)

Afterward, the cracks approach the confined wire mesh, and drop in load resistance is observed at 30 mm positive lateral displacement. Even after the fracture of wire mesh from the compression face, the specimen still capable of resisting the sufficient magnitude of lateral loads, and ultimate lateral displacement capacity is reached up to 40 mm. The ultimate

displacement is 14.28% improved as compare to WC-RCD and CCD specimens. In addition, the ultimate capacity achieved by WC-RMD is equivalent to the WC-RSED specimen.

6.3.4 Cyclic Behaviour of Wire Mesh Confined Retrofitted Initially Slight Damaged (WC-RSD) Specimen

The performance of wire mesh confined retrofitted slight damage specimen subjected to quasi static reverse cyclic loading is prepared and shown in Fig. 6.20. The improvement in peak load carrying capacity of WC-RSD is very much similar to the WC-RMD. The peak load of 38.20 kN at 15 mm positive lateral displacement, whereas 42.27 kN peak load at 15mm lateral negative lateral displacement is observed. The lateral displacement capacity of the WC-RSD specimen is 45 mm i.e., 28.57% improved over CCD and WC-RSED specimen, whereas, 14.28% improved as compare to WC-RMD specimen. It has been observed from Fig. 6.20 that the drop in load at positive displacement has been observed at 35 mm positive lateral displacement in WC-RSD specimens. The form of hybrid fiber persists the slower rate of degradation between the peak load and sudden drop of load in the retrofitted specimens. The participation of macro fiber becomes inefficient at the large size macro cracks; hence, the rupture of wire mesh is observed in the specimen WC-RSD. The presence of hybrid fiber contributing to resisting the opening of micro and macro cracks consequently imparts the ductility in the behavior of specimens, and wire mesh confinement improves the initial stiffness of retrofitted specimens.

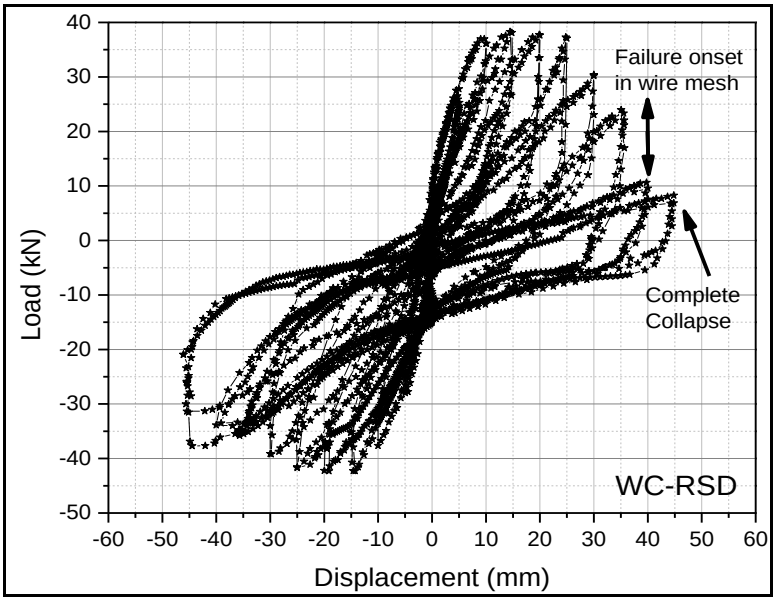

Fig. 6.20 - Hysteresis Behaviour of Wire Mesh Confined HP-HFRC Retrofitted Initially Slight Damage Specimen (WC-RSD)

It can be concluded that the lower damage indices of BCJ left the higher residual stresses in the reinforcement and concrete of controlled specimen, therefore, even after the failure of wire mesh and HP-HFRC confinement, still the core concrete of the specimen perform through the bond between the concrete and partially pre-yielded reinforcement which could be beneficial for maintaining the limit state of collapse during an earthquake even at the stage of failure of retrofitted material.

6.4 EFFECT OF INITIAL DAMAGE LEVEL ON THE DUCTILITY OF WIRE MESH CONFINED HP-HFRC RETROFITTED BEAM COLUMN JOINT SPECIMENS

The displacement ductility is calculated to quantify the seismic performance of the retrofitted specimen. The displacement ductility is defined as the ratio of ultimate displacement to the yield displacement. The specimen is considered a complete failure at the 80% drop of the peak strength; the displacement corresponding to complete failure on the backbone curve is considered as an ultimate displacement. A horizontal line is drawn parallel to the x-axis from the point of ultimate displacement and meets the y-axis. Further, a point is located on the backbone curve, which represents the 50% drop in the peak load. The yield displacement is found by drawing a tangent from the origin and pass through the 50% drop of the peak load of the back born curve to the point where the tangent meet to the horizontal line representing the 80% drop of peak strength parallel to the x-axis. The displacement ductility of all the specimens is calculated as per the procedure described in chapter 5, section 5.4 and the results are discussed in subsequent sections.

6.4.1 Comparison between Control Specimen and Wire Mesh Confined Retrofitted Specimens

The comparison of ductility between CCD and WC-RCD has been done using the backbone hysteresis curve, as shown in Fig. 6.21. It is very important to discuss the trajectory of CCD and WC-RCD specimen till failure to find the effect of retrofitting strategy and initial damage level on the ductility of the retrofitted specimen. The trajectory is divided into two segments a) pre-peak response and, b) post-peak response. The peak of CCD is observed at 15 mm and 25 mm positive and negative displacement, respectively, and failure is observed at 35 mm lateral displacement. The higher slope of the WC-RCD pre-peak backbone curve specimen over CCD specimen reflects the improvement in initial stiffness. In addition, the significant improvement in post peak backbone curve is observed. The yield positive and negative displacement of CCD and WC-RCD specimen is calculated. The ductility of CCD and R-CD

specimens is 3.4 and 3.41, respectively. It has been observed that the ductility improved by 0.29% in WC-RCD specimen which is not significant because the confinement offered by the wire mesh confined HP-HFRC is capable enough to increase the load carrying capacity of WC-RCD specimen but, the fracture of wire mesh results in rapid degradation of load in post peak stage. But, it is worth to mention here that the initially complete damaged specimen after retrofitted using wire mesh confined HP-HFRC enables the specimen to attain the original lateral displacement capacity. In addition to that the core concrete and main reinforcement have already completely damaged and yielded so, the resistance offered by these components is almost negligible.

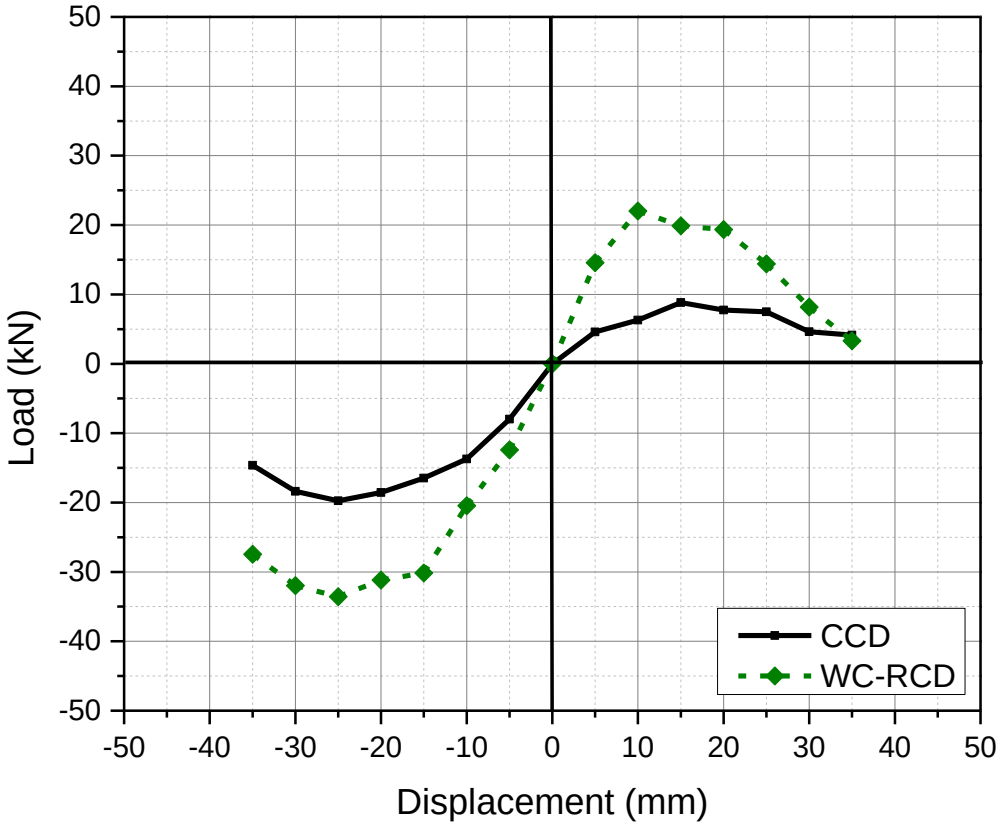

Fig. 6.21 - Backbone Hysteresis Curve of CCD and WC-RCD Specimen

The backbone hysteresis curve of the WC-RSED specimen is prepared and compared with CCD response; the response of the same is shown in Fig. 6.22. The initial stiffness of wire mesh confined HP-HFRC offers a significant improvement in the pre-elastic and post-elastic region. The ductility of the WC-RSED specimen is 3.57, which is 5% enhancement over CCD specimen. The improvement in ductility is moderate as compared to CCD because the sudden fracture of wire mesh brings the post peak curve rapidly down; therefore, the required

post elastic plateau has not been obtained. It is noteworthy to mention here that the specimen WC-RSED achieved the 14.28% improvement in lateral displacement capacity. This behavior is attributed to the presence of wire mesh confined HP-HFRC and the remaining residual stresses after obtaining the initial damage level. It has been observed that the presence of residual stress in reinforced concrete beam column joint helped in lengthen the plateau of the backbone hysteresis curve even when the HP-HFRC exhibited the severe cracks and wire mesh got fractured.

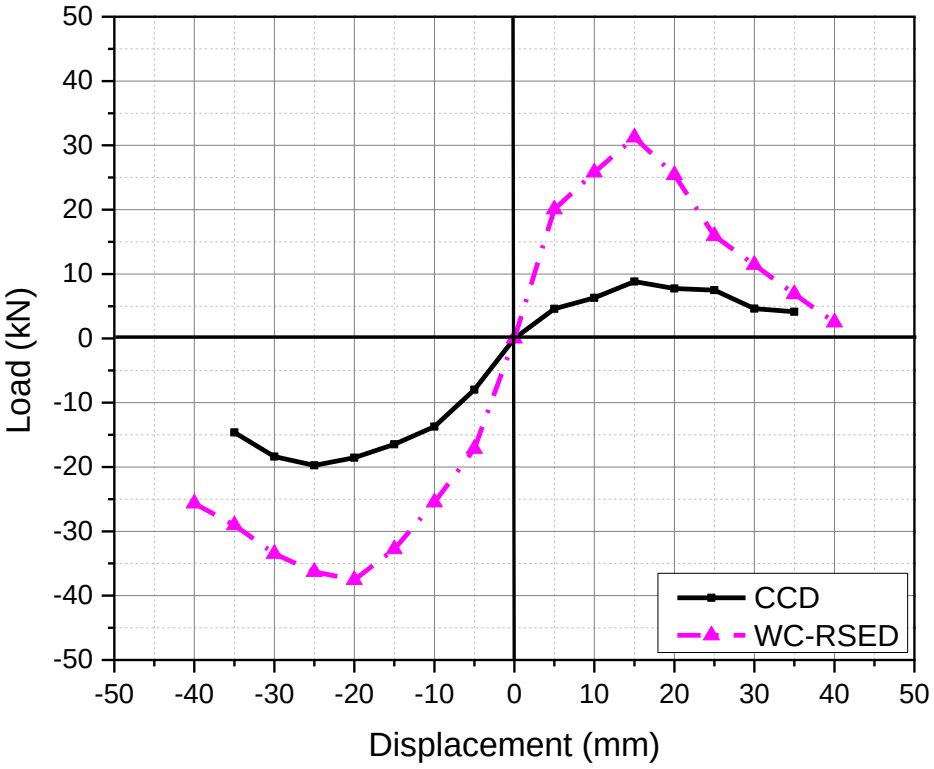

Fig. 6.22 - Backbone Hysteresis Curve of CCD and WC-RSED Specimen

The response of R-MD is significantly better than WC-RCD and WC-RSED specimens. Also, the major improvement has been observed in the post elastic region as shown in Fig. 6.23. It can be observed that the increase in slope in pre-peak backbone hysteresis curve reflects the improvement in initial stiffness. Further, the slope of the post elastic region is decreased as compared to WC-RCD and WC-RSED specimen concerning the increase in lateral displacement, which reflects the improvement in ductility. The ductility of WC-RMD is 5.11, which is52.82% higher than CCD specimen. The reason for the improvement in ductility is the lesser post elastic strength degradation and higher lateral displacement capacity. Also, the lateral displacement capacity is increased from 35 mm to 40 mm. The

lower initial damage imparts the higher non-linear rotational capacity, and hence the specimen improves the lateral displacement capacity.

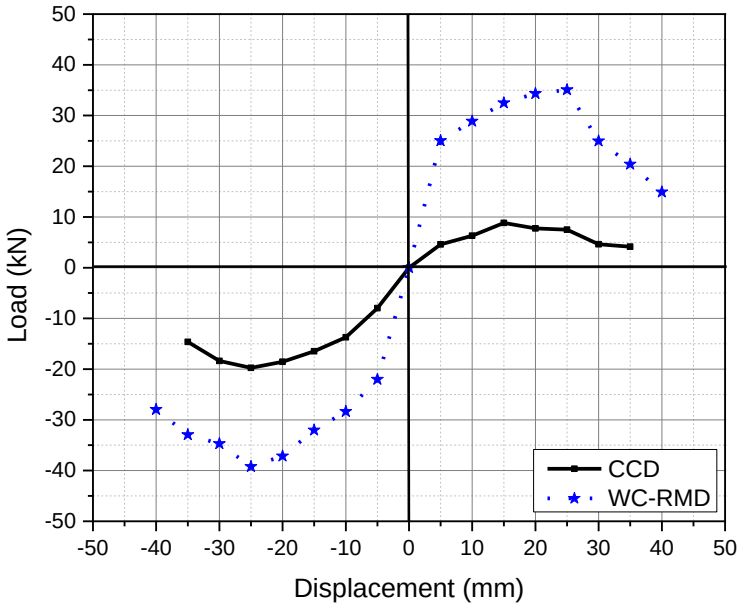

Fig. 6.23 - Backbone Hysteresis Curve of CCD and WC-RMD Specimen

The significant improvement in pre-elastic and post-elastic behaviour of wire mesh confined retrofitted initially slight damage specimens (WC-RSD) has been observed as compared to CCD, as shown in Fig. 6.24. The improvement in initial stiffness and post peak plateau indicates the improvement in ductility. The ductility, i.e., 5.55 of WC-RSD specimen is improved by 63.23% over CCD specimen, as shown in Fig. 6.25. The longest post elastic plateau is exhibited by the WC-RSD specimen among the entire retrofitted specimen; also, the lateral displacement capacity is increased by 28.57% compared with CCD specimen.

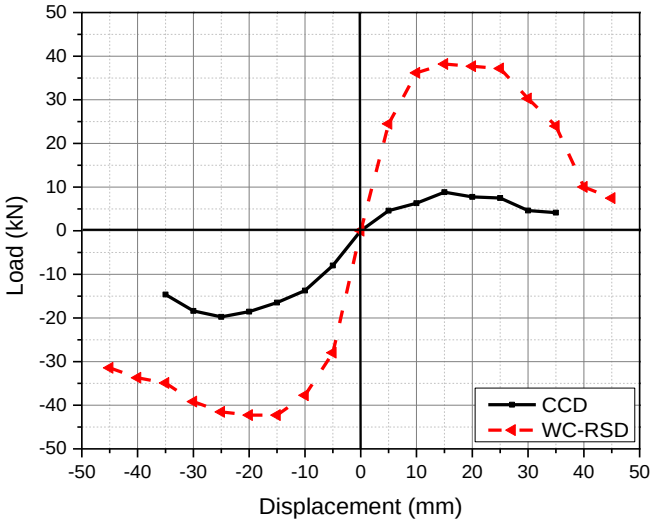

Fig. 6.24 - Backbone Hysteresis Curve of CCD and WC-RSD Specimen

The ductility of WC-RCD, WC-RSED, WC- RMD, and WC-RSD improved by 0.29%, 5%, 52.82%, and 63.23%, respectively, as shown in Table 6.1. The improvement in the ductility of retrofitted specimen observed due to the following reason; a) Presence of hybrid fibers resist the growth of opening of cracks at the micro and macro level which helps in decaying the load gradually with the incremental higher lateral displacement and, b) Wire mesh confinement impart the large post peak plateau even after macro crack opening and, c) Combined effect of wire mesh and HP-HFRC reflects the large post peak plateau; consequently enhance the ductility among all retrofitted specimens.

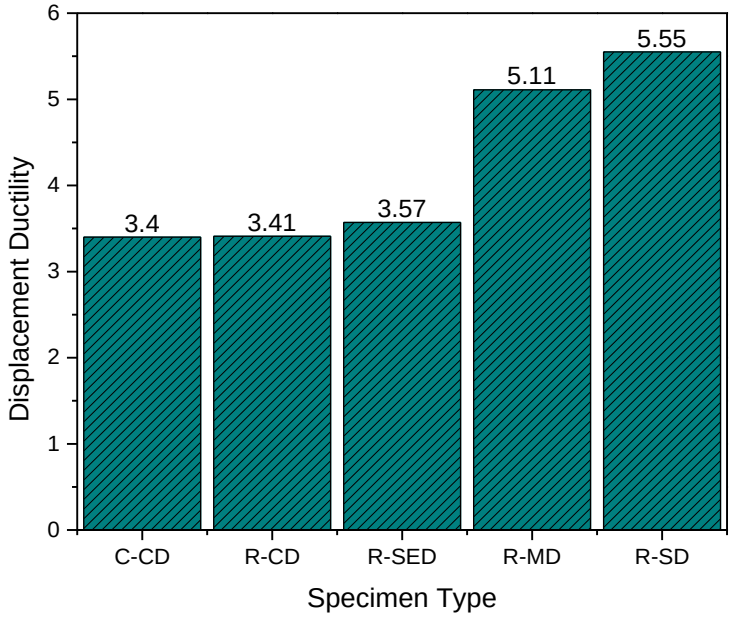

Fig. 6.25 - Displacement Ductility of Controlled and Wire Mesh Confined HP-HFRC Retrofitted BCJ

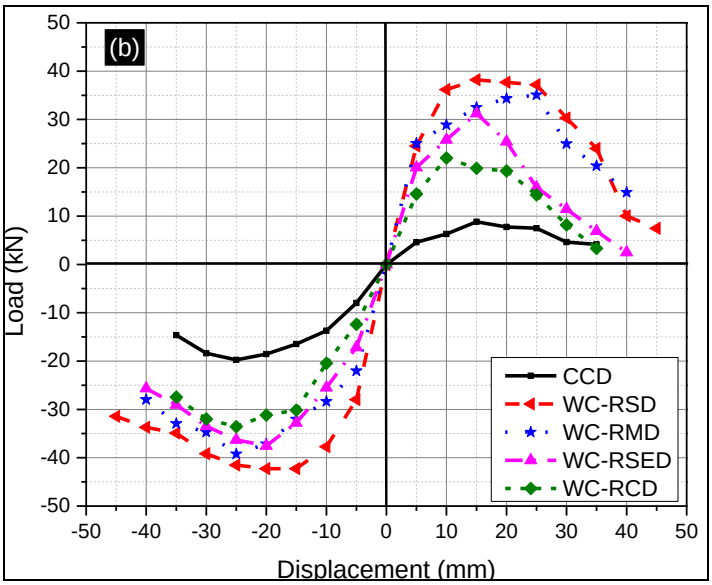

Fig. 6.26 - Displacement Ductility of Control and Retrofitted Beam Column Joint

The confinement offered by wire mesh and HP-HFRC impart the shifting of hinge formation from joint area to face of the joint. The enhancement in displacement ductility (crack bridging behaviour of hybrid fibers at the micro and macro level) because of the larger post peak plateau is observed. The confinement also reduces the rate of strength and stiffness degradation at higher lateral drift; consequently; stable post peak plateau is obtained (see Fig. - 6.26). The presence of wire mesh is HP-HFRC renders the lower rate of strength and stiffness degradation. But, the rupture of wire mesh resulted in the absence of confinement on the retrofitted beam column joint area, which promotes the rapid rate of strength and stiffness degradation. However, till then, the improved post peak plateau than the control specimen is generated because of wire mesh confinement. The presence of residual stress in an initially damaged specimen governs the extent of improvement in ductility.

Table 6.1 - Displacement Ductility of Control and Wire Mesh Confined HP-HFRC Retrofitted BCJ Specimen

Specimen Identity	Maximum				Ultimate				Displacement (D)		
	Positive		Negative		Positive		Negative		Yield D	Ultimate D	Ductility UD*/YD**
	Pm max (kN)	Dm (mm)	Pm max (kN)	Dm (mm)	Pu max (kN)	Du (mm)	Pu max (kN)	Du (mm)			
CCD	8.83	15	19.74	25	4.14	35	14.60	35	17.4	59.2	3.40
WC-RCD	19.88	15	33.57	25	3.32	35	27.44	35	17.27	58.96	3.41
WC-RSED	31.23	15	37.54	20	2.49	40	25.66	40	15.41	54.96	3.57
WC-RMD	35.06	25	39.22	25	14.92	40	27.96	40	12.51	64.02	5.11
WC-RSD	38.20	15	42.27	15	7.47	45	31.44	45	12.61	70	5.55

*UD- Ultimate Displacement; **YD – Yield Displacement

6.5 STIFFNESS DEGRADATION

The interaction of strong ground motion with a framed structure degrades the stiffness in successive cycles. The lower rate of stiffness degradation enables the structure to lengthen the post elastic plateau and helps in improving the seismic performance of the structure or vice versa. So, assessment of the seismic performance of retrofitted structure elements in terms of

stiffness is the utmost required parameter. The stiffness degradation is defined by the change in secant modulus corresponding to the peak load at each drift ratio. The secant modulus is defined as the slope of the line that passes from the origin to a displacement reversal point of interest on the lateral load versus story drift loops *(Kaya et al., 2019)*. The procedure to calculate the stiffness degradation is schematically illustrated in chapter 5, section 5.5.

6.5.1 Comparison between Control Specimen and Wire Mesh Confined Retrofitted Specimens

The stiffness degradation during positive and negative displacement of CCD and WC-RCD specimens is calculated for each cycle and shown in Fig. 6.27. The average initial stiffness of specimen WC-RCD improved by 2.39 times than CCD. The improvement in ultimate stiffness is 0.53 times than CCD, as shown in Table 6.2. The higher rate of stiffness degradation is observed with the successive increment of positive lateral displacement however, the rate of stiffness degradation is lower during negative lateral displacement. This pattern of stiffness degradation shows that the governing mode of failure in the retrofitted specimen is the compression face of the beam. The initial higher stiffness helps the specimen to resist moderate earthquake whereas if the longer duration of seismic ground motion is an encounter with this type of retrofitted structure element the rapid deterioration will be obtained along with the minimal residual stiffness at ultimate failure

The comparison of stiffness degradation between CCD and WC-RSED is plotted and shown in Fig. 6.27. It has been observed that the rate of stiffness degradation with respect to successive increment in positive lateral displacement is higher than the negative lateral displacement. The stiffness during positive lateral displacement rapidly degraded up to 2.5% lateral drift; afterward, ultimate collapse is observed at 5% lateral drift. However, the degradation during negative displacement is rapid until 2% drift. This behaviour is very much similar to WC-RCD specimen because of the ultimate collapse of the specimen is governing by the compression face of the beam.

It is worth mentioned here that the WC-RSED specimen regains the 14.28% improvement in lateral drift capacity as compare to CCD specimen and still, the average residual stiffness at failure remains higher than CCD specimen.

It has been observed that the specimen WC-RMD exhibited the improvement in stiffness by 5.44 and 2.76 times during positive and negative lateral displacement respectively over the C-CD specimen. The pattern of stiffness degradation is different than CCD, WC-RCD, and

WC-RSED as shown in Fig. 6.27. It has been observed that the slope of the stiffness degradation degraded as the lateral displacement capacity increases hence, a lower rate of degradation is obtained. The retrofitting strategy significantly improves the ultimate displacement capacity of the WC-RMD specimen. The 14.28% ultimate displacement capacity is increased over CCD specimen which is the potential evidence of improvement in the performance of WC-RMD specimen. Also, the role of residual stress plays a significant role in sustaining the stiffness once the HP-HFRC retrofitted layer and wire mesh is failed. It has also been observed that the stiffness at the collapse of the WC-RMD specimen is slightly higher than CCD stiffness value obtained at the collapse state.

The performance of the WC-RSD specimen is very much similar to the WC-RMD specimen, as shown in Fig. 6.27. It has been observed that the specimen WC-RSD exhibited the improvement in stiffness by 5.33 and 3.07 times during positive and negative lateral displacement respectively, as compared with CCD specimen. However, the rapid reduction in stiffness degradation in the WC-RSD specimen is observed up to 2.5 % drift ratio, and afterward, the rate of degradation is decreased. Like in WC-RMD specimen, the improvement in lateral displacement capacity has been observed; the ultimate displacement capacity of WC-RSD specimen is increased up to 28.57% over CCD specimen.

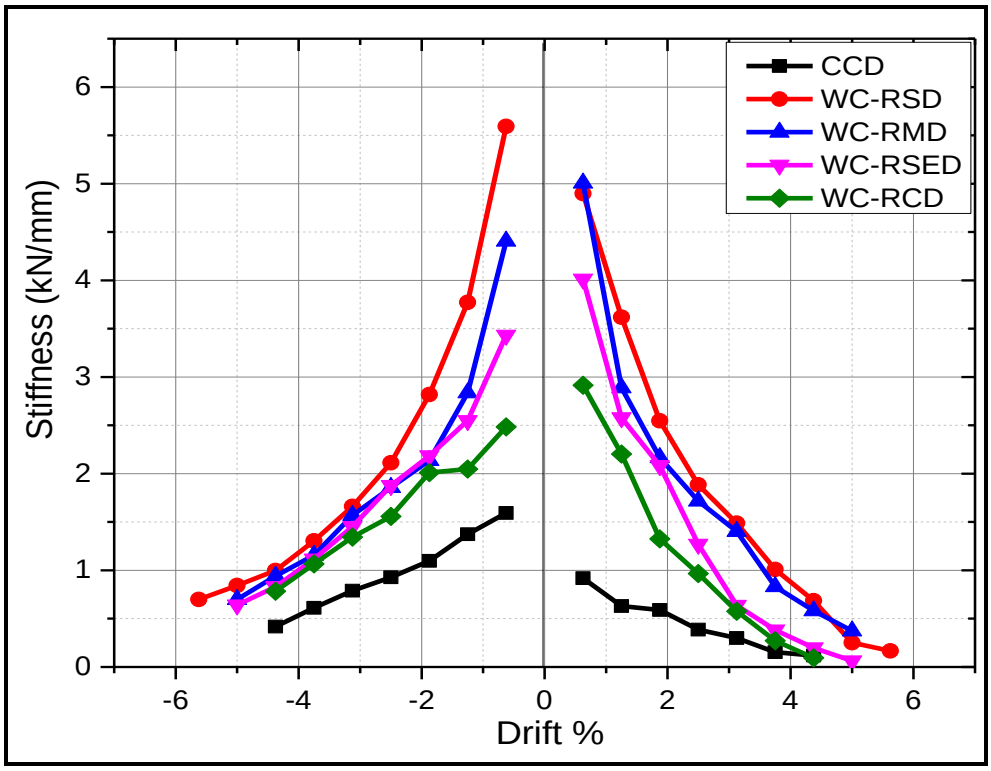

Fig. 6.27 - Stiffness Degradation versus Drift Ratio of Control and Retrofitted Specimen

Table 6.2 - Stiffness Degradation versus Drift Ratio of Control and all the Retrofitted Specimen

CCD		WC-RSD		WC-RMD		WC-RSED		WC-RCD	
Drift (%)	Stiffness kN/mm	Drift (%)	Stiffness kN/mm	Drift (%)	Stiffness kN/mm	Drift (%)	Stiffness kN/mm	Drift (%)	Stiffness kN/mm
4.375	0.11843	5.625	0.166	5	0.37318	5	0.06234	4.375	0.09493
3.75	0.15417	5	0.25062	4.375	0.58264	4.375	0.19689	3.75	0.27249
3.125	0.3	4.375	0.68524	3.75	0.83215	3.75	0.3817	3.125	0.57606
2.5	0.387	3.75	1.00986	3.125	1.40276	3.125	0.63792	2.5	0.96744
1.875	0.58867	3.125	1.48706	2.5	1.71652	2.5	1.26975	1.875	1.32594
1.25	0.63	2.5	1.88442	1.875	2.16553	1.875	2.08227	1.25	2.20216
0.625	0.918	1.875	2.54668	1.25	2.88822	1.25	2.579	0.625	2.91442
--	--	1.25	3.618	0.625	5.00711	0.625	4.01194	--	--
-0.625	1.593	0.625	4.898	--	--	--	--	-0.625	2.48378
-1.25	1.3733	--	--	-0.625	4.40662	-0.625	3.4319	-1.25	2.04691
-1.875	1.09867	-0.625	5.59283	-1.25	2.83622	-1.25	2.54905	-1.875	2.01113
-2.5	0.928	-1.25	3.77168	-1.875	2.1362	-1.875	2.18463	-2.5	1.5586
-3.125	0.78972	-1.875	2.81833	-2.5	1.85783	-2.5	1.87731	-3.125	1.34312
-3.75	0.61233	-2.5	2.11331	-3.125	1.56895	-3.125	1.45181	-3.75	1.06597
-4.375	0.41831	-3.125	1.66107	-3.75	1.15676	-3.75	1.11601	-4.375	0.78408
--	--	-3.75	1.30556	-4.375	0.94114	-4.375	0.82985	--	--
--	--	-4.375	0.9972	-5	0.6991	-5	0.64153	--	--
--	--	-5	0.84269	--	--	--	--	--	--
--	--	-5.625	0.69878	--	--	--	--	--	--

It has been observed that the initial stiffness in the positive drift of WC-RCD, WC-RSED, WC-RMD, and WC-RSD improved in the range of 5.30 – 1.82 times then CCD, whereas 3.51- 1.55 times in negative drift. Overall the average initial stiffness has improved in the range of 4.405 – 1.68 times than CCD in all the retrofitted specimens. It is worth mentioning that the residual stresses at the ultimate failure of all retrofitted specimens are higher than the CCD even at a higher drift ratio, i.e., 5%. The stiffness corresponding to each lateral drift is shown in Table 6.2.

6.6 STRENGTH DEGRADATION

The lower rate of strength degradation at higher lateral drift enables the specimen to utilize the post elastic strength effectively. Therefore, the effect of retrofitting strategy and initial damage level on the strength degradation behaviour of beam column joint is studied and

presented in this section. The change in peak load in consecutive cycles of the same directional drift is used to calculate the strength degradation *(Sasmal et al., 2013)*. The comparison of all the retrofitted specimen with a control specimen has been done and presented in sections below;

6.6.1 Comparison between Control Specimen and Wire Mesh Confined Retrofitted Specimens

The strength degradation with respect to lateral drift of specimen CCD and WC-RCD is calculated and the response is shown in Fig. 6.28. The strength degradation of CCD and WC-RCD is measured for the positive and negative lateral displacement. From Table 6.3, it has been observed that 53.05% and only 27.77% strength is degraded in CCD specimen at the ultimate lateral drift capacity. The difference of strength degradation percentage shows that the CCD specimen is completely damaged from the compression face (subjected to positive displacement), but marginal strength degradation happened from the tension face. This behaviour shows that the compression face of the beam has not been able to resist the lateral displacement, and strength degraded rapidly. The initially complete damage than wire mesh confined retrofitted specimen WC-RCD exhibited 84.91%, and 18.27% strength is degraded at ultimate lateral drift capacity i.e., 4.37%. The slope of the strength degradation during positive displacement is higher than the CCD specimen, which reflects the rapid rate of strength degradation.

The performance comparison in terms of strength degradation has been done between the CCD and WC-RSED specimens. Fig. 6.28 shows that the strength reduction has been onset at 2.5% and 3.125% positive and negative drift, respectively. In addition, the drift capacity of WC-RSED is improved by 14.28% as compared to CCD specimens. The higher amount of strength reduction, i.e., 92.01% during positive displacement is attained by WC-RSED specimen, which is 1.73 times higher than the ultimate strength degradation of CCD specimen as shown in Table 6.3. In addition, the strength reduction of WC-RSED specimen during negative displacement is 31.65%, which is 1.13 times higher than the ultimate strength reduction capacity of CCD specimen during negative displacement. It has been observed that the slope of strength reduction of WC-RSED specimen is higher than CCD specimen, but the higher drift capacity of WC-RSED exhibited the improvement in seismic performance.

The significant improvement in the rate of strength degradation of WC-RMD specimen is observed as compared to the CCD specimen. It has been observed from Fig. 6.28 that the

slope of strength degradation is lower than CCD specimen. In addition, it can also be observed that the shifting of initial damage level shifts the onset of strength degradation from 2.5% to 3.75% in positive lateral drift whereas at the same lateral negative drift i.e. 3.75 the strength degradation has been started during the negative drift. The strength degradation of WC-RMD at the ultimate positive and negative drift is 1.08 and 1.03 times than CCD specimen as shown in Table 6.3. Likewise in the WC-RSED specimen, the drift capacity of WC-RMD is improved by 14.28% as compared to CCD specimen. The comparison of CCD specimen and WC-RSD specimen is shown in Fig. 6.28. It has been observed that the strength reduction in positive and negative displacement is 81.73% and 25.61%, respectively. It has also been observed that the improvement in lateral drift capacity of WC-RSD specimen is 28.57% than CCD specimen. Therefore, it can be concluded that the maximum improvement is observed as the damage level shifts from complete to slight. The presence of wire mesh confined hybrid fibers shifts the slope of strength reduction at various drift level i.e., 3.125%, 4.375%, and 5% during the positive drift. The same pattern of a shift in slope is also observed in negative drift i.e. 2.5%, 4.375%, and 5.625%. The shifting of the slope of strength reduction during lateral drift reflects the effectiveness of fiber-matrix bond and confinement offered by wire mesh. The significant observations in terms of strength criteria are the outset of strength degradation is delayed, and the slope of strength reduction getting reduced as the damage level shifted from complete to slight. The effectiveness of fiber and wire mesh in post-elastic region resulted in a lower rate of degradation in strength concerning incremental lateral displacement and helps to perform in a ductile manner.

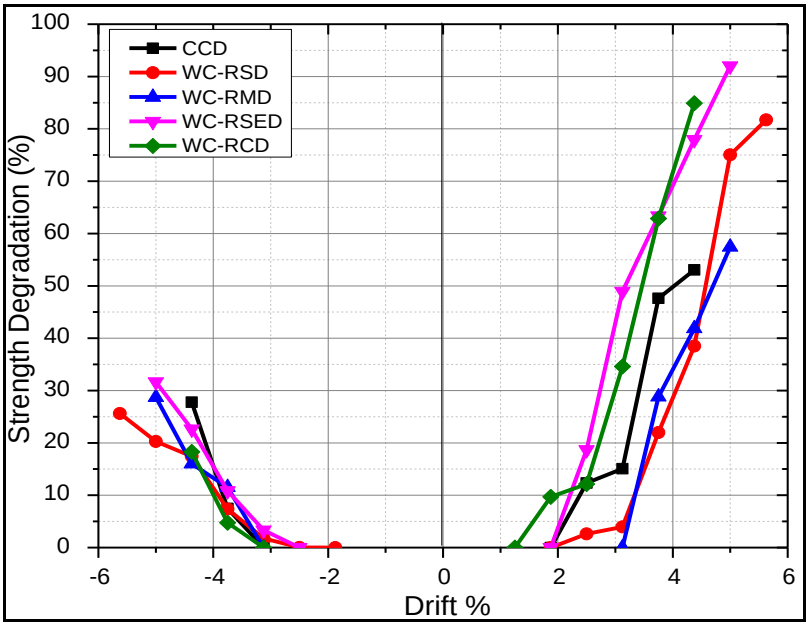

Fig. 6.28 - Strength Degradation versus Drift Ratio of Control and Retrofitted Specimen

Table 6.3 - Strength Degradation versus Drift Ratio of Control and Retrofitted Specimen

WC-RCD		WC-RSED		WC-RMD		WC-RSD		CCD	
Drift (%)	Strength degradation (%)	Drift (%)	Strength degradation (%)	Drift (%)	Strength degradation (%)	Drift (%)	Strength degradation (%)	Drift (%)	Strength degradation (%)
4.375	84.91209	5	92.01639	5	57.4342	5.625	81.72312	4.375	53.05776
3.75	62.87928	4.375	77.93751	4.375	41.85092	5	75.03467	3.75	47.62174
3.125	34.60296	3.75	63.33804	3.75	28.81331	4.375	38.49423	3.125	15.06229
2.5	12.13685	3.125	48.94027	3.125	0	3.75	21.97022	2.5	12.34428
1.875	9.68367	2.5	18.6944	2.5	--	3.125	3.95757	1.875	0
1.25	0	1.875	0	1.875	--	2.5	2.61779	1.25	--
0.625	--	1.25	--	1.25	--	1.875	0	0.625	--
0	--	0.625	--	0.625	--	1.25	--	0	--
-0.625	--	0	--	0	--	0.625	--	-0.625	--
-1.25	--	-0.625	--	-0.625	--	0	--	-1.25	--
-1.875	--	-1.25	--	-1.25	--	-0.625	--	-1.875	--
-2.5	--	-1.875	--	-1.875	--	-1.25	--	-2.5	--
-3.125	0	-2.5	0	-2.5	--	-1.875	0	-3.125	0
-3.75	4.76133	-3.125	3.33205	-3.125	0	-2.5	0.02096	-3.75	7.47414
-4.375	18.27	-3.75	10.82922	-3.75	11.52599	-3.125	1.76967	-4.375	27.77518
--	--	-4.375	22.64293	-4.375	16.02035	-3.75	7.3521	--	--
--	--	-5	31.65468	-5	28.70612	-4.375	17.44078	--	--
--	--	--	--	--	--	-5	20.26562	--	--
--	--	--	--	--	--	-5.625	25.61798	--	--

6.7 ENERGY DISSIPATION

The energy dissipation of beam column joint during post elastic rotation renders the ductility to the frame structure. Also, the capability of frame structure/structure elements to dissipate the energy during the long duration of the earthquake increases the safety of the user. The energy dissipation is calculated as the area enclosed in the hysteresis loop at different drift ratio, and the procedure of calculation is mention in chapter 5, section 5.7. Per cycle energy dissipation and cumulative energy dissipation of the controlled and retrofitted specimen is calculated and presented in Fig. 6.29 – 6.30.

6.7.1 Comparison between Control Specimen and Wire Mesh Confined Retrofitted Specimens

It has been observed from Figure 6.29 that the per cycle energy dissipation capacity of the WC-RCD specimen is increased over the CCD. It is also worth mentioned here that the retrofitting using wire mesh and HP-HFRC improve the lateral drift capacity even if the beam column joint is initially completely damaged. It reflects that the retrofitting material and strategy enable the specimen to dissipate the energy at higher lateral drift.

The comparison of energy dissipation at the ultimate drift ratio of CCD and WC-RCD revealed that the WC-RCD specimen exhibited 1.32 times more energy than CCD specimen, as shown in Fig. 6.29. It has been observed that at the 11^{th} cycle, the energy dissipation significantly decreases; the decrease in energy dissipation capacity reflects the fracture of wire mesh. The retrofitted layer of wire mesh confined HP-HFRC exhibited higher mechanical property along with the confinement effect, and the presence of fiber helps to dissipate the energy higher than CCD at each cycle. In addition, the specimen WC-RCD regains the lateral drift capacity equivalent to the CCD specimen. The comparison in cumulative energy dissipation is shown in Fig. in 6.30. It has been observed that the energy dissipation increased consecutively until the ultimate failure of the WC-RCD specimen. The cumulative energy dissipation of the WC-RCD specimen is higher than CCD at all the drift ratio which reflects the capacity of initial damage than retrofitted specimen to sustain the stresses during strong ground motion.

The per cycle energy dissipation response of the WC-RSED specimen revealed the significant improvement in energy dissipation capacity over CCD specimen. The improvement in per cycle energy dissipation in the WC-RSED specimen at ultimate capacity is 2.21 times than CCD specimen. The presence of fibre matrix interaction in HP-HFRC dissipates the higher energy as compared to control concrete because of the fiber crack bridging phenomenon. Also, the presence of wire mesh as a retrofitting material prolongs the energy dissipation plateau than CCD specimens. The complete failure of the hybrid fiber-matrix bond and fracture of wire mesh are shown at the 14^{th} cycle (see Fig. 6.29). The cumulative energy dissipation exhibited exponential growth, as shown in Fig. 6.30. It has been observed that as the lateral drift increased the energy dissipated by the WC-RSED specimen is far better than the CCD specimen. It is also observed that the specimen WC-RSED improved the drift capacity by 14.28% more than the CCD specimen. Therefore, it can be concluded that the retrofitting on initially severe damage specimen sustain the strong ground motion for the longer duration.

The per cycle energy dissipation of WC-RMD and CCD specimen is prepared from the load hysteresis plot; the response of the same is shown in Fig. 6.29. It has been observed that the

per cycle energy dissipation significantly higher than CCD specimen as the lateral displacement increased. The presence of hybrid fiber controls the opening of crack at the micro and macro both the level. Therefore, the participation of hybrid fiber continually increased with the increase in cycles. Consequently, the energy dissipation increased. Due to the confinement effect of wire mesh, the significant improvement in energy dissipation is observed at the higher cycles. Eventually, the 2.84 times improvement in per cycle energy dissipation at ultimate lateral drift is observed as compared to CCD specimen.

The cumulative energy dissipation of both the specimen (CCD and WC-RMD) has been prepared and shown in Fig. 6.30. It has been observed that as the cycle increased, the energy dissipated by the WC-RMD specimen is far better than the CCD specimen. It is also observed that the specimen WC-RMD specimen regains the drift capacity equivalent to WC-RSED but 14.28% more than the CCD specimen. Therefore, it can be concluded that the retrofitting on initially moderate damage specimen sustain the strong ground motion for the longer duration. The specimen WC-RSD exhibited 3.17 times improvement in per cycle energy dissipation over CCD specimen as shown in Fig. 6.29. The participation of fiber-matrix bond and wire mesh confinement is effectively utilized as the initial damage level shift from complete to slight. The various kink in a trajectory of per cycle energy dissipation of WC-RSD specimen revealed the opening of crack and degradation in fiber-matrix bond. From Fig. 6.30, it can be seen that exponential growth in CED up to ultimate drift ratio i.e., 5.625% is the maximum improvement impart by the retrofitting strategy among all the specimens.

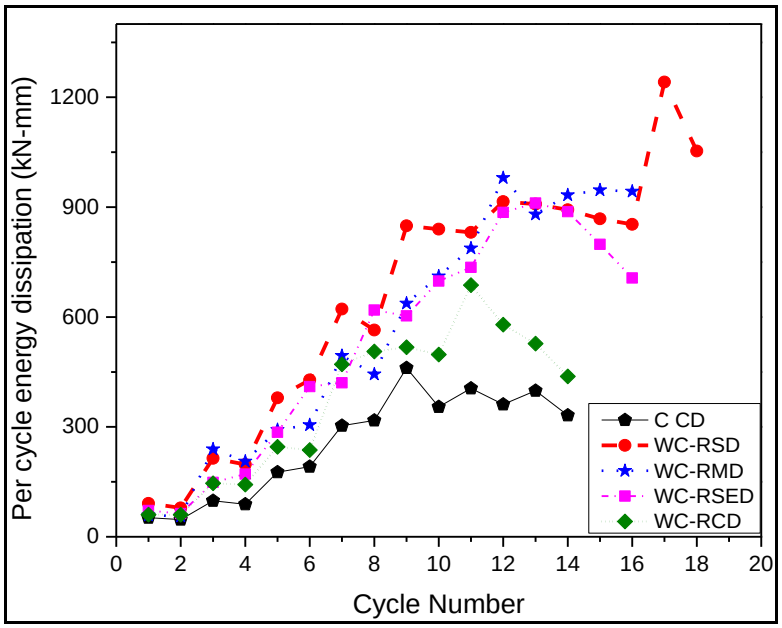

Fig. 6.29 - Per Cycle Energy Dissipation versus Lateral Loading Cycle of Control and Retrofitted Specimen

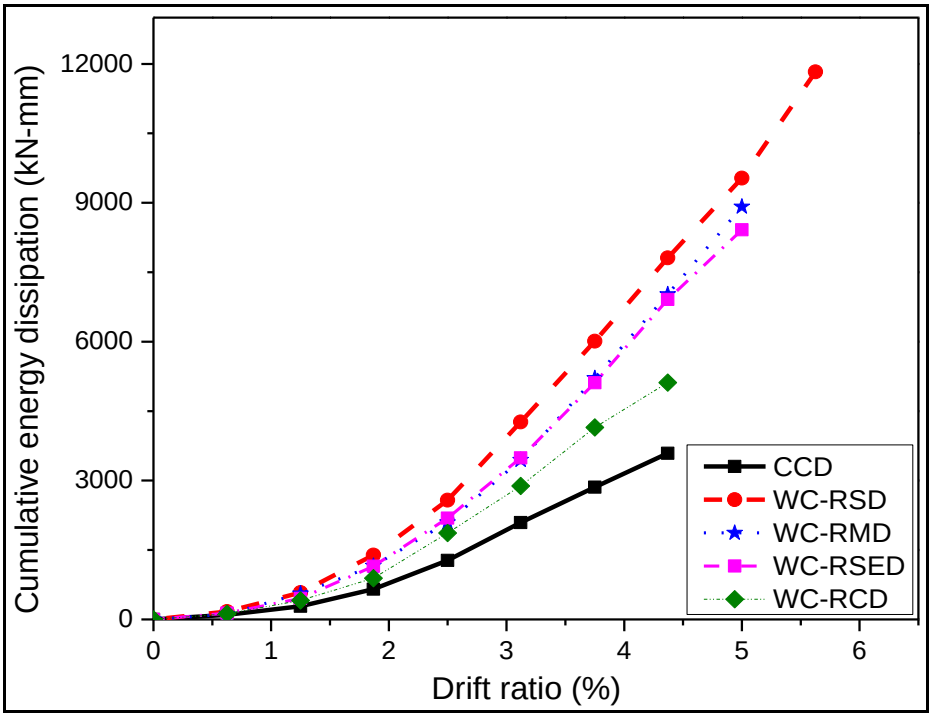

Fig. 6.30 - Cumulative Energy Dissipation versus Lateral Loading Cycle of Control and Retrofitted Specimen

Table 6.4 - Cumulative Energy Dissipation of Control and Retrofitted Specimen

Drift Ratio (%)	C-CD (kN-mm)	Drift Ratio (%)	WC-RCD (kN-mm)	Drift Ratio (%)	WC-RSED (kN-mm)	Drift Ratio (%)	WC-RMD (kN-mm)	Drift Ratio (%)	R-SD (kN-mm)
0	0	0	0	0	0	0	0	0	0
0.625	98.81	0.625	120.46	0.625	134.93	0.625	114.97	0.625	169.78
1.25	286.13	1.25	408.97	1.25	454.6	1.25	559.69	1.25	581.08
1.87	654.09	1.87	891.19	1.87	1150.06	1.87	1156.89	1.87	1388.86
2.5	1275.22	2.5	1867.97	2.5	2189.35	2.5	2094.81	2.5	2575.20
3.12	2091.05	3.12	2882.98	3.12	3490.56	3.12	3443.48	3.12	4264.20
3.75	2858	3.75	4148.93	3.75	5111.81	3.75	5211.06	3.75	6010.20
4.37	3588.28	4.37	5114.34	4.37	6910.93	4.37	7024.81	4.37	7811.60
--	--	--	--	5	8416.03	5	8914.08	5	9532.83
--	--	--	--	--	--	--	--	5.625	11827.67

It has been observed that the WC-RCD specimen exhibited a higher amount of per cycle energy dissipation compared with CCD at ultimate lateral displacement, i.e., 35 mm. At the initial lateral drift, i.e., 5 mm, the energy dissipated by the WC-RCD, WC-RMD, WC-RSED,

and WC-RSD is similar to the CCD, but the significant improvement in per cycle energy dissipation has been observed as the lateral displacement increased from 5 mm to 45 mm (see Fig. 6.29). The resistance offered by hybrid fiber at a micro and macro level, along with the confinement offered by wire mesh, increased energy dissipation at incremental lateral displacement.

Fig. 6.30 depicts the significant improvement in the cumulative energy dissipation of the retrofitted specimens. The WC-RCD exhibited 1.42 times higher cumulative energy dissipation than CCD and regained the lateral drift capacity, i.e., 4.375%. The WC-RMD, WC-RSED, and WC-RSD revealed the cumulative energy dissipation 2.48, 2.35, and 3.29 times higher than CCD, as shown in Table 6.4. The 14.28% and 28.57% improvement in lateral drift capacity of WC-RMD, WC-RSED, and WC-RSD respectively prolong the stability of initially damage and then retrofitted BCJ at higher drift. The improvement in cumulative energy dissipation and lateral drift property helps the structure to perform in a ductile manner and sustained the stresses at a higher drift ratio during an earthquake.

6.7 JOINT STRESSES

The equation 6.1 – 6.3 is used to calculate the joint shear stress and principal tensile stress.

$$\tau_{jh} = \frac{P}{A_{h\ core}}\left(\frac{L_b}{d_b} - \frac{L_b + 0.5\ D_c}{L_c}\right) \tag{6.1}$$

$$\sigma_t = \frac{\sigma_p}{2} + \sqrt{\frac{{\sigma_p}^2}{4} + {\tau_{jh}}^2} \tag{6.2}$$

Where $\sigma_p$is the axial compressive stress in the joint region and calculated using equation 6.3

$$\sigma_p = (N_c + P)/(b_c h_c) \tag{6.3}$$

Where the applied cyclic load (P) at the end of the beam is obtained from the experimental load displacement hysteresis curve (peak of each cycle). The length of the beam (L_b), the length of the column (L_c), the total depth of the beam (D_c) and the effective depth of the beam (d_b) are taken from the beam column joint geometrical dimension. The horizontal cross-sectional area (Ah core) of the joint core is calculated by using the cross-sectional area participating in resisting the horizontal shear force. Where τ_{jh}, σ_t,σ_p, and Nc is the joint horizontal shear stress, principle tensile stress, axial compressive stress, and axial compressive load applied using a hydraulic jack, respectively. The b_c and h_c is the width of

the column and depth of column in the considered direction of shear. The development of horizontal joint shear strength led to stimulating the principal tensile stress (σ_t) in a joint. The joint stress and principal tensile stress of all retrofitted specimen is compared with the control specimen as described in sections below;

6.7.1 Comparison between Control Specimen and Wire Mesh Confined Retrofitted Specimens

The horizontal joint stress of WC-RCD and CCD is calculated and presented graphically and in tabular form in Fig. 6.31, and Table 6.5. The joint shear stress capacity increased up to 1.25% positive drift; afterward, the shear stress capacity degraded rapidly till the ultimate lateral drift capacity i.e., 4.37%. While during negative drift, the joint shear stress of WC-RCD increased up to 2% lateral drift, after that, the shear stress capacity starts degraded till the failure. The maximum improvement in positive and negative drift is 2.49 and 1.69 times than CCD specimens.

The principal tensile stress of WC-RCD and CCD specimen is also calculated and shown in Fig. 6.32. The WC-RCD specimen sustained the stress at 1% and 3% positive and negative lateral drift; afterward, the resistance starts degrading. The maximum improvement in principal tensile capacity in the WC-RCD specimen during positive and negative drift is 1.57 and 1.44 times over CCD specimen. The presence of hybrid fiber with confined wire mesh increases the initial principal tensile stress carrying capacity, however, as the onset of the crack and led to the fracture of wire mesh resulted in rapid degradation of tensile stress carrying capacity.

The maximum improvement in the joint shear stress of the WC-RSED specimen is 3.52 and 1.89 times than CCD specimen. From Fig. 6.31, it can also be analysed that the joint shear strength resistance increased till the 1.87 and 2.5% lateral positive and negative drift respectively afterward, the steep drop in capacity is observed. Even during steep degradation in the joint stress capacity of the WC-RSED specimen still the specimen capable enough to achieve 14.28% higher lateral drift than CCD specimen.

Likewise, a similar increment in principal tensile stress in the WC-RSED specimen is observed over CCD specimen as shown in Fig. 6.32. The maximum improvement is observed until 1.87% and 2.5% lateral positive and negative drift respectively, and then a steep drop in capacity is observed. This behaviour attribute to the failure of the hybrid fiber-matrix bond as the lateral displacement increased. Also, the failure of wire mesh confinement decreases the resistance capacity drastically.

The joint shear stress of WC-RMD and CCD specimen is shown in Fig. 6.31, and Table 6.5. It has been observed that the WC-RMD exhibited the maximum improvement up to 3.12%, thereafter, the joint stress capacity is reduced. Likewise, WC-RSED, the lateral drift capacity of WC-RMD is increased by 14.28% than CCD specimen.

The R-MD specimen resists the principal tensile stresses up to 3.12% in both positive and negative drift; after that, the degradation in resistance capacity starts degrading as shown in Fig. 6.32. At the ultimate drift ratio (5%), the principal tensile resistance capacity is 3.33 MPa and 4.91 MPa under positive and negative displacement, respectively, which is 47.98% and 49.24% higher than CCD specimen resistance capacity.

The post elastic performance of WC-RMD specimen is significantly improved as compared to WC-RCD and WC-RSED specimens also. The improvement in post elastic performance reflects the effective utilization of the strong bond of fiber-matrix interaction and confinement offered by the wire mesh around the joint area.

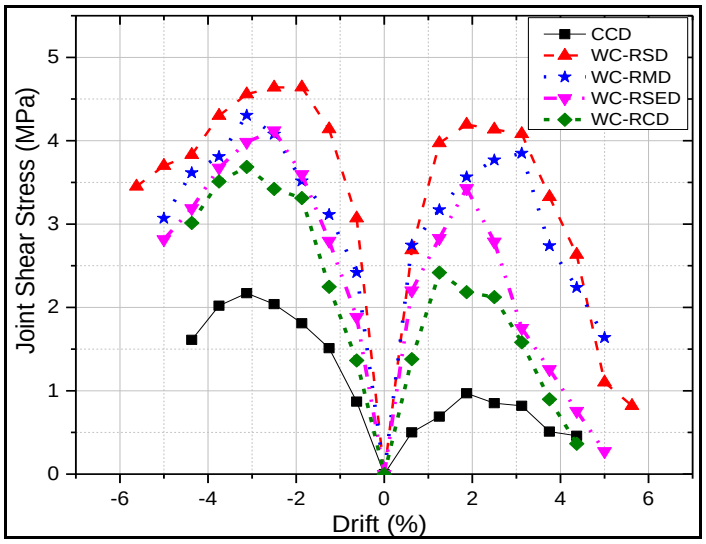

Fig. 6.31 - Joint Shear Stress versus Drift Ratio of Control and Retrofitted Specimen

The improvement in the joint shear stress carrying capacity of the WC-RSD specimen is observed up to 1.87% in both positive and negative lateral drift. Thereafter, the slower rate of degradation in capacity is observed up to 3% lateral drift; further, the ultimate collapse of the WC-RSD is observed at 5.67% lateral drift as shown in Fig. 6.31. The lower rate of degradation in between 1.87% - 3% reveled the effectiveness of wire mesh confined HP-FFRC in the initially slight damaged specimen. The principal tensile stress of WC-RSD specimen shows a similar trend like joint stress. The performance of WC-RSD specimen is improved up to 3%, and thereafter, the stress carrying capacity is decreased. The slope of degradation is also getting reduced as compare to C-CD specimen as shown in Fig. 6.32. The

lower degradation of principal tensile resistance capacity of WC-RSD specimen as compare to CCD specimen reflects the significant improvement in post elastic/post rotational capacity.

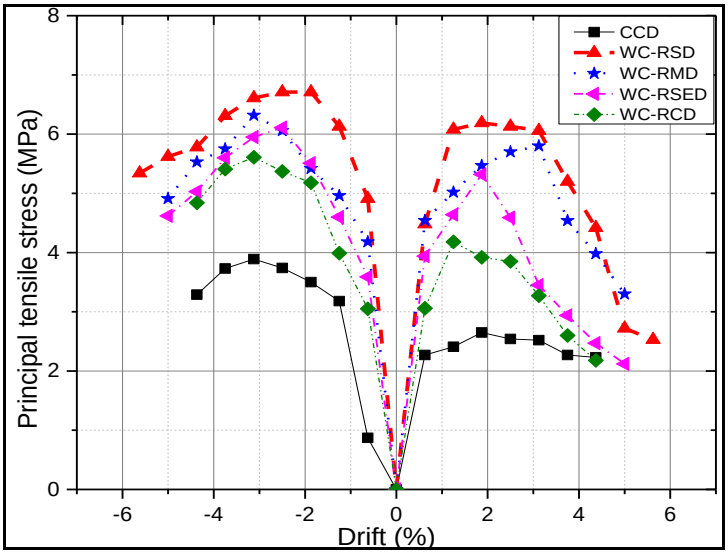

Fig. 6.32 - Principal Tensile Stress versus Drift Ratio of Control and Retrofitted Specimen

Table 6.5 - Joint Shear Stress versus Drift Ratio of Control and Retrofitted Specimen

CCD		WC-RSD		WC-RMD		WC-RSED		WC-RCD	
Drift (%)	Joint Shear Stress (MPa)	Drift (%)	Joint Shear Stress (MPa)	Drift (%)	Joint Shear Stress (MPa)	Drift (%)	Joint Shear Stress (MPa)	Drift (%)	Joint Shear Stress (MPa)
4.37	0.46	5.625	0.82	5	1.639	5	0.27368	4.37	0.365
3.75	0.51	5	1.101	4.37	2.239	4.37	0.75648	3.75	0.897
3.12	0.82	4.37	2.633	3.75	2.74	3.75	1.25707	3.12	1.581
2.5	0.85	3.75	3.326	3.12	3.85	3.12	1.75074	2.5	2.124
1.87	0.97	3.12	4.081	2.5	3.769	2.5	2.78781	1.87	2.183
1.25	0.69	2.5	4.137	1.87	3.566	1.87	3.4288	1.25	2.417
0.625	0.5	1.87	4.194	1.25	3.171	1.25	2.83117	0.625	1.38
0	0	1.25	3.972	0.625	2.748	0.625	2.20203	0	0
-0.625	0.87	0.625	2.688	0	0	0	0	-0.625	1.363
-1.25	1.51	0	0	-0.625	2.419	-0.625	1.88368	-1.25	2.247
-1.87	1.81	-0.625	3.07	-1.25	3.114	-1.25	2.79824	-1.87	3.312
-2.5	2.04	-1.25	4.14	-1.87	3.517	-1.87	3.59731	-2.5	3.422
-3.12	2.17	-1.87	4.641	-2.5	4.079	-2.5	4.12172	-3.12	3.686
-3.75	2.02	-2.5	4.64	-3.12	4.306	-3.12	3.98438	-3.75	3.511
-4.37	1.61	-3.12	4.559	-3.75	3.81	-3.75	3.67536	-4.37	3.013
--	--	-3.75	4.3	-4.37	3.616	-4.37	3.18839	--	--
--	--	-4.37	3.831	-5	3.07	-5	2.81701	--	--
--	--	-5	3.7	--	--	--	--	--	--
--	--	-5.625	3.452	--	--	--	--	--	--

Table 6.6 - Principal Tensile Stress versus Drift Ratio of Control and Retrofitted Specimen

CCD		WC-RSD		WC-RMD		WC-RSED		WC-RCD	
Drift (%)	Principal tensile stress (MPa)	Drift (%)	Principal tensile stress (MPa)	Drift (%)	Principal tensile stress (MPa)	Drift (%)	Principal tensile stress (MPa)	Drift (%)	Principal tensile stress (MPa)
4.37	2.23	5.625	2.53	5	3.3	5	2.12	4.37	2.179
3.75	2.27	5	2.72	4.37	3.98	4.37	2.47	3.75	2.6
3.12	2.52	4.37	4.42	3.75	4.54	3.75	2.94	3.12	3.27
2.5	2.54	3.75	5.2	3.12	5.8	3.12	3.45	2.5	3.85
1.87	2.65	3.12	6.06	2.5	5.7	2.5	4.59	1.87	3.92
1.25	2.41	2.5	6.13	1.87	5.47	1.87	5.32	1.25	4.18
0.625	2.27	1.87	6.19	1.25	5.02	1.25	4.64	0.625	3.06
0	0	1.25	6.08	0.625	4.54	0.625	3.94	0	0
-0.625	0.872	0.625	4.48	0	0	0	0	-0.625	3.05
-1.25	3.18	0	0	-0.625	4.18	-0.625	3.59	-1.25	3.99
-1.87	3.5	-0.625	4.91	-1.25	4.96	-1.25	4.6	-1.87	5.18
-2.5	3.74	-1.25	6.13	-1.87	5.42	-1.87	5.51	-2.5	5.37
-3.12	3.89	-1.87	6.71	-2.5	6.06	-2.5	6.11	-3.12	5.61
-3.75	3.73	-2.5	6.71	-3.12	6.32	-3.12	5.95	-3.75	5.41
-4.37	3.29	-3.12	6.61	-3.75	5.75	-3.75	5.6	-4.37	4.84
--	--	-3.75	6.31	-4.37	5.53	-4.37	5.03	--	--
--	--	-4.37	5.78	-5	4.91	-5	4.62	--	--
--	--	-5	5.62	--	--	--	--	--	--
--	--	-5.625	5.34	--	--	--	--	--	--

It has been observed that an increase in joint shear resistance of retrofitted specimen enables the specimen to resist the large shear forces which imposed on the structure during strong ground motion. The failure of the joint in shear resulted in brittle failure; however, in the present study, the failure shifted to the joint face and usage of hybrid fiber imparts the ductility consequently, improve the post peak performance. From Table 6.5, it can be concluded that the use of wire mesh confined HP-HFRC lifts the joint resistance to 4 times as compared with CCD. Fig. 6.32 shows the joint principal tensile stress of controlled (CCD) and retrofitted specimens (WC-RSD, WC-RMD, WC-RSED, and WC-RCD).

The retrofitted specimens exhibited a significant improvement in the resistance of principal tensile stresses in positive and negative drift. The WC-RSED resist the tensile stress up to 2% and 2.5% positive and negative drift whereas the specimens WC-RMD and WC-RSD enable

to resist the principal tensile stresses at 3% positive and negative drift. It has been concluded that as the initial damage level shift from complete to slight, not even the ability to resist the drift has been prolonging maximum up to 1.28 times but also the resistance of principal tensile stress has been improved in the range of 1.72- 2.39 times as compared to CCD specimen as shown in Table – 6.6.

The gain in resistance of principal tensile stresses because of confinement offered from the HP-HFRC and wire mesh. The delay in the opening of cracks at the micro and macro level due to the presence of hybrid fiber enhance the principal tensile resistance, further, the synergistic effect of wire mesh and hybrid fiber offers the confinement which significantly improves the resistance in positive and negative drift.

6.8 CRACK AND FAILURE ANALYSIS

The cracking pattern in the control and retrofitted beam column joint corresponding to the lateral drifts is also evaluated. It has been observed the cracking pattern of retrofitted specimens is significantly changed as compared to CCD specimens. The higher lateral drift led to spall the concrete from the compression face of CCD. The chunk of concrete separates from the compression face of the beam, followed by the yielding of the main reinforcement, as shown in Fig. 6.2 – 6.4. In addition, the number of cracks appears in the joint region of the controlled specimen. The premature failure of the compression face of the CCD specimen restricted the overall performance of the BCJ.

The failure in WC-RCD, WC-RSED, WC-RMD, and WC-RSD specimen observed at the face of the joint (see Fig. 6.33 – 6.45). The severe failure is observed at the face of the joint in the WC-RCD specimen. It has been observed that the crack path deviated from the interface of the joint towards the beam portion. In addition, no crack is propagated towards the joint area because of the increase in the principal tensile strength capacity of the joint by providing the wire mesh confined HP-HFRC. It has been observed from Fig. 6.34 that the cracks are not observed in the back face of the joint area also. The same observations are drawn from the testing of the second WC-RCD specimen at the collapse state (see Fig. 6.35 – 6.36).

The collapsed state of the WC-RSED specimen is shown in Fig. 6.37 – 6.42. It has been observed that the crack initially occurred in the joint interface and then propagates towards the other end, but, the joint area is free from the cracks. The hinge formation at the face of the joint is observed in the WC-RSED specimen and the maximum part of the whole energy of

the specimen is dissipated through this location. A slippage of fiber and large crack width is observed at the higher lateral drift, as shown in Fig. 6.38 & 6.40.

Likewise, WC-RSED, a similar kind of crack pattern, is observed in specimen WC-RMD as shown in Fig. 6.41 – 6.44. The slippage of hooked and crimped fiber is observed at the ultimate lateral drift, as shown in Fig. 6.42. Also, the wire mesh fracture is observed at the ultimate lateral drift. It has also been observed that even at the complete failure of specimen WC-RMD, the spalling of concrete is eliminated. The reason is the presence of hybrid steel fibers which control the spalling of concrete at the micro crack stage as well as the macro crack stage.

The crack pattern of specimen WC-RSD is shown in Fig. 6.45. It has been observed that the crack occurred at the interface of the joint and widened as the lateral drift increased. The maximum fraction of total energy is dissipated from this portion only.

It can be concluded that the wire mesh confined HP-HFRC imparts the higher principal tensile strength at the joint region however, the magnitude of resistance differs according to the initial damage level of the specimen. Nevertheless, the resistance is sufficient to shift the failure from the joint area of BCJ to the face of the joint. The formation of the plastic hinge in a beam rather than joint (weak beam/strong column mechanism) recognized a better way to enhance the performance of a reinforced concrete (RC) building during strong ground motion. The failure in the joint resulted in brittle shear failure, which affects the clause of limit state of collapse in a structure. Therefore, the formation of a plastic hinge in the beam is the required criteria during an earthquake to avoid the global failure of the RC structures.

At higher lateral drift, the slippage of micro and macro fibers has been observed (see Fig. 6.38, 6.40 and 6.42). The larger crack width is the result of the effective role of macro fiber (Hooked geometry) in a higher rate of stiffness retention, a lower rate of strength degradation, and dissipates the energy in the post elastic region at higher drift.

In addition, the confined wire mesh also improves the post elastic performance of BCJ. However, the higher rate of strength degradation has been observed afterward the fracture of confined wire mesh. The fracture in confined wire mesh is observed at higher drift in the retrofitted specimens (see Fig 6.42).

Fig. 6.33 - Crack Pattern of Wire Mesh Confined HP-HFRC Retrofitted Control Complete Damage (WC-RCD) Specimen I

Fig. 6.34 - Crack Extended on the Back Side of the Wire Mesh Confined HP-HFRC Retrofitted Control Complete Damage (WC-RCD) Specimen I

Fig. 6.35 - Crack Pattern of Wire Mesh Confined HP-HFRC Retrofitted Control Damage (WC-RCD) Specimen II

Fig. 6.36 - Back View of the Crack Pattern of Wire Mesh Confined HP-HFRC Retrofitted Control Damage (WC-RCD) Specimen II

Fig. 6.37 - Crack Pattern of Wire Mesh Confined HP-HFRC Retrofitted Severe Damage (WC-RSED) Specimen I

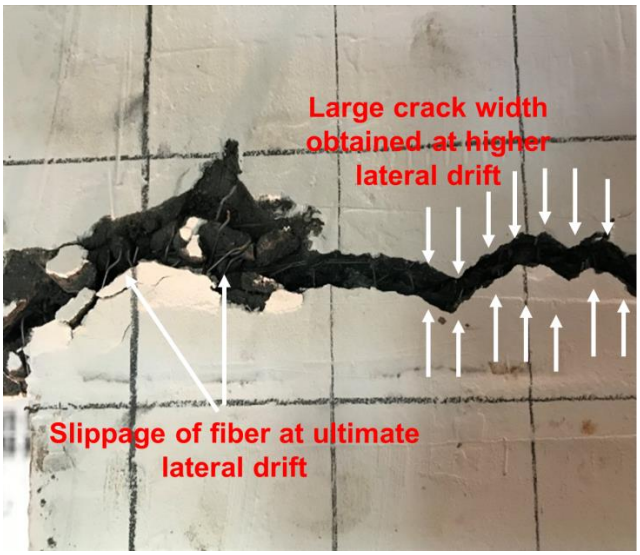

Fig. 6.38 - Close View of Fiber Slippage during Propagation of Cracking at Higher Drift in Wire Mesh Confined HP-HFRC Retrofitted Severe Damage (WC-RSED) Specimen I

Fig. 6.39 - Crack Pattern of Wire Mesh Confined HP-HFRC Retrofitted Severe Damage (WC-RSED) Specimen II

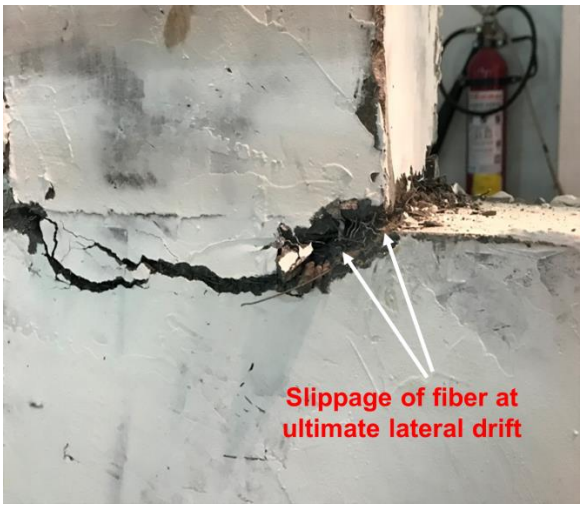

Fig. 6.40 - Absence of Spalling of Concrete and Slippage of Fiber at Ultimate Drift in Wire Mesh Confined HP-HFRC Retrofitted Severe Damage (WC-RCD) Specimen II

Fig. 6.41 - Crack Pattern of Wire Mesh Confined HP-HFRC Retrofitted Moderate Damage (WC-MD) Specimen I

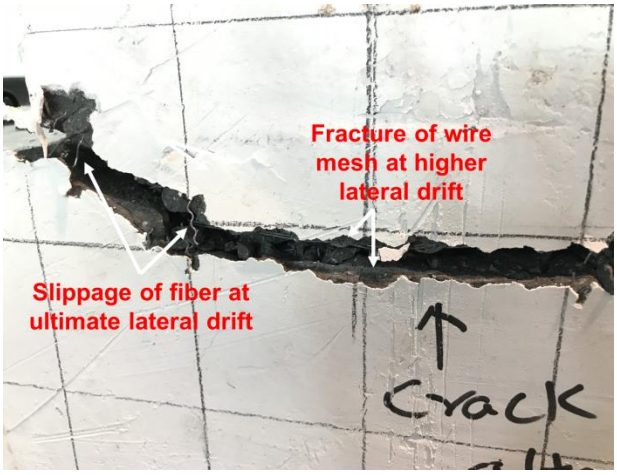

Fig. 6.42 - Slippage of Fiber and Fracture of Wire Mesh at Higher Drift in Wire Mesh Confined HP-HFRC Retrofitted Moderate Damage (WC-MD) Specimen I

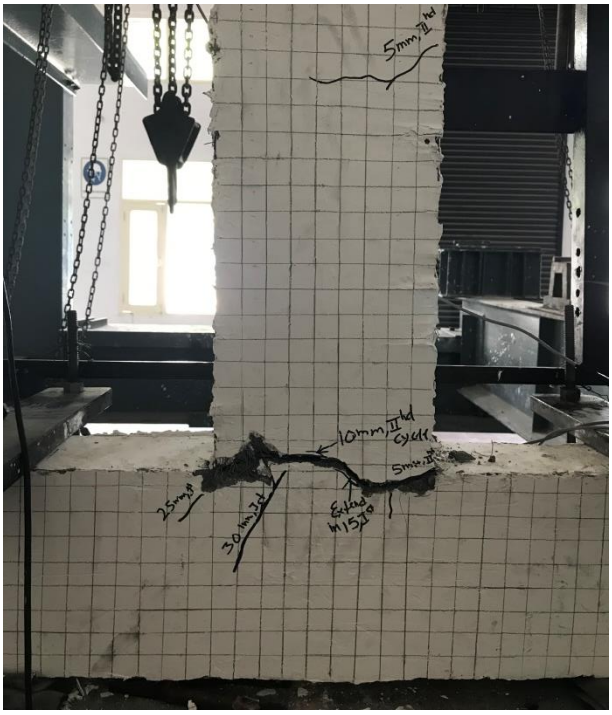

Fig. 6.43 - Crack Pattern of Wire Mesh Confined HP-HFRC Retrofitted Moderate Damage (WC-MD) Specimen II

Fig. 6.44 - Large Crack Width at the Joint Face in Wire Mesh Confined HP-HFRC Retrofitted Moderate Damage (WC-MD) Specimen II

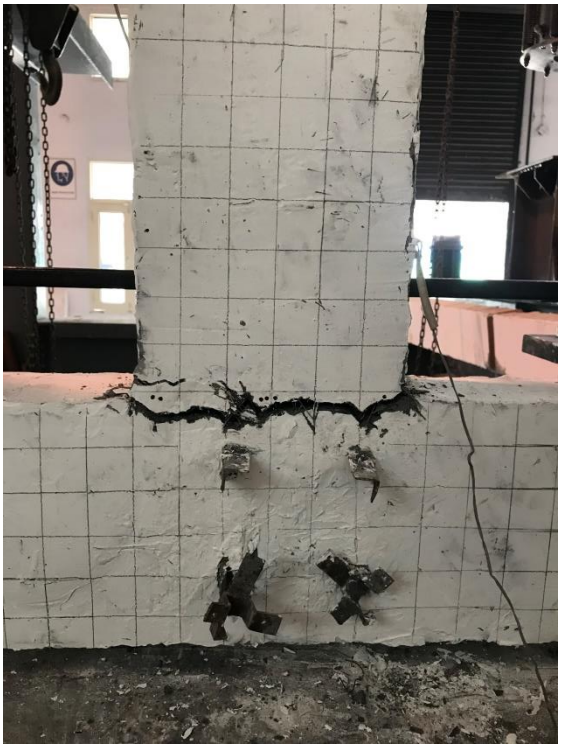

Fig. 6.45 - Crack Pattern of Wire Mesh Confined HP-HFRC Retrofitted Slight Damage (WC-RSD) Specimen I

6.9 PERFORMANCE COMPARISON IN HP-HFRC AND WIRE MESH CONFINED HP-HFRC RETROFITTED INITIAL DAMAGED BEAM COLUMN JOINT

The comparison in seismic performance of HP-HFRC retrofitted initial damaged BCJ and wire mesh confined HP-HFRC retrofitted initially damaged BCJ has been done in terms of peak load capacity, displacement ductility, ultimate lateral drift capacity, strength degradation and, cumulative energy dissipation.

6.9.1 Peak Load Capacity and Displacement Ductility

The peak load capacity and ductility of the retrofitted specimen is a major factor to analyse the improvement. Therefore, the improvement in peak load and displacement ductility is analysed based on the obtained results. The comparison in peak load capacity and displacement ductility of control specimen, HP-HFRC confined, and wire mesh confined HP-HFRC retrofitted specimen. It has been observed that the peak load capacity and displacement ductility of the retrofitted specimen significantly depends upon the following;

- Type of retrofitting strategy and;
- Level of Initial Damage

The effects of both the parameters are discussed below;

The peak load capacity and ductility of control complete damage (C-CD), HP-HFRC (R-CD), and wire mesh confined HP-HFRC retrofitted (WC-RCD) initial complete damage specimen has been examined from the obtained load hysteresis behaviour. The performance of all the specimens is shown in Fig. 6.46. It has been seen that the peak load carrying capacity is increased with the HP-HFRC retrofitting, further improvement in peak load capacity has been observed when the initially complete damage specimen retrofitted using wire mesh confined HP-HFRC i.e., WC-RCD. It has been observed that the maximum improvement in peak load carrying capacity is 1.87 times than the control specimen in the WC-RCD specimen. The effect of retrofitting on the ductility of control completely damaged and initially damaged than retrofitted specimens are also evaluated. It has been observed that the specimen retrofitted using HP-HFRC exhibited the improvement in ductility whereas, the specimen retrofitted using wire mesh confined HP-HFRC shows a moderate improvement in ductility as compared to control specimen but lower than R-CD. It might be due to the following mechanism; fracture of wire mesh imposes the stresses on the initially distress concrete core and 80% of the peak load falls rapidly in the successive lateral cycles. At this moment, the micro and macro fibers are already slipped out from the matrix, and large width cracks have been observed.

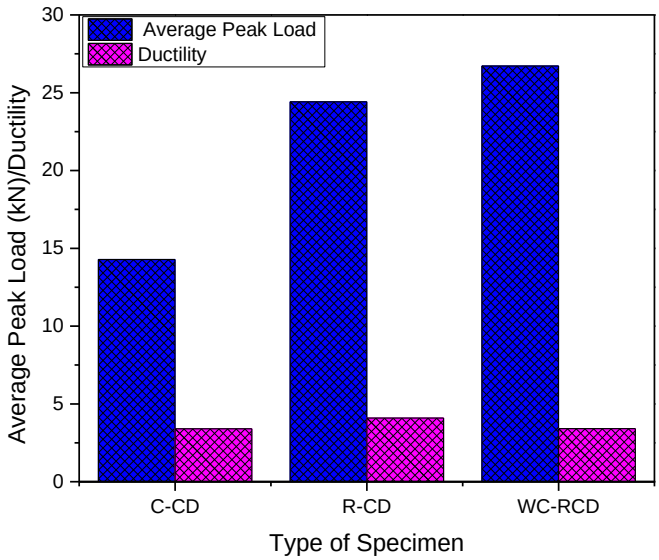

Fig. 6.46 - Comparison in Peak Load and Displacement Ductility of C-CD, HP-HFRC and Wire Mesh Confined HP-HFRC Retrofitted Initial Complete Damage Specimen

The peak load capacity and ductility of control complete damage (C-CD), HP-HFRC (R-SED) and wire mesh confined HP-HFRC retrofitted (WC-RCD) initial severe damage specimen has been calculated and shown in Fig. 6.47. It has been seen that the peak load

carrying capacity of HP-HFRC retrofitted initial severe damaged specimen increased 1.66 times than CCD. Further, when the specimen retrofitted using wire mesh confined HP-HFRC the average peak load carrying capacity is increased up to 2.40 times than the control specimen. Also, the peak load carrying capacity improvement of WC-RSED is improved 1.44 times than the R-SED specimen. Therefore, It can be concluded that the shifting of retrofitting strategy from HP-HFRC to wire mesh confined HP-HFRC 66% improvement in average peak load carrying capacity has been observed.

The effect of retrofitting on the ductility of control completely damaged and initially damaged than retrofitted specimens (R-SED and WC-RSED) are also evaluated. It has been observed that the specimen retrofitted using confined HP-HFRC exhibited the improvement in ductility whereas, the specimen retrofitted using wire mesh confined HP-HFRC shows a moderate improvement in ductility as compared to control specimen but lower than R-CD. It might be due to a similar mechanism as explained for the WC-RCD specimen in the previous section. The initially distress concrete core degrades the strength rapidly once the wire mesh fraction has begun.

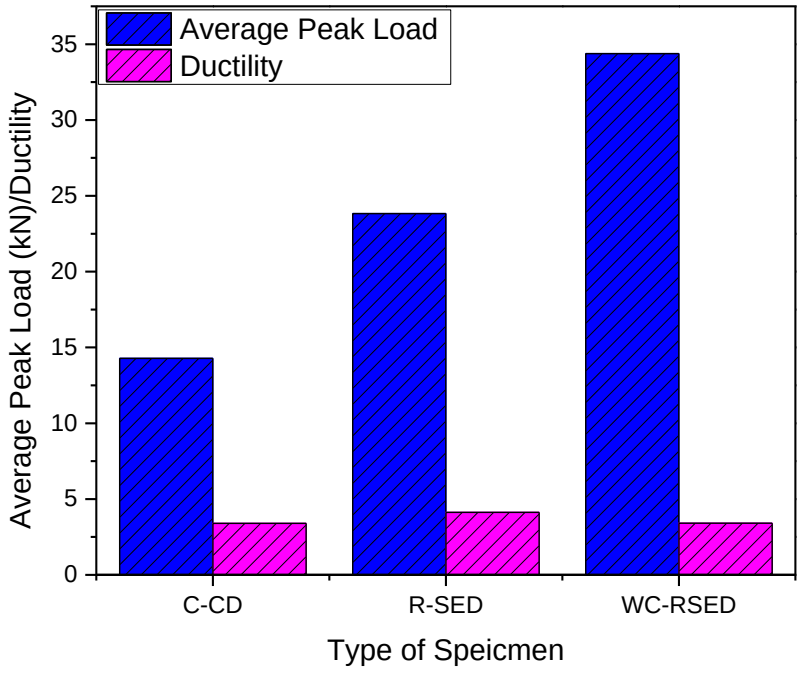

Fig. 6.47 - Comparison in Peak Load and Displacement Ductility of C-CD, HP-HFRC and Wire Mesh Confined HP-HFRC Retrofitted Initial Severe Damage Specimen

The comparison between peak load capacity and ductility of control complete damage (C-CD), HP-HFRC (R-MD) and, wire mesh confined HP-HFRC retrofitted (WC-RMD) initial

Moderate damaged specimen is shown in Fig. 6.48. It has been seen that the peak load carrying capacity of HP-HFRC retrofitting initial severe damaged specimen increased 1.84 times than C-CD. Further, when the specimen retrofitted using wire mesh confined HP-HFRC, the average peak load carrying capacity is increased up to 2.60 times than the control specimen. Also, the peak load carrying capacity improvement of WC-RSED is improved 1.41 times than the R-SED specimen. Therefore, it can be concluded that the shifting of retrofitting strategy from HP-HFRC to wire mesh confined HP-HFRC improved the average peak load carrying capacity.

The effect of retrofitting on the ductility of control completely damaged and initially damaged than retrofitted specimens (R-MD and WC-RMD) are also evaluated. It has been observed that the specimen retrofitted using HP-HFRC exhibited the improvement in ductility; further, the specimen retrofitted using wire mesh confined HP-HFRC shows a significant improvement in ductility as compared to control specimen. The maximum improvement in ductility is observed in WC-RMD specimen, i.e., 1.50 times than C-CD. It might be due to the synergistic effect of wire mesh confined HP-HFRC at the moderate initial damaged state. The initially distress concrete core sufficient to bear stress transferred during wire mesh fracture incident and degradation in post peak load has not been observed rapidly.

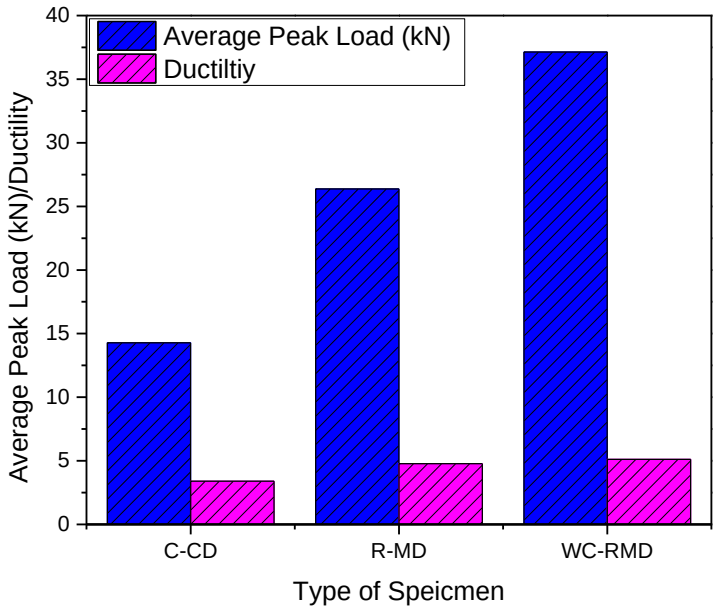

Fig. 6.48 - Comparison in Peak Load and Displacement Ductility of C-CD, HP-HFRC and Wire Mesh Confined HP-HFRC Retrofitted Initial Moderate Damage Specimen

The peak load capacity and ductility of control complete damage (C-CD), HP-HFRC (R-SD) and, wire mesh confined HP-HFRC retrofitted (WC-RSD) initial severe damage specimen

has been calculated and shown in Fig. 6.49. It has been seen that the peak load carrying capacity of HP-HFRC confined retrofitting initial severe damaged specimen increased 1.97 times than C-CD. Further, when the specimen retrofitted using wire mesh confined HP-HFRC, the average peak load carrying capacity is increased up to 2.81 times than the control specimen. Therefore, It can be concluded that the shifting of retrofitting strategy from confined HP-HFRC to wire mesh confined HP-HFRC improved the average peak load carrying capacity.

The effect of retrofitting on the ductility of control completely damaged and initially damaged than retrofitted specimens (R-SD and WC-RSD) are also evaluated. It has been observed that the specimen retrofitted using confined HP-HFRC exhibited the improvement in ductility whereas, the specimen retrofitted using wire mesh confined HP-HFRC shows a significant improvement in ductility as compared to control specimen and HP-HFRC retrofitted specimen.

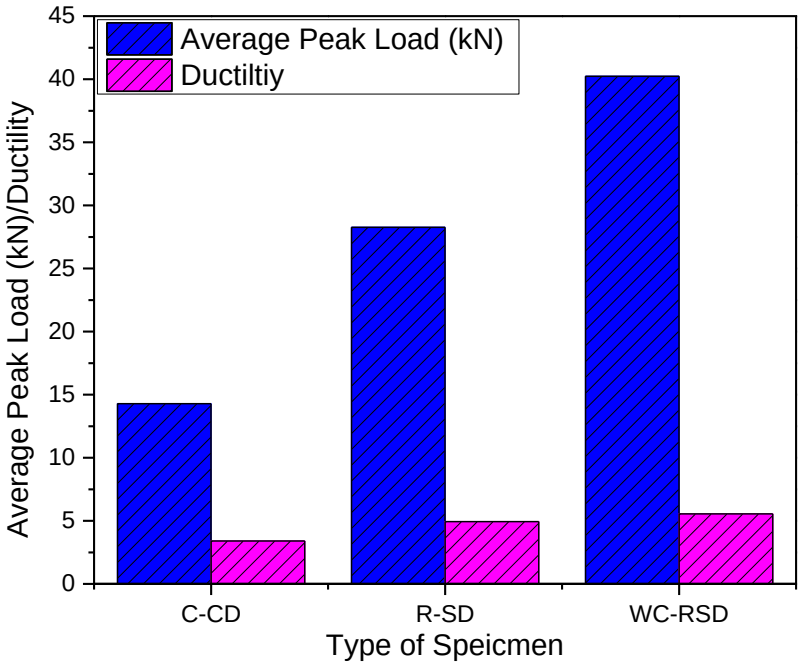

Fig. 6.49 - Comparison in Peak Load and Displacement Ductility of C-CD, HP-HFRC and Wire Mesh Confined HP-HFRC Retrofitted Initial Slight Damage Specimen

It has been observed that the displacement ductility is significantly improved as the damage level shifts from complete to slight. It can be observed from Fig. 6.50 that the maximum improvement is observed in WC-RSD specimen i.e. 63.23% over the C-CD specimen. Moreover, the ductility of WC-RCD and WC-RSED is lesser than the R-CD and R-SED

specimen because the presence of wire mesh confined HP-HFRC significantly improved the peak load carrying capacity but the lateral load carrying capacity degraded more than 80% of its peak load rapidly once, the fracture of wire mesh is taken place. But, as the initial damage level shift from sever to slight the wire mesh confined HP-HFRC retrofitted specimen exhibited the higher ductility than the specimen retrofitted only using HP-HFRC.

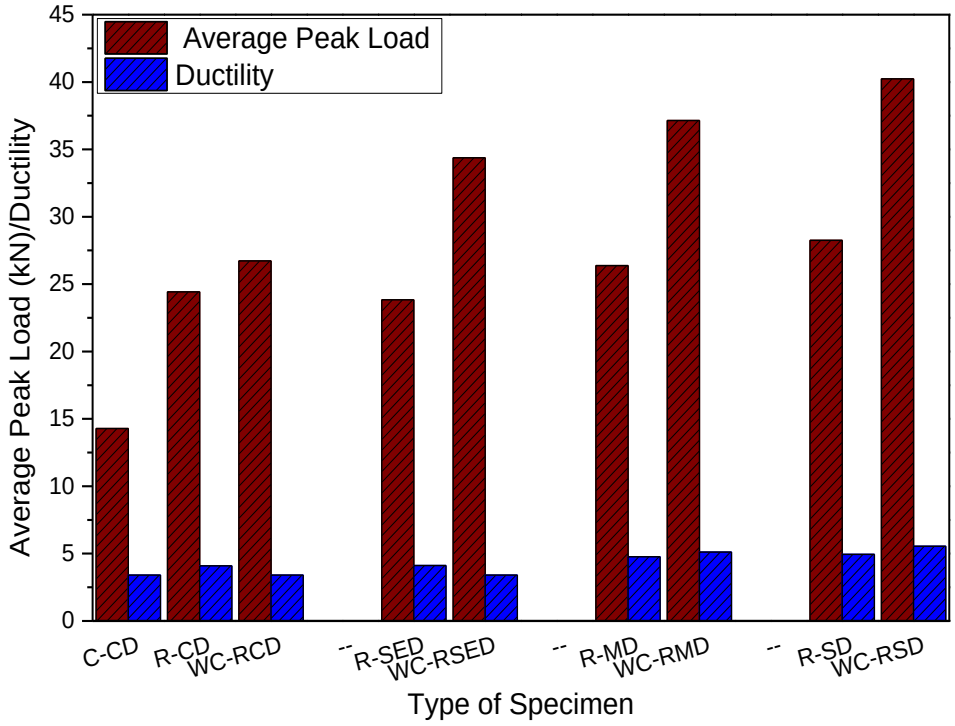

Fig. 6.50 - Comparison of Average Peak Load and Displacement Ductility of control and Retrofitted Specimens

6.9.2 Ultimate Drift Capacity (UDC)

The effect of retrofitting strategy on the ultimate drift capacity of initially damaged retrofitted beam column joint specimens is compared. The performance in terms of ultimate drift capacity between the HP-HFRC and wire mesh confined HP-HFRC retrofitting strategy for each damage level is compared and detailed discussion has been done in subsequent sections;

The UDC of control complete damage, HP-HFRC retrofitted initially complete damage (R-CD) and wire mesh confined HP-HFRC retrofitted initially complete damage (WC-RCD) specimen has been prepared and shown in Fig. 6.51. It has been observed that the control specimen collapsed at 4.37% ultimate lateral drift, whereas the specimen R-CD failed at 3.12%. After the retrofitting using HP-HFRC, the initially complete damaged specimen has not been able to regain the original drift capacity. The HP-HFRC overly improved the peak

load carrying capacity of R-CD specimen, but once the severe failure occurs in overlay, the core controlled concrete and reinforcement could not be able to sustain the higher stresses which are transferred by the retrofitted material to the core concrete. Therefore, the specimens failed early than the C-CD specimen.

The complete initially damaged and then wire mesh confined retrofitted specimen (WC-RCD) regain the original lateral drift capacity i.e., 4.37%. It has been observed that the additional confinement offered by wire mesh enables the specimen to rotate in non-linear state at higher lateral drift. This property helps the specimen to dissipate the energy for long-duration earthquakes.

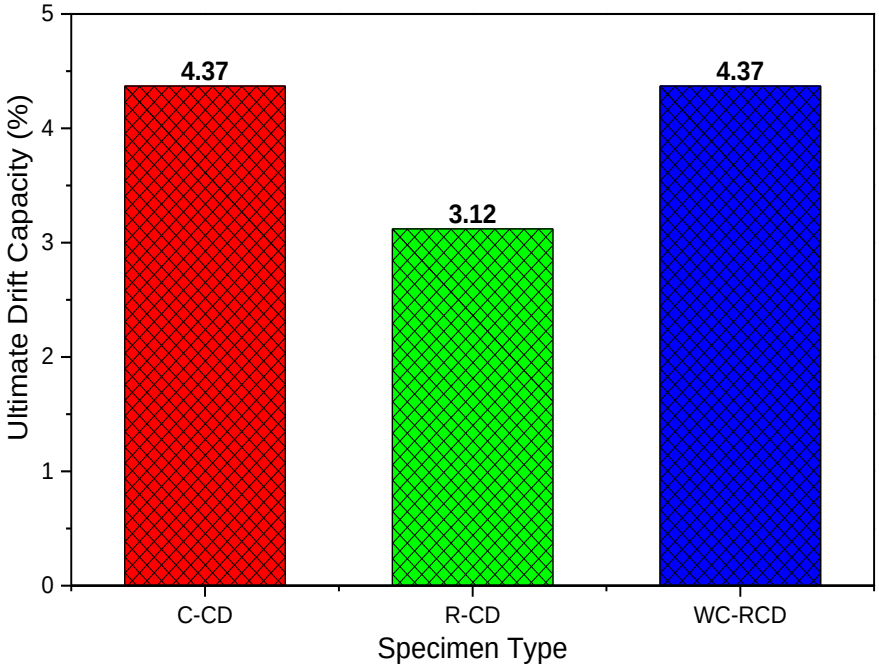

Fig. 6.51 - Comparison in UDC of C-CD, HP-HFRC and Wire Mesh Confined HP-HFRC Retrofitted Initial Complete Damage Specimen

The UDC of control complete damage, HP-HFRC retrofitted initially severe damage (R-SED) and wire mesh confined HP-HFRC retrofitted initially severe damage specimen (WC-RSED) has been prepared and shown in Fig. 6.52. It has been observed that the control specimen collapsed at 4.37% ultimate lateral drift, and the specimen R-CD regain the original lateral drift capacity. The initially severe damaged specimen has been able to regain the original drift capacity after the retrofitting using HP-HFRC. It has been observed that the fiber present in the mix effectively bridges the crack even at the higher drift. The onset of failure in HP-HFRC overlay transfer the stresses to the initial severe damage core controlled

concrete, along with partially yielded reinforcement. The extent of damage in controlled concrete significantly affects the stress carrying capacity of specimen once the retrofitted material fails; as in the present case, the HP-HFRC retrofitted specimen (R-SED) regain the original lateral drift capacity.

Further, the effect of confinement using wire mesh confined HP-HFRC retrofitting on initially sever damage specimen (WC-RSED) is evaluated. The ultimate drift capacity of the WC-RSED specimen is 5%, which is 0.63 times more than the C-CD and R-CD specimen. The additional confinement effectively increases the ultimate lateral drift capacity of the specimen.

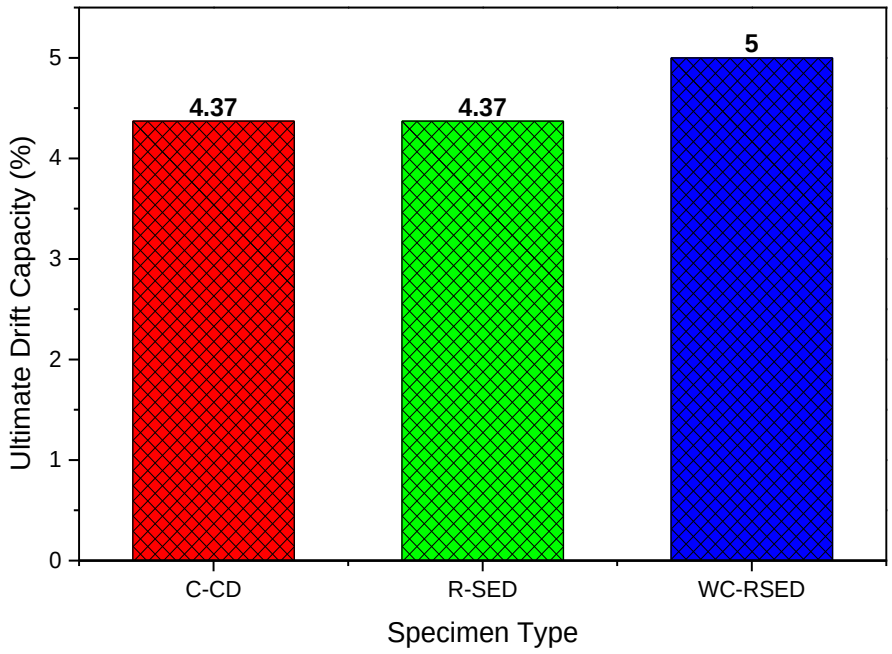

Fig. 6.52 - Comparison in UDC of C-CD, HP-HFRC and Wire Mesh Confined HP-HFRC Retrofitted Initial Severe Damaged Specimen

The UDC of control complete damage, HP-HFRC retrofitted initially moderate damaged (R-CD), and wire mesh confined HP-HFRC initially moderately damaged specimen (WC-RMD) has been prepared and shown in Fig. 6.53. It has been observed that the control specimen collapsed at 4.37% ultimate lateral drift and the specimen R-CD and WC-RCD not only regain the original lateral drift capacity but also attained 0.63 times higher ultimate drift as compare to C-CD specimen. The initially severe damaged specimen and then retrofitted using HP-HFRC and wire mesh confined HP-HFRC strategy enable the distress element to perform under higher drift capacity as compare to the C-CD specimen.

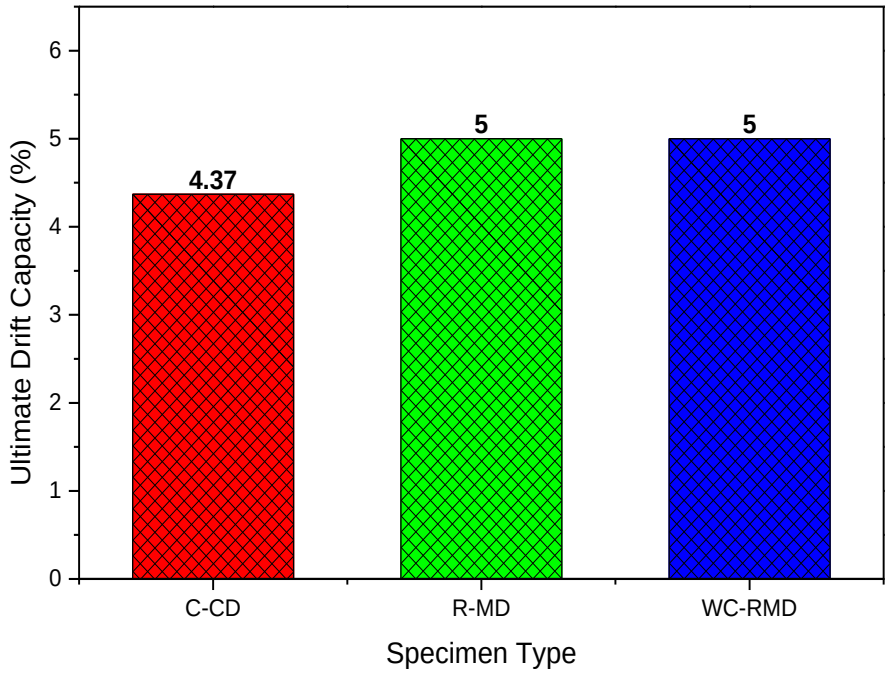

Fig. 6.53 - Comparison in UDC of C-CD, HP-HFRC, and Wire Mesh Confined Retrofitted Initial Moderate Damage Specimen

The UDC of control complete damage, HP-HFRC retrofitted initially slightly damaged (R-SD), and wire mesh confined HP-HFRC retrofitted initially slightly damaged specimen (WC-RSD) has been prepared and shown in Fig. 6.54. It has been observed that the control specimen (C-CD) collapsed at 4.37% ultimate lateral drift and the specimen R-SD perform 0.63 times better than the C-CD specimen. The maximum efficiency of the HP-HFRC retrofitted initially damaged beam column joint is improved up to 5% lateral drift capacity. The higher mechanical property, presence of hybrid fibers, and densest microstructure of HP-HFRC enable the matrix to make an efficient bond with the old concrete and main reinforcement; consequently, initial slight damage specimen sustained higher drift after retrofitting.

Further, the improvement in drift capacity has been observed in wire mesh confined HP-HFRC retrofitted initially slight damage specimen (WC-RSD). The WC-RSD specimen has been able to sustain at 5.675% lateral drift ratio, which is the maximum improvement among all retrofitted specimens. The synergistic effect of wire mesh and HP-HFRC confinement significantly increases the ultimate lateral deformation capacity of the retrofitted initial slightly damaged specimen.

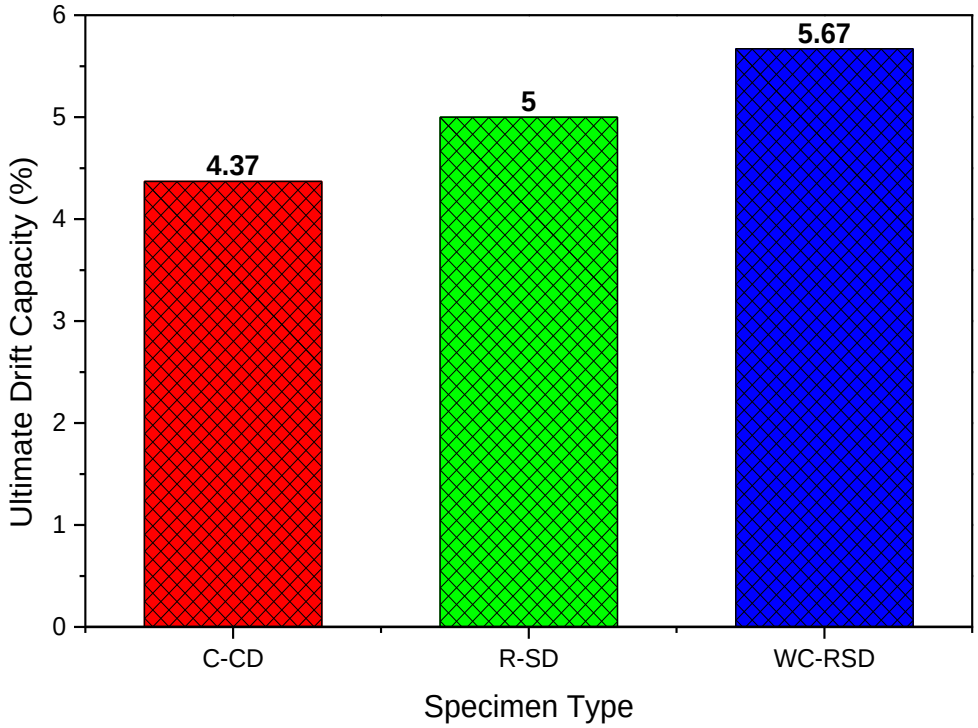

Fig. 6.54 - Comparison in UDC of C-CD, HP-HFRC and Wire Mesh Confined HP-HFRC Retrofitted Initial Slight Damage Specimen

From Fig. 6.55, it can be concluded that the specimen C-CD completely collapsed at 4.37% lateral drift. The specimen R-CD completely collapses at 3.12% ultimate drift, which is lesser than the C-CD specimen. The specimen retrofitted using wire mesh confined HP-HFRC i.e., WC-RCD regain the lateral drift capacity, i.e., 4.37 %, which is equivalent to C-CD specimen. This is observed only because of the effect of confinement offered by the wire mesh confined HP-HFRC.

Further, the specimen R-SED and WC-RSED are compared and found that the WC-RSED specimen collapse at 5% lateral drift whereas, the specimen R-SED collapses at 4.37% which is equivalent to the C-CD specimen. The maximum improvement in drift capacity is observed in the WC-RSD specimen, which is 1.29 times more than the C-CD specimen.

Therefore, it can be concluded that the initial damage level of the specimen significantly affects the overall performance of the retrofitted specimen. Also, the type of retrofitting strategy very much based on the extent of initial damage or up to what extent the practitioner wants to improve the performance of initially damaged specimens.

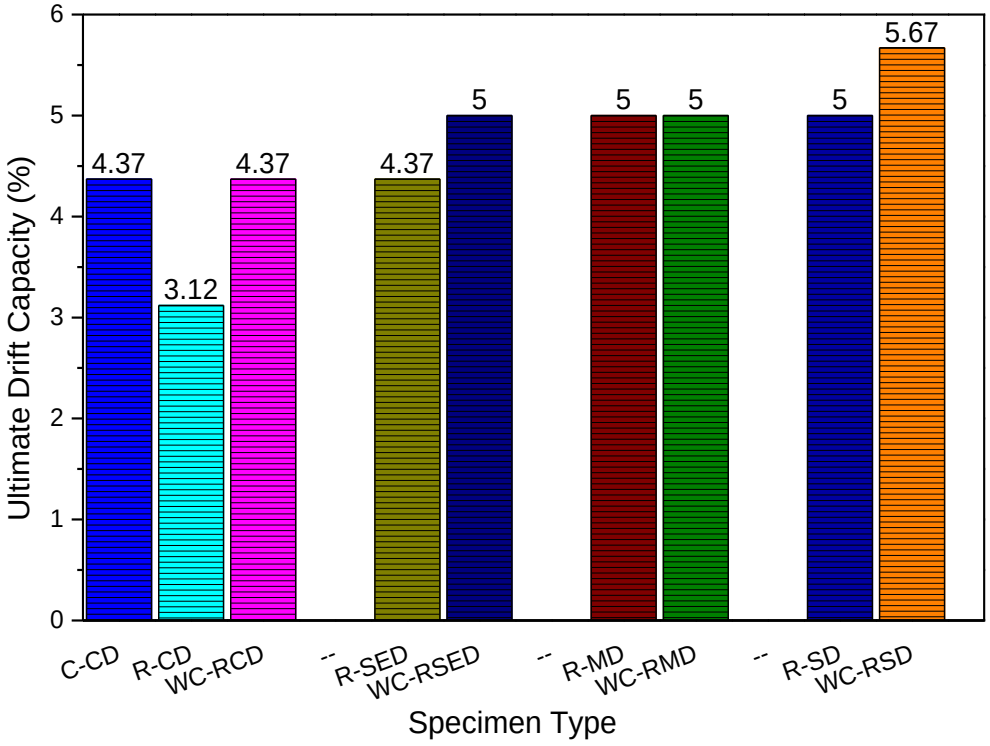

Fig. 6.55 - Comparison in UDC of C-CD, HP-HFRC and Wire Mesh Confined HP-HFRC Retrofitted Initially Damage Specimens

6.9.3 Strength Degradation

The effect of retrofitting strategy on the strength degradation of initially damaged retrofitted beam column joint specimens is compared with the control specimen. The performance in terms of strength degradation between the HP-HFRC and wire mesh confined HP-HFRC retrofitting strategy for each damage level is compared, and detailed discussions have been done in sections provided below;

The strength degradation of control complete damage (C-CD), HP-HFRC initially retrofitted complete damage (R-CD), and wire mesh confined HP-HFRC initially complete damage specimen (WC-RCD) is shown in Fig. 6.56. It has been seen that the performance of retrofitted specimens either HP-HFRC or wire mesh confined HP-HFRC, both have been improved. However, degradation in retrofitted specimens starts early than C-CD. Also, the rate of strength degradation is higher than the controlled specimen. The specimen R-CD exhibited the fast rate of strength degradation in positive and negative drift followed by the wire mesh confined HP-HFRC retrofitted specimen. The reduction in the rate of strength degradation has been found in the WC-RCD specimen. The failure in wire mesh confined

retrofitted specimen has been done by following two stages; firstly, the failure of HP-HFRC overlay and, secondly the crack propagates from overlay to wire mesh and failure of wire mesh resulted in a large amount of strength degradation around the damaged area of beam column joint.

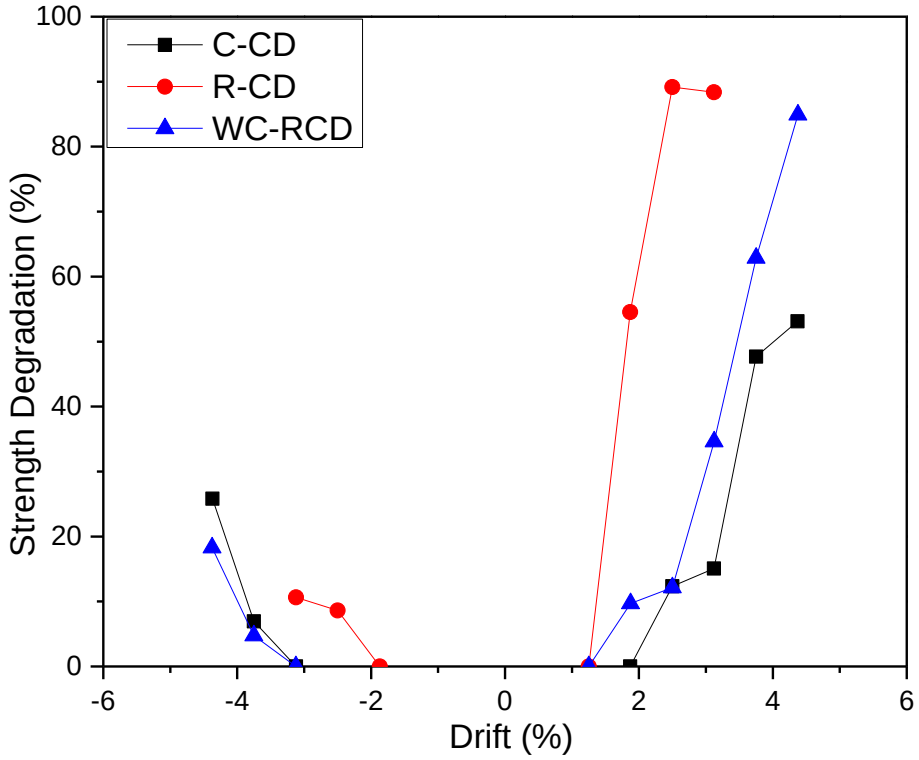

Fig. 6.56 - Comparison in Strength Degradation of C-CD, HP-HFRC and Wire Mesh Confined HP-HFRC Retrofitted Initial Complete Damage Specimen

The comparison in strength degradation of control complete damage (C-CD), HP-HFRC retrofitted initially severe damage (R-CD), and wire mesh confined HP-HFRC retrofitted initially severe damage specimen (WC-RSED) has been done and shown in Fig. 6.57. It has been observed that the onset of damage has been observed at 2.5%, 1.87%, and 2.5% positive drift in C-CD, R-SED, and WC-RSED specimens.

It has been observed that as the confinement shifts from HP-HFRC to wire mesh confined HP-HFRC, the onset of damage level shifts from 1.875 to 2.5%. Also, it has been observed that the significant slope reduction has been during the negative drift. The WC-RSED specimen exhibited lower strength degradation during negative drift and higher overall drift capacity.

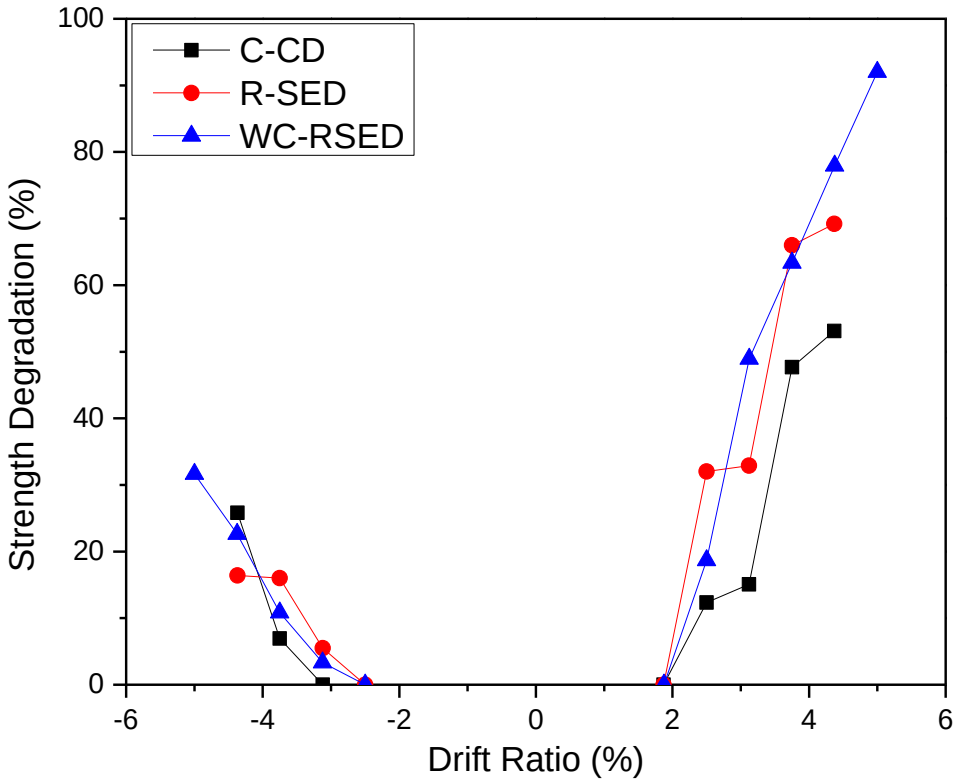

Fig. 6.57 - Comparison in Strength Degradation of C-CD, HP-HFRC and Wire Mesh Confined HP-HFRC Retrofitted Initial Severe Damage Specimen

The strength degradation of control complete damage (C-CD), HP-HFRC retrofitted initially moderate damage (R-MD), and wire mesh confined HP-HFRC retrofitted initially moderate damage specimen (WC-RMD) is shown in Fig. 6.58. It has been seen that the performance of retrofitted specimens either HP-HFRC or wire mesh confined HP-HFRC, is improved than the control specimen. However, the significant change in the onset of reduction of strength has been observed in confined HP-HFRC and wire mesh confined HP-HFRC retrofitted initially moderately damaged specimen. The reduction starts early in R-MD as compared to the WC-RMD specimen. It has been observed that the onset of reduction during positive drift has been observed at 2.5%, 1.87%, and 3.125% in C-CD, R-MD, and WC-RMD, respectively.

The significant difference also has been observed in the increment in ultimate lateral drift, which indicates that the retrofitting strategies are capable enough to perform at a higher drift ratio even if already damaged. Also, the lower rate of strength degradation is observed as the drift ratio increase which is not observed in C-CD specimen

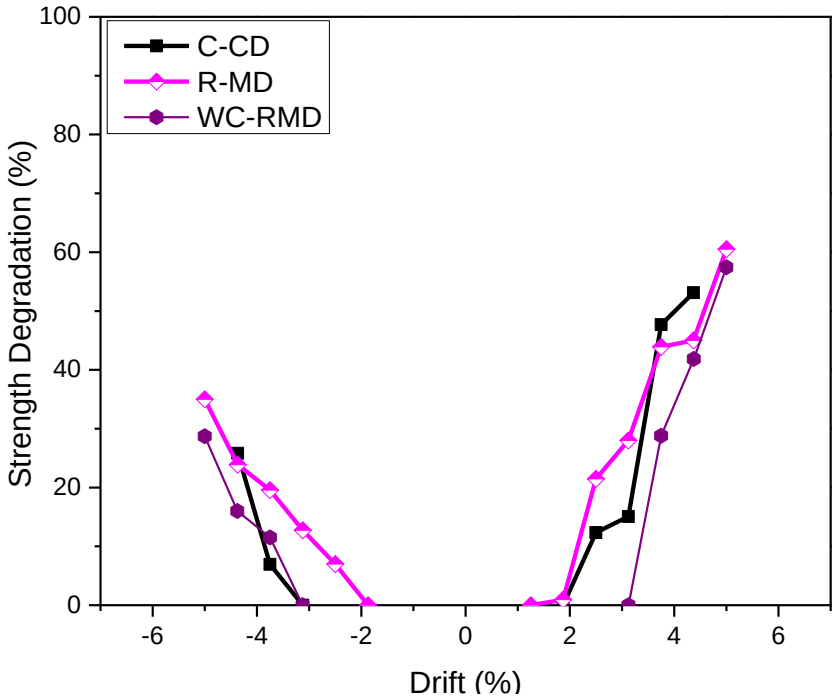

Fig. 6.58 - Comparison in Strength Degradation of C-CD, HP-HFRC and Wire Mesh Confined Retrofitted Initial Moderate Damage Specimen

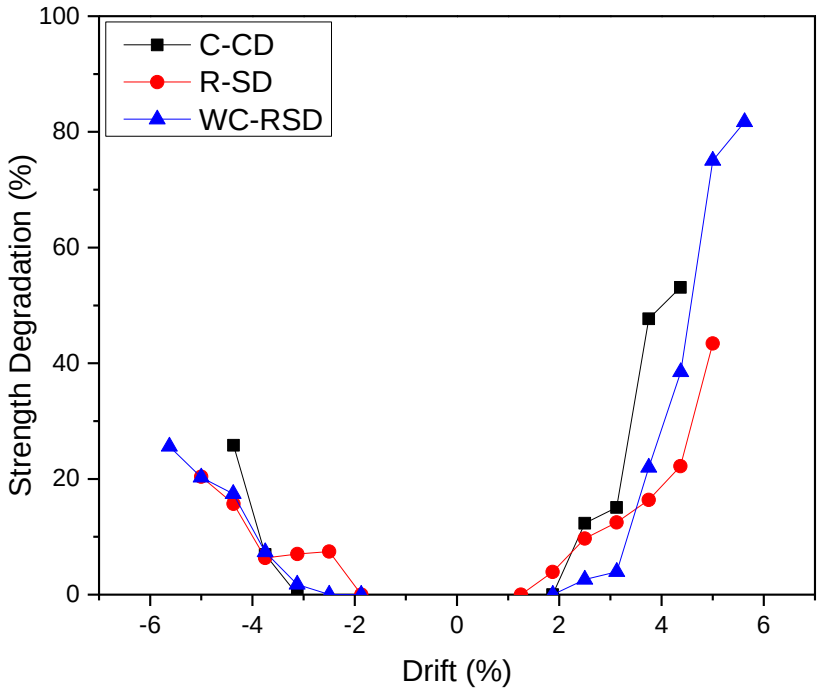

Fig. 6.59 - Comparison in Strength Degradation of C-CD, HP-HFRC and Wire Mesh Confined HP-HFRC Retrofitted Initial Slight Damage Specimen

The comparison in strength degradation of control complete damage (C-CD), HP-HFRC retrofitted initially slight damage (R-SD), and wire mesh confined HP-HFRC retrofitted

initially slight damage specimen (WC-RSD) has been done and shown in Fig. 6.59. The lower rate of strength degradation in the retrofitted specimen is observed as compared to C-CD. The efficacy of retrofitting is more pronounced when the retrofitting strategy shifted from HP-HFRC to wire mesh confined HP-HFRC. The confinement offered by the HP-HFRC and wire mesh imparts the strength retention capacity to the retrofitted beam column joint. Consequently the lower strength reduction empowered the performance of retrofitted specimens at higher drift. It has been observed that the onset of strength degradation is shifted as the initial damage level shifts from complete to slight. In addition, the slope of strength degradation is reduced as the damage level shift. The kink in the strength degradation plot represents the presence of fiber-matrix bond slippage phenomenon. Also, the capacity of the retrofitted specimen is increased as the retrofitting strategy shifted from only HP-HFRC to wire mesh confined HP-HFRC.

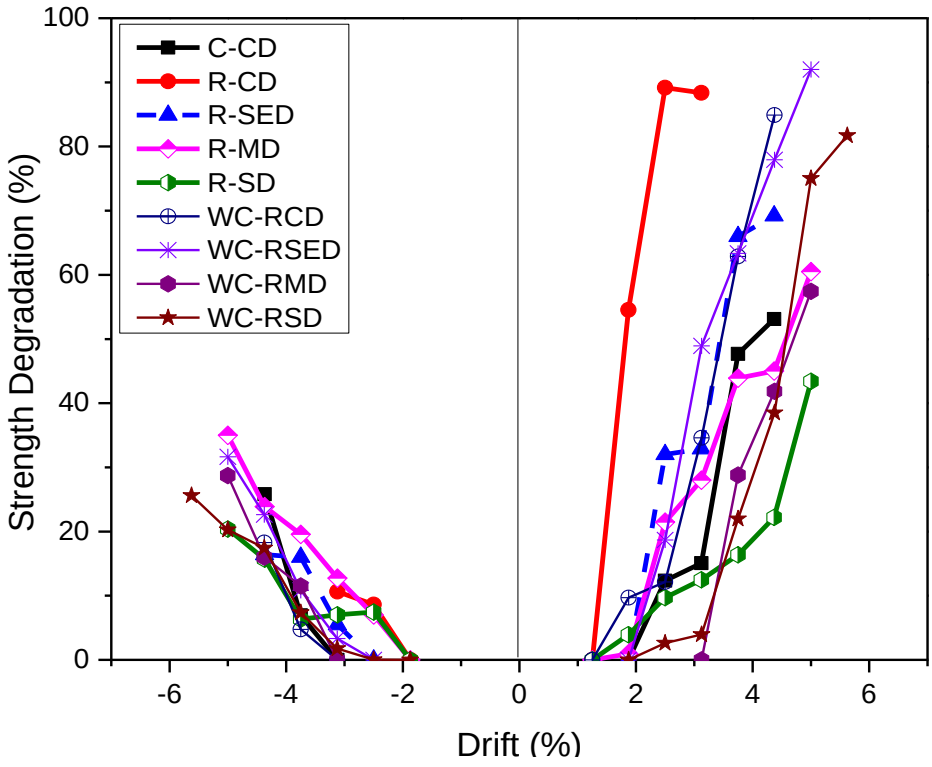

Fig. 6.60 - Comparison in Strength Degradation of HP-HFRC and Wire Mesh Confined HP-HFRC Retrofitted Specimen

It has also been observed that the higher strength degradation is found during positive drift whereas lower during the negative drift, as shown in Fig. 6.60. This happens because the face of a beam subjected to negative drift is already designed to resist the tension; however, compression face of beam unable to resist the positive lateral drift (tensile stress) but the

retrofitting using HP-HFRC and wire mesh confined HP-HFRC lift the performance against the developed tensile stresses during the positive lateral drift.

6.9.4 Energy Dissipation

The effect of retrofitting strategy on the cumulative energy dissipation capacity of initially damaged retrofitted beam column joint specimens is compared with the control specimen. The performance between the HP-HFRC and wire mesh confined HP-HFRC retrofitting strategy for each damage level is compared, and detailed discussions are provided below;

The comparison between the control specimen (C-CD), HP-HFRC retrofitted initially complete damage (R-CD), and wire mesh confined HP-HFRC retrofitted initially complete damage specimen (WC-RCD) is done and shown in Fig. 6.61. It has been observed that the cumulative energy dissipation (CED) is significantly improved after both retrofitting techniques. Both the specimen exhibited exponential growth in CED. Initially, the dissipation of energy is much more in the R-CD specimen; however, the WC-RCD specimen exhibited a consistent pattern of energy dissipation and regained the original drift capacity, whereas the specimen C-CD is failed at 3.12% lateral drift. It has been observed that the confinement offered using wire mesh enhance the energy dissipation capacity at higher drift level and avoid the condition of the sudden release of energy as observed in R-CD.

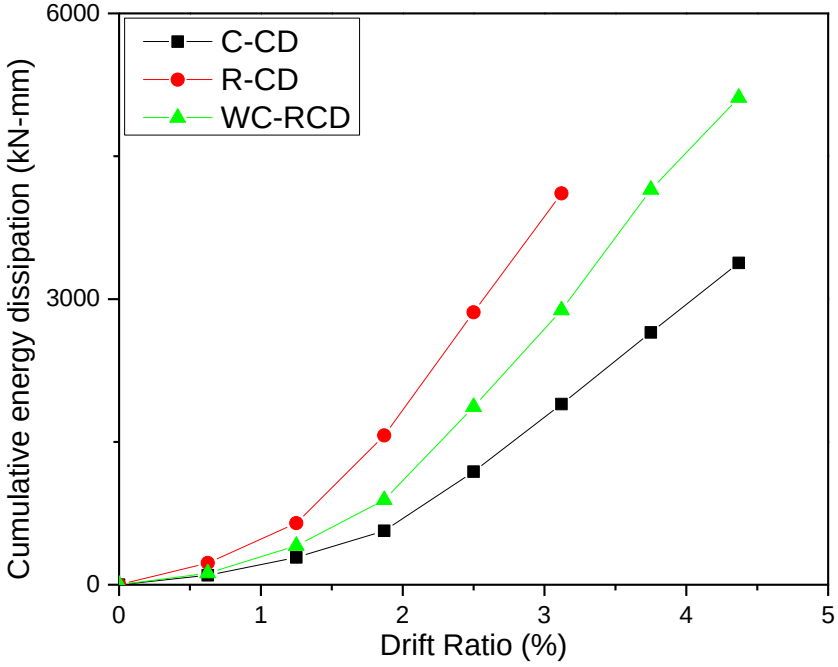

Fig. 6.61 - Comparison in Cumulative Energy Dissipation of C-CD, HP-HFRC and Wire Mesh Confined HP-HFRC Retrofitted Initial Complete Damage Specimen

The comparison of cumulative energy dissipation of control complete damage (C-CD), HP-HFRC confined initially severe damage (R-SED), and wire mesh confined HP-HFRC initially severe damage specimen (WC-RSED) is shown in Fig. 6.62. It has been observed that as the initial damage level shifts from complete to severe, energy dissipation and ultimate drift ratio changed significantly. Eventually, initially, the energy dissipated by both the retrofitted specimen is similar. But as the drift ratio increased, the HP-HFRC retrofitted specimen (R-SED) dissipate the complete energy till 4.37% lateral drift whereas, the wire mesh confined HP-HFRC retrofitted specimen dissipate the energy till 5% lateral drift which is a significant improvement in cumulative energy dissipation. Also, the sharp increase in energy dissipation of the WC-RSED specimen is found at higher drift levels because of the interaction of stresses with wire mesh confined wrapping around the initial damage beam column joint.

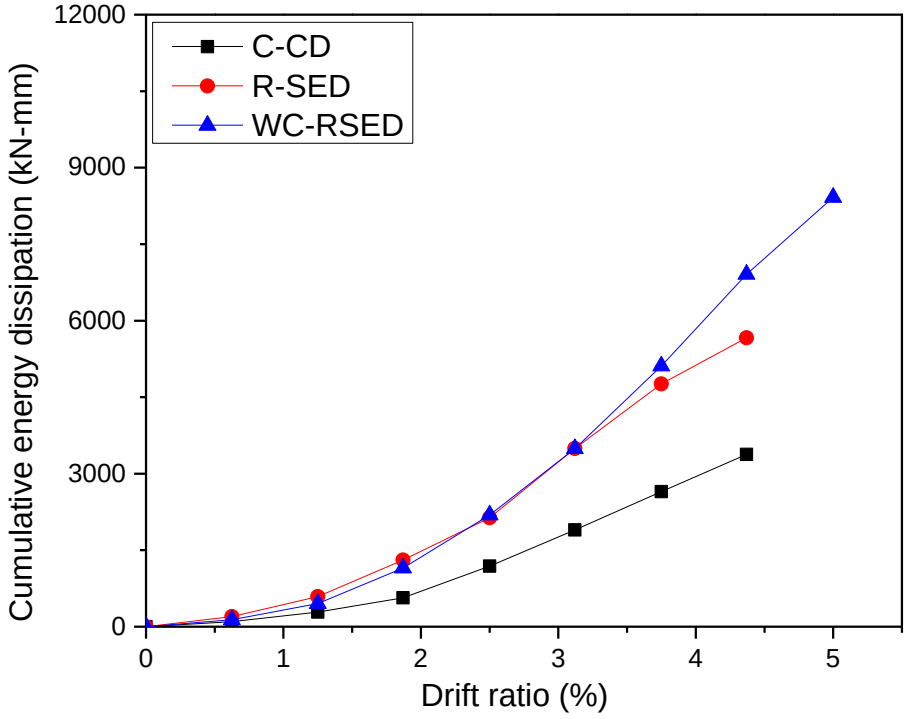

Fig. 6.62 - Comparison in Cumulative Energy Dissipation of C-CD, HP-HFRC and Wire Mesh Confined HP-HFRC Retrofitted Initial Severe Damage Specimen

Fig. 6.63 shows the comparative performance assessment of cumulative energy dissipation of control complete damage (C-CD), HP-HFRC confined initially severe damage (R-MD), and wire mesh confined HP-HFRC initially severe damage specimen (WC-RMD). It has been observed that both the scheme of retrofitting on initially moderate damaged specimens performed excellently. It has been observed that, as the lateral drift ratio increased, the amount of CED increased significantly as compared to the C-CD specimen. The maximum

improvement in energy dissipation is 8914 kN-mm in WC-RMD followed by R-MD, i.e., 7452 kN-mm. Both the specimen attained the same lateral drift capacity, but still, the exponential growth is higher in WC-RMD.

The confinement offered using two distinct techniques, i.e., confined HP-HFRC and wire mesh confined HP-HFRC. Among both the techniques, the wire mesh HP-HFRC performed excellent, as the initial damage level shift from complete to moderate. In wire mesh confined HP-HFRC retrofitting, Initially, the contribution of confined HP-HFRC improves the CED; further, at higher drift, the overlay of HP-HFRC is at the verge of failure, but wire meshes effectively hold the stresses and lengthen the period of energy dissipation.

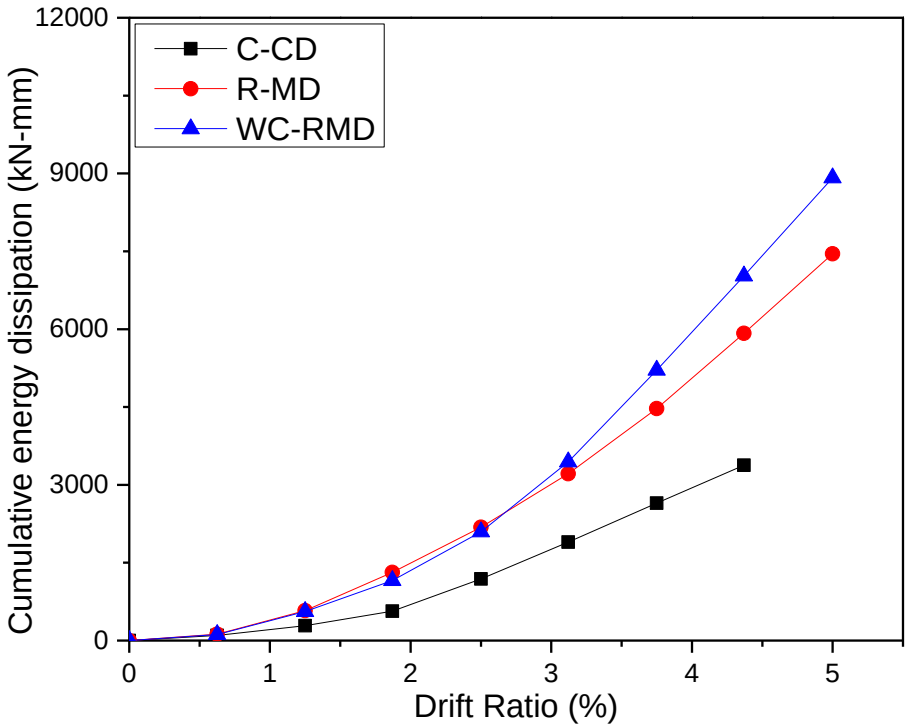

Fig. 6.63 - Comparison in Cumulative Energy Dissipation of C-CD, HP-HFRC and Wire Mesh Confined HP-HFRC Retrofitted Initial Moderate Damage Specimen

Likewise, in R-MD and WC-RMD, the initially slight damage specimen retrofitted using HP-HFRC and wire mesh confined HP-HFRC revealed the excellent improvement in cumulative energy dissipation as shown in Fig. 6.64. The maximum improvement in CED is observed in the WC-RSD specimen, followed by R-SD. The improvement in WC-RSD is 1.32 and 3.50 times than R-SD and C-CD specimens. The improvement in R-SD is 2.62 times than CCD specimens. Also, the lateral drift capacity is maximum (5.67%) in the WC-RSD specimen, followed by R-SD (5%) and CCD (4.37%).

Based on these results, it can be concluded that the effect of confinement is significant in wire mesh confined HP-HFRC retrofitting scheme than only HP-HFRC. Also, the performance of both types of scheme largely depends upon the extent of initial damage of the beam column joint. The wire mesh confined HP-HFRC retrofitted specimen performed excellently at higher drift ratio, and ultimate drift capacity increases. This property helps the retrofitted member to bear the stress for the longer duration of the earthquake.

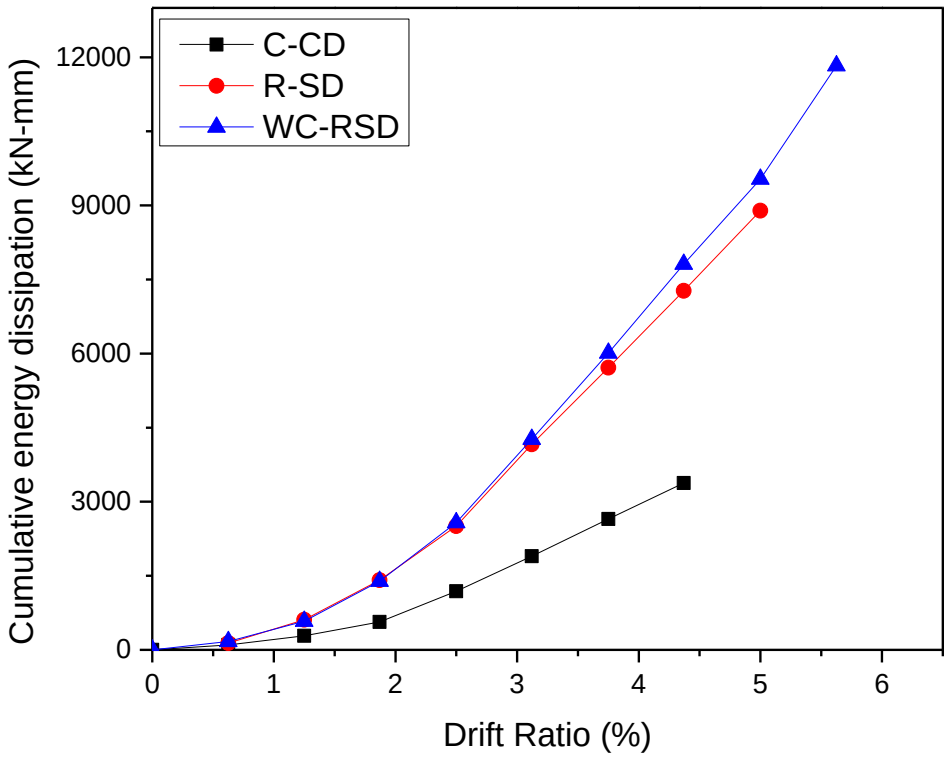

Fig. 6.64 - Comparison in Cumulative Energy Dissipation of C-CD, HP-HFRC and Wire Mesh Confined HP-HFRC Retrofitted Initial Slight Damage Specimen

Fig. 6.65 depicts the comparison of cumulative energy dissipation between the retrofitted specimens and the control specimen. The WC-RCD exhibited 1.32 times higher cumulative energy dissipation than C-CD and regained the lateral drift capacity, i.e., 4.375%. The WC-RMD, WC-RSED, and WC-RSD revealed the cumulative energy dissipation 2.48, 2.35, and 3.50 times higher than C-CD. It can be observed that the specimen C-CD dissipates the energy till a drift ratio of 4.37%, whereas, the R-CD specimen, due to complete pre-yielding of reinforcement, dissipate the energy only up to 3.12% drift ratio which is 28.60% lesser than the C-CD specimen. Further, the R-SED, R-MD, and R-SD dissipate the energy 1.58, 1.65, and 2.02 times higher energy then C-CD at a drift ratio of 4 .37%. This shows that the behaviour of retrofitted specimens is much better than that of the control specimen in terms

of energy dissipation. The improvement in cumulative energy dissipation and lateral drift capacity helps the structure to perform in a ductile manner and sustained the stresses at a higher drift ratio during an earthquake.

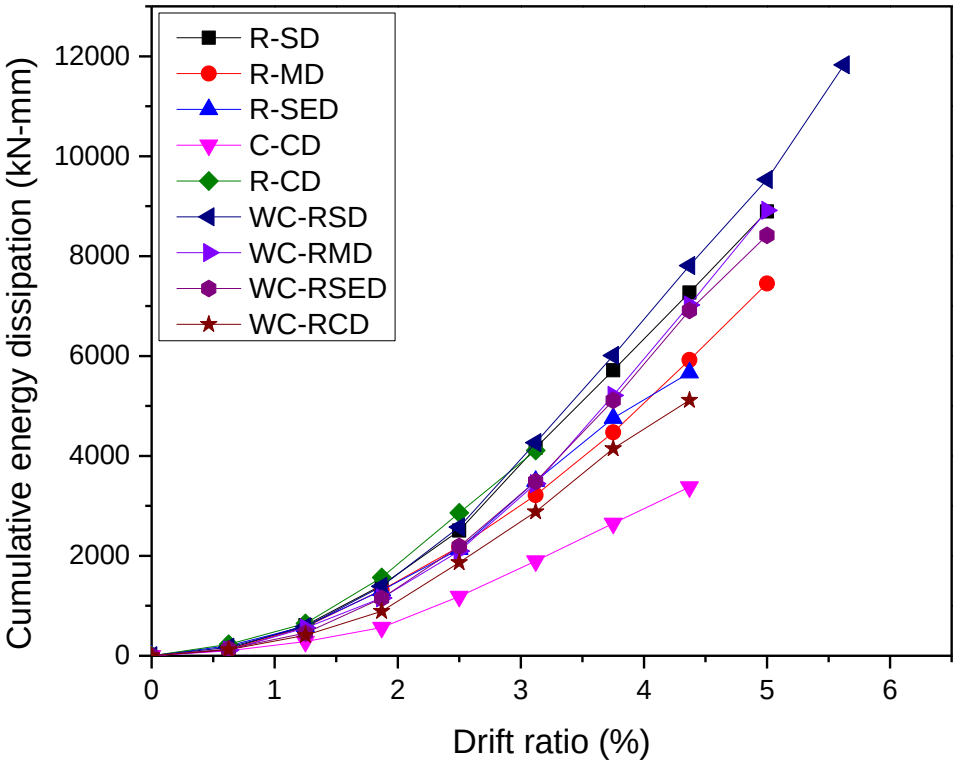

Fig. 6.65 - Comparison in Cumulative Energy Dissipation of C-CD, HP-HFRC and Wire Mesh Confined HP-HFRC Retrofitted Specimen

CHAPTER 7

CONCLUSIONS

7.1 GENERAL

The complete research program has been divided into three segments; In the first segment, high performance hybrid fiber reinforced concrete (HP-HFRC) is developed using trial and error method further, the refinement in the HP-HFRC mix design has been done usingmodifiedAndreasen and Andersen (A&A) optimum packing model; In the second segment, eight beam column joints have been initially damaged to achieve the four distinct damage level (complete, severe, moderate and slight) which are based on the Park and Ang damage model and then retrofitted using confined HP-HFRC. In the third segment, more eight beam column joint specimens damaged under reversed cyclic loading to obtain the complete, severe, moderate, and slight initial damage level. The initially damaged specimens are processed for retrofitted using a wire mesh confined HP-HFRC.

The performance of confined HP-HFRC and wire mesh confined HP-HFRC retrofitted initially damaged specimens tested under reversed cyclic loading and the performance in terms of load displacement hysteresis, displacement ductility, energy dissipation, strength and stiffness degradation, and principal tensile stress are compared with control specimen. Following conclusions are drawn after the accomplishment of the research program;

7.2 DEVELOPMENT OF HIGH PERFORMANCE HYBRID FIBER REINFORCED CONCRETE (HP-HFRC)

1. The low sand/cement ratio is favourable to produce the high performance concrete. The presence of fly ash and quartz powder improved the strength property of the matrix. However, the comparison between fly ash and quartz powder shows that the fly ash is a better ingredient to produce the HPC.
2. The fly ash imparts a significant contribution in developing the densest microstructure then quartz powder. The microstructure of prepared HP-HFRC revealed the efficient fiber matrix interaction and high peaks of C-S-H in fly ash based HP-HFRC then quartz based HP-HFRC. The high-temperature behaviour of fly ash contained HP-HFRC and quartz powder contained HP-HFRC shows a similar pattern of mass loss, however, the amount of mass loss is different. The 28 days strength of HP-HFRC using trial and error method is less than 100 MPa.

3. The refinement in HP-HFRC has been done using modified Andreasen and Andersen (A&A) optimum packing model. The prepared mix exhibited the flowability 81%, 28-day compressive strength 125.4 MPa, excellent durability, and microstructural properties than the HP-HFRC prepared using trial and error method.
4. The presence of hybrid fiber in dense matrix improved the strength significantly. The presence of small-scale and long scale fibers sustained the load for a longer time and imparted the crack bridging phenomenon to HP-HFRC.

7.3 RETROFITTING OF INITIALLY DAMAGED BEAM COLUMN JOINT USING HP-HFRC

The experimental results of the current study show that the HP-HFRC is a promising retrofitting material to improve the performance of the initial distressed exterior beam column joint for opted geometrical dimensions. It has been observed that after the retrofitting of exterior beam column joint using HP-HFRC, all the structural parameters such as lateral load carrying capacity, lateral drift, ductility, peak to peak stiffness, strength degradation, energy dissipation, joint principal tensile stress, etc. either improve or regain its original strength. Some of the major conclusions are as under;

1. The maximum improvement in lateral load carrying capacity and ductility of HP-HFRC retrofitted specimen is obtained at initially slight damage level. However, the improvement in load carrying capacity and ductility is decreased as the initial damage level of the beam column joint shifts from slight to complete.
2. The drift capacity of confined HP-HFRC retrofitted specimen is increased maximum in case of the slightly damaged retrofitted specimen but, the initially complete damaged specimen not even able to regain the original drift capacity. Also, the strength degradation is found rapidly in the case of the initial complete damaged specimen. But, the slope of the strength degradation decreases as the initial damage level shifts from complete to slight. It is concluded that HP-HFRC retrofitting methodology exhibits excellent performance when the specimen is initially severe, moderate, and slightly damaged but comparable when the specimen is initially completely damaged.
3. The low level of initial damage of beam column joint is favourable to improve the peak to peak lateral stiffness. However, irrespective of the initial damage level, the residual lateral stiffness of all the retrofitted specimens is still higher than the residual stiffness of the control specimen at the ultimate drift ratio.

4. The per cycle energy dissipation is increased with the application of HP-HFRC as a retrofitting material on the initially damaged beam column joint. The extent of improvement in per cycle energy and cumulative energy depends upon the level of initial damage. The improvement in per cycle energy and cumulative energy dissipation is decreases as the residual stress in the initial damage beam column joint increases.
5. The retrofitting using HP-HFRC improves the joint principal tensile stress carrying capacity than the control specimen. Also, the lower rate of post elastic tensile strength degradation is observed. These improvements are attained in retrofitted initially slightly damaged specimen; however, the tensile stress carrying capacity is decreased and degradation rate of post elastic tensile stress carrying capacity is higher as the initial damage level shifts from complete to slight.

Based on the above findings, it is concluded that the developed HP-HFRC exhibited higher compressive strength, i.e., more than 120 MPa in comparison of control concrete having a compressive strength of 25.6 Mpa, renders the confinement around the initially damaged joint panel of the specimen. Consequently, this property of HP-HFRC increases the peak load carrying capacity, initial stiffness, strength, energy dissipation, and joint principal tensile stress capacity of retrofitted initially damaged specimens.

Also, the hybrid steel fibers have been used to develop HP-HFRC. The presence of hybrid fibers in dense matrix empowered the matrix post elastic performance. This property of HP-HFRC contributes to improving the ductility, ultimate lateral drift capacity, post elastic stiffness, energy dissipation, strength retention at higher drift, and lower the rate of degradation of post elastic joint principal tensile stress capacity.

The effect of the initial damage level of beam column joint on the efficacy of HP-HFRC is also monitored. Based on the obtained results, it is concluded that, as the initial damage level shifts from slight to complete, the efficacy of HP-HFRC as a retrofitting material is reduced. The lower residual stresses in the main reinforcement and core concrete of initially damaged specimens have not been able to contribute to resisting the stresses specifically in the post elastic region.

7.4 RETROFITTING OF INITIALLY DAMAGED BEAM COLUMN JOINT USING WIRE MESH CONFINED HP-HFRC

The initially damaged exterior beam column joints are retrofitted using wire mesh confined HP-HFRC. The experimental results for the opted geometrical dimension beam column joint depict that the wire mesh confined HP-HFRC enhances the confinement around the initially

damaged beam column joint. Consequently, the performance of retrofitted beam column joint using wire mesh confined HP-HFRC is improved in terms of peak load carrying capacity, ductility, ultimate lateral drift capacity, strength, stiffness, energy dissipation, and joint principal tensile stress capacity. Some of the major conclusion is as under:

1. The retrofitting of the initially damaged specimen using wire mesh confined HP-HFRC significantly depends upon the initial damage state of the specimen. The maximum improvement in lateral load carrying capacity and ductility is exhibited by the initially slightly damaged retrofitted specimen. But, the increment in the initial damage level of beam column joint decreases the improvement in lateral load carrying capacity and ductility of wire mesh confined HP-HFRC retrofitted specimen.
2. The confinement of wire mesh confined HP-HFRC increases the lateral drift capacity of all the specimens, excluding the initially completely damaged retrofitted specimen. Nonetheless, the proposed retrofitting strategy enables the initial complete damage specimen to regain the original drift capacity after retrofitting, but rapid strength degradation is observed as the lateral drift increased. The reduction in initial damage level from complete to slight reduces the rate of strength degradation, which is recommendable for structure during a severe earthquake.
3. The WC-RSD specimen exhibited the maximum improvement in stiffness followed by the WC-RSED, WC-RMD, WC-RSD and CCD. Further, the wire mesh confined HP-HFRC retrofitted specimen enables to retain the stiffness at the ultimate drift ratio and also lower the rate of stiffness degradation as the initial damage level reduced.
4. The maximum improvement of 3.50 times higher than the control specimen is attained by wire mesh confined HP-HFRC retrofitted initial slight damaged specimen, but, if the initial damage level of beam column joint shifts from slight to complete, then the performance of wire mesh confined HP-HFRC retrofitted beam column joint degrades.
5. The presence of wire mesh, hybrid fibers with high strength bridge the cracks at micro and macro scale in post-elastic region. The higher energy utilized by the matrix to allow the propagation of crack improved the principal tensile stress of the joint. The lower rate of post elastic tensile strength degradation is observed in retrofitted initially slightly damaged specimen; however, the peak tensile stress carrying capacity is reduced and the rate of degradation of post elastic tensile stress carrying capacity is higher, as the initial damage level shifts from slight to complete.

It is concluded that the wire mesh confined HP-HFRC retrofitting methodology improves the performance of all the initial damage levels of beam column joint. The presence of HP-HFRC and wire mesh improves the property in the following ways; the presence of hybrid fibers in HP-HFRC delay the onset of cracks and growth of the opening of cracks at the micro and macro level as compared to conventional concrete. So, the improvement in peak load carrying capacity, initial stiffness, and delay the onset of strength and stiffness degradation is observed. But, at higher lateral drift, the microfibers slipped out from the matrix consequently, affects the performance. Thereafter, the micro cracks transformed into macro sizes but, the amalgamation of long-length fiber and wire mesh confinement maintain the peak load and generate the large post peak plateau. This action add-on the peak load carrying capacity, ductility, ultimate lateral drift capacity, energy dissipation, stiffness and strength retention and low rate of degradation of principal tensile in the post elastic region.

The effect of initial damage level on the performance of wire mesh confined retrofitted initially damaged beam column joint is also assessed. Based on the obtained results, it is concluded that the initial damage level governs the amount of residual stresses in a beam column joint. The lower the initial damage level resulted in higher residual stress and vice versa. The retrofitting using wire mesh confined HP-HFRC on the specimen having higher residual stress exhibited the higher peak load capacity, ductility, ultimate lateral drift capacity, strength, stiffness, and principal tensile stress capacity retention at higher drift. The higher residual stresses in the reinforcement and concrete of controlled specimens enable to assist the wire mesh confined HP-HFRC overlay in the post elastic stage; therefore, the overall performance of the specimen is improved. But, if the specimen is initially complete damage, then after the failure of HP-HFRC confinement and wire mesh, the initially completely yielded reinforcement and damaged core concrete of the specimen could not be able to perform at higher drift/post elastic region.

The performance between HP-HFRC and wire mesh confined HP-HFRC retrofitting strategy is compared. It is concluded that the HP-HFRC retrofitting strategy improves the performance of the initially damaged beam column joint through the confinement and bond between dense matrix and hybrid fiber only. But, the wire mesh confined HP-HFRC retrofitting strategy contributes by two-way action in improvement of initially damaged beam column joint; firstly the micro and macro fiber contributes until the macro fiber slipped out from the matrix (large wide crack opening); secondly, the wire mesh confinement actively

participates once the hybrid fiber slipped out resulted in lengthening the post elastic plateau and reflects the enhancement in the post elastic rotational capacity.

Therefore, it can be concluded that the two-way action contribution provided by wire mesh confined HP-HFRC is better as compare to only HP-HFRC to excel in the performance of the initially damaged beam column joint. However, the improvement in the performance of the retrofitting beam column joint using both types of strategy depends upon the type and size of the joint.

7.5 SCOPE OF FUTURE WORK

The present work has been done to study the effectiveness of HP-HFRC and wire mesh confined HP-HFRC as a retrofitting material to retrofit the initially damaged beam column joint. However, the following areas can be considered as scope of the future work.

1. The scope of combining some other types of fibers such as crimped, hooked, and polyvinyl fiber or a combination of crimped, hooked, and polypropylene can be verified to retrofit a damaged beam column joint.
2. Performance of retrofitted exterior beam column joint using several layers of wire mesh with different percentages of fibers in HP-HFRC can be evaluated experimentally and validated using FEM studied.
3. The use of HP-HFRC and wire mesh confined HP-HFRC can apply to retrofit the ductile detailed exterior beam column joint and non-ductile/ductile interior beam column joint.

REFERENCES

ACI 352 (2002): Recommendations for design of beam-column connections in monolithic reinforced concrete structures. American Concrete Institute, Farmington Hills, MI.

ACI 549.1R-1999 Guide for the Design, Construction, and Repair of Ferrocement, American Concrete Institute, Farmington Hills, MI.

Akguzel U, Pampanin S. Effects of variation of axial load and bidirectional loading on seismic performance of GFRP retrofitted reinforced concrete beam-column joint. Journal of composite for Construction 2010; 14(1): 94-104.

Alcocer S, Jisra JO. Strengthening of reinforced concrete frame connection rehabilitated by jacketing. ACI Structure Journal 1993; 90(3): 249–261.

Ali MDZ. (2014). *Shear demand and shear deformation in exterior beam-column joints*. (ME Dissertation, Department of Civil Engineering, National Institute of Technology Rourkela). http://ethesis.nitrkl.ac.in/5982/1/e-149.pdf

Al- Salloum, YA, Alsayed SH, Almusallam TH, Siddiqui NA. Seismic Performance of shear deficient exterior rc beam-column joints repaired using CFRP composite. Proceedings of the 7th Saudi Engineering Conference (SEC7) 2008.

Alsadey S, Effect of Superplasticizer on Fresh and Hardened Properties of Concrete Journal of Agricultural Science and Engineering 2015; 1 (2): 70-74.

Antonopoulos CP, Triantafillou, TC. Experimental Investigation of FRP-Strengthened RC Beam-Column Joints, Journal of Composite for Construction (2003); 7(1): 39–49. https://doi.org/10.1061/(ASCE)1090-0268(2003)7:1(39).

ASCE/SEI 31/03, Seismic Evaluation of Existing Buildings. American Society of Civil Engineers (ASCE); 2002. https://doi.org/10.1061/9780784406700

ASCE/SEI 41-06. Seismic Rehabilitation of Existing Buildings. American Society of Civil Engineers; 2007. https://doi.org/10.1061/9780784414859

ASTM C 1202. Standard Test Method for Electrical Indication of Concrete's Ability to Resist Chloride Ion Penetration, American Society of Testing and Material 2019.

ASTM C39, Standard Test Method for Compressive Strength of Cylindrical Concrete Specimens, American Society of Testing and Material 2014.

ASTM C1585-13, Standard Test Method for Measurement of Rate of Absorption of Water by Hydraulic-Cement Concretes, ASTM International, West Conshohocken, PA, 2013, www.astm.org.

ASTM C 1856, Standard Practice for Fabricating and Testing Specimens of Ultra-High Performance Concrete, American Society of Testing and Material, 2018.

Bache HH. Densified cement/ultra fine particle based materials. Second International Conference on Superplasticizers in Concrete; Ottawa, Canada; 1981.

Badagha DG, Chauhan PG, Modhera CD, Utilization of various Fibers in Mortar, Lambart Academic Publishing, 2018; ISBN 978-613-9-90015-2.

Baert G, Hoste S, De Schutter G, De Belie N, Reactivity of fly ash in cement paste studied by means of thermogravimetry and isothermal calorimetry, Journal of Thermal Analysis and Calorimetry 2008; 94(2): 485–492. doi:10.1007/s10973-007-8787-z.

Balsamo A, Colombo A, Manfredi G, Negro P, Prota A. Seismic Behavior of a Full-scale RC Frame Repaired using CFRP Laminates. Engineering Structures 2005; 27 (5): 769-780.

Bedirhanoglu I, Ilki A, Kumbasar N, Precast fiber reinforced cementitious composites for seismic retrofit of deficient rc joints – A pilot study, Engineering Structures 2013; 52: 192–206.

Beschi C, Meda A, Riva P. Column and Joint Retrofitting with High Performance Fiber Reinforced Concrete Jacketing. Journal of Earthquake Engineering 2011; 15(7): 989-1014, doi: 10.1080/13632469.2011.552167.

Beschi C, Riva P, Metelli G, Meda A, HPFRC Jacketing of Non Seismically Detailed RC Corner Joints. Journal of Earthquake Engineering Journal of Earthquake Engineering 2015; 19(1): 25-47. DOI: 10.1080/13632469.2014.948646.

Birchall JD, Howard AJ, Kendall K. Flexural strength and porosity of cement. Nature. 1981; 289: 388–390.

Bindhu KR, Sukumar PM, Jaya KP. Performance of exterior beam-column joints under seismic type loading. ISET Journal of Earthquake Technology 2009;46(2):47-64.

Beckingsale CW.1980. *Post Elastic Behaviour of Reinforced Concrete Beam-Column Joints*. (Doctoral Dissertation, Department of Civil Engineering, University of Canterbury Christchurch). https://ir.canterbury.ac.nz/handle/10092/7749

Bentur A, Mindess S, Fiber Reinforced Cementitious Composites, CRC Press, 2006.

Bonacci, J. F., and Wight, J. K., , 1996 "Displacement-Based Assessment of Reinforced Concrete Frames in Earthquakes," Mete A. Sozen Symposium: A Tribute from His Students, SP-162, J. K. Wight and M. E. Kreger, eds., American Concrete Institute, Farmington Hills, Mich., pp. 117-138.

BS EN 196-1: (1995). Methods of testing cement. Determination of strength

Chalioris CE, Favvata MJ, Karayannis CG. Reinforced concrete beam-column joints with crossed inclined bars under cyclic deformations. Earthquake Engineering & Structural Dynamics 2008; 37(6): 881–897.

Cheyrezy M, Maret V, Frouin L. Microstructure investigation of reactive powder concrete, Cement and Concrete Research 1995; 25(7): 1491−1500.

Chidambaram RS, Agarwal P. Seismic behavior of hybrid fiber reinforced cementitious composite beam–column joints. Materials & Design. 2015; 5(86):771-81.

Chidambaram, R, Agarwal, P. Performance Evaluation of Geogrid-Confined Beam-Column Joints with Steel Fiber Reinforced Concrete under Cyclic Loading. Journal of Testing and Evaluation 2015; 44(1): 582-598. http://dx.doi.org/10.1520/JTE20150037.

Do J-Y, Kim D-K, AHP-Based Evaluation Model for Optimal Selection Process of Patching Materials for Concrete Repair: Focused on Quantitative Requirements, International Journal of Concrete Structures and Materials, 2012; 6(2): 87 -100.

Dong Z, Keru W. Fracture properties of high-strength concrete. Journal of Materials in Civil Engineering, 2001; 13(1): 86-8.

Deschner F, Winnefeld F, Lothenbach B, Seufert S, Schwesig P, Dittrich S, Goetz-Neunhoeffer F, Neubauer J, Hydration of Portland cement with high replacement by siliceous

fly ash, Cemant and Concrete Research 2912; 42: 1389–1400. doi:10.1016/J.CEMCONRES.2012.06.009.

Emmons PH (1993). Concrete repair and maintenance illustrated: problem analysis, repair strategy, techniques. RS Means Co.

Endindeniz M, Khan LF, Zureick A-H. Repair and Strengthening of Reinforced Concrete Beam Column Joints: State of the Art. ACI Structural Journal 2005; 102(2): 1-14.

El-Amoury T, Ghobarah A. Seismic Rehabilitation of Beam-Column Joint using GFRP Sheets. Engineering Structures 2002; 24 (11): 1397-1407.

FEMA 356, Prestandard and Commentary for the Seismic Rehabilitation of Buildings. American Society of Civil Engineers (ASCE); 2000.

Feylessoufi A, Crespin M, Dion P, Bergaya F, Damme HV, Richard P. Controlled rate thermal treatment of reactive powder concretes. Advanced Cement Based Material 1997; 6 (1): 21−27.

Fraay ALA, Bijen JM, Haan YMD, The reaction of fly ash in concrete a critical examination, Cement and Concrete Research 1989; 19: 235–246. doi:10.1016/0008-8846(89)90088-4.

Fuller, W. B., & Thompson, S. E. (1907). The laws of proportioning concrete.

Funk, J. E., & Dinger, D. R. (2013). Predictive process control of crowded particulate suspensions: applied to ceramic manufacturing. Springer Science & Business Media.

Ganesan N, Indira PV, Sabeena MV, Behaviour of hybrid fibre reinforced concrete beam-column joints under reverse cyclic loads, Material Design 54 (2014) 686–693, https://doi.org/10.1016/j.matdes.2013.08.076.

Ganesan N, Indira PV, Sabeena MV. Behaviour of hybrid fibre reinforced concrete beam–column joints under reverse cyclic loads. Materials and Design 2014; 54: 686–693.

Geng, ZJ, Chajes MJ, Chou TW, Pan DYC. The retrofitting of reinforced concrete column-to-beam connections. Composite Science Technology 1998; 58(4): 1297–1305.

Gergely J, Pantelides CP, Nuismer RJ, Reaveley LD. Bridge pier retrofit using fiber-reinforced plastic composites. Journal of Composite for Construction 1998; 2(4): 165–174

Gergely J, Pantelides CP. and Reaveley LD. Shear Strengthening of RCT-Joints using CFRP Composites. Journal of Composites for Construction 2000; 4(2): 56-64.

Ghobarah A, Said A. Shear strengthening of beam-column joints, Engineering Structures 2002; 24: 881–888.

Granata PJ, Parvin A. An Experimental Study on Kevlar Strengthening of Beam-Column Connections. Composite Structures 2001; 53(2):163-171.

Graybeal BA. Material property characterization of ultra –high performance concrete. Federal Highway Administration Report No FHWA-HRT-06-103. 2006 www.fhwa.dot.gov/publications/research/infrastructure/structures/06103/06103.pdf.

Graybeal BA, Compressive behavior of ultra-high-performance fibre-reinforced concrete. ACI Materials Journal 2007; 104(2): 146.

Graybeal BA. Material property characterization of ultra-high performance concrete. United States. Federal Highway Administration. Office of Infrastructure Research and Development; 2006 Aug 1.

Graybeal BA (2005). *Characterization of the behavior of ultra-high performance concrete*. (Doctoral Thesis, University of Maryland).

Grünewald, S. (2004), *Performance-based design of self-compacting fibre reinforced concrete*. (Ph.D. Dissertation, Delft University of Technology)

Hamid NH, Hadi ND, Ghani KD. Retrofitting of Beam-Column Joint Using CFRP and Steel Plate. International Journal of Civil, Environmental, Structural, Construction and Architectural Engineering 2013; 7 (12): 941-946.

Hadi MNS, Tran TM. Retrofitting non seismically detailed exterior beam-column joints using concrete covers together with CFRP jacket. Construction and Building Materials 2014; 63: 161-173.

Hoff, G. C. Use of steel fiber concrete in bridge decks and pavements, in steel fiber reinforced concrete. US- Sweden Joint Seminar (NSF-STU) 67−108. 1985.

IS 12269: 2013 Ordinary Portland Cement, 53 Grade — Specification, Bureau of Indian Standard, New Delhi

IS 456: 2000 Plain and Reinforced Concrete - Code of Practice (CED 2: Cement and Concrete), Bureau of Indian Standard, New Delhi

IS 5816 – 1999 Method of Test Splitting Tensile Strength of Concrete (CED 2: Cement and Concrete), Bureau of Indian Standard, New Delhi

IS: 8112 – 2013 Ordinary Portland Cement, 43 Grade — Specification, Bureau of Indian Standard, New Delhi

IS 2386 (Part 1) – 1963 Methods of Test for Aggregates for Concrete, Part I: Particle Size and Shape (CED 2: Cement and Concrete), Bureau of Indian Standard, New Delhi

IS 383 – 1970 Specification for Coarse and Fine Aggregates From Natural Sources For Concrete (CED 2: Cement and Concrete), Bureau of Indian Standard, New Delhi

IS 1786 -1985 High Strength Deformed Steel Bars and Wires for Concrete Reinforcement, Bureau of Indian Standard, New Delhi

IS 10262: 2009 Concrete mix proportioning: Guidelines, Bureau of Indian Standard, New Delhi

IS 13920 (2009/2016): Ductile detailing of reinforced concrete structures subjected to seismic forces - Code of practice (CED-39): Earthquake Engineering, Bureau of Indian Standard, New Delhi

IS 1893: Part 1 (2002): Criteria for earthquake resistant design of structures; General Provisions and Buildings (CED – 39): Earthquake Engineering, Bureau of Indian Standard, New Delhi

IS 4326 (1993): Code of practice for earthquake resistant design and construction of buildings (CED 39): Earthquake Engineering, Bureau of Indian Standard, New Delhi

IS 15988 (2013): Seismic Evaluation and Strengthening of Existing Reinforced Concrete Buildings – Guidelines, Bureau of Indian Stan dard, New Delhi.

Jang JG, Kim HK, Kim TS, Min BJ, Lee HK. Improved flexural fatigue resistance of PVA fiber-reinforced concrete subjected to freezing and thawing cycles. Construction and Building Materials. 2014; 30(59):129-35.

Jain SK, Jaiswal A. Post-earthquake handling of buildings and reconstruction issues emerging from the 2001 Bhuj Earthquake. Proceedings of the Seventh US National Conference on Earthquake Engineering, Boston, USA, July 2002.

Jaiswal K, Sinha R, Goyal A. Reinforced concrete frame building with masonry infill walls designed for gravity loads. World Housing Encyclopedia (www. world-housing. net). Earthquake Engineering Research Institute and International Association for Earthquake Engineering, India/Report. 2003;19.

Johari MAM, Zeyad AM, Bunnori NM, K. Ariffin S, Engineering and transport properties of high-strength green concrete containing high volume of ultrafine palm oil fuel ash, Construction and Building Material 2012; 30: 281–288. doi:10.1016/j.conbuildmat.2011.12.007.

Joshi RC, Nagaraj ST, Generalization of flow behavior of cement -fly -ash pastes and mortars", Journal of Material in Civil Engineering 1990; 2(3): 128-135.

Justus J, Bajare D, Korjakins A, Mezinskis G, Locas J. Microstructural investigations of ultra-high performance concrete obtained by pressure application within the first 24 hours of hardening. Construction Science 2013; 14(1): 50–57.

Kalogeropoulos GI, Tsonos A-D G, Konstandinidis D. Pre-earthquake and post earthquake retrofitting of poorly detailed exterior RC beam column joints. Engineering Structures 2016; 109: 1-15.

Karayannis C, Chalioris C, Sirkelis G. Local retrofit of exterior rc beam-column joints using thin r/c jackets - an experimental study. Earthquake Engineering Structure Dynamics 2008; 37(5): 727-746.

Kaya O, Yalçın C, Parvin A, Altay S. Retrofitting of Reinforced Concrete Beam-Column Joints by Composites--Part I: Experimental Study. ACI Structural Journal 2019; 116(1): 17-29.

Khana MI, Al-Ostaa MIK, Ahmada S, Rahman MK. Seismic behavior of beam-column joints strengthened with ultra-high performance fiber reinforced concrete, Composite Structure 2018; 200: 103-119

Kheni D, Scot RH, Deb SK, Dutta A. Ductility Enhancement in Beam-Column Connections Using Hybrid Fiber-Reinforced Concrete. ACI Structural Journal 2015; 112 (2): 167-178.

Kim, DJ, Park SH, Ryu GS, Koh KT, Comparative flexural behavior of Hybrid Ultra High Performance Fiber Reinforced Concrete with different macro fibers, Construction and Building Material 2011; 25(11): 4144–4155, https://doi.org/10.1016/ j.conbuildmat. 2011.04.051.

Kumar P, Patnaik A, Chaudhary S, A review on application of structural adhesives in concrete and steel–concrete composite and factors influencing the performance of composite connections. International Journal of Adhesion and Adhesives 2017; 77: 1-14.

Kondraivendhan B, Bhattacharjee B, Flow behavior and strength for fly ash blended cement paste and mortar, Int. J. Sustain. Built Environ 2015; 4(2): 270-277. https://doi.org/10.1016/J.IJSBE.2015.09.001.

Kwon S, Nishiwaki T, Kikuta T, Mihashi H, Mechanical properties of ultrahigh-performance hybrid fibre-reinforced cement- based composites, Int. Symp. Ultra-High Perform. Fiber–Reinforced Concrete UHPFRC, Marseille, Fr., 2013.

Lakshmanan N. Seismic evaluation and retrofitting of buildings and structures. ISET Journal of earthquake technology. 2006; 43(1):31-48.

Lankard, D. R. Slurry infiltrated fiber concrete (SIFCON) properties and application, in potential for very high strength cement based material. Proceeding of Material Research Society 1984 Fall meeting.

Lee D H, Kim D, Lee K, Analytical approach for the earthquake performance evaluation of repaired/retrofitted RC bridge piers using time-dependent element, Nonlinear Dynamics, 2009; 56: 463 - 482.

Le-Trung K, Lee K, Lee J, Lee DH, Woo S. Experimental study of RC beam–column joints strengthened using CFRP composites. Composites: Part B 2010; 41(1): 76–85.

Macgregor JG. Reinforced Concrete Mechanics and Design, Prentice Hall Inc., 1988.

Markovic, I. (2006), *High-performance hybrid-fibre concrete: Development and utilisation*. (Ph.D. Dissertation, Delft University of Technology).

Mehta P, Aïtcin P. Principles Underlying Production of High-Performance Concrete. Cement, Concrete and Aggregates 1990; 12 (2): 70-78. https://doi.org/10.1520/CCA10274J. ISSN 0149-6123.

Mohammad A., Mosaberpanah, O. Eren, Effect of quartz powder, quartz sand and water curing regimes on mechanical properties of UHPC using response surface modelling, Advances in Concrete Construction 2013; 5(5): 481–492. doi:https://doi.org/10.12989/acc.2017.5.5.481.

Mohammadi Y, Singh SP, Kaushik SK, Properties of steel fibrous concrete containing mixed fibres in fresh and hardened state, Construction and Building Material, 2008; 22 (5): 956-965

Mohammed AN, Johari MA, Zeyad AM, Tayeh BA, Yusuf MO. Improving the engineering and fluid transport properties of ultra-high strength concrete utilizing ultrafine palm oil fuel ash. Journal of Advanced Concrete Technology 2014; 12(4):127-37.

Mukherjee A, Joshi M. FRPC reinforced concrete beam-column joints under cyclic excitation, Composite Structure 2005; 70(2): 185–199. https://doi.org/10.1016/j.compstruct.2004.08.022.

Murty CVR, Goswami R, vijayanarayanan AR, Mehta VV. Some Concept in Earthquake Behaviour of Buildings. Gujarat State Disaster Management Authority 2012. http://www.iitk.ac.in/nicee/IITK-GSDMA/EBB_001_30May2013.pdf

Niroomandi A, Maheri A, Maheri MR, Mahini SS. Seismic performance of ordinary RC frames retrofitted at joints by FRP sheets. Engineering Structures 2010; 32(8):2326-36.

Ollivier JP, Maso JC, Bourdette B. Interfacial transition zone in concrete. Advanced cement based materials 1995; 2(1): 30-8. doi:10.1016/1065-7355(95)90037-3.

Ozbakkaloglu T, Saatcioglu M. Rectangular stress block for high-strength concrete. ACI Structural Journal 2004; 101(4) :475-83.

Ozer B, Ozkul HM, Effect of Initial Water Curing on Sorptivity Properties of Ordinary Portland and Pozzolanic Cement Concretes, Journal of Materials in Civil Engineering 2017; 29(8): 040170731 – 040170738.

Parvin A, Wu SH. Ply angle effect on fiber composite wrapped reinforced concrete beam–column connections under combined axial and cyclic loads. Composite Structure 2008; 82(4): 532–538.

Pantelides CP, Gergely J, Reaveley LD, Volnyy VA. Retrofit of RC Bridge Pier with CFRP Advanced Composites. Journal of Structural Engineering 1999; 125 (10): 1094-1099.

Pantelides CP, Gergely J. Carbon-Fibre-Reinforced Polymer Seismic Retrofit of RC Bridge Bent: Design and In Situ Validation. Journal of Composites for Construction 2002; 6(1): 52-60.

Pantelides CP, Alameddine F, Sardo T. Imbsen R. Seismic Retrofit of State Street Bridge on Interstate 80. Journal of Bridge Engineering 2004; 9 (4): 333- 342.

Pantazopoulou S, Bonacci J. Consideration of Questions about Beam-Column Joints," ACI Structural Journal 1992; 89(1): 27-36.

Parra-Montesinos GJ, Peterfreund SW (2005). Highly damage-tolerant beam-column joints through use of high-performance fibre-reinforced cement composites. ACI Structural Journal 2005; 102(3): 487-495.

Parra-Montesinos, G., and Wight, J. K., 2002, "Prediction of Strength and Shear Distortion in R/C Beam-Column Joints," S. M. Uzumeri Symposium: Behavior and Design of Concrete Structures for Seismic Performance, SP-197, S. A. Sheikh and O. Bayrak, eds., American Concrete Institute, Farmington Hills, Mich., pp. 191-214.

Parra-Montesinos, G., High-Performance Fiber-Reinforced Cement Composites: An Alternative for Seismic Design of Structures, ACI Structural Journal 2005; 102(5): 668-675.

Park Y, Ang AHS, Mechanistic seismic damage model for reinforced concrete, Journal of Structural Engineering 1985;111(4): 722–739, https://doi.org/10.1061/(ASCE)0733-9445

Rahhal V, Talero R, Influence of two different fly ashes on the hydration of portland cements, Journal of Thermal Analysis and Calorimetry 2004; 78 (1): 191–205. doi:10.1023/B:JTAN.0000042167.46181.17.

Patnala VS, Neelima P, Kumar RP. Effect of weak and soft stories on seismic performance of reinforced concrete frames with unreinforced brick infills. The Indian Concrete Journal 2016; 90 (2): 19-26.

Prota A, Nanni A, Manfredi G, Cosenza E. Selective upgrade of under-designed R.C. concrete beam-column joints using CFRP. ACI Structure Journal 2004; 101 (5): 699–707.

Rangaraju PR, Kizhakommudom H, Li Z, Schiff SD. Development of high-strength/high performance concrete/grout mixtures for application in shear keys in precast bridges. McLean, VA: FHWA. 2013.

Park JW, Kim DH, Yoon SG, Lee JY, Shear Deterioration of Reinforced Concrete Beam-Column Joints, 15th World Conf Earthq. Eng, Lisbon Port, 2012.

Paulay T, Priestley MN. Seismic design of reinforced concrete and masonry buildings. John Wiley and Sons, Inc.1992: ISBN:9780471549154; DOI:10.1002/9780470172841

Priestley MJ. Displacement-based seismic assessment of reinforced concrete buildings. Journal of earthquake engineering 1997; 1(01): 157-92.

Rossi P, Acker P, Malier Y. Effect of steel fibres at two different stages: the material and the structure. Materials and Structures 1987; 20(6): 436-9.

Richard P. Cheyrezy M. Reactive Powder Concretes with high ductility and 200-800 MPa compressive strength, ACI special Publication 1994; 144-24: 507−518.

Richard P, Cheyrezy MH. Reactive powder concrete. Cement and Concrete Research 1995;25(7):1501-11.

Reda MM, Shrive NG, Gillott JE. Microstructural investigation of innovative UHPC. Cement and Concrete Research 1999; 29(3): 323-9.

Rossi P. Development of new cement composite material for construction. InInnovations and Developments in Concrete materials and Construction, Proceedings of the International Conference, University of Dundee, Scotland 2002 Sep (pp. 17-29).

Saleh IS, Effect of External and Internal Sulphate on Compressive Strength of Concrete International Journal of Applied Engineering Research 2017; 12(20): 10324-10333.

Sasmal S, Ramanjaneyulu K, Novák B, Srinivas V, Kumar KS, Korkowski C, Roehm C, Lakshmanan L, Iyer NR. Seismic retrofitting of nonductile beam-column sub-assemblage using FRP wrapping and steel plate jacketing. Construction and Building Material 2011; 25: 175-182.

Sasmal S, Ramanjaneyulu K, Balthasar N, Lakshamanan N, Analytical and experimental investigations on seismic performance of exterior beam-column subassemblages of existing RC-framed building, Earthq. Eng. Structual Dyn 2013; 42: 1785–1805.

Shah AH, Sharma UK, Kamath P, Bhargava P, Reddy GR, Singh T. Effect of ductile detailing on the performance of a reinforced concrete building frame subjected to earthquake

and fire. Journal of Performance of Constructed Facilities; 2016: 30(5):04016035.

Shannag MJ, Alhassan MA, Seismic Upgrade of Interior Beam-Column Subassemblages with High-Performance Fiber-Reinforced Concrete Jackets. ACI Structural Journal 2005; 102(1): 131-138.

Siddique S, Shrivastava S, Chaudhary S, Durability properties of bone china ceramic fine aggregate concrete, Construction and Building Material 2018; 173: 323 – 331.

Singh SP, Fatigue Strength of Hybrid Steel-Polypropylene Fibrous Concrete Beams in Flexure, Procedia Engineering, 2011; 14: 2446 – 2452.

Singh V, Bansal PP, Kumar M. Experimental studies on strength and ductility of ferrocement jacketed RC beam-column joints. International Journal of Civil and Structural Engineering 2015; 5(3): 199.

Sorelli L, Constantinides G, Ulm FJ, Toutlemonde F. The nano-mechanical signature of ultra high performance concrete by statistical nanoindentation techniques. Cement and Concrete Research 2008; 38 (12): 1447–1456.

SP 34 (1987): Handbook on Concrete Reinforcement and Detailing (CED 2: Cement and Concrete), Bureau of Indian Standard, New Delhi.

Tasdemir C, Tasdemir MA, Lydon FD, Barr BI. Effects of silica fume and aggregate size on the brittleness of concrete. Cement and Concrete Research 1996; 26(1): 63-8.

Tayeh BA, Bakar BA, Johari MM, Voo LY. Utilization of ultra high performance fibre concrete (UHPFC) for rehabilitation- a review. The 2nd International Conference on Rehabilitation and Maintenance in Civil Engineering 2013; 54: 525–538.

Tuan NV, Ye G, Breugel KV, Fraaij ALA, Dai B.D. The study of using rice husk ash to produce ultra high performance concrete. Construction and Building Materials 2011; 25 (4): 2030–2035.

Voort TL. Design and field testing of tapered H-shaped Ultra High Performance Concrete piles. Iowa State University; 2008.

Xiao R, Deng Z-C, Shen C. Properties of ultra high performance concrete containing superfine cement and without silica fume. Journal of Advance Concrete Technology 2014; 12 (2): 73–81.

Yazıcı H. The effect of curing conditions on compressive strength of ultra high strength concrete with high volume mineral admixtures. Building and environment 2007 ;42(5) :2083-9. 2089.

Yu R, Spiesz P, Brouwers HJH. Effect of nano-silica on the hydration and microstructure development of ultra high performance concrete (UHPC) with low binder amount. Construction and Building Material 2014; 65: 140–150.

Yu, R, Spiesz P, Brouwers HJH, "Development of Ultra-High Performance Fibre Reinforced Concrete (UHPFRC): towards an efficient utilization of binders and fibres", Construction and Building Material 2015; 79: 273-282. https://doi.org/10.1016/j.conbuildmat.2015.01.050.

Zhang J, Zhao Y, Li H, Experimental Investigation and Prediction of Compressive Strength of Ultra-High Performance Concrete Containing Supplementary Cementitious Materials, Adv. Mater. Sci. Eng. 2017; 2017: doi:10.1155/2017/4563164.

Zhang J, Stang H, Li VC. Fatigue life prediction of fiber reinforced concrete under flexural load. International Journal of Fatigue 1999; 21(10): 1033-49.

Zohrevand P, Mirmiran A. Behavior of ultra high-performance concrete confined by fiber-reinforced polymers, Journal of Material in Civil Engineering 2011; 23(12): 1727–1734. doi: 10.1061/(ASCE)MT.1943-5533.0000324.

Zohrevand P, Mirmiran A, Seismic response of ultra-high performance concrete-filled FRP tube columns, Journal of Earthquake Engineering 2012; 17: 155–170. https:// doi.org/10.1080/13632469.2012.713560.

ANEXURE – A

Table A1 – Particle Size Distribution of Binder and Filler Material

Sr. No.	size µm	Silica Fume (%pass)	Cement (%pass)	Metakaoiline (%pass)	Ennore sand (%pass)
1	3500	100	100	100	100
2	3080.544	100	100	100	100
3	2711.357	100	100	100	100
4	2386.415	100	100	100	100
5	2100.416	100	100	100	100
6	1848.692	100	100	100	100
7	1627.136	100	100	100	100
8	1432.133	100	100	100	100
9	1260.499	100	100	100	100
10	1109.435	100	100	100	100
11	976.475	100	100	100	99.77
12	859.45	100	100	100	98.73
13	756.449	100	100	100	96.15
14	665.793	100	100	100	91.39
15	586.001	100	100	100	84.09
16	515.772	100	100	100	74.37
17	453.96	100	99.91	100	62.81
18	399.555	100	99.75	100	50.36
19	351.67	100	99.58	100	38.13
20	309.525	100	99.38	100	27.13
21	272.43	100	99.16	100	18.06
22	239.78	100	98.92	100	11.24
23	211.044	100	98.68	100	6.6
24	185.752	100	98.45	100	3.78

25	163.49	100	98.24	100	2.28
26	143.897	100	98.03	100	1.59
27	126.652	100	97.78	100	1.29
28	111.473	100	97.42	100	1.12
29	98.114	100	96.85	100	0.98
30	86.355	100	95.95	100	0.81
31	76.006	100	94.6	100	0.61
32	66.897	100	92.69	100	0.41
33	58.88	100	90.15	100	0.24
34	51.823	99.48	86.95	100	0.12
35	45.613	98.13	83.13	99.83	0.04
36	40.146	95.78	78.76	99.47	0
37	35.335	92.3	73.95	98.82	0
38	31.1	87.7	68.82	97.81	0
39	27.373	82.14	63.51	96.4	0
40	24.092	75.89	58.16	94.58	0
41	21.205	69.29	52.89	92.37	0
42	18.664	62.68	47.8	89.82	0
43	16.427	56.36	42.96	86.99	0
44	14.458	50.55	38.43	83.93	0
45	12.726	45.37	34.24	80.71	0
46	11.201	40.86	30.4	77.36	0
47	9.858	36.98	26.9	73.91	0
48	8.677	33.65	23.73	70.35	0
49	7.637	30.75	20.86	66.66	0
50	6.722	28.17	18.27	62.83	0
51	5.916	25.8	15.94	58.84	0
52	5.207	23.56	13.84	54.7	0
53	4.583	21.39	11.95	50.44	0

54	4.034	19.26	10.25	46.13	0
55	3.55	17.19	8.73	41.87	0
56	3.125	15.25	7.38	37.75	0
57	2.75	13.53	6.18	33.81	0
58	2.421	12.13	5.13	30.04	0
59	2.131	11.11	4.22	26.44	0
60	1.875	10.49	3.44	23.05	0
61	1.651	10.19	2.78	19.97	0
62	1.453	10.1	2.22	17.31	0
63	1.279	10.1	1.76	15.12	0
64	1.125	10.1	1.38	13.37	0
65	0.991	10.1	1.07	11.93	0
66	0.872	9.96	0.82	10.63	0
67	0.767	9.54	0.62	9.32	0
68	0.675	8.76	0.46	7.9	0
69	0.594	7.64	0.33	6.38	0
70	0.523	6.27	0.22	4.84	0
71	0.46	4.8	0.13	3.39	0
72	0.405	3.38	0.06	2.14	0
73	0.357	2.15	0	1.18	0
74	0.314	1.2	0	0.53	0
75	0.276	0.55	0	0.16	0
76	0.243	0.17	0	0	0
77	0.214	0	0	0	0
78	0.166	0	0	0	0
79	0.128	0	0	0	0
80	0.1188	0	0	0	0
81	0.113	0	0	0	0
82	0.1	0	0	0	0

83	0.088	0	0	0	0
84	0.077	0	0	0	0
85	0.068	0	0	0	0
86	0.06	0	0	0	0
87	0.053	0	0	0	0
88	0.046	0	0	0	0
89	0.041	0	0	0	0
90	0.036	0	0	0	0
91	0.032	0	0	0	0
92	0.028	0	0	0	0
93	0.024	0	0	0	0
94	0.022	0	0	0	0
95	0.019	0	0	0	0
96	0.017	0	0	0	0
97	0.015	0	0	0	0
98	0.0146	0	0	0	0
99	0.013	0	0	0	0
100	0.011	0	0	0	0
101	0.01	0	0	0	0

Table A2 - Optimized Curve and A&A Model Target Curve for Selected Mix

Particle size (μm)	Ennore sand (% pass)	Metakaolin (% pass)	Cement (% pass)	Silica fume (% pass)	Optimized mix (% pass)	A&A Model curve (% pass)
0.01	0	0	0	0	0	0
0.011	0	0	0	0	0	0
0.013	0	0	0	0	0	0
0.015	0	0	0	0	0	0
0.017	0	0	0	0	0	0
0.019	0	0	0	0	0	0
0.022	0	0	0	0	0	0
0.024	0	0	0	0	0	0
0.028	0	0	0	0	0	0
0.032	0	0	0	0	0	0
0.036	0	0	0	0	0	0
0.041	0	0	0	0	0	0
0.046	0	0	0	0	0	0
0.053	0	0	0	0	0	0
0.06	0	0	0	0	0	0
0.068	0	0	0	0	0	0
0.077	0	0	0	0	0	0
0.088	0	0	0	0	0	0
0.1	0	0	0	0	0	0
0.113	0	0	0	0	0	0
0.128	0	0	0	0	0	0
0.0146	0	0	0	0	0	0
0.166	0	0	0	0	0	0
0.1188	0	0	0	0	0	0
0.214	0	0	0	0	0	0

0.243	0	0	0	0	0	0
0.276	0	0	0	0.17	**0.015894825**	0
0.314	0	0.16	0	0.55	0.058878199	0.470717994
0.357	0	0.53	0	1.2	0.136889361	0.954376486
0.405	0	1.18	0	2.15	0.255994302	1.445142006
0.46	0	2.14	0.06	3.38	0.434214926	1.956478491
0.523	0	3.39	0.13	4.8	0.646792686	2.488632989
0.594	0	4.84	0.22	6.27	0.879527368	3.033542502
0.675	0	6.38	0.33	7.64	1.113269662	3.598476826
0.767	0	7.9	0.46	8.76	1.32887026	4.181482367
0.872	0	9.32	0.62	9.54	1.517269755	4.785941706
0.991	0	10.63	0.82	9.96	1.679214693	5.408237744
1.125	0	11.93	1.07	10.1	1.829925976	6.04513755
1.279	0	13.37	1.38	10.1	1.992563749	6.7103063
1.453	0	15.12	1.76	10.1	2.191219877	7.393110498
1.651	0	17.31	2.22	10.1	2.435032925	8.099155796
1.875	0	19.97	2.78	10.19	2.739980151	8.825080848
2.131	0	23.05	3.44	10.49	3.11495213	9.578986191
2.421	0	26.44	4.22	11.11	3.571274052	10.35497238
2.75	0	30.04	5.13	12.13	4.114849617	11.15503071
3.125	0	33.81	6.18	13.53	4.745027788	11.98370626
3.55	0	37.75	7.38	15.25	5.459281011	12.83711621
4.034	0	41.87	8.73	17.19	6.248725248	13.72025841
4.583	0	46.13	10.25	19.26	7.109246918	14.63051325
5.207	0	50.44	11.95	21.39	8.033190734	15.57068158
5.916	0	54.7	13.84	23.56	9.017110499	16.54138794
6.722	0	58.84	15.94	25.8	10.06671493	17.54411972
7.637	0	62.83	18.27	28.17	11.19238114	18.57851329
8.677	0	66.66	20.86	30.75	12.41037035	19.64688203

9.858	0	70.35	23.73	33.65	13.73806394	20.74934306
11.201	0	73.91	26.9	36.98	15.19237741	21.88855932
12.726	0	77.36	30.4	40.86	16.79470951	23.06402964
14.458	0	80.71	34.24	45.37	18.55608841	24.27719672
16.427	0	83.93	38.43	50.55	20.48193887	25.53046265
18.664	0	86.99	42.96	56.36	22.56404096	26.82429304
21.205	0	89.82	47.8	62.68	24.77866664	28.15976923
24.092	0	92.37	52.89	69.29	27.08442252	29.53857379
27.373	0	94.58	58.16	75.89	29.42888707	30.96247697
31.1	0	96.4	63.51	82.14	31.7471175	32.43225217
35.335	0	97.81	68.82	87.7	33.96940384	33.94987502
40.146	0	98.82	73.95	92.3	36.02781384	35.51650042
45.613	0.04	99.47	78.76	95.78	37.88816481	37.13419848
51.823	0.12	99.83	83.13	98.13	39.51579418	38.80398139
58.88	0.24	100	86.95	99.48	40.89360919	40.52826511
66.897	0.41	100	90.15	100	42.02237647	42.30826111
76.006	0.61	100	92.69	100	42.91563726	44.14605918
86.355	0.81	100	94.6	100	43.61470787	46.04339923
98.114	0.98	100	95.95	100	44.1246147	48.00240617
111.473	1.12	100	96.85	100	44.47926396	50.02476752
126.652	1.29	100	97.42	100	44.74874486	52.11284943
143.897	1.59	100	97.78	100	45.02521367	54.26854201
163.49	2.28	100	98.03	100	45.48293013	56.49413061
185.752	3.78	100	98.24	100	46.37517514	58.79201113
211.044	6.6	100	98.45	100	47.99563329	61.16429023
239.78	11.24	100	98.68	100	50.62630768	63.61351772
272.43	18.06	100	98.92	100	54.4627195	66.14226398
309.525	27.13	100	99.16	100	59.54040375	68.75296065
351.67	38.13	100	99.38	100	65.67665912	71.44825973

399.555	50.36	100	99.58	100	72.48531197	74.23104737
453.96	62.81	100	99.75	100	79.40608654	77.19647427
515.772	74.37	100	99.91	100	85.83278652	80.32413989
586.001	84.09	100	100	100	91.22282482	83.11060563
600	85.3	100	100	100	91.89035354	86.15297128
665.793	91.39	100	100	100	95.25006422	88.48450384
756.449	96.15	100	100	100	97.87604497	90.87290304
866.15	98.73	100	100	100	99.29937068	93.51720216
976.475	99.77	100	100	100	99.87311438	95.7065681
1109.435	100	100	100	100	**100**	98.15183395
1180	100	100	100	100	100	99.09013364
1260.499	100	100	100	100	100	99.80096673
1432.133	100	100	100	100	100	100
1627.136	100	100	100	100	100	100
1848.692	100	100	100	100	100	100
2000	100	100	100	100	100	100
2100.416	100	100	100	100	100	100
2386.415	100	100	100	100	100	100
2711.357	100	100	100	100	100	100
3080.544	100	100	100	100	100	100
3500	100	100	100	100	100	100

ANNEXURE – B

DAMAGE INDICIS CALCULATION

- **Example for calculating the damage index (DI)**

The equation 1 is used to calculate the DI

$$D = \frac{\delta_M}{\delta_u} + \frac{\beta}{F_y \delta_u} \int dE \qquad (5.1)$$

- δ_u = Maximum displacement experienced by the structure i.e. 35 mm
- δ_M = Maximum displacement of the cycle considered i.e. 5mm, 10mm, 15mm, 20mm, 25mm, 30mm and 35mm
- $\int dE$ = Hysteretic energy demand under the cyclic displacement
- F_y = Yield strength of the structure, calculated from the load hysteresis curve of control specimen
- Factor "β" = Strength degradation parameter depends upon volumetric transverse ratio, shear span to depth ratio, normalized axial force, and tensile force, who's value is taken as 0.1 in the present study

Calculation of damage index for 5 mm displacement level

- *δ_u = 5mm*
- *δ_M = 35 mm*
- *dE = 49.05 kN-mm*
- *Fy is calculated as;*
- *+ side peak load = 8.839 kN*
- *0.8 Pu (yield load positive side)= 8.839 x 0.8 = 7.072 kN*
- *-ve Side Peak load = 19.743 kN*
- *0.8 Pu (yield load negative side)=19.743 x 0.8 = 15.794kN*
- *Average peak load = (7.072+15.794)/2 = 11.433 kN*
- β= 0.1
- D_5 = 0.15

Likewise the damage index for each cycle is calculated